UNIVERSITÀ
DEGLI STUDI
DI PADOVA

Sede Amministrativa: Università degli Studi di Padova

Centro di Ateneo di Studi e Attività Spaziali "Giuseppe Colombo" - CISAS

CORSO DI DOTTORATO DI RICERCA IN: Scienze, Tecnologie e Misure Spaziali

CURRICOLO: Scienze e Tecnologie per Applicazioni Satellitari e Aeronautiche

CICLO XXXIV

SIMULATION AND MODELLING TURBULENT SPRAY DYNAMICS

Thesis written with the financial contribution of China Scholarship Council (CSC)

Coordinatore: Ch.mo Prof. Francesco Picano

Supervisore: Ch.mo Prof. Francesco Picano

Dottornado: Jietuo Wang

Abstract

Turbulent sprays are complex multi-phase flows where two or more distinguished phases move together, mutually exchanging mass, momentum, and energy. These complex flows play a crucial role in many industrial applications and in a large variety of natural and environmental processes, whose significance has been further emphasized during the outbreak of the COVID-19 pandemic since respiratory events such as sneezing are kinds of turbulent sprays laden with pathogen-bearing droplets. Therefore, it is vital to achieve a satisfactory comprehension of the mechanisms governing the process and enhance the model capabilities for applications. The present dissertation investigates physics and modelling of the dispersion/evaporation of droplets within turbulent jet-spray conditions, employing both high-fidelity simulations as well as low-order modelling approaches.

To this purpose, the present research was firstly concentrated on the effect of bulk Reynolds number on the clustering and evaporation process of dispersed droplets within a turbulent jet by employing a solver based on a low-Mach number Navier-Stokes equations and the point-droplet approximation for the Lagrangian phase under the Direct Numerical Simulation (DNS) approach. A detailed and systematic analysis was reported in Paper I, where we discussed how lower is the evaporation rate with respect to what expected by the classical model. Using the DNS data as reference, the model capabilities for Lagrangian droplets evolution under the Large-eddy Simulation (LES) framework by considering the parcel concept has been analysed (Paper II). Then, the focus was moved to a more practical topic, i.e. virus transmission via respiratory droplets due to the sudden outbreak of the COVID-19 pandemic. Actually, the SARS-CoV-2 virus mainly spreads from an infected individual's mouth or nose when they speak, cough and sneeze, ejecting turbulent puff clouds carrying pathogen-bearing droplets of different sizes, from drops, $\mathcal{O}(1\text{mm})$, to small aerosols, $\mathcal{O}(1\mu\text{m})$. To better evaluate the exposure risk related to these respiratory droplets, accurate and computationally intensive LES of turbulent puffs emitted during sneezes in different environmental conditions were performed. The simulations showed how different could be droplet evaporation and virus exposure as a function of environmental conditions (Paper III). Inspired by previous findings showing an extended droplet evaporation time with respect to the widely used D^2-law model, a revision of the D^2-law has been proposed and tested against reference data from DNSs (Paper IV). On the footing of this revised D^2-law and an effective correction to the classical Stokes drag to account for droplet inertia as well as considering the latest research on turbulent jets and puffs, an integrated framework able to describe the evaporation-falling-travelling dynamics of respiratory droplets for different environmental conditions and respiratory activities are being put forward and used to assess the effectiveness of physical distancing and face coverings, which was elucidated in Paper V.

Keywords: Dispersed two-phase turbulent flows, diluted spray, evaporation, low-order modelling, respiratory droplets, virus transmission

Preface

This thesis deals with numerical and theoretical studies of evaporating droplets dispersed in turbulent spray conditions. A brief introduction about the relevance of the present work and the description of mathematical formulations, along with some important outcomes of this work, are presented at the beginning, which is followed by five papers appended. The papers' format has been altered to concede with the present thesis, but their contents are the same as their original counterparts.

Paper I Wang, J. , Dalla Barba, F., & Picano, F. (2021). Direct numerical simulation of an evaporating turbulent diluted jet-spray at moderate Reynolds number. *Int. J. Multiph. Flow*, 137, 103567.

Paper II Wang, J., & Picano, F. (2021). Assessment of the parcel model in evaporating turbulent diluted sprays within a Large-Eddy-Simulation approach. *in preparation.*

Paper III Wang, J., Alipour, M., Soligo, G., Roccon, A., De Paoli, M., Picano, F., & Soldati, A. (2021). Short-range exposure to airborne virus transmission and current guidelines. *Proc. Natl. Acad. Sci. U.S.A.*, 118 (37), e2105279118.

Paper IV Dalla Barba, F., Wang, J., & Picano, F. (2021). Revisiting D^2-law for the evaporation of dilute droplets. *Phys. Fluids*, 33(5), 051701.

Paper V Wang, J., Dalla Barba, F., Roccon, A., Sardina, G., Soldati, A., & Picano F. (2021). Modeling the direct virus exposure risk associated with respiratory events. *J. R. Soc. Interface*, in press.

January 2022, Padova

Jietuo WANG

Division of work between authors

The advisor of this project is Francesco Picano (F.P.). Authors' contributions for each paper are depicted as following:

Paper I J.W. was responsible for preparing the simulation setup, carrying out the simulations, analyzing the results and drafting the manuscript; Support for methodological analysis, code validation, data visualization and paper revision were implemented by F.D.; F.D. supervised, performed and designed the research, also revised and edited the paper.

Paper II The simulations and analyses were performed by J.W.; F.P. designed the research; The paper was written by J.W. with inputs from F.P..

Paper III M.A., M.D., F.P., and A.S. designed research; J.W., M.A., A.R., and M.D. performed research; J.W., G.S., and A.R. contributed new reagents/analytic tools; J.W., M.A., G.S., A.R., M.D., and F.P. analyzed data; and G.S., A.R., F.P., and A.S. wrote the paper.

Paper IV F.D. designed the research, conducted theoretical analysis, analyzed data and drafted the paper; J.W. performed simulations for validation, analyzed data and visualized results and edited the paper; F.P. supervised, designed the research and revised the paper.

Paper V J.W. performed the simulations, analyzed data and wrote the original draft; F.D. performed the formal and methodological analysis, A.R. analyzed data, performed research and wrote the original draft; G.S cured data and revised and edited the paper; A.S. and F.P. supervised, performed and designed the research; revised and edited the paper.

Conferences

Part of the work in this dissertation has been presented at the following international conferences.

Jietuo WANG and Federico DALLA BARBA & Francesco PICANO. *Assessment of the parcel model in LES of turbulent evaporating sprays.* BICTAM-CISM Symposium on Dispersed Multiphase Flows: from Measuring to Modeling. Online, March 02-05, 2021

Jietuo WANG and Federico DALLA BARBA & Francesco PICANO. *Evaporation of turbulent diluted jet at Re = 10,000 and assessment of the D^2-law model.* EUROMECH Colloquium 621: Transport and fluxes in dispersed turbulent flows. Online, June 30 - July 02, 2021

Jietuo WANG, Mobin ALIPOUR, Giovanni SOLIGO, Alessio ROCCON, Marco DE PAOLI, Federico DALLA BARBA, Francesco PICANO, and Alfredo SOLDATI, *Respiratory droplets dynamics: transport & low order modeling.* HZDR, 18th Multiphase Flow Conference – Simulation, Experiment and Application. Online, November 08-12, 2021

Jietuo WANG and Federico DALLA BARBA & Francesco PICANO. *DNS and assessment of the D^2-law for evaporation in turbulent diluted sprays.* APS-DFD, 74th Annual Meeting of the American Physical Society's Division of Fluid Dynamics. Phoenix, AZ, USA, November 21-23, 2021

Alfredo SOLDATI, Jietuo WANG, Mobin ALIPOUR, Giovanni SOLIGO, Alessio ROCCON, Maroco DE PAOLI, Fracncesco PICANO. *Short-range exposure to airborne virus transmission and current guidelines* APS-DFD, 74th Annual Meeting of the American Physical Society's Division of Fluid Dynamics. Phoenix, AZ, USA, November 21-23, 2021

Contents

Chapter 1

Introduction and Background

1.1 Introduction on turbulent spray

Turbulent evaporating sprays, characterized as a dispersed liquid phase being transported by a turbulent gaseous one, are encountered everywhere around us. As a challenging research area of fluid mechanics, this multiphase complex flow plays an important role in our modern life, ranging from automobile industry to respiratory disease transmission, and from agriculture to manufacturing. Despite the technical and scientific relevance of the problem, the understanding and modelling of the fundamental mechanisms regulating the evaporation and dispersion of droplets in turbulent sprays is still a challenging matter due to the unsteady, multiscale and multiphase processes involved in these complex flows. In automobile industry, for instance, an improved understanding of such processes would contribute significantly to the development of high-efficiency and low-emission internal combustion engines. In these applications, the liquid fuel is often directly injected into a hot-temperature and high-pressure combustion chamber where undergoes a phase transition, via primary and secondary atomization, followed by a fierce chemical reaction process within the turbulent gaseous environment. Such a complex process completes in a very short time inside the combustion chamber where many different multi-scale, multiphase and unsteady phenomena are involved. A typical example is the formation of pollutants which is related to the fluctuations of temperature and reactant concentrations. In particular, soot forms through a pyrolysis process in fuel-rich regions where high temperature subsists without enough oxidizer to react [11, 103, 166]. This phenomenology can be observed within droplet clusters, where the concentration of the fuel droplets can be even a thousand times higher than its bulk value giving rise to a peak in the fuel vapour concentration. Another recent instance relies in the transmission of respiratory infections, as highlighted in the COVID-19 pandemic. In fact, the SARS-CoV-2 virus, like many other respiratory diseases, spreads from an infected individual to other susceptible individuals through virus-laden droplets formed in the respiratory tract and emitted from the mouth and nose while breathing, speaking, singing, coughing and sneezing[138]. The size of these droplets span over a wide range of diameters: from large drops, $\mathcal{O}(1\ mm)$, to small droplets, $\mathcal{O}(1\ \mu m)$ [16, 36, 60, 138, 144, 215]. These droplets, released together with a puff/jet of buoyant moist turbulent air, are then dispersed in the surrounding ambient and exposure or inhalation of these droplets leads to a potential risk of infection [33, 34, 36]. The lifetime of respiratory droplets is controlled basically by the competition among gravitational forces, drag forces, and evaporation, whereas recent studies proposed the unrevealing importance of turbulent jet/puff on governing the droplet's fate[175]. Investigating the transport and deposition of these droplets is thus of fundamental importance to quantitatively determine the infection risks associated with the droplets' fate and design effective guidelines for disease transmission prevention, which is also beneficial to better prepare ourselves to tackle possible waves of the outbreak of COVID-19 or a similar disease in the future.

In this context, the present thesis focuses on the dynamics of dispersed evaporating droplets within a turbulent dilute jet-spray. The main goals in this work are to extend the fundamental understanding of this complex physical phenomenon, to improve the capability of existing models to accurately reproduce it, and eventually to utilize the knowledge obtained and models established to address practical problems, such as the virus transmission through respiratory droplets. In the following sections of this chapter, a general introduction about turbulent sprays is presented, including phenomenological descriptions, introductory concepts and relevant researches, which were not sufficiently discussed in the appended papers.

1.2 Structure of a turbulent spray

1.2.1 Macroscopic description of turbulent spray

In the following, the formation process of droplets from a column of liquid phase with a non-swirling turbulent jet is briefly described. For a comprehensive explanation of the overall evolution of a turbulent spray, the author recommends Lin and Reitz [115] and Jenny et al. [93]. When a high-velocity liquid flow are ejected from a nozzle-like exit into a quiescent environment, the development of fine spray driven by different physical mechanisms will go through five stages: (i) establishment of a jet; (ii) formation of liquid ligaments from the jet; (iii) fragmentation of ligaments into large droplets; (iv) further disintegration of large droplets into smaller ones with a stabilized size. In many engineering applications, liquid flow is supplied in the form of liquid sheets whose fragmentation into ligaments and disintegration into droplets can also be depicted by the simple concept above even though, the atomization process could be more complicated at each stage. The second stage, in particular, is not easy to treat and is beyond the scope of this study. Numerical approaches for this includes level-set[154], Volume of Fluid (VoF)[59], phase field method[190].

Fig.1.1 shows a schematic illustration of the atomization process of a liquid jet issuing from a round exit. Conventionally, the so-called primary atomization occurs close to the nozzle region where Kelvin-Helmholtz and Rayleigh-Taylor instabilities develop at the gas-liquid interface promoting the jet fragmentation and giving rise to a system of large droplets and ligaments enclosed within the environmental gas [126]. Further downstream, secondary atomization follows: the aerodynamic forces, arising as a consequence of the relative inter-phase velocities, causes interface instabilities that lead to a further disintegration of droplets and ligaments into even smaller fragments [93, 126]. In the zone near the injector, mean fractional volume of the liquid phase is so close to $\mathcal{O}(1)$ that the liquid phase cannot treated as *dispersed* elements. Away from the injector, as the thick liquid sheets engulf the surrounding gas and become unstable, the void fraction starts to increase with the formation of ligaments and large droplet. Zones characterized by these processes are termed as dense spray region, where the volume fraction of liquid is still high, droplet deformation and collisions are dominant, and the vaporization rate is negligible. The dense regime terminates when the surface tension prevails on aerodynamic stresses preventing a further fragmentation [93]. Further

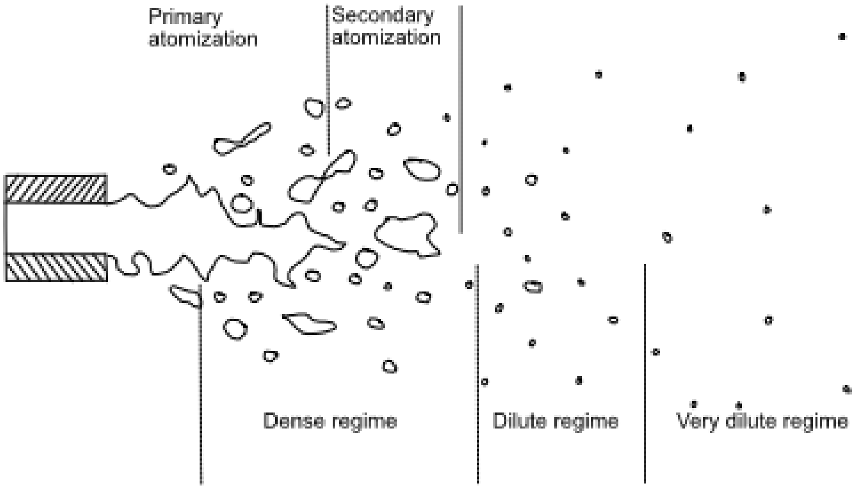

Figure 1.1: A schematic diagram of various flow regimes and atomization processes of a round liquid jet issuing into stagnant gas (taken from [93])

downstream, a dilute regime establishes where the liquid volume fraction is small enough that the droplet mutual interactions, such as collisions and coalescence, can be neglected [70], and the vaporization process becomes significant as most of liquids evaporates at this stage of the turbulent spray evolution [67]. In the dilute regime, small droplets evolve preserving a spherical shape due to the dominance of the surface tension on aerodynamic stresses [64, 70, 93]. Even though the presence of liquid phase still exerts a considerable effect on the flow in terms of mass, momentum, and energy balance, in dilute conditions the droplet size is usually below, or comparable to, the dissipative scales of the turbulent flow. In these conditions the point-droplet approximation is widely accepted and the hybrid Eulerian-Lagrangian framework is considered suitable and reliable for the numerical description of problem [64]. In this framework, the mass, momentum, and energy exchanges between the Eulerian carrier phase and Lagrangian point-droplets can be accounted for via distributed sink-source terms in the right hand side of the balance equations governing the Eulerian phase while the droplet kinematic and thermodynamic variables are evolved in the Lagrangian frame [39, 51, 57, 64, 127]. Details about the regimes classification on particle-laden flows and correspondent approaches to model these drops can be found in Sec.1.2.4.

1.2.2 Turbulence

All of the aforementioned processes within a spray take place within the underlying role played by turbulence. Actually, turbulent flows, characterized essentially by irregularity, unsteadiness and chaos, are involved in most natural phenomena and engineering applications. This temporal-spatial randomness of turbulence leads to a really challenging problem when one tries to predict it with a deterministic approach. Meanwhile, turbulence is capable of efficiently transporting and mixing fluids due to the richness of vortical structures (eddies) occurring on multiple length scales, which is of primary importance in many applications. Reynolds [170] firstly distinguished the turbulent dynamics by observing the motion of dye ejected into a long pipe full of water. Later Reynolds [171] established that a fluid medium is characterized by a single dimensionless parameter, Re (Reynolds number), and the turbulence likely develops when this parameter exceeds about *4,000* in pipe flows.

The definition of Re is quantitatively described as follows:

$$Re = \frac{UL}{\nu}, \tag{1.1}$$

where U and L are the characteristic velocity and length scale of the flow, respectively, with the kinematic viscosity being denoted by ν which is the ratio of dynamic viscosity μ and density ρ of the flow, i.e. $\nu = \mu/\rho$. The Reynolds number indicates the relation between inertial and viscous forces; large Re number generally indicates the dominance of the inertial effect over the damping action of the viscosity, resulting in a high level of turbulence. Stronger the turbulence, the higher the mixing. That is the reason why the automobile industry always attempts to increase the injection pressure of the fuel supplied, so stronger turbulence promotes the rapid mixing of liquid fuel with the oxidizer, leading to higher combustion efficiency[4].

According to the concept introduced by Richardson [172], a hierarchy structure of eddies with a wide range of sizes exists within developed turbulence. This concept, termed as *energy cascade*, provides a qualitative picture about how the turbulent energy of the overall flow is transferred from large scale eddies to smaller and smaller ones through a breaking-down mechanism. In the *energy cascade* concept, kinetic energy enters the turbulent motion through the production mechanism at the largest scales comparable to the characteristic length scale of the system L_0. These eddies of large scale lose their stability and create smaller eddies inheriting kinetic energy from their *parent* eddies. This cascade process persists until a very small scale is reached where the kinetic energy initially acquired from the largest eddies is dissipated into heat due to the viscous action. Kolmogorov [106] advanced this scenario and quantified the size of the smallest eddies that are responsible for dissipating the energy. Kolmogorov hypothesized that, at sufficiently high Reynolds number, the small-scale turbulence is statistically isotropic, and its statistics have a universal form that can be determined by two parameters, namely the kinematic viscosity, ν, and the dissipation rate of the turbulent kinematic energy, ϵ. The demarcation length scale, L_{EI}, used to separate the isotropic small eddies and the anisotropic eddies is around $\frac{1}{6}L_0$ with L_0 being the largest size of eddies[163]. Provided the two parameters, the smallest scales, often referred to as Kolmogorov scales, can be defined as follows:

$$\eta = (\frac{\nu^3}{\epsilon})^{1/4} \tag{1.2}$$

which becomes smaller and smaller as the Reynolds number is increased. Below the length scale L_{EI} occurs the universal equilibrium range which, according to the second similarity hypothesis[163], could be divided into two subranges, i.e. inertial subrange and dissipation range, by a length scale $L_{DI} \simeq 60\eta$. In the inertial range, with scales ranging from L_{DI} to L_{EI}, the effect of inertia on the energy dissipation is predominant. Below the lower limit of the inertial subrange, the inertial effect of the fluid is not significant anymore so that the turbulent motion in this range ($< L_{DI}$) experiences significant viscous effects.

Concerning the particular properties of turbulence, such as randomness, irregularity, unsteadiness as well as richness of temporal-spatial scales, a simple analytical theory to calculate quantities of interest and practical relevance is infeasible. In this context, various numerical approaches or models have been developed and advanced with achieving the goal of obtaining the relevant properties of the turbulent flows. A particular example is the Reynolds averaged Navier-Stokes (RANS) method, which has been widely and mainly applied in the industrial area due to its simplicity in performing prediction on complex geometries. In this technique, the unsteadiness of flows is averaged out, and the effect of the fluctuation on the mean motion must be modelled, which is achieved by decomposing all quantities of the flow into a time-averaged value and a fluctuating one. The decomposition process introduces unknown terms. The conventional closure models for these unknown terms include a Reynolds stress model (RSM) or a turbulent viscosity model, such as $\kappa - \epsilon$[95]. RANS does demand lower computational power but involves complicated models, and detailed information about the flow structure are not accessed. In contrast, the Direct Numerical Simulation (DNS), which resolves all length and time scales present in turbulent flow, has shown its capability to capture the whole physics of turbulent flows in order to understand the complex phenomena involved[127]. Since no modelling is applied, the approach requires computational resources prohibitively expensive in some contexts, when high Reynolds numbers conditions or a large number of degrees of freedom are involved. However, investigations using this direct approach are still limited since the size of meshes needs to be extremely small so as to capture a cascade of energy in a realistic manner. Considering the request of finite computation resources and reasonable prediction details, Large Eddy Simulation (LES), which lies between DNS and RANS, represents an alternative. In LES, as in DNS, the large-scale energetic turbulent motions are directly solved while the effects of the sub-grid scale (sgs) motions on the resolved flow field must be modelled. This is based on the rationale that the structure of large eddies in turbulent flows is generally characterised by geometry while that of small eddies is more universal. A detailed discussion is referred to Sec. 1.2.6.

1.2.3 Free round-jet

Before moving onto the multiphase dynamics, being turbulent sprays initially jets so free shear flows, they inherently own the general properties of turbulent flows and exhibit their unique features. In a classical picture, we can consider a Newtonian fluid originating from a round shape exit with a diameter D and flowing into a quiescent environment. As air from the irrotational surrounding fluid is entrained into the jet due to the high vortical activity arising in outer regions, the jet *grows up* in the radial direction, denoted as r, with axial distance, denoted as x, along which the jet velocity decays. During the spread and decay process, the momentum flux remains constant while the mass flux, as it must, increases along the axial direction. A sketch shows the flow field structure of a jet issuing from a round-shape nozzle, see Fig.1.2. Generally speaking, three regions can be defined with downstream distance in an axisymmetric round jet, which are the near field, the far field, and the intermediate field between the other two.

The near field ($x/D \leq 10$) is a region where a potential core appears together with the establishment of vortical structures in the shear layer due to the initial instability created by the jet. Initial conditions also affect the mean velocity profile at the exit. George [80] argued that the differences observed in the far field could be attributed to the difference in the large-scale vortical structures created in the near field that propagate into the fully developed region. Beyond the near field is the transition/intermediate region ($10 \leq x/D \leq 30$) where appears the Re-dependent evolution and interaction between the energetic vortical structures. From an engineering view, this region affects the transfer of mass, heat, and momentum, thus it can benefit practical applications, such as fuel-air

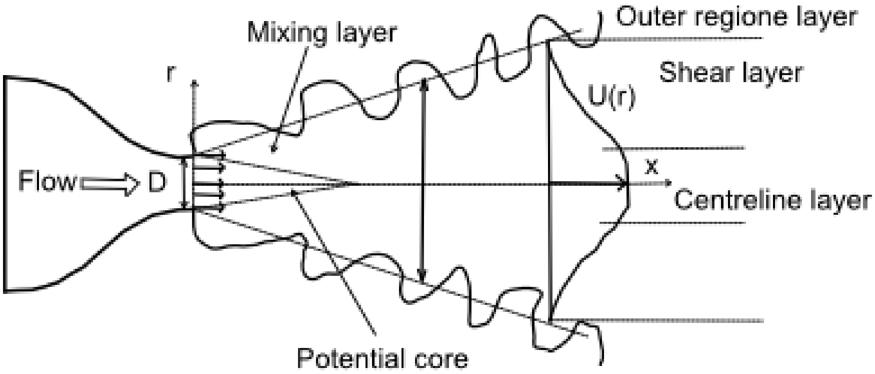

Figure 1.2: A sketch of the free round-jet issuing into the stagnant air (taken from[17])

;

mixing, by controlling the flow evolution in this region. Researches focusing on these two fields of the turbulent jet can be separated into two points: the effect of initial conditions and controlling the large-scale vortical structure arising from the near field[111].

The far field (x/D≥30) is the fully-developed region where the flow is featured as self-similar and equilibrium. In this region, the variation of centreline velocity, $U_0(x)$, and the jet's half width, $r_{1/2}$, , could be scaled as:

$$\frac{U_0(x)}{U_J} = \frac{B}{(x-x_0)/D}, \tag{1.3}$$

$$r_{1/2}(x) = S(x-x_0) \tag{1.4}$$

with B being velocity decay constant, ~6 [163]. x_0 indicates the virtual origin from which the self-similar solution approached by a round jet can be represented by a flow induced from a point source of momentum[54]. $r_{1/2}(x)$ is the lateral position where the local velocity is half of the centreline velocity and S is the spreading rate. Meanwhile, the axial gradient could be smaller than its counterpart in the radial direction, resulting in the legitimacy of thin shear layer approximation by considering an appropriate scaling. Recent research works carried out by Burattini et al. [40, 41] and Thiesset et al. [202] improve current understanding of turbulent round-jet, in particular scale-by-scale energy budget and equilibrium similarity on the far field. For other research details related to the turbulent free round-jet, an exhaustive review was delivered by Ball et al. [17], especially focusing on characterization, entrainment, effects of the initial conditions and similarity, length scales, spectral analysis and coherent structures. Kaushik et al. [102] reviewed the CFD studies performed in the last few decades to show the controlled and uncontrolled jet characteristics.

1.2.4 Dispersed particle/droplet

Regimes

The turbulent flow itself is a problem notoriously difficult to solve, so the move-in of a second phase makes it even more challenging. Indeed, the complexities introduced by dispersed phase range from the multiway coupling method between particles/droplets and the carrier flow, to the properties of particles/droplets, like shape, size, deformability and number etc. Due to the vastness of subject matter, only small rigid spheres carried by turbulent flows are of interest in the present work. It should be noted that small droplets behave as rigid spheres. Comprehensive reviews on this topic have been done by Balachandar and Eaton [15], Brandt and Coletti [38]. Here, the author simply describes different regimes characterizing the interaction level between two phases and the simulation/modelling methods for dispersed particles. Particular attention will be given on the dilute regime whose definition is detailed below.

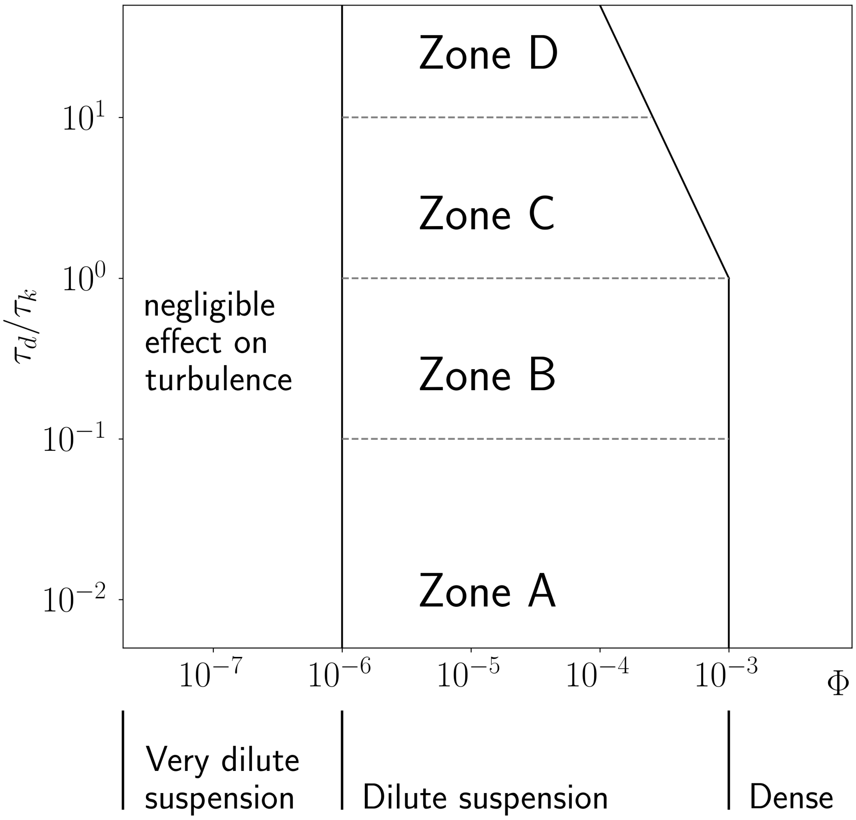

Figure 1.3: Classification map of particle-laden turbulent flows (Figure taken from [64, 65])

Elghobashi [64], based on the experimental and Direct Numerical Simulation (DNS) data of particle-laden flows at the time, proposed an original two-dimensional map classifying multiphase flows. Then, the classification map has been slightly modified by Balachandar and Eaton [15], Elgobashi [65], and largely enriched into three-dimension by Brandt and Coletti [38] recently. Fig.1.3 is a regime diagram, reproduced from [65], showing the different regimes characterizing the particle-laden flows. In order to depict the interaction level between the particles and carrier flows, three regimes are defined according to the critical parameter Φ, the volume fraction occupied by the dispersed particles (some researchers prefer the mass loading Ψ, defined as the mass ratio between two phases). In this context, low Φ ($\leq 10^{-6}$) represent a *very dilute suspension* regime where the volume fraction of dispersed particles is so small that interactions between particle-particle and particle-flow are negligible and the overall particle inertia so small that the presence of inertial particles scarcely changes the dynamics of carrier flow. This regime is often termed as the one-way coupling regime, where particle dispersion is dominated by the state of turbulence but the reciprocal influence is insignificant. Increasing Φ up to 10^{-3} (or the mass of two phases is comparable) will inevitably lead to the so-called *dilute suspension* regime in which, except for the influence exerted from the carrier phase to the dispersed one, the global particle inertia starts to play a significant role in modulating flow dynamics, and the mutual interaction between particles is still unimportant. In this regime, inertial particles could modify the turbulence dynamics and vice versa (thus termed two-way coupling). Meanwhile, within the dilute suspension regime, several zones can be categorized by taking into account Stokes number St, defined as the ratio between characteristic particle relaxation time τ_d and the timescale τ_k characterizing local velocity fluctuation in the turbulence (here k denotes Kolmogorov timescale). When particle Stokes number is of the order $\mathcal{O}(1)$, a striking phenomenon called inertial clustering becomes extremely strong, which will be detailed in section(1.2.4). Back to the Fig.1.3, further increasing the particle loading ($\Phi \geq 10^{-3}$) in the flows will finally enter the *dense suspension* regime where, in addition to the two-way coupling between the dispersed particle and carrier flows, particle/particle interactions (such as break-up, agglomeration and collision) take place, hence called four-way coupling. It is worth noting that a demarcation line between the dilute regimes and dense regime shifts towards lower Φ, as Elghobashi [64] argued, due to the increasing tendency of particle/particle collision to emerge at higher values of τ_d/τ_k. In the case with very large particle loading, i.e. $\Phi \sim 1$, the interparticle collision play a dominant role, called granular flow regime which is not visible in Fig1.3.

As mentioned above, within the dilute suspension regime at a given Φ value, there are several zones, depending on the particle Stokes number $St = \tau_d/\tau_k$, as showed in Fig.1.3. For each Zone, multiscale modelling approaches to simulate the turbulent flows bearing particles have been developed and summarized in Ref.[15]. In Zone A, the Stokes number of dispersed droplets is so small (up to $\mathcal{O}(10^{-1})$) that their motion is assumed to be ruled exclusively by the surrounding carrier phase, leading to an almost overlap of trajectory between particles and the local fluid. These droplets/particles were referred to as microparticles in Elgobashi [65] who shown that these tracers-like particles could increase both turbulence kinetic energy (TKE) and its dissipation rate (ϵ) relative to values in particle-free flows. Therefore, one can consider the particle-laden flows characterized by these features as a single-phase fluid, and use the dusty gas approach [44, 122] or equilibrium Eulerian approach [71, 73] to simulate it. In addition to solving the mass, momentum, and energy equations of the 'mixture', the former approach simply takes into account the mass fraction equation of dispersed phase, whereas the velocity field of particles is also explicitly expressed in the latter, resulting in a more accurate prediction of the slip velocity of moving particles and, hence, potentially capturing physical phenomenon like inertial particle clustering[168]. Balachandar and Eaton [15] claimed that the principal advantage of this method is the computational simplicity. Given $St \leq 0.2$, quite accurate simulation results could be obtained[72, 167, 185]. Increasing the St, we move out from Zone A and enter a new Zone B where the single-fluid approach is insufficient to reproduce the dynamics of two-phase flow since these dispersed particles, named as *ghost particles* in [65], are capable of modifying the turbulent energy spectrum. Instead, the Eulerian approach, treating the particulate phase in a continuum way as the carrier one, is applicable[53, 75]. The properties of dispersed particles are represented as fields. In this context, mutual interaction between two phases could be taken into account in the two-phase approach by adding source/sink terms obtained from the Eulerian fields of particles to the carrier phase formulations. The merit of dealing with the dispersed particles in such a continuum way is to relax the limitation of Stokes number imposed on the dusty gas/ equilibrium Eulerian method[15]. The Eulerian approach, nevertheless, becomes computation-expensive when the particulate phase with a wide range of sizes are of interest in the particle-laden flows, demanding the use of the probability density function approach to derive the governing equations[76].

Concerning particles with higher Stokes number ($1 \leq St \leq 10$) and small size (compared to the Kolmogorov length scale of the flow), Zone C in Fig.1.3, they do not respond to fast fluctuations of the surrounding fluid as quickly as microparticles do but deviate from the trajectories of the surrounding fluid. Elgobashi [65] referred particles in this range of St as *large particles* who are potential to reduce the local TKE and ϵ relative to that of particle-free flows. While microparticles tend to be trapped within the vortical structure of turbulent flows, *large particles* cross these structures and preferentially populate in regions featured by high local strain-rate. To address particles in this range, one can resort to the Lagrangian point approach in which a Lagrangian description of particles is adopted and information for all particles, such as position, mass, momentum, is independently obtainable by solving equations on each Lagrangian element. This approach is especially favourable in the context where the polydispersity of dispersed particles introduces a wide range of time and length scales. Other advantages of the Lagrangian point approach over its Eulerian counterpart compose of the capability to capture the size-dependent information of dispersed particles, no fundamental restriction on St number because of the uniqueness property, and minimizing numerical diffusion in dispersed-phase field[198]. Along with many advantages offered by the Lagrangian point approach, opportunities for improvement in some aspects exist. For instance, the effects of dispersed particles on the carrier flow are modelled through localized sink/source terms, which means enough particles in each cell is required to have a smooth feedback force from the particles[147, 198]. The Lagrangian point approach as well as other aforementioned methods, explicitly or implicitly, assume that the particle size is much smaller than the smallest undisturbed flow scales of the surrounding flows. Above the limit of Lagrangian point-particle approximation, $St \sim 10$, is Zone D, where the typical size of particles within turbulence could be comparable or larger than the Kolmogorov scales of the carrier phase, termed as finite-size particles. A fully resolved method, in this context, is required to completely resolve all the scales of the ambient fluid and flow scales introduced by dispersed particles. The main restriction of this fully resolved approach to be applied is the particle number seeded into the carrier flow[15]. Comprehensive reviews on this topic can be found in Brandt and Coletti [38].

In the present work, as discussed in the methodology chapter, we employed the two-way coupling method by imposing a low-Mach number approximation for the Eulerian carrier flow and Lagrangian point-approach for rigid spherical particles/droplets.

Preferential concentration

When the movement of small inertial particles is of interest in turbulent flows, an attractive characteristic is the preferential concentration of particles denser than the carrier fluid, forming clusters and void regions, which is also known as inertial clustering. The complexity of this phenomenon[130] has drawn considerable attention from the community of fluid dynamicists, leading to a very large number of laboratory experiments, numerical simulations and theoretical studies with a specific purpose to understand the mechanisms controlling inertial clustering, quantify the structure or properties characterizing the clusters, and analyze the effect of this striking phenomenon on others, such as particle collision and coalescence, droplet evaporation, turbulence modulation, etc. For more details, readers are referred to exhaustive reviews on this topic in [15, 38, 61, 143]. Here, the author would like to give a concise description of the mechanisms proposed and characterization methods related to this phenomenon.

The most intuitive explanation of inertial clustering is often cited as centrifuging effect: particles denser than the fluid, due to their inertia, are prone to be centrifuged out from vortical structures and easily trapped in convergent regions of the flow. Considerable evidence has been provided supporting the highly correlated relationship between regions characterized by low enstrophy and high strain-rate, and regions of high population density of heavy particles. Bec et al. [23], setting random flow fields with Gaussian statistics, performed simulations to investigate the setting velocity of inertial spherical particles. He showed that the divergence of particle velocity field is positive in regions where the vorticity dominates, and, consequently, inertial particles tend to concentrate in high strain-rate/low enstrophy regions. Squires and Eaton [195] tracked inertial particles in a DNS of forced homogeneous turbulence, finding the move intensive preferential concentration for Stokes number (based on integral scale) of 0.15, with peak concentrations over 30 times the mean. Tanaka et al. [200] found strong correlation between particle concentration and vorticity iso-contours in qualitative visualizations obtained from *DNS* results. Bec et al. [23], via analyzing the relative fraction of particles in the vortical regions as a function of Stokes number St_κ in a three-dimensional DNS, found that relative particle number tends to decrease in vortical regions as the St_κ close to unity, indicating a movement of heavy particles towards regions dominated by high strain-rate. Gibert et al. [83] measured the mixed particle velocity–acceleration structure function in a von Karman flow and showed trends consistent with inertial clustering in high strain-rate regions. However, inertial clustering is most intensive as St_κ close to $\mathcal{O}(1)$ below which the small particle inertial is sufficient enough to drive them from vortices[20]. At a higher Stokes number, the centrifuging effect is not that relevant to explain clustering. To cover this lack, a new explanation, known as *sweep-stick* mechanism, was put forward by CHEN et al. [46] who found, in two-dimensional turbulent cases, a strong correlation between the inertial particle sampling and zero-acceleration points in a wide range of scales. As they explained, zero-acceleration points moving with the local velocity of flows are *swept* by the fluid; and particles that meet a zero-acceleration point moves with the fluid velocity (referred as *stick*), forming clusters in their vicinity. Coleman and Vassilicos [52] argued that, in the inertial range, inertial clustering establishes from large-eddy structure sweeping smaller ones, which means the *sweep-stick* mechanism even hold in large scales independent of Stokes number. On the other hand, as the centrifuging effect is only dominant for the small Stokes number regime ($St \ll \mathcal{O}(1)$), [37] argued that, outside this regime, a reasonable explanation could be the path-history mechanism: inertial particles can retain a short memory of their interaction with turbulence at earlier times along its path history, displaying important contribution to determine droplets velocity at the current time and generating clusters. The significance of history effects was also emphasized by Gustavsson and Mehlig [87], Liu et al. [119].

As the preferential concentration of inertial particles appears over a wide range of scales in turbulence, several mathematical tools have been developed to characterize this phenomenon. Readers are referred to find more comprehensive reviews in [1, 143]. Here, only the most widely used approaches are listed together with representative research works where they were employed:

- **Clustering index (CI)**: The definition of CI as the variance-to-mean ratio of particle number in a specific area/volume is naturally built on the property of Poisson distributions whose variance is equal to the mean. This method was introduced to cloud physics by Baker [13], and, recently, used to quantify the clustering in spray dynamics[57, 206]. As A. et al. [1] suggested, particular caution should be taken when one interprets this approach. Due to its inherent volume dependence, it presents contributions from a range of spatial scales instead of a unique one.

- **Box-counting method**: This method is actually an improved approach based on the clustering index mentioned above. Certain spatial bins with a specific size are employed to count particle numbers, and correspondent Probability Density Functions per box are compared to the Poisson distribution. Using this approach, Aliseda et al. [5], Fessler et al. [74] showed evidences supporting Wang and Maxey [207]'s observations that clustering become more intensive for Stokes number near $\mathcal{O}(1)$. Similar to the clustering index, this method is dependent on the length scale chosen to define the spatial volume counting the particles.
- **Correlation dimension**: This correlation dimension is an extensively used approach in the field of dissipative dynamic system theory and was introduced to characterize the particle clustering by Bec et al. [22]. It is essentially defined as the small-scale power-law scaling of the probability to find two particles separated by a given distance and was used in the context of particle clustering by Bec et al. [21, 22].
- **Radial distribution function (RDF) or pair correlations**: The RDF, also very often cited as pair correlation[1, 143], is typically defined as the probability of finding a second particle at a certain radial distance away from a reference particle, compared to a case where particles are homogeneously sampled. This method has a great advantage in quantifying turbulence-driven clustering of particles or droplets in a scale-by-scale way, and thus has been extensively employed to investigate this complex phenomenon[86, 158, 182, 217, 224]. However, as Baker et al. [14] argued, the RDF is essentially calculated over whole particle fields without taking into account individual clusters, providing information more global than local.
- **Voronoi diagram**: Monchaux et al. [142] introduced the use of Voronoi analysis to quantify the clustering in the context of particle-laden flows. The n-dimensional space is uniquely decomposed into independent cells attached to each particle, with each Voronoi cell containing an ensemble of points closer to the reference particle than any other. If particles are randomly distributed in the space, the probability density function of the cell size is close to a Γ function, whereas inertial particles will show a broader PDF[38, 69]. The main advantage is that the inverse of the volume of each Voronoi cell is strictly equal to the local particle number density, allowing evaluate the local particle distribution at a self-adapted spatial scale. Baker et al. [14] also mentioned the high computing efficiency of the Voronoi diagram, even dealing with a very large set of particles. This method has received considerably positive responses from the community in this field, and several researchers have used it to study the particle clustering in turbulence flows[151, 158, 165, 199, 211, 220]. However, the Voronoi diagram is not recommended to use when particle number density is low since it tends to subsampling bias, affecting some important observables[38, 140, 141].

1.2.5 Evaporation of turbulent sprays

Droplets evaporation within sprays involves mass and heat exchange processes in a turbulent environment, thus being of great significance for practical applications. In combustion systems, for instance, the droplet vaporization process is the governing factor for combustion. Another example is the evaporating respiratory droplets whose fate could be directly linked to virus transmission. Early studies focused on the evaporation process of a single droplet in a quiescent atmosphere where the so-called D^2-law controls the evaporation rate of a liquid droplet. The origin of the D^2-law could be traced back to the theoretical work of Langmuir [110] who, after analysing the experimental results of Morse [145], put forward the proportional relationship between the mass loss rate of a spherical drop and its radius (also to diameter) by assuming the analogy between the diffusion and conduction heat transfer. This framework, later, was complemented by Spalding[192, 193] who considered the inward conduction of partial reaction heat to provide the latent heat of droplet vaporization in a combustion context. According to the D^2- law, droplet temperature is unchanged during the evaporation process, and its surface decreases linearly with time, determined by an evaporation rate constant which is dependent on the thermal-physical properties of the droplet itself and the surrounding air, due to the rapid mixing assumption. Due to its simplicity, D^2-law, since introduced (over 100 years), has received the most attention and has been applied in many research applications, e.g. non-reactive and reactive evaporation of liquid droplets[194, 212, 213]. However, recent researches reported significant deviation of droplets evaporation behaviour from this classical model[31, 32, 55, 123, 206]. A big step of the infinite conductivity model came from Abramzon and Sirignano [3]'s work in which the effects of Stefan flow on heat and mass transfer between the gas and droplet are taken into account. Indeed, the influence of Stefan flow on the evaporation process is essential, especially in the case that the partial pressure of vapour in the surrounding gas is not small compared with the total pressure[58]. In the Abramzon-Sirignano model, named by the two authors, two correction factors were introduced to consider the relative thermal conduction and diffusion variation of gas-liquid film thickness due to the Stefan flow. The basis of this consideration is that the rates of molecular transport by thermal conduction or diffusion going through the film should be equivalent to the real intensity of convective heat or diffusive mass between the droplet surface and the surrounding flow. This model is robust, as they claimed, that could be employed in very low Reynolds number situations as well as boundary layer cases[30]. Chen and Pereira [47] applied both the rapid mixing model (D^2-law) and the Abramzon-Sirignano model in many-droplet spray calculations and showed that the latter approach could provide superior agreement with the experimental results. Pinheiro and Vedovoto [160], by assessing droplet evaporation models mostly employed in spray combustion situations against the benchmark data from experiments, concluded that the Abramzon-Sirignano model is the only choice since it does not overestimate the evaporation rate for any environmental conditions. Bellan and Harstad [25] argued that the non-equilibrium phenomena which appear in the gas-droplet interface should be taken into account in modelling droplet evaporation. This statement originated from their previous finds on modelling droplet combustion that the non-equilibrium evaporation behaviours prevail when a high evaporation rate presents[26], which was consistent with their later observations about remarkable non-equilibrium effects on droplets size usually found in practical spray calculations[136]. On the root of these shreds of evidence, Miller et al. [136] fully described a model based on the non-equilibrium Langmuir-Knudsen evaporation law, assuming a non-uniform temperature distribution across the droplet radius. In the same work, they also evaluated a number of well-established evaporation models that are usually used in simulating turbulent sprays. They showed that most of these models behaved almost identical performance when the evaporation rates were relatively low. Nevertheless, the non-equilibrium evaporation framework agrees most favourably with a broader range of experimental measurements for the temporal evolution of droplets size and temperature. Sirignano [188] classified droplet vaporization models into six types, from the simplest D^2-law to the most challenging Navier-Strokes solutions, among which the difference is the treatment of the heating of liquid phase that is generally the rate-controlling phenomenon in droplet evaporation, especially in high-temperature ambient conditions.

Together with the development of theoretical description and modelling approach of droplet vaporization, the interaction between evaporating droplets and the ambient air is another highlighted research topic. Mashayek [127, 128] simulated the dispersion of evaporating droplets within compressible homogeneous turbulence using the two-way coupling method. 5.5×10^5 Lagrangian particles were tracked. They found largest vaporization rate in the regions characterized by the highest strain rate; the evaporation rate decreased as the initial droplet diameter, latent heat, boiling temperature or initial mass faction increased, and the rate increased as the environmental temperature increased. Birouk and co-workers [31, 32] measured the vaporization rate of suspended alkane droplets in homogeneous isotropic turbulence with zero mean relative velocity between the gas and droplets. They found a linear relationship between droplet surface with time but the evaporation rate constant, e.g. the slope of D^2 v.s. time, increased with Reynolds number. Reveillon and Demoulin [169]performed DNSs to study a forced isotropic turbulent flow laden with evaporating droplets with the one-way coupling method. They showed that droplet clusters are formed due to the turbulence, resulting in higher local vapour concentration and, in turn, slowing down the droplet vaporization rate. Independent of the initial Strokes number, three stages of droplets evaporation process were defined: single-droplet mode with a nearly D^2-law decay rate, cluster mode where droplets are embedded in vapour pocket close to saturation, and gaseous mode with the vapour evolution being controlled by the classical turbulent mixing. Dalla Barba and Picano [57] performed DNS of a saturated turbulent jet laden with evaporating droplets, aiming to investigate the effects of entrainment and clustering on the vaporization and spray properties. They find that, near the nozzle, clustering occurs due to fluctuations near the shear layer due to the entrainment; the surrounding droplet-free air gets entrained, leading to high number density fluctuations. Further downstream, they observed clustering attributed to a combination of inertial effects and intermittent dynamics in the boundary layer. Experimental evidence was also reported by Sahu and co-workers[176, 177], who showed that the formation of droplet clustering slows down the evaporation rate of acetone droplets in a turbulent spray. They attributed that to the compression of inter-droplets distance and the resulting higher vapour concentration from neighbouring droplets.

1.2.6 LES modelling of Turbulent sprays

Turbulent sprays in applications and environments occur at a very high Reynolds number, e.g. the exhalation process during violent respiratory events such as cough and sneeze can generate puff-like turbulent jets with Reynolds number of the order 10,000[33], which can be even higher for the fuel injection process in a typical turbine combustor[132]. DNS, in these cases, is inapplicable since the computational cost increases as the cube of the Reynolds number. With the aim of accurate and reliable results of the dynamics of turbulent flows, LES has emerged as a promising approach that solves the spatially filtered conversation equations and has been extensively employed to study various aspects of particle-laden flows ranging from dispersion, evaporation, vapour mixing and combustion[93]. The key of LES approach is to use a *filter* to separate the resolved, large-scale eddies (containing predominantly of energy and anisotropy) from the small-scale, dissipative turbulent motions (universal property), which need to be represented by simple models. The scale at which filtering occurs is the numerical grid size, below which the physics and mechanisms are modelled, known as sub-grid scale (*sgs*) modelling. Much of the pioneering work on LES focused on modelling the sub-grid Reynolds term arising during *filtering* the momentum equation, among which the most common model came from Smagorinsky [189] based on the eddy-viscosity hypothesis. Yoshizawa [218], Germano [81], and Moin et al. [139] made substantial contributions on *sgs* modelling on the basis of Smagorinsky's work, known as the dynamic Smagorinsky model for compressible flow. In order to obtain the *sgs* viscosity, Yoshizawa and Horiuti [219] put forward a *sgs* kinetic energy equation, in which Kim and Menon [105] employed a local dynamic model to compute the modelling parameters. These eddy-viscosity models implicitly assume a unidirectional transfer of energy from the resolved part to the subgrid-scales side, whereas the energy transfer from subgrid to resolved scales could be facilitated by the actual *sgs* Reynolds stress, referred as 'backscatter' in isotropic turbulent flows[43, 121]. To address the 'backscatter' issue, Chumakov and Rutland [50], Lu et al. [121], Pomraning and Rutland [162] developed and enhanced a dynamic structure model by introducing an *sgs* tensor obtained from the *sgs* kinetic energy. Useful overviews of LES approaches for single-phase flows are given by Piomelli [161].

In two-phase flows such as turbulent sprays, considerable contributions have been made in employing LES approaches to investigate the multiscale interaction between phases. One of the essential components of theis application is the modelling of *sgs* motion of the dispersed phase. In an Eulerian-Lagrangian framework, the dynamics of particles or droplets are predominantly affected by the interactions that occur between the dispersed phase and turbulent motion at the particle scale. When the spatial filtering is applied, the dispersed phase is prevented from interacting with the unresolved turbulent motion, which, in principle, cannot be neglected unless the LES is well resolved (namely, energy fraction removed from the turbulent flows is insignificant)[9]. Multiple pieces of evidence have been provided that the unresolved flow structure should be taken into account in order to get accurate predictions on droplets dynamics such as preferential concentration (see 1.2.4)[108, 137]. The first attempt to account for the effect of *sgs* flow velocity on droplet motion came from Wang and Squires [208] who incorporated to the droplet motion equation a *sgs* component of flow velocity obtained with the local subgrid kinetic energy. Since this seminal work, many *sgs* models for the dispersed phase sprang up. These models, according to [109, 124], could be classified into two groups: stochastic models, which are designed to regain the whole *sgs* velocity field by introducing a stochastic noise to the motion equation of particles, and the structural models, which aim to reconstruct some statistical features of the *sgs* velocity field using approximate deconvolution of resolved flow fields. Amiri et al. [6], considering three different stochastic models, performed LESs of particle-laden channel flow, highlighting the importance of temporal correlation of *sgs* components and flow anisotropy, especially in the near-wall region. By assuming the analogy to turbulent dispersion model developed for the Reynolds-averaged Navier-Stokes equation[66], Shotorban and Mashayek [187] proposed a Langevin-equation-based model for the subgrid fluid velocity *seen* by the droplets, which works well for droplets with small inertia. On the basis of the same Langvien equation, Pozorski and Apte [164] proposed a stochastic model for residual flow velocity based on the *sgs* turbulent kinetic energy. However, the statistics of the *sgs* fluid motion *felt* by droplets used to close the Langvien equation are different from those of the *sgs* fluid, which was assumed the same in Shotorban and Mashayek [187]'s work. The authors recommended to use it in situations involving large inertia particles. Bini and Jones [28][27] proposed a Brownian-like model in order to represent the direct influence of unfiltered flow velocity on the *p-th* stochastic particle, which was achieved by introducing a non-linear subgrid force term to account for the far from Gaussian behaviour of particle acceleration observed in experiments. They showed the capability of the proposed model in accurately reproducing droplet dispersion in a particle-laden turbulent mixing layer. After that, this particle dispersion model has been used to study turbulent sprays[29, 97], focusing on the *SGS* statistics of droplet dispersion. Structural models, on the other hand, are developed to reconstruct the subgrid flow velocity in an approximation deconvolution method, which was firstly used by Kuerten and Vreman [108] as the subgrid closure in the motion equation of droplets. The authors performed LES of particle-laden turbulent channel flow at shear Reynolds number $Re_\tau = 150$ in order to study the capability of LES in predicting turbophoresis phenomena. The same flow configuration was used in [125, 184, 186] to study the effect of the approximate deconvolution approach. All of these authors reported a substantial improvement in some statistics of fluid velocity compared to simulations without a subgrid model in the particle equation of motion. While Shotorban et al. [184] and Kuerten [107] found the beneficial effect of the subgrid model in predicting turbophoresis, Marchioli et al. [125] claimed that the approximate deconvolution method was not able to provide satisfactory predictions of phenomena like preferential clustering and wall accumulation. They attributed that to the inherent restriction of this approach in which only part of the subgrid velocity field can be retrieved near the cut-off length by mimicking the behaviour of a sharp spectral filter[124]. Geurts and Kuerten [82] considered a mixed model, namely deconvolution-stochastic-forcing model: the approximate deconvolution part recover energy at small resolved scales, whereas the stochastic model is responsible for the smallest, fully unsolved scales. To determine the properties of the stochastic part in LES, they performed DNS of particle-laden turbulent channel flow as an *pripori* study. Both shear Reynolds number Re_τ and Stokes number St are varied. They found less dependence of stochastic contributions on fluid velocity on the Reynolds number and droplets inertia. Later, the concept of *mixed* stochastic-deconvolution model was then extended by Michałek et al. [135]. It is worth noting that all these subgrid models developed for LES of particle motion have shown the significant impact of Stokes number on the model performance[109].

With quite some researches devoted to the subgrid modelling on both the carrier phase and dispersed phase, considerable efforts have been made to apply LES to investigate the spray flows laden with evaporating particles. Early studies on vaporizing sprays were focused on using database generated from DNS results to guide development of LES approaches[112, 152, 153]. In LES of a three-dimensional temporal mixing layer carrying evaporating droplets, for instance, Okong'o and Bellan [153] represented the unfiltered flow field by introducing corrections to the resolved flow field based on the *sgs* variance in order to proper computation of source terms. They found a favourable agreement for the global characteristics of the mixing rates between LES and DNS, whereas all filtered source terms were overestimated by the LES. On the basis of the hydrodynamic coupling, one step towards simulating evaporating sprays is to consider the *sgs* scalar flux, such as evaporation and *sgs* correlations between velocity and composition variables[93]. Bini and Jones [29] simulated the turbulent sprays laden with acetone droplets using the LES-Lagrangian particle framework, correspondent to the experimental configuration of Chen et al. [48]. In addition to the *sgs* model for particle acceleration, stochastic modelling of sub-filter evaporation was introduced, and it was shown that the essential characteristics of the flow were reproduced to a good accuracy with respect to the experimental measurements. Later, the same research group applied Large-Eddy Simulation to evaporating kerosene and acetone sprays to study the effect of turbulence and temperature fluctuations on the jet structures under cold and vaporizing conditions[97]. They used an equilibrium model for droplet evaporation in combination with the Ranz-Marshall correlation, which also incorporated the same stochastic model as [29] to represent the effects of sub-filter velocity fluctuations on droplets dispersion and vaporization rates. Comparisons of numerical data with measurements[150, 222, 223] showed good agreements for mean droplet size and mean liquid concentration. They also reported that smaller droplets tend to be dragged into the core region, and the droplets evaporation process in the turbulent spray was size-selective with smaller droplets evaporating faster. Aiming to better understand the complex processes involved in turbulent sprays issued into high-temperature and high-pressure conditions, Irannejad and Jaberi [90] performed Large-Eddy Simulations of high speed evaporating spray in combination with full coupling terms between Lagrangian spray/droplet fields and the Eulerian gas flow. They observed gas flow caused by the evaporated vapour containing high kinetic energy and a non-linear correlation between injection pressure and droplet evaporation rate. Due to the competing force between evaporation and vapour convection, however, the spray penetration keeps unchanged with various injection pressure. In a series of paper focusing on combustion systems, Monen's group and Jones's group have carried out extensive works exploring droplet-laden turbulent sprays employing Large-Eddy Simulation method[63, 77, 78, 96, 98–101, 131, 133, 134, 146, 157, 179, 180, 196]. More recently, Large-Eddy Simulation of respiratory jets, such as breath, speech[2], cough[24, 42, 79, 117, 155, 203] and sneeze[117, 155, 205], have been performed to obtain different quantities of interest in the context of COVID-19 pandemic. More details are provided in the next section.

1.3 Respiratory flows

Breathing out, speaking, singing, coughing and sneezing are respiratory activities producing discontinuous jet/puff flows that can be physically described as a point-source emission of a warm and moist cloud of turbulent air carrying respiratory liquid droplets with a wide range of initial sizes. The movement of these turbulent, multiphase gas clouds is driven by the momentum of the gas phase itself rather than the droplet phase. With the Reynolds number ranging from $\mathcal{O}(10^3)$, tidal breathing and speeching, to $\mathcal{O}(10^4)$, i.e. sneezing and coughing, these respiratory flows are emitted with various rates and reach different distances in the turbulent gas-phase regime determined by the air volume and momentum of the ejection. As elucidated by Bourouiba [36], the main distinctions among these respiratory flows include the total gas volume exhaled (about 0.5 L for typical emissions and 1-4 L for violent events), the emission momentum controlled by the duration (about 2 seconds for tidal breathing and 0.2-0.5 second for coughing and sneezing), the fraction volume of the liquid phase, droplet size distribution, droplets amount (from $\mathcal{O}(10^2)$ to $\mathcal{O}(10^6)$), and the emission frequency. Droplets carried by these respiratory flows may directly bump into an object, e.g. an individual's face, settle in the proximity of the emission source, or remain suspended status travelling a much longer time and further distance, see Fig. 3.3. Such a scenario has been mentioned and discussed numerous times during the last two-year covid-19 pandemic since the SARS-CoV-2 virus, like many other respiratory viruses, spreads from an infected individual to other susceptible individuals through virus-laden droplets emitted during various respiratory events. The size of these droplets spans over a broad range of values: from tiny drops, $\mathcal{O}(1\ \mu m)$, to large droplets, $\mathcal{O}(1\ mm)$, which, together with the puff/jet of buoyant moist turbulent air[34] and the environmental ambient[49, 205], regulates the fate of droplets. By reasonably assuming that a droplet, regardless of its initial size, is carrying at least one virus copy, their different fates as described above can be correlated to three distinguished virus transmission routes: direct contact or fomites[214], droplets transmission[91] and airborne transmission[62, 201, 204]. While, in the first route, a healthy person comes into direct contact with an infected individual (direct contact) or touches a contaminated surface (fomites), the other two pathways can lead to inhalation and subsequent deposition of pathogen-laden droplets in the respiratory mucosa. The key differentiating factor between these two routes is the aerodynamics behaviour of the pathogen-laden droplets. In particular, droplet transmission [91] refers to the infection propagation associated with large droplets, which motion is governed by gravity and that behave ballistically. By opposite, airborne transmission [62, 201, 204] refers to the spread of the disease associated with smaller droplets, which motion is governed by aerodynamic drag and evaporation and that behave as aerosols, i.e. droplets/particles that remain airborne and can spread for long distances. As the latest research suggests that fomites are unlikely to be a significant source of infection for SARS-CoV-2 [62, 113, 174], understanding the role played by the two latter infection routes is crucial to establish effective guidelines for pathogens transmission prevention. Indeed, extensive researches have been done to significantly advance our understanding of different scientific problems ranging from the transmission pathways of respiratory diseases to mitigation strategies for reducing the infection risk [138].

The fundamental works in this direction can date back to the time, a few years after the Spanish flu pandemic[191]. In the 1930s, Wells [212] theoretically studied the evaporation behaviour of free-falling water droplets using a simple calculation, based on the classical D^2-law [110] and Stokes's law, which revealed the interplay of evaporation and gravity determining the lifetime of respiratory droplets with various initial sizes by showing a classical curve, referred as *Wells evaporation-falling curve of droplets*[215]. From this curve, Wells showed that there is always a critical size (about $100\mu m$) for a normal environmental condition that dichotomises particles that would fall to the ground and droplets that would evaporate out at the same time. This finding established the fundamentals of a theoretical model predicting droplets and droplet nuclei transmission according to the size of respiratory droplets. In particular, droplets larger than $100\mu m$ in diameter, which settle out of the respiratory flow quickly by gravity, can lead to effective infection within a short distance away from the source. Small droplets/aerosols with an initial diameter less than $100\mu m$ can evolve into dried-out infectious nuclei that remain airborne in the air for a considerable long time and could be transported over long distances by the respiratory flow. Wells' work is pioneering in differentiating droplet and airborne transmission, also corroborated by the fact that small droplets could evolve into droplet nuclei by evaporation [213], micro-metric particles of non-volatile materials (e.g. mucus) that can potentially carry the virus contributing to the spread of the disease. This framework is so

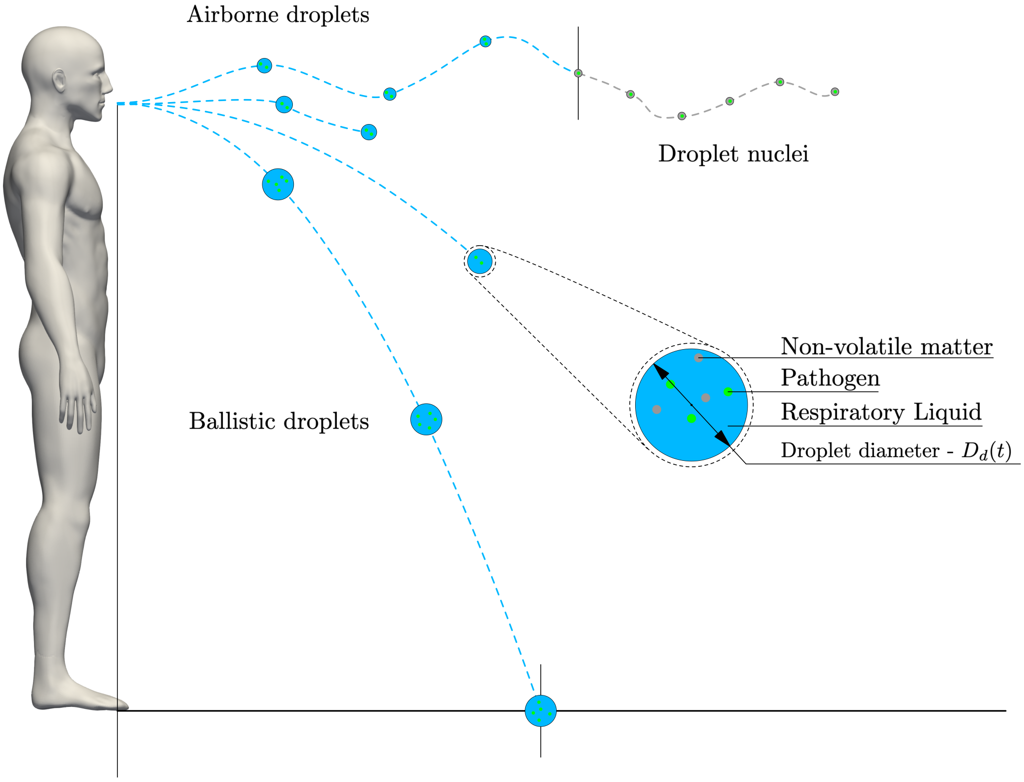

Figure 1.4: Sketch showing the different fates of respiraotry droplets

concise, readable and expressive that, since reported, it has been extended over the last 90 years, and largely used in most public health guidelines [16, 34]. The Wells model, however, presents a major weakness [16, 34, 49, 148, 215]: the evaporation time of the droplets is estimated using the classical D^2-law [110] (or constant temperature model), which states that the droplet surface reduces linearly with time at a rate determined by ambient conditions. This evaporation model ignores the presence of a turbulent cloud of moist air, which, as recently demonstrated in recent studies, plays a crucial role in the fate of respiratory droplets [138, 175], as well as the presence of the surrounding droplets. This leads to wrong estimates of the evaporation times and results in much shorter predicted droplet lifetimes [148, 205]. Thanks to the advancement in the fields of mass and heat transfer, Xie et al. [215] proposed a systematic extension of the Wells's classical model, which approximates respiratory flows as a circular steady-state non-isothermal turbulent jet, and is capable of describing the evaporation and motion of droplets exhaled during respiratory events in different conditions (relative humidity, air velocity, and respiratory jets). Xie et al. [215] showed that the largest free-falling droplets that would evaporate out before reaching the ground from a height of 2 m are between $60\mu m$ and $100\mu m$, and the lifetime of droplets are significantly prolonged with respect to the estimates obtained by Wells' theory in all environmental conditions tested. Meanwhile, by assuming the exhaled velocity of respiratory air at 1 m/s for breathing, 10 m/s for coughing, and 50 m/s for sneezing, Xie et al. [215] concluded that the longest distance travelled by these droplets were less than 1 m, more than 2 m, and more than 6 m, respectively. This model has been utilized in various investigations, such as respiratory flow turbulence by Wei and Li [209], droplet nuclei by Liu et al. [118], and droplet composition by [156]. Bourouiba [33], by directly observing the evolution of violent respiratory events[33, 35], demonstrated that such flows are turbulent buoyant clouds suspended with droplets of various sizes, which guided them to develop both discrete and continuous theoretical models of droplets fallout from the turbulent buoyant momentum puff in order to predict the transmission range of pathogens. Their studies highlighted the importance of the multiphase nature of turbulent puff clouds in extending the spatial and temporal ranges of respiratory droplets carrying the infectious pathogen. In particular, the local warm and moist environment within the turbulent puff cloud could extremely extend the lifetime of a droplet, an extension factor up to 1000, with respect to isolated droplets, which allow virus-laden droplets of various sizes to be transported around 7-8 m in a violent respiratory event[34]. More recently, this model has been slightly modified to evaluate the influence of drag and the inertia of droplets during the evolution of exhaled puffs[16]. Instead of focusing on violent events like coughing and sneezing, Yang et al. [216] incorporated the results of high-fidelity simulations on speech jets [2], and proposed a simplified dose-response model to quantify the spatio-temporal dependence of virus infection risk driven by speech-generated-aerosols between two speakers. This model assumes the continuous speaking activities as quasi-steady, jet-like flows and fast aerosolization of speech droplets. They showed that both physical distancing and exposure time should be imposed to control the infection probability. In particular, speakers should keep the contact time below 8 minutes for a physical distancing of 1 m and 16 minutes for 2 m. Other studies and associated comments can be found in the work of Bahl et al. [12]. Although current models are capable of providing useful guides for designing precaution rules such as physical distancing and exposure times, it is premature to say that they are satisfactory without considering the contributions from experimental studies.

Another seminal work on respiratory events came from the early experiments of Duguid [60] who gave the typical size distribution of droplets emitted during various respiratory events. Though it is extensively accepted that the predominant range of droplet size is $1\mu m$-$500\mu m$[85], different respiratory events could expel different numbers of droplets. Duguid [60] reported that a healthy individual averagely produced around 1,000,000 and 5,000 droplets during a sneezing and coughing event, respectively, and 250 droplets during "speaking loudly one hundred words" due to the fact that the definition of one speaking event is not as distinct as coughing or sneezing events. Traditionally, violent respiratory activities have received much attention since they produce a massive amount of droplets potentially carrying infectious pathogens. Jennison [92], regardless of the health status of the subject, reported that 4600-40,000 droplets are exhaled during a sneezing event. Loudon and Roberts [120], Piomelli [161] suggested that an average emission of droplets during a cough is 450. Lindsley et al. [116] found the dependency of droplets number exhaled per cough on the health status of an individual, suggesting 1100-308,600 droplets per cough for a health subject and 900-302,200 droplets for a patient with influenza. Compared to the coughing and sneezing events, breathing and speaking are mild events and capable of producing only small droplets, which are more correlated to the airborne transmission[7]. Holmgren et al. [89] found that the number of droplets produced during tidal breathing was between 300 and 3.7×10^4 per exhalation. Chao et al. [45], combining interferometric Mie imaging and particle image velocimetry (PIV), estimated the total number of droplets expelled during speaking ranged from 112 to 6720 by counting 1-100 numbers. Asadi et al. [10] reported that the droplet emission rate during normal speech is positively correlated with the loudness of vocalization, ranging from approximately 1 s^{-1} to 50 s^{-1} particles for low to high amplitudes, regardless of the language spoken. However, more recent studies [8, 197] by visualizing small speech droplets with an intense sheet of laser light revealed mean droplet emission rates of $1,000\ \mathrm{s}^{-1}$ with peak emission rates as high as $10,000\ \mathrm{s}^{-1}$, indicating a higher total integrated volume than previous results [10, 45, 60, 144]. With the richness of experimental data on droplets size distribution, analysis works have been done to modelize the characteristic of droplet size[16, 94, 149]. For instance, on basis of the dataset from Duguid [60] and Loudon and Roberts [120], Nicas et al. [149] suggested log-normal distribution for the size of droplets exhaled with the geometrical standard deviation around 8-9. Han et al. [88] observed the coexistence of bimodal and multimodal size distribution for a single sneezing event, which was obtained by the superposition of several physical processes. Balachandar et al. [16], using both a log-normal distribution and a Pareto distribution to fit the experimental data of Duguid [60], Loudon and Roberts [120], provided an alternative for modelizing both datasets with a Pareto distribution of power 2. For a exhaustive review on this subject, the readers are referred to Gralton et al. [85] and Zhou and Zou [225].

In addition to the fundamental works like the model of Wells [212] and the experiments of Duguid [60] as well as correspondent investigations followed, the understanding of respiratory flows has been further advanced more recently by Bourouiba [33] who experimentally demonstrated that the airflow exhaled during respiration quickly evolves as it enters the ambient, and finally transforms into a turbulent cloud/puff. This transformation characterizes the expiratory event as two phases propagation: 1) jet phase, linked to the early jet evolution when momentum is continuously provided (constant momentum flux); and 2) puff phase, linked to the late evolution where momentum injection ceases and the jet momentum remains constant. This two phases propagation theory can date back to the experiments of Sangras et al. [178] who, on the basis of the self-similarity hypothesis, derived two scaling laws for the distance travelled by a turbulent interrupted jet: for the starting jet phase (constant momentum flux), the distance travelled by the jet front L grows over time as $L \propto t^{1/2}$, while, for the puff phase (constant momentum), the penetration distance grows as $L \propto t^{1/4}$. Both numerical results[49, 205, 210] and experimental data[2] published recently has been benchmarked against this theoretical scaling law, receiving a good agreement. Bourouiba [33] also showed that, due to the buoyancy force, the turbulent cloud could move upwards, enabling small droplets to reach a higher position where the airborne transmission may be facilitated. The findings of turbulent puffs in extending droplet travelling distance suggested a shift from the paradigm of isolated droplets being considered to a new one taking into account the importance of turbulent puffs[33, 34, 36]. Inspired by the new paradigm, Chong et al. [49], using direct numerical simulations, reported that droplets in a turbulent cloud at high environmental relative humidity (90%) have a lifetime $\mathcal{O}(100)$ longer than that estimated with the isolated droplet theory. Ng et al. [148] attempted to quantify the effect of ambient temperature and relative humidity on droplets transported by a coughing puff. They observed that in cold and moist ambient conditions, air could not contain much moisture. Therefore, the warm and humid exhaled vapour puff becomes supersaturated when entering the cold ambient air, so the droplets carried by the puff tend to experience vapour condensation before evaporating at long time. The colder the ambient air, the more critical this non-monotonic behaviour is. Considering the computational cost, the Large-Eddy Simulation approach is more favourable for researchers to obtain different variables of interest. Abkarian et al. [2] carried out Large-Eddy Simulations of mild respiratory jets, i.e. breathing and speaking events, to investigate the dynamics of puff cloud and quantify their spatiotemporal growth. They showed that speech events could create a conical, turbulent flow at a typical half-angle of 10°, which likely reaches a distance over 2 meters away from the mouth of a speaker in 30 seconds of conversation. These results were later integrated into Yang et al. [216]'s research in which a simplified dose-response model was proposed to quantify the spatio-temporal dependence of virus infection risk driven by speech generated-aerosols between two speakers. Liu et al. [117] performed six large eddy point-droplet simulations to analyse the fluid dynamics of a turbulent, puff-like jet produced from a coughing or sneezing event. The primary purpose of their numerical works was to evaluate the theoretical framework proposed by Balachandar et al. [16]. Interestingly, they observed that a small portion of puff with a vortex ring-like structure was detached from the main flow and travelled over a relatively large distance carrying a proportionate amount of suspended droplets. In order to assess the reliability of current health guidelines, as it will be shown in paper III, we employed finely resolved Large-Eddy Simulations to study droplet-laden turbulent puffs emitted during sneezing events in a wide range of environmental conditions. They observed substantial variation in droplets' evaporation or condensation determined by their local temperature and relative humidity micro-environment. Their findings demonstrated that the actual evaporation time of droplets could be up to two orders of magnitude larger than what is currently predicted, which indicates the exposure risk associated with airborne respiratory droplets, especially in the close proximity of an infected individual, is much higher than the estimated with the models that constitute the foundation of current health protection guidelines. Other studies applying Large-Eddy Simulation include: Khosronejad et al. [104] applied LES with fairly high resolution to reveal the underlying mechanisms of particulate saliva transport during coughing events with and without face-coverings, reporting that either medical or non-medical facial masks can effectively restrict the spreading of saliva droplets; Ge et al. [79] simulated a coughing jet considering different inlet velocity profiles as well as variable mouth opening area in a closed ambient conditions, and showed favorable influence of higher room temperature on shortening droplets penetration; Behera et al. [24] analyzed the effect of co-flow on distance travelled by a cough jet without considering the existence of dispersed droplets, which help to understand the importance of ambient on transmission rate; Trivedi et al. [203] performed 10 independent LES realizations of a cough jet to evaluate the stochasticity of respiratory flow due to turbulence and its influence on short-range distribution of droplets carrying infectious disease; Calmet et al. [42] numerically investigated the turbulent buoyant cloud carrying droplets emitted during a coughing event. Their results indicated that the critical droplet size susceptible to inhalation was less than 1 μm. These studies primarily focused on the coughing events with the longest simulation time being 10 seconds.

1.4 Research objectives

From the previous introduction, it appears that extensive researches, experimental measurement, numerical investigation and theoretical analysis, have been already applied to turbulent spray dynamics. However, despite the highly scientific and practical relevance of this subject, it is still premature to draw a conclusion that a fundamental understanding of this phenomenon has been thoroughly achieved, and the capabilities of existing numerical models for practical applications are satisfied. Accordingly, the main motivation of this study has been detailed in the form of the following objectives:

- Fundamental study of the dispersion dynamics of evaporating droplets within turbulent spray conditions at high Reynolds number which is quite common in respiratory activities and combustors;

- Comprehensively assessment of the robustness of the parcel model in modelling Lagrangian point-droplets approximation within a turbulent evaporating jet using the LES approach;
- Systematic analysis of the impact of a turbulent cloud of moist air exhaled during violent respiratory events under various environmental conditions on the airborne time and lifespan of pathogen loaded droplets and correspondent comparison vs current guidelines;
- Re-examine the deficiency of classical D^2-law model in predicting point-droplets evaporation behaviours and explore possible solutions to improve it;
- Integrate the above investigations and latest research findings on respiratory jets to extend the capability of seminal Wells theory in predicting the fate of virus-laden droplets exhaled during various expiratory events

Thesis Structure

The thesis is written in the paper-collection format. The work is divided into four chapters plus an appendix collecting the papers. The present chapter provides an extended introduction to the field of turbulent sprays with an emphasis on the dispersion of evaporating droplets. The following Chapter 2 gives details about the mathematical formulations and the in-house code package, CYCLON. Later, in Chapter 3, a brief summary of the main findings of this research is presented. Finally, an outlook is provided for the perspectives of these investigations.

Chapter 2

Methodology

As the main aim of the present work is to numerically investigate the dynamics of evaporating droplets within a turbulent diluted spray, the governing equations for physical variables of both the continuous phase flows and the dispersed phase droplets are elucidated in this chapter. The numerical algorithm utilized in this work simulates the dilute spray conditions using a hybrid Eulerian-Lagrangian approach in which the carrier phase is described through an Eulerian approach and equations are derived treating the dispersed phase by a Lagrangian point of view. The set of equations governing the multiphase flow is initially accounted for by introducing three sink/source terms which represent the contributions from the dispersed phase to the gas flow, see Sec. 2.1. Sec. 2.2, under the point-droplet approximation, shows the equations for droplet position, velocity, mass and temperature in a dilute regime context. Sec. 2.3 presents the filtered equations with the appearance of several unknown terms due to the spatial filtering with the Large-eddy Simulation approach. It is worth noting that the *sgs* modelling is only considered for carrier flows, not for the dispersed phase. In order to simply solve the carrier phase equations without neglecting the effect of local variations of the gas density and temperature, a low Mach number expansion of gas-phase equations has been adopted, see Sec. 2.4. Indeed, in a low Mach number regime, only the effect of acoustic wave propagation on fluid dynamics of the carrier flows are ignored. Finally, a brief description of the in-house code package is provided in Sec. 2.5.

2.1 Instantaneous equations for gas phase

The carrier phase considered is a Newtonian fluid, and the diffusion between two species is assumed to follow Fick's law, on the basis of which two mass equations have been taken into account: one concerning the carrier phase globally and another relative to the vapour species. In this context, the governing equation describing the conservation law of mass, known as *continuity equation*, can be written as:

$$\frac{\partial \rho}{\partial t} + \frac{\partial (\rho u_i)}{\partial x_i} = S_m \tag{2.1}$$

where ρ represents the density of carrier flow, u_i is the i-th components of the flow velocity, and S_m is the mass coupling term between phases. Applying the Newton's second law of motion, the momentum equation can be expressed as:

$$\frac{\partial(\rho u_i)}{\partial t} + \frac{\partial(\rho u_i u_j)}{\partial x_j} = \frac{\partial \tau_{ij}}{\partial x_j} - \frac{\partial p}{\partial x_i} + \rho g_i + S_{p,i} \tag{2.2}$$

where τ_{ij} is the viscous stress tensor, p is the pressure, g_i is the gravitation acceleration, and $S_{p,i}$ represents the momentum coupling term between phases. For Newtonian fluid as considered in present work, the viscous part of the symmetric stress tensor is a function of the dynamic viscosity, μ, and can be written as:

$$\tau_{ij} = \mu \left(\frac{\partial u_i}{\partial x_j} + \frac{\partial u_j}{\partial x_i} \right) - \frac{2}{3}\mu \frac{\partial u_k}{\partial x_k}\delta_{ij}$$

in which δ_{ij} is the Kronecker delta function, i.e. if $i = j$ $\delta_{ij} = 1$ and otherwise $\delta_{ij} = 0$.

For the description of double species flow, i.e. vapor and air in the current work, the instantaneous conservation equation governing the local variation of vapor mass fraction, Y_v, can be simply derived from the scalar transport equation and written as follows:

$$\frac{\partial(\rho Y_v)}{\partial t} + \frac{\partial(\rho Y_v u_j)}{\partial x_j} = \frac{\partial}{\partial x_j}(\rho \mathcal{D} \frac{\partial Y_v}{\partial x_j}) + S_m \tag{2.3}$$

with $\mathcal{D}$ representing the binary diffusivity of the vapor into the gas. Here, an equal diffusivity between the gas and the vapor is assumed. In order to completely describe the instantaneous flow variables, the balance equation for energy conservation can be expressed as:

$$\frac{\partial(\rho e_t)}{\partial t} + \frac{\partial(\rho e_t u_j)}{\partial x_j} = \frac{\partial}{\partial x_j}(\kappa \frac{\partial T}{\partial x_j}) + \frac{\partial(\tau_{ij} u_j)}{\partial x_i} - \frac{\partial(p u_j)}{\partial x_i} + u_j \rho g_j + S_e \tag{2.4}$$

where $e_t = e + \frac{1}{2}u_i u_i$ is the total specific energy of the gas phase with e being the specific internal energy, κ is the the thermal conductivity of the carrier mixture and S_e is the energy coupling term between phases.The last equation treating the carrier flows as ideal gas reads as follows:

$$p = \rho R T \tag{2.5}$$

with *R=8314.3 J/(kg·K)* is the universal gas constant and T the gas temperature.

2.2 Mathematical description for evaporating particles

The present work describes the dispersion of evaporating droplets in dilute turbulent conditions using a Lagrangian point-droplet approach. In order to derive the balance equations of droplets position, acceleration, mass and temperature, some hypotheses have been implemented: 1) droplets are modelled as rigid spheres whose size is considered to be smaller than the Kolmogorov length scale of the flow fields; 2) the density of droplets is assumed to be constant and much larger than that of carrier flows such that only drag force (also buoyant force for respiratory flows) and inertia are necessary for droplet movement; 3) the initial fractional volume of liquid phase is in the two-way coupling regime so that droplets collisions and coalescence are rare events and are neglected; 4) the thermal conductivity of droplets is hypothesized to be infinitive such that the temperature inside droplet volume is uniform, but droplet temperature could vary with time; 5) the heat transfer process mainly occurs at a relatively low temperature between dispersed phase and carrier flows through the convective process while no position is available for radiative heat transfer from droplets. Under these hypotheses, droplet dispersion and vaporization are formulated in the following part.

2.2.1 Droplet dispersion

The balance equations for droplet position and acceleration derived from the Maxey and Riley [129]'s formulation by considering viscous drag, buoyant force and gravitational force per mass read as follows:

$$\frac{dx_{d,i}}{dt} = u_{d,i}, \tag{2.6}$$

$$\frac{du_{d,i}}{dt} = \frac{(u_i - u_{d,i})}{\tau_d} + (1 - \frac{\rho}{\rho_l})g_i, \tag{2.7}$$

where $x_{d,i}$, $u_{d,i}$ are the i-th components of droplet's position and velocity, respectively, u_i is the i-th component of gas phase velocity which is known at the droplet location, and ρ_l is the liquid density. The droplet relaxation time τ_d is expressed as:

$$\tau_d = \frac{8}{3}\frac{\rho_l}{\rho}\frac{r_d}{C_D}\frac{1}{\|u_i - u_{d,i}\|} \tag{2.8}$$

in which r_d is the droplet radius and C_D is the droplet drag coefficient which could be determined by the drag law[221]:

$$C_D = \begin{cases} \frac{24}{Re_d}(1 + \frac{Re_d^{2/3}}{6}), & \text{if } 0 < Re_d < 1000 \\ 0.424, & \text{otherwise} \end{cases} \tag{2.9}$$

where Re_d is the droplet Reynolds number functional of droplet size and the relative velocity of droplet and the gas phase at droplet's location, i.e. $Re_d = 2\rho\| u_i - u_{d,i}\| r_d/\mu$. In the current work, the Schiller-Naumann correlation is adopted to account for the effect of the finite Reynolds number of the droplets on the drag., based on which the acceleration equation of droplets can be re-expressed as:

$$\frac{du_{d,i}}{dt} = \frac{1 + 0.15\ Re_d^{0.687}}{\tau_d}(u_i - u_{d,i}) + (1 - \frac{\rho}{\rho_l})g_i, \tag{2.10}$$

with τ_d being simplified as $\tau_d = 2\rho_l r_d^2/(9\mu)$.

2.2.2 Droplet evaporation

The droplet evaporation proceeds by absorbing heat supplied by the carrier phase to balance the amount of energy required by the latent heat of vaporization. During this process, droplet temperature tends to a lower value, whereas the heat transfer increases because of the increment of temperature difference between liquid phases and the carrier flows. To describe this phenomenon, the classical evaporation model proposed by the seminal work of Langmuir [110] and others[84, 194], which is also referred to as D^2-law, has received extensive attention, e.g. both non-reactive and reactive evaporation of liquid droplets[194, 212, 213], due to its simplicity to implement. According to this model, droplet temperature is unchanged during the evaporation process, but its surface decreases linearly with time, determined by an evaporation rate constant which is dependent on the thermal-physical properties of droplet itself and the surrounding air, due to the rapid mixing assumption. However, this model does not take into account the effect caused by the balance between heat flux and latent enthalpy. Recent researches reported significant deviation of droplets evaporation behaviour from this classical model[31, 32, 55, 123, 206]. In this work, the evaporation model proposed by Abramzon and Sirignano [3] has been employed for the droplet mass equation, while the droplet temperature is calculated with formulations based on the first law of thermodynamics following the approach of Bini and Jones [29]. These models are obtained by introducing some corrections to the classical model in order to account for the effect of Stefan flow on heat and mass transfer. The evaporation formulations calculate the rate of change of droplet size and temperature as follows:

$$\frac{dm_d}{dt} = -\frac{1}{3\tau_d}\frac{Sh}{Sc}m_d \ln{(1+B_m)}, \tag{2.11}$$

$$\frac{dT_d}{dt} = \frac{1}{3\tau_d}\left[\frac{Nu}{Pr}\frac{c_{p,g}}{c_l}(T-T_d) - \frac{Sh}{Sc}\frac{L_v}{c_l}\ln(1+B_m)\right], \tag{2.12}$$

where m_d and T_d are droplet's mass and temperature, respectively. The parameter $c_{p,g}$ is the heat capacity at constant pressure of the gaseous component of the carrier mixture, c_l is the liquid specific heat, and L_v the latent heat of vaporization of the liquid phase evaluated at the droplet temperature. In equations (2.11) and (2.12), the Schmidt number, $Sc = \mu/(\rho\mathcal{D})$, and Prandtl number, $Pr = \mu/(c_p k)$ are employed to compute the mass diffusivity and thermal conductivity, respectively. Besides, the Nusselt number, Nu_0, and Sherwood number, Sh_0, are estimated as a function of the droplet Reynolds number through the Frössling correlation:

$$Nu_0 = 2 + 0.552 Re_d^{\frac{1}{2}} Pr^{\frac{1}{3}}, \tag{2.13}$$

$$Sh_0 = 2 + 0.552 Re_d^{\frac{1}{2}} Sc^{\frac{1}{3}}, \tag{2.14}$$

A correction is then applied to Nu_0 and Sh_0 to account for the effect of Stefan flow [3]:

$$Nu = 2 + \frac{Nu_0 - 2}{\ln(1+B_t)}\frac{B_t}{(1+B_t)^{0.7}}, \qquad B_t = \frac{c_{p,v}}{L_v}(T-T_d), \tag{2.15}$$

$$Sh = 2 + \frac{Sh_0 - 2}{\ln(1+B_m)}\frac{B_m}{(1+B_m)^{0.7}}, \qquad B_m = \frac{Y_{v,s}-Y_v}{1-Y_{v,s}}, \tag{2.16}$$

in which B_m and B_t represent the spalding mass and heat transfer number[194]. The parameter $c_{p,v}$ is the specific heat capacity of the pure vapor at constant pressure, Y_v is the vapor mass fraction evaluated at the droplet position, whereas $Y_{v,s}$ is the vapor mass fraction evaluated at the droplet surface. The latter corresponds to the mass fraction of the vapor, in a fully saturated vapor-gas mixture, evaluated at the droplet temperature. In order to estimate $Y_{v,s}$ we employ the Clausius-Clapeyron relation:

$$\chi_{v,s} = \frac{p_{ref}}{p_0} exp\left[\frac{L_v}{R_v}\left(\frac{1}{T_{ref}} - \frac{1}{T_d}\right)\right], \tag{2.17}$$

where $\chi_{v,s}$ is the vapor molar fraction evaluated at the droplet temperature and p_0 the thermodynamic pressure. The parameter p_{ref} is the saturated vapor pressure evaluated at the reference temperature T_{ref}, whereas $R_v = \mathcal{R}/W_l$ is the specific constant of the vapor being W_l its molar mass

. The saturated vapor mass fraction is then,

$$Y_{v,s} = \frac{\chi_{v,s}}{\chi_{v,s} + (1 - \chi_{v,s}) \frac{W_g}{W_l}}. \tag{2.18}$$

with W_g the molar mass of gas mixture.

2.2.3 Coupling source terms

Consistently with previous studies in this field [39, 127], the effect of the dispersed phase on the carrier one is accounted for by employing three sink/source coupling terms in the right-hand side of the mass, momentum, and energy equations, S_m, $S_{p,i}$,and S_e, respectively:

$$S_m = -\sum_k \frac{dm_d^k}{dt} \delta(x_i - x_{d,i}^k), \tag{2.19}$$

$$S_{p,i} = -\sum_k \frac{d}{dt}(m_d^k u_{d,i}^k) \delta(x_i - x_{d,i}^k), \tag{2.20}$$

$$S_e = -\sum_k \frac{d}{dt}(m_d^k c_l T_d^k) \delta(x_i - x_{d,i}^k). \tag{2.21}$$

where the Lagrangian variables $x_{d,i}^k$, $u_{d,i}^k$, m_d^k and T_d^k are the position, velocity, mass and temperature of the k-th droplet, respectively, whereas the parameter c_l is the specific heat of the liquid phase. The summations are taken over the whole droplet population located within the domain (index k). The delta function, $\delta(x_i - x_{d_i}^k)$, accounts for the fact that the sink/source terms act only at the Eulerian positions occupied, at a given time, by the point-droplets, consistent with the point-particle assumption. The term S_m, representing the mass transition due to evaporation, appears in both the global *continuity equation* eq. (2.1) and the vapour *continuity equation* eq. (2.3) due to the fact that the evaporation process, notwithstanding only involving the liquid phase and vapour, contributes to the density variation of the carrier phase globally. The coupling term of momentum transition between two phases, $S_{p,i}$, is expressed in eq. (2.20), composing of two mechanisms: the momentum transfer due to the mass transition arising from the evaporation process and the drag force between two phases. Based on the hypothesis that the heat flux transferred from a single droplet to the carrier flow has the same intensity as that of reverse direction, the coupling term S_e expressed in eq. (2.21) considers heat transfer, enthalpy and kinetic energy flow. In the numerical algorithm, the Eulerian terms eq. (2.19)-(2.21) are calculated, in correspondence of each node of the computational grid, by volume averaging the mass, momentum, and energy sources arising from all the droplets located within the grid cell pertaining to the considered grid node.

2.3 Large-Eddy Simulation

The LES equations are obtained by applying a spatial filter to the governing equations (2.1) to (2.4). The spatially filtered value of a function $f = f(\mathbf{x}, t)$ is defined as its convolution with a filter function, G, according to:

$$\overline{f}(\mathbf{x}, t) = \int_{\Omega} G(\mathbf{x} - \mathbf{x}'; \Delta) f(\mathbf{x}', t) d\mathbf{x}' \tag{2.22}$$

where the integration is carried out over the entire domain, Ω. The filter function, G, has a width $\Delta = [(r\Delta_\theta)\Delta_r\Delta_z]^{1/3}$which may vary with position. In turbulent flows where fluid density variations in the resolved and unresolved scales arise, the most straightforward way of taking into consideration these fluctuations is through the adaption of a density-weighted (or Favre-weighted) filtering[68]: $\tilde{f} = \widetilde{\rho f}/\overline{\rho}$. The governing equations of Eulerian phase after filtering can be written as:

$$\frac{\partial \overline{\rho}}{\partial t} + \frac{\partial \overline{\rho}\tilde{u}_j}{\partial x_i} = \overline{S}_m \tag{2.23}$$

$$\frac{\partial \overline{\rho}\tilde{u}_i}{\partial t} + \frac{\partial (\overline{\rho}\tilde{u}_i\tilde{u}_j)}{\partial x_j} = -\frac{\partial \overline{p}}{\partial x_j} + \frac{\partial \tilde{\tau}_{ij}}{\partial x_j} - \frac{\partial \tau^R_{ij}}{\partial x_j} + \overline{\rho} g_i + \overline{S}_{p,i} \tag{2.24}$$

$$\frac{\partial \overline{\rho}\tilde{Y}_v}{\partial t} + \frac{\partial \overline{\rho}\tilde{Y}_v\tilde{u}_j}{\partial x_j} = \frac{\partial}{\partial x_j}(\overline{\rho}\mathcal{D}\frac{\partial \tilde{Y}_v}{\partial x_j}) - \frac{\partial \tilde{q}_v}{\partial x_j} + \overline{S}_m \tag{2.25}$$

$$\frac{\partial \overline{\rho}\tilde{e}_t}{\partial t} + \frac{\partial \overline{\rho}\tilde{e}_t\tilde{u}_j}{\partial x_j} = \frac{\partial}{\partial x_j}(\kappa\frac{\partial \tilde{T}}{\partial x_j}) - \frac{\partial \overline{pu_j}}{\partial x_i} + \frac{\overline{\tau_{ij}u_j}}{\partial x_i} - \frac{\partial \tilde{q}_e}{\partial x_i} + \tilde{u_j}\overline{\rho} g_j + \overline{S}_e \tag{2.26}$$

with

$$\tau^R_{ij} = \overline{\rho}(\widetilde{u_iu_j} - \tilde{u}_i\tilde{u}_j), \quad \tilde{q}_v = \overline{\rho}(\widetilde{Y_vu_i} - \tilde{Y}_v\tilde{u}_i), \quad \tilde{q}_e = \overline{\rho}(\widetilde{e_tu_i} - \tilde{e}_t\tilde{u}_i)$$

where τ^R_{ij} is the residual stress tensor as well as $\tilde{q}_v$ and $\tilde{q}_e$ the *sgs* extra-diffusion terms of scalar quantities. In present work, the residual stress tensor τ^R_{ij} is modelled by using Smagorinsky model[189]:

$$\tau^R_{ij} = -2\overline{\rho}(C_s\Delta)^2\|\tilde{S}_{ij}\|\tilde{S}_{ij} \qquad \tilde{S}_{ij} = \frac{1}{2}(\frac{\partial \tilde{u}_i}{\partial x_j} + \frac{\partial \tilde{u}_j}{\partial x_x}) \qquad \|\tilde{S}_{ij}\| = \sqrt{2\tilde{S}_{ij}\tilde{S}_{ij}}$$

where $\tilde{S}_{ij}$ is the resovled rate of strain tensor, C_s is a Constant (0.12) and $\Delta = [(r\Delta_\theta)\Delta_r\Delta_z]^{1/3}$ is typical cell size. For other two other *sgs* scalar fluxes, it is usual to adopt a gradient model[183]:

$$\tilde{q}_v = \overline{\rho}D_{sgs}\frac{\partial \tilde{Y}_v}{\partial x_i} \qquad \tilde{q}_e = \overline{\rho}\alpha_{sgs}\frac{\partial \tilde{e}}{\partial x_i}$$

where the *sgs* diffusivity is assumed proportional to the Smagorinsky eddy-viscosity with a constant turbulent Schmidt and Prandtl numbers.

For the liquid phase part, the effect of the subgrid-scale terms is not taken into consideration. Hence, only the resolved part of the Eulerian fields is used in the equations of the dispersed phase. The Lagrangian equations under the LES framework are the same as the equations shown in Sec. 2.2 except for the variables from the Eulerian phase, e.g. $\tilde{u}_i$, $\tilde{Y}_v$ and $\tilde{T}$.

2.4 Low-Mach number approximation

In the present work, the turbulent spray is assumed as a compressible low-Mach-number flow. In order to derive the low-Mach Navier-Stokes equations, we nondimensionalize the equations (2.1) - (2.5) by using some variables of carrier phase evaluated at the spray inlet section as reference quantifies denoted by the subscript ∞, e.g. the bulk density, ρ_∞, pressure, p_∞, and velocity, u_∞, of the jet evaluated at the inlet section. The jet inlet radius, R, is adopted as the typical length scale. Moreover, reference variables also include dynamic viscosity, μ_∞, the thermal conductivity, κ_∞, binary diffusion coefficient, $\mathcal{D}_\infty$, specific gas constant, R_∞ and the specific heat, $c_{p\infty}$. With these quantities, other variables considered in the non-dimensionalization procedure, i.e. the reference time, temperature, specific energy and specific enthalpy, can be derived as:

$$t_\infty = \frac{R}{u_\infty} \quad T_\infty = \frac{p_\infty}{R_\infty \rho_\infty} \quad e_\infty = \frac{p_\infty}{\rho_\infty} \quad h_\infty = \frac{p_\infty}{\rho_\infty}$$

Moreover non-dimensional groups considered also include:

$$Sc = \frac{\mu_\infty}{\rho_\infty \mathcal{D}_\infty} \quad Pr = \frac{c_{p\infty}\mu_\infty}{\kappa_\infty} \quad Fr = \frac{u_\infty}{\sqrt{gR}} \quad Re = \frac{\rho_\infty u_\infty R}{\mu_\infty}$$

where Sc, Pr, Fr, and Re are respectively the Schmidt number, Prandtl number, Froude number and Reynolds number of the carrier flow. The reference variables are selected such that flow variables after nondimensionlization remain order $\mathcal{O}(1)$ for any reference low-Mach number

$$Ma = \frac{u_\infty}{\sqrt{\gamma p_\infty / \rho_\infty}}$$

with $\gamma = c_{p,g}/c_{v,g}$ being the specific heat ratio of the carrier flow. To avoid the dependence on γ, $\widetilde{Ma} = \sqrt{\gamma} Ma$ is used. By dividing each equations for carrier flows with the correspondent non-dimensional variables group, the non-dimensionalization procedure imposed on eq. (2.1), (2.2), (2.4) and (2.5) leads to:

$$\frac{\partial \rho}{\partial t} + \frac{\partial (\rho u_i)}{\partial x_i} = S_m, \tag{2.27}$$

$$\frac{\partial (\rho Y_v)}{\partial t} + \frac{\partial (\rho Y_v u_j)}{\partial x_j} = \frac{1}{ReSc}\frac{\partial}{\partial x_j}(\mu \frac{\partial Y_v}{\partial x_j}) + S_m, \tag{2.28}$$

$$\frac{\partial (\rho u_i)}{\partial t} + \frac{\partial (\rho u_i u_j)}{\partial x_j} = \frac{1}{Re}\frac{\partial \tau_{ij}}{\partial x_j} - \frac{1}{\widetilde{Ma}^2}\frac{\partial p}{\partial x_i} + \frac{1}{Fr^2}\rho \hat{i} + S_{p,i}, \tag{2.29}$$

$$\frac{\partial (\rho e_t)}{\partial t} + \frac{\partial (\rho e_t u_j)}{\partial x_j} = \frac{\gamma}{\gamma - 1}\frac{1}{RePr}\frac{\partial}{\partial x_j}(\kappa \frac{\partial T}{\partial x_j}) + \frac{\widetilde{Ma}^2}{Re}\frac{\partial (\tau_{ij} u_j)}{\partial x_i} - \frac{\partial (p u_j)}{\partial x_i} + \frac{\widetilde{Ma}^2}{Fr^2} u_j \rho \hat{j} + \frac{\gamma}{\gamma - 1} S_e \tag{2.30}$$

The low-Mach number equations for the carrier flow can be derived by expanding each variable in eq.(2.27)-(2.30) with the following asymptotic series:

$$f(x,t) = f_0(x,t) + f_1(x,t)\widetilde{Ma} + f_2(x,t)\widetilde{Ma}^2 + f_3(x,t)\widetilde{Ma}^3 + \mathcal{O}(\widetilde{Ma}^3) \tag{2.31}$$

with f_0, f_1, f_2 and f_3 are the zeroth-, first-, second-, and third-order of the quantity f. By imposing the same order of all terms in the left- and right-hand side of equations obtained through expansion procedure above, the conservation equations for the gas phase in an open environment can be expressed as:

$$\frac{\partial \rho_0}{\partial t} + \frac{\partial(\rho u_i)_0}{\partial x_i} = S_{m0}, \tag{2.32}$$

$$\frac{\partial(\rho Y_v)_0}{\partial t} + \frac{\partial(\rho Y_v u_j)_0}{\partial x_j} = \frac{1}{ReSc}\frac{\partial}{\partial x_j}(\mu\frac{\partial Y_v}{\partial x_j})_0 + S_{m0}, \tag{2.33}$$

$$\frac{\partial(\rho u_i)_0}{\partial t} + \frac{\partial(\rho u_i u_j)_0}{\partial x_j} = \frac{1}{Re}\frac{\partial \tau_{ij0}}{\partial x_j} - \frac{\partial p_2}{\partial x_i} + \frac{1}{Fr^2}\rho_0\widehat{i} + S_{p,i0}, \tag{2.34}$$

$$\frac{\partial(\rho e_t)_0}{\partial t} + \frac{\partial(\rho h_t u_j)_0}{\partial x_j} = \frac{\gamma}{\gamma-1}\frac{1}{RePr}\frac{\partial}{\partial x_j}(\kappa\frac{\partial T}{\partial x_j})_0 + \frac{\gamma}{\gamma-1}S_{e0} \tag{2.35}$$

with $h_t = e_t + p/\rho$ being the total enthalpy per unit mass. It is worth noting that, in low Mach number regime, acoustic wave propagates within carrier flows exerting negligible influence on the system such that the zero- and first-order pressure appearing during expanding the momentum equation are uniform over the whole flow domain whereas only the second-order term is non-uniform. Since the present work studies evaporating jet issuing into an open environment, the thermodynamic pressure can be assumed to be uniform over space and constant over time. By introducing the nondimensional correlations between total energy and enthalpy and the thermodynamic pressure of carrier flows, i.e. $p_0 = (\rho e_t)_0(\gamma - 1) = (\rho h_t)_0((\gamma - 1)/\gamma)$, Eq. (2.35) can be further simplified as:

$$\frac{\partial u_{i0}}{\partial x_i} = \frac{1}{RePr}\frac{1}{p_0}\left[\frac{\partial}{\partial x_i}\left(\kappa\frac{\partial T}{\partial x_i}\right)_0 + S_{e0}\right] \tag{2.36}$$

This equation is of particular importance because it explicitly describes a correlation between the velocity divergence of the carrier phase field, thermal conduction and energy transition between two phases due to the evaporation process.

2.5 Description of the code package

The numerical results reported in the present work has been computed by employing an in-house MPI-parallel code, called *CYCLON*, which has undergone extensive validations and testing campaigns[51, 57, 159, 173]. This numerical algorithm, based on a hybrid Eulerian-Lagrangian approach and the point-droplet approximation, was written with the FORTRAN 90 programming computer language in order to simulate turbulent sprays both with DNS and LES approaches. The code package *CYCLON* consists of two main parts in structure: an initial Eulerian algorithm dedicated to advance in time the flow fields by solving the Low-Mach number formulations of the Navier-Stokes equations, and an updated Lagrangian solver designed to synchronously evolve the mass, momentum, and temperature equations of dispersed droplets under point-particle approximation. The Lagrangian solver estimates the coupling terms arising in the spray equations, granting a fully coupling between the carrier flows and the liquid phase. For the Eulerian part, second-order, central finite difference schemes on a staggered cylindrical mesh are employed for the spatial discretization, whereas the temporal evolution is performed by a low-storage, third-order Runge-Kutta algorithm. The same Runge-Kutta scheme is adopted for the latter. Besides, the numerical tool engages MPI directives in order to maximize computational performance. For more details about parallelization, see Dalla Barba [56].

The Eulerian computational domain is a cylinder. The droplet-laden jet-spray is injected through

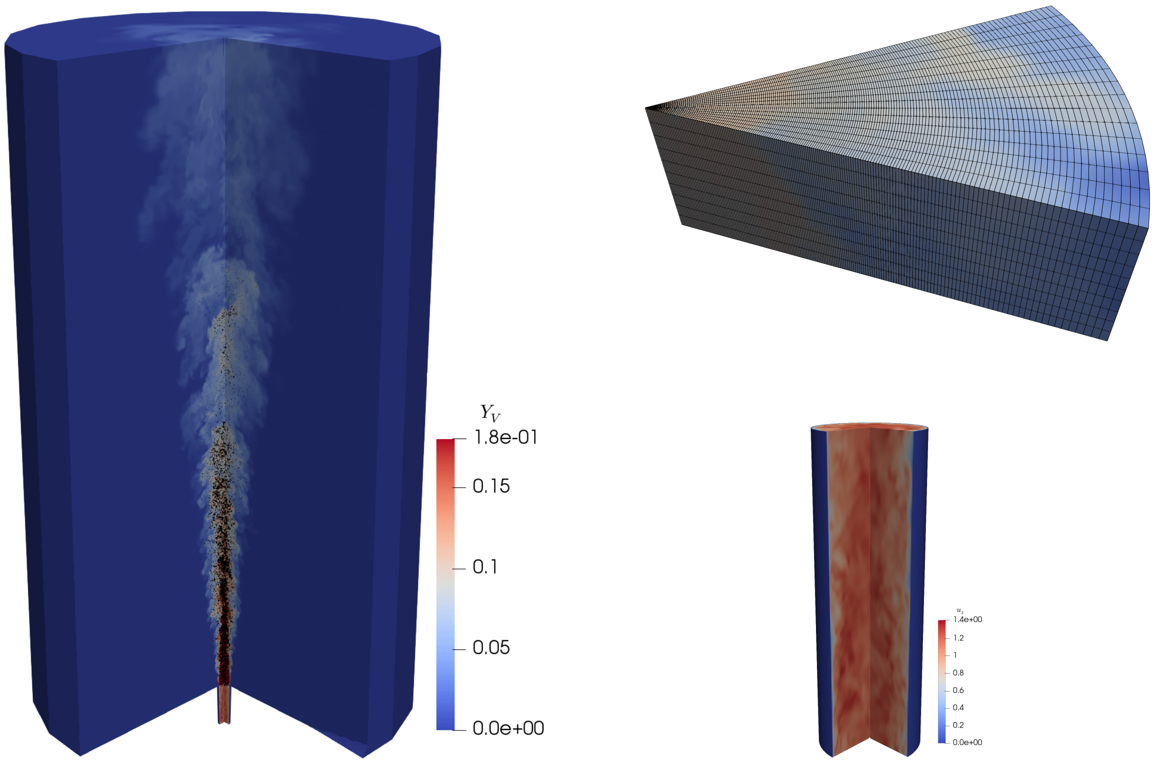

Figure 2.1: Left panel: A sketch of the 3D cylindrical domain where a representative ensemble of the whole droplet population is plotted with black points; Upper right panel: a local sector of the mesh structure; Lower right panel: the turbulent periodic pipe. The colors contour the vapor mass fraction field, Y_v, within the jet and the axial instantaneous velocity, U_z, of the turbulent pipe, respectively[206].

a circular orifice of radius R located at the centre of the lower base of the domain and streams out towards the opposite one. The domain extends in the azimuthal, θ, radial, r and axial, z, directions and is discretized by means of a staggered, cylindrical grid mesh. The computational grid is uniform along the azimuthal direction, whereas it is stretched along the radial and axial ones. More details can be found in Ciottoli et al. [51], Dalla Barba and Picano [57], Wang et al. [206]. The grid spacing is maintained of the same order of the Kolmogorov length scale for the whole downstream evolution of the jet-spray. A convective boundary condition is adopted at the outlet section located on the upper base of the domain. An adiabatic, traction-free boundary condition is prescribed at the side boundary of the domain, making the entrainment of external fluid possible, which, in the present work, consists of dry air in Paper I & II and moist air in Paper III-V. Time-dependent and fully turbulent boundary conditions are prescribed on the inflow section by means of a companion DNS reproducing a fully-developed, periodic pipe flow. A fully turbulent velocity field is assigned on the jet inflow by a Dirichlet condition. This two-dimensional field is computed on a cross-sectional slice of the turbulent pipe. Excluding the circular inflow, the remaining part of the domain base is impermeable and adiabatic. The turbulent pipe extends for $2\pi \times 1R \times 6R$ in the azimuthal, θ, radial, r and axial, z directions. An equispaced, staggered grid discretizes the pipe domain in order to match the corresponding jet-grid nodes at the pipe discharge. The use of a companion pipe simulation makes it possible to prescribe fully turbulent inflow conditions, including physically meaningful turbulent fluctuations. On the one hand, the flow in practical applications is usually turbulent even before the inflow, while a top-hat inflow is typical of a strong contraction before the inlet. On the other hand, the use of a fully developed turbulent inflow, instead of a steady top-hat one, avoids the transitional region downstream the inflow, accelerating the establishment of far-field turbulent jet-spray dynamics, which weakly depend on inflow condition details. A sketch of the cylindrical domain, the mesh structure inside a slice of the domain and the turbulent periodic pipe are shown in Fig. 2.1.

Chapter 3

Summary of results

In the following sections, the main findings of Papers (I-V) are summarized briefly. More results of the appended papers are provided in the final part of the thesis.

3.1 Paper I

Direct numerical simulation of an evaporating turbulent diluted jet-spray at moderate Reynolds number

Widening the availability of data from three-dimensional Direct Numerical Simulation (DNS) of evaporating jet-sprays over a higher range of Reynolds numbers is crucial to advance the comprehension of turbulent spray dynamics and enhance the capabilities of existing models in reproducing the phenomena. However, most of the numerical datasets and studies available in the literature are limited to relatively low Reynolds numbers due to the high computational requirements of DNS. On this ground, we performed a DNS of a moderate Reynolds number turbulent jet-spray ($Re = 10,000$) in an open environment and dilute conditions to investigate the dispersion and evaporation behaviours of acetone droplets. The problem is numerically tackled by employing the Eulerian-Lagrangian framework and the point-droplet approximation, combined with a two-way coupling concept, including the mass, momentum and energy exchanges between two phases.

The gaseous jet-spray is composed of dry air and acetone vapour, whereas the surrounding environment is filled with dry air. The simulation reproduces the evaporation of monodisperse acetone droplets, continuously injected within the turbulent gaseous phase at a bulk Reynolds number $Re = 2\rho U_0 R/\mu = 10,000$. After establishing statistically-steady conditions for both the phases, a systematic and comprehensive dataset of both instantaneous and average Eulerian and Lagrangian observables was collected. In the present study, the dataset is also compared to a previous DNS concerning a lower Reynolds number case ($Re = 6,000$), which, from the physical point of view, corresponds to a lower jet velocity [57].

The effects of the jet Reynolds number on the turbulent evaporation of droplets in dilute jet-sprays are investigated. In both the cases considered in the present study, a strong evaporation rate is observed in the mixing layer, where the entrainment of dry air dilutes the saturated jet core. A longer evaporation length is found for the higher Reynolds number jet-spray. We relate this growth of the evaporation length to the lower average vaporization rate, observed at $Re = 10,000$, by scaling the data by the jet advection reference time-scale, $t_0 = R/U_0$. This lower rate is attributed to a higher droplet relative inertia (Stokes number), which slows down the vapour-liquid mass exchange.

A strong inhomogeneous and segregated droplet distribution is observed in both the considered cases. This is found to originate in the mixing layer of the jet near-field and to propagate in the downstream direction. In the jet mixing layer, we identify different features: entrained bubbles of dry air depleted of droplets and saturated gas clouds full of droplets coming from the saturated core. Since droplets located in dry regions evaporate fast, whereas droplets in vapour-saturated clouds cannot evaporate, these dynamics tend to intensify the clustering in the downstream evolution of the jet. Besides, in the far-field, small-scale clustering is also observed. The inhomogeneous distribution of the segregated phase strongly impacts the Lagrangian evolution of the droplets: the droplet size spectrum becomes extremely wide, even starting from a monodisperse distribution. This extreme widening of the droplet size spectrum is associated with broadening the probability density functions of the evaporation rate and saturation level sampled by the droplets. These findings could play a role in explaining the fast widening of the droplet spectrum in warm clouds [181].

Finally, we address the evaluation of the accuracy of the well-established D^2-law in approximating the droplet evolution for the cases considered in the present paper. Firstly, we found that the actual droplet evaporation time varies by more than 50% of its mean value. This highlights how the evolution of the droplet histories strongly deviates from the D^2-law. Secondly, we observe that, whereas the trend of the mean evaporation (flight) time, t_f^e, can be approximated by a linear law of the droplet mean square diameter, its slope is much lower than the value predicted by considering the bulk thermodynamical properties of the environment. In addition, we show how, after a time much longer than t_f^e, the evaporation process is still not terminated. This peculiar aspect is attributed to clustering dynamics. Aggregates of droplets with nearly saturated atmospheres may survive for a longer time before fully evaporating. Hence, some droplets may preserve relatively large sizes for long distances and times. Despite the differences between steady-state jet-sprays, which are considered in the present paper, and respiratory flows, this aspect should be taken into account in modelling the evaporation and dispersion of infectious droplets. Indeed, even in these cases, some droplets may persist much longer than what was expected using the D^2-law, especially if its evaluation is based on the bulk thermodynamic properties of the environment.

To conclude, we believe that the dataset and the analysis presented in this study are relevant to improve the knowledge about the dynamics of turbulent evaporating sprays, providing, at the same time, a benchmark test-case for developing more accurate low-order and high-fidelity models.

3.2 Paper II

Assessment of the parcel model in evaporating turbulent diluted sprays within a Large-Eddy-Simulation approach

The computational cost related to the Lagrangian method tracking all particles could be extremely expensive when an enormous number of particles/droplets need to be handled in two-phase fluid systems. One approach to alleviate this problem is to reduce the total number of dispersed particles tracked in the simulation by representing a group of droplets having the same properties with a computational particle, so called parcel. However, a systematic analysis investigating its soundness within simulations of turbulent flows bearing evaporating droplets is still missing. In this paper, to cover this lack, we address the well-resolved Large-eddy Simulations (LESs) of a turbulent diluted acetone jet-spray considering different ratios of computation particles to physical particles, i.e. parcel ratio.

All thermal-physical properties, as well as simulation parameters in this work, are the same as that in Paper I, except for a coarse mesh dedicated to the LES approach and the parcel concept. In particular, the cylindrical domain is discretized by a coarse factor 4 in each direction with respect to the corresponding DNS mesh reported in Paper I. To assess the robustness of the parcel concept, five parcel ratios were used together with a case presenting all physical particles, i.e. 1, 4, 16, 64, 256, and 1024. The parcel concept was realized by simply reducing the number of droplets injected of the inlet per timestep while the coupling source terms contributed from each parcel were multiplied with the same ratio values before they were used to calculate the Eulerian variables. All simulations were initialized by considering a single-phase jet made of air and acetone vapour until statistically steady conditions had been attained. Then, droplets were continuously injected, and simulations continued to run for additional times to achieve statistically steady conditions for the two-phase jet-spray before proceeding to the collection of data. By benchmarking against the corresponding fully resolved DNS from Paper I, the present work showed the extent to which the parcel ratio does not cause a significant change the fluid and droplet phase statistics.

Numerical results demonstrated the robustness of the parcel concept when the ratio between computational and physical particles is carefully implemented. In particular, an appropriate parcel ratio, which keeps the same number of computational particles per cell as its DNS to LES Eulerian counterpart, e.g. 64 in the present work, could provide robust results on mean statistics of droplets. Further increasing the parcel ratio would lead to a significant underestimation of the mean behaviours of droplet evaporation. Two reasons are highlighted: The statistical errors introduced by the grid-based estimate of average field variables; The strongly spatially non-uniform distribution of parcels. We believe that the findings showed in the present work may contribute to improving the capabilities of current models in accurately and efficiently reproducing the flow physics and particle/droplet dynamics in a wide range of problems with scientific and technical interests.

3.3 Paper III

Short-range exposure to airborne virus transmission and current guidelines

Respiratory diseases can be transmitted among human subjects through pathogen-laden droplets/aerosols exhaled during respiratory events, which physically produce an interrupted multiphase turbulent jet/puff. In Paper I, we have already proved that the evaporation process within such a high-Re number turbulent spray condition is extremely complex and cannot be accurately captured with simplified models, like the classical D^2-law, which is also true for respiratory droplets/aerosols. In particular, fluid motions driving the virus transmission during violent respiratory events are intermittent, have a strongly organized and coherent nature and control the transport of the dispersed species in such a way that the overall distribution will not resemble those given by methods in which these motions are ignored. However, very little is known about the quantitative effect of the turbulent cloud of moist air exhaled during violent respiratory events on the airborne time and lifespan of virus-loaded droplets, which is of essential importance for designing health guidelines, especially during the COVID-19 pandemic.

In this work, we used finely resolved simulations and experiments to investigate the evaporation and dispersion dynamics of the respiratory droplets released during a sneeze. The sneezing jet is characterized by a temperature of $T_j = 308K$ and a relative humidity $RH_j = 90\%$ and the overall injection duration is about *0.6 s* with the peak velocity being *20 m/s*. Around 1,000,000 droplets, following a log-normal distribution for their initial size, were issued during the injection stage. A total of 7 simulations were performed using the Large-eddy simulation approach: a benchmark simulation, four production simulations and two additional simulations used to test the sensitivity of the results.

In order to assess the reliability of the numerical tool in accurately reproducing a sneezing event, the dataset of the time evolution of the jet front in the test simulation was collected to concurrently benchmark against experimental results and theoretical scaling laws available in the literature. First, we identified two different propagation phases, i.e. jet phase and puff phase: for the starting jet phase (constant momentum flux), the distance travelled by the jet front L grows over time as $L \propto t^{\frac{1}{2}}$, while, for the puff phase (constant momentum), the penetration distance grows as $L \propto t^{\frac{1}{4}}$. Moreover, both simulations and experiments exhibit very similar behaviour and are in excellent agreement with the analytical scaling law.

For the four production simulations, we considered the same emission and only changed environmental parameters (temperature T = *278 K and 293 K* and humidity RH = *50% and 90%*), and a strong variation in droplet's evaporation or condensation in accordance with their local temperature and humidity micro-environment were observed. Two flaws in current health guidelines are confirmed. A first flaw is identified in the standard prediction of the evaporation times: models currently used in public health guidelines grossly underestimate by at least one order of magnitude the actual evaporation time, especially in low temperature and high humidity situations. A second flaw is represented by the threshold used to differentiate between large and small droplets; while this definition can be meaningful in healthcare environments where the term aerosol refers to a specific group of operations, from a fluid dynamics perspective, this criterium is questionable as the behaviour of droplets is influenced by the local flow conditions (e.g. breath/cough/sneeze) and even large droplets (60/100 μm, considered as ballistic in most guidelines) stay suspended in the environment for a considerable amount of time.

These flaws lead to a consistent underestimation of the infection risk: formation of droplet-nuclei is delayed with respect to predictions, and droplets remain in the most infectious condition (liquid) for a much longer time. In addition, the flow conditions generated by violent expiratory events (sneeze) allow 60/100 μm droplets to remain airborne for a significant amount of time. As highlighted by the virus exposure maps, this leads to a remarkable risk of infection via airborne particles also in the short-range transmission, which should be better addressed by the health scientists and practitioners in calibrating new guidelines to mitigate the infection risk.

3.4 Paper IV

Revisiting D^2-law for the evaporation of dilute droplets

In a wide range of applications, the estimate of droplet evaporation time is based on the classical D^2-law, which, assuming a fast mixing and fixed droplet properties, states that the droplet surface decreases linearly with time at a determined rate. In paper I, however, we have provided evidence supporting that the evolution of the droplet histories strongly deviates from the D^2-law, whereas the trend of the mean evaporation time can be approximated by a linear law of the droplet mean square diameter, with its slope being much lower than the value predicted by the classical model. This is also true in respiratory events where droplets' lifetime could be extended up to two order magnitudes longer than that estimated by the Wells theory which is actually based on the classical D^2-law.

To find the reason of the inability of D^2-law in accurately estimating droplet evaporation, we thoroughly revisited this classical model and found that: In a dilute regime, the droplet's temperature tends to an asymptotic value, which is lower than the environmental quantity, due to the balance between liquid latent enthalpy and convective heat transfer. The transition time needed to reach the asymptotic temperature is around $6\tau_d$, droplet response time, when the ambient temperature is $20°C$. Neglecting this effect inevitably results in a relatively large evaporation rate constant, as in the classical D^2-law. To cover this leak, we proposed a revision of the classical model by a proper estimate of the asymptotic droplet properties.

In order to validate the proposed revision, we performed 6 DNSs of a turbulent jet-spray laden with monodispersed water droplets. The former four simulations considered different dilute levels at the inflow, i.e. the liquid mass fraction $\Psi_0 = 0.007; 0.0028; 0.0058; 0.01$. In the additional two simulations, the fully resolved equations of droplet evaporation were suppressed by the classical D^2-law and the proposed revised model to evolve the droplet radius. The spatial distribution of mean droplet size and mean liquid mass fraction, as well as the mean droplet surface against the mean droplet flight time, were compared. We found that the results computed using the revised D^2-law are in excellent agreement with the reference DNSs in the most dilute setups. Even in the less dilute case where the increasingly mutual interactions of droplets would slow down the evaporation, the revised D^2-law is still capable of predicting the evaporation behaviours more accurately than the classical model.

One more validation was performed by employing our model against the dataset from recent independent works[49, 148] on respiratory droplets evaporation in order to highlight the generality of the present work. Comparing the numerical results on droplets expelled during a coughing event at an environmental condition $T = 30°C$ $RH = 90\%$, the revised formulation accurately reproduces the temporal evolution of mean droplet surface, whereas the classical prediction strongly overestimates the vaporization rate, leading to shorter evaporation times.

The present findings can contribute to improving practical estimates of droplet evaporation behaviours, such as respiratory activities.

3.5 Paper V

Modelling the direct virus exposure risk associated with respiratory events

Droplets released during respiratory events play a crucial role in transmitting respiratory diseases (e.g. SARS-CoV-2) from an infected host to a susceptible individual. Traditionally, the fate of these droplets is estimated using the Wells theory which has been the pillar of past and current guidelines published by health organizations. Numerous convincible pieces of evidence have been produced to point out the weaknesses of this classical framework, e.g. the dependence on the D^2-law, ignorance of the presence of a turbulent cloud of moist air. In light of the most recent understanding of respiratory events, we used this body of developed knowledge to move away from the isolated drop emission to the turbulent, multi-phase puff model.

This study developed a simple physical model to predict the evaporation-falling-travelling performance of droplets expelled during various respiratory activities in different ambient conditions. The proposed model revises the outdated Wells theory exploiting the better knowledge on turbulent droplets transport by jets or plumes developed in the last few decades, as well as the state-of-the-art understanding of respiratory ejections. In particular, the model consists of three main components: the revised D^2-law as proposed in Paper IV(3.4); a correction to the Stokes law by taking into account the effect of droplet's initial Reynolds number; and the two-stage propagation theory elucidated in Paper III(3.3). The model, therefore, relies on a simple algebraic formulation and, without the need of solving complex systems of non-linear differential equations, it is capable of accurately estimating the dispersion, evaporation, and settling behaviours of droplets within a turbulent multiphase jet/puff. Moreover, the model can take into account different respiratory events (speaking, coughing, sneezing) and different ambient conditions (temperature and relative humidity) except for very cold and humid environments where the decay of droplet surface would not be simply characterized by a linear behaviour [148]. Reference data from well-recognized model [215], high-fidelity simulations [148, 205] and latest experimental investigations [114] have been used to benchmark the present model, confirming its capability to accurately predict the spatial-temporal evolution of respiratory droplets.

Using the proposed framework, we systematically assess the effects of physical distancing and face coverings on virus exposure maps and thus on the infection risk. We show that the infection risk is vastly impacted by the ambient conditions and respiratory event considered, indicating the non-existent of a universal safe distance. Finally, using the proposed model and exploiting experimental data on the penetration of respiratory droplets through face masks, we assess the effects of face masks on the infection risk. We confirm that face masks provide excellent "outward" protection, effectively reducing the infection risk near an infected person. Overall, we believe that the present model represents a substantial improvement of older models and, thanks to its simple but effective mathematical background, can be widely used by policymakers to design effective guidelines for the prevention of direct contagion.

Chapter 4

Conclusions and future work

4.1 Conclusions

The present thesis mainly focuses on the evaporation dynamics of dispersed droplets within turbulent dilute spray-jet conditions. Particular interests include the preferential sampling of evaporating droplets as well as practical problems like virus transmission via droplets/aerosols exhaled during respiratory activities. To this purpose, high-fidelity simulations, e.g. Direct numerical simulation (DNS) and Large-eddy simulation (LES), have been performed to advance the fundamental understanding of turbulent spray dynamics, which, in turn, helped to improve the accuracy of existing models to reproduce it. The overall conclusions of the dissertation are illustrated as follows.

From the DNS study of evaporating turbulent diluted spray at relative high Re number, we identified two mechanisms controlling the preferential sampling of droplets: clusterings are initially established due to the fluctuating mixing-layer interface and propagate downstream where the turbulent inertia takes a leading role. Droplets form clusters surrounded by high vapor concentration, promoting heterogeneous Lagrangian statistics like the strongly wide saturation level spectrum, which, in turn, affects the evaporation behavior of droplets. By evaluating the accuracy of D^2-law in approximating droplets evolution, we showed to which extend the classical model underestimates the evaporation time.

The computational cost associated with the Lagrangian method tracking an enormous number of particles in a two-phase fluid system can be hugely alleviated by introducing the parcel concept within LES framework. Our systematic analyses demonstrated the robustness of parcel concept when the parcel ratio is carefully selected. In particular, an appropriate parcel ratio, which keeps the same number of computational particles per cell as its DNS counterpart, could provide satisfactory results on mean statistics of droplets, whereas further increasing the parcel ratio would lead to a significant underestimation of the mean behaviors of droplets evaporation.

By performing finely resolved simulations and experiments of sneezing to bridge fluid dynamics and virological data with a sufficient level of accuracy, we provided evidence of the high infection risk associated with airborne respiratory droplets in the close proximity of an infected individual. This risk, evaluated for different environmental situations (temperature and humidity), is much higher than that estimated with the models that constitute the foundations of current health protection guidelines: drops evaporate much slower than what is currently predicted and can carry their viral load much farther. Building on present data, we are able to produce original virus exposure maps, which can be an instrument for health scientists and practitioners to calibrate new safety measures.

By revisiting the classical D^2-law for evaporation of point-approximated droplets, we found that, in dilute regimes, the temperature of evaporating droplets tends to an asymptotic equilibrium, which is lower than the environmental value, due to the balance between convective heat flux and droplet latent enthalpy. Together with inspirations from Paper I and Paper III, we proposed a revision of the classical D^2-law capable of accurately estimating droplet evaporation rate in dilute conditions by a proper estimate of the asymptotic droplet properties.

The success in revising D^2-law together with the most recent findings on multiphase flow physics motivated us to establish an effective framework, which relies on a simple algebraic formulation, capable of accurately estimating the dispersion, evaporation, and settling behaviors of droplets exhaled during different respiratory events in different environments condition. After thoroughly validating against multi-dimensional reference data, the proposed model was utilized to assess the effects of physical distancing and face coverings on mitigating the infection risk. We showed that the risk of infection is vastly impacted by the ambient conditions and the type of respiratory activity, suggesting the non-existence of a universal safe distance. Meanwhile, wearing face masks provides excellent protection, effectively limiting the transmission of pathogens even at short physical distances, i.e. 1 meter.

4.2 Scope for future work

It has been presented in this thesis that the numerical study of turbulent sprays is a multifaceted problem for researchers willing to perform fundamental and practical investigations. Some of them have been studied in the present work whereas others still wait to be discovered. Further understanding of this phenomenon will perhaps benefit from advancements of both numerical algorithms and modeling strategies. Regarding possible directions for future work based on the current project, one possibility could be involving more complex physical phenomena into turbulent dilute sprays, e.g. combustion. The in-house code package is able to simulate turbulent premixed combustion without introducing evaporating droplets[18, 19]. In reality, the chemical reaction process occurs simultaneously with the droplets evaporation and vapor mixing, whose complexity could be aggravated due to the existence of clustering of evaporating droplets[169]. To accurately simulate and model the whole combustion process, therefore, the multi-scale dynamic mechanisms of clustering formation (turbulent inertia, stick-sweep, air entrainment, etc.) need to be clearly understood and clusters impact should be better quantified.

Another possibility for future work is to integrate and test different *sgs* models for the Lagrangian phase in the context of Large-eddy simulation. Although the present work did not consider any particle *sgs* model, in LES of particle-laden flows like a jet-spray, such a closure model is indeed required of very high Reynolds number for the description of dispersed phase, not only pertaining to the effects of unresolved carrier flow momentum and energy transport on particle dynamics, also to the influence of the unsolved particle dynamics having on the continuous phase. One interesting question in this context is to know the extent to which the clustering effects can be captured by the resolved flow field and how much needs to be included by the Lagrangian *sgs* model. Promising candidates could be the stochastic models, which are designed to regain the whole *sgs* velocity field by introducing a stochastic noise to the motion equation of particles, and the structural models, which aim is to reconstruct some statistical features of the *sgs* velocity field using approximate deconvolution of resolved flow fields[124].

Last, further theoretical works could be carried out to extend the existing one-dimension model for direct contagion risks associated with respiratory droplets to a two-dimensional framework. On basis of the current model, both axial and radial distribution of droplet/aerosol concentration could be obtained by assuming the expiratory flows as a conical, quasi/steady jet with a fixed cone angle. Such a model can potentially provide more quantitative information on spatial estimation of the exposure risk.

Acknowledgement

The present work in this thesis was carried out in the CISAS "Giuseppe Colombo" at the University of Padova during the period 2018-2021. The dissertation would not complete without the support from many people to which I am very grateful.

I would begin with thanking my supervisor Prof. Francesco Picano who offered me the opportunity to pursue my PhD in Padova and made strategic advices during the research. He gave me full freedom to carry out the research on my own pace, never push but always ready to give support and advices. My knowledge of the physics and modeling of multiphase flows are developed by his patient and detailed supervision. I always admire his profound knowledge in many fields but more importantly his attractive personality. Very often I feel him as a friend. Thanks to him, the three-year PhD study became a joyful, memorable and fruitful journey.

I am deeply indebted to the China Scholarship Council (CSC) and the Department of Industrial Engineering, University of Padova, for providing financial support over the period of my doctoral study. Consorzio Interuniversitario per il Calcolo Automatico (CINECA supercomputing center, Bologna, Italy) is gratefully acknowledged for generous allowance of computer resources. I would like to express my sincere gratitude to my Master supervisor—prof. Haifeng LIU in Tianjin University, China. Under the supervision of him I gained my first experience and knowledge on research.

I appreciate the friendly atmosphere created by my colleagues and friends for making the time at the institute very enjoyable. It was great times not only in the office but also in the mountains. Special thanks to Dr. Federico Dalla Barba for timely discussions and generous advice on technical problems, to Dr. Francesco De Vanna for his help he provided when I just started FORTRAN programming and to Michele Cogo for the good spirit he brought to the office.

It was a great experience to collaborate with Dr. Alessio Roccon, Dr. Giovanni Soligo and other coworkers from TU Vienna, with whom I had many enlightening discussions. My warmest regard also to Prof. Alfredo Soldati. Although I didn't work with him in-person, I appreciate all help and guidance he provided on the collaboration project of Covid and on our journal papers published recently.

At this moment, the people that I am missing most are my parents, who always love and support me. Thank them for everything they have done for me.

Bibliography

[1] Shaw R. A., A. B. Kostinski, and Michael L. Larsen. Towards quantifying droplet clustering in clouds. *Q. J. R. Meteorol. Soc*, 128(582):1043–1057, 2002.

[2] Manouk Abkarian, Simon Mendez, Nan Xue, Fan Yang, and Howard A. Stone. Speech can produce jet-like transport relevant to asymptomatic spreading of virus. *Proc. Natl. Acad. Sci. U.S.A*, 117(41):25237–25245, 2020.

[3] B. Abramzon and W. A. Sirignano. Droplet vaporization model for spray combustion calculations. *Int. J. Heat Mass Transf.*, 32(9):1605–1618, 1989.

[4] Avinash Alagumalai. Internal combustion engines: Progress and prospects. *Renewable and Sustainable Energy Reviews*, 38:561–571, 2014.

[5] Alberto Aliseda, Alain Cartellier, F Hainaux, and Juan C Lasheras. Effect of preferential concentration on the settling velocity of heavy particles in homogeneous isotropic turbulence. *Journal of Fluid Mechanics*, 468:77–105, 2002.

[6] A Elhami Amiri, S Kazemzadeh Hannani, and F Mashayek. Large-eddy simulation of heavy-particle transport in turbulent channel flow. *Numerical Heat Transfer, Part B: Fundamentals*, 50(4):285–313, 2006.

[7] Elizabeth L Anderson, Paul Turnham, John R Griffin, and Chester C Clarke. Consideration of the aerosol transmission for covid-19 and public health. *Risk Analysis*, 40(5):902–907, 2020.

[8] Philip Anfinrud, Valentyn Stadnytskyi, Christina E. Bax, and Adriaan Bax. Visualizing speech-generated oral fluid droplets with laser light scattering. *N. Engl. J. Med.*, 382(21): 2061–2063, 2020.

[9] Vincenzo Armenio, Ugo Piomelli, and Virgilio Fiorotto. Effect of the subgrid scales on particle motion. *Physics of Fluids*, 11(10):3030–3042, 1999.

[10] Sima Asadi, Anthony S. Wexler, Christopher D. Cappa, Santiago Barreda, Nicole M. Bouvier, and William D. Ristenpart. Aerosol emission and superemission during human speech increase with voice loudness. *Sci. Rep.*, 9(1):2348, 2019.

[11] Antonio Attili, Fabrizio Bisetti, Michael E. Mueller, and Heinz Pitsch. Formation, growth, and transport of soot in a three-dimensional turbulent non-premixed jet flame. *Combust. Flame*, 161(7):1849–1865, 2014.

[12] Prateek Bahl, Con Doolan, Charitha de Silva, Abrar Ahmad Chughtai, Lydia Bourouiba, and C Raina MacIntyre. Airborne or droplet precautions for health workers treating coronavirus disease 2019? *The Journal of infectious diseases*, 2020.

[13] Bradley A Baker. Turbulent entrainment and mixing in clouds: A new observational approach. *Journal of Atmospheric Sciences*, 49(5):387–404, 1992.

[14] Lucia Baker, Ari Frankel, Ali Mani, and Filippo Coletti. Coherent clusters of inertial particles in homogeneous turbulence. *Journal of Fluid Mechanics*, 833:364–398, 2017.

[15] S. Balachandar and John K. Eaton. Turbulent dispersed multiphase flow. *Annu. Rev. Fluid Mech.*, 42(1):111–133, 2010.

[16] S. Balachandar, S. Zaleski, A. Soldati, G. Ahmadi, and L. Bourouiba. Host-to-host airborne transmission as a multiphase flow problem for science-based social distance guidelines. *Int. J. Multiph. Flow*, 132:103439, 2020.

[17] CG Ball, H Fellouah, and A Pollard. The flow field in turbulent round free jets. *Progress in Aerospace Sciences*, 50:1–26, 2012.

[18] F. Battista, F. Picano, G. Troiani, and C. M. Casciola. Intermittent features of inertial particle distributions in turbulent premixed flames. *Phys. Fluids*, 23(12):123304, 2011.

[19] Francesco Battista, Guido Troiani, and Francesco Picano. Fractal scaling of turbulent premixed flame fronts: application to les. *International Journal of Heat and Fluid Flow*, 51: 78–87, 2015.

[20] Jeremie Bec. Fractal clustering of inertial particles in random flows. *Physics of fluids*, 15(11): L81–L84, 2003.

[21] Jeremie Bec, Luca Biferale, Massimo Cencini, Alessandra Lanotte, Stefano Musacchio, and Federico Toschi. Heavy particle concentration in turbulence at dissipative and inertial scales. *Physical review letters*, 98(8):084502, 2007.

[22] Jérémie Bec, Massimo Cencini, Rafaela Hillerbrand, and Konstantin Turitsyn. Stochastic suspensions of heavy particles. *Physica D: Nonlinear Phenomena*, 237(14-17):2037–2050, 2008.

[23] Jeremy Bec, Luca Biferale, Guido Boffetta, Antonio Celani, Massimo Cencini, Alessandra Lanotte, S Musacchio, and Federico Toschi. Acceleration statistics of heavy particles in turbulence. *Journal of Fluid Mechanics*, 550:349–358, 2006.

[24] Sachidananda Behera, Rajneesh Bhardwaj, and Amit Agrawal. Effect of co-flow on fluid dynamics of a cough jet with implications in spread of covid-19. *Physics of Fluids*, 33(10): 101701, 2021.

[25] J Bellan and K Harstad. Analysis of the convective evaporation of nondilute clusters of drops. *International journal of heat and mass transfer*, 30(1):125–136, 1987.

[26] Josette Bellan and Martin Summerfield. Theoretical examination of assumptions commonly used for the gas phase surrounding a burning droplet. *Combustion and Flame*, 33:107–122, 1978.

[27] M. BINI and W. P. JONES. Large-eddy simulation of particle-laden turbulent flows. *J. Fluid Mech.*, 614:207–252, 2008.

[28] M Bini and WP Jones. Particle acceleration in turbulent flows: A class of nonlinear stochastic models for intermittency. *Physics of Fluids*, 19(3):035104, 2007.

[29] M Bini and WP Jones. Large eddy simulation of an evaporating acetone spray. *International Journal of Heat and Fluid Flow*, 30(3):471–480, 2009.

[30] R Byron Bird, Warren E Stewart, and Edwin N Lightfoot. *Transport phenomena*, volume 1. John Wiley & Sons, 2006.

[31] Madjid Birouk and Iskender Gökalp. A new correlation for turbulent mass transfer from liquid droplets. *International Journal of Heat and Mass Transfer*, 45(1):37–45, 2002.

[32] Madjid Birouk and Iskender Gökalp. Current status of droplet evaporation in turbulent flows. *Progress in Energy and Combustion Science*, 32(4):408–423, 2006.

[33] Dehandschoewercker E. & Bush J. W. Bourouiba, L. Violent expiratory events: on coughing and sneezing. *J. Fluid Mech.*, 745:537–563, 2014.

[34] L. Bourouiba. Turbulent gas clouds and respiratory pathogen emissions: Potential implications for reducing transmission of covid-19. *JAMA*, 323(18):1837–1838, 2020.

[35] Lydia Bourouiba. Images in clinical medicine. a sneeze. *N. Engl. J. Med.*, 375(8):e15, 2016.

[36] Lydia Bourouiba. The fluid dynamics of disease transmission. *Annu. Rev. Fluid Mech.*, 53 (1), 2021.

[37] Andrew D Bragg, Peter J Ireland, and Lance R Collins. On the relationship between the non-local clustering mechanism and preferential concentration. *Journal of Fluid Mechanics*, 780:327–343, 2015.

[38] Luca Brandt and Filippo Coletti. Particle-laden turbulence: Progress and perspectives. *Annual Review of Fluid Mechanics*, 54, 2021.

[39] A. Bukhvostova, E. Russo, J.G.M. Kuerten, and B. J. Geurts. Comparison of dns of compressible and incompressible turbulent droplet-laden heated channel flow with phase transition. *Int. J. Multiph. Flow*, 63:68–81, 2014.

[40] Paolo Burattini, RA Antonia, and L Danaila. Scale-by-scale energy budget on the axis of a turbulent round jet. *Journal of Turbulence*, (6):N19, 2005.

[41] Paolo Burattini, Robert A Antonia, and Luminita Danaila. Similarity in the far field of a turbulent round jet. *Physics of fluids*, 17(2):025101, 2005.

[42] Hadrien Calmet, Kiao Inthavong, Ambrus Both, Anurag Surapaneni, Daniel Mira, Beatriz Egukitza, and Guillaume Houzeaux. Large eddy simulation of cough jet dynamics, droplet transport, and inhalability over a ten minute exposure. *Physics of Fluids*, 33(12):125122, 2021.

[43] Claude Cambon, Nagi N Mansour, and Fabien S Godeferd. Energy transfer in rotating turbulence. *Journal of Fluid Mechanics*, 337:303–332, 1997.

[44] GF Carrier. Shock waves in a dusty gas. *Journal of Fluid Mechanics*, 4(4):376–382, 1958.

[45] C. Y. H. Chao, M. P. Wan, L. Morawska, G. R. Johnson, Z. D. Ristovski, M. Hargreaves, K. Mengersen, S. Corbett, Y. Li, X. Xie, and D. Katoshevski. Characterization of expiration air jets and droplet size distributions immediately at the mouth opening. *J. Aerosol Sci.*, 40 (2):122–133, 2009.

[46] L. CHEN, S. GOTO, and J. C. Vassilicos. Turbulent clustering of stagnation points and inertial particles. *J. Fluid Mech.*, 553(-1):143, 2006.

[47] X-Q Chen and JCF Pereira. Computation of turbulent evaporating sprays with well-specified measurements: a sensitivity study on droplet properties. *International journal of heat and mass transfer*, 39(3):441–454, 1996.

[48] Yung-Cheng Chen, Sten H. Stårner, and Assaad R. Masri. A detailed experimental investigation of well-defined, turbulent evaporating spray jets of acetone. *Int. J. Multiph. Flow*, 32 (4):389–412, 2006.

[49] Kai Leong Chong, Chong Shen Ng, Naoki Hori, Rui Yang, Roberto Verzicco, and Detlef Lohse. Extended lifetime of respiratory droplets in a turbulent vapor puff and its implications on airborne disease transmission. *Phys. Rev. Lett.*, 126(3):034502, 2021.

[50] Sergei G Chumakov and Christopher J Rutland. Dynamic structure subgrid-scale models for large eddy simulation. *International journal for numerical methods in fluids*, 47(8-9):911–923, 2005.

[51] P. P. Ciottoli, F. Battista, R. Malpica Galassi, F. Dalla Barba, and F. Picano. Direct numerical simulations of the evaporation of dilute sprays in turbulent swirling jets. *Flow Turbulence Combust.*, 106(3):993–1015, 2021.

[52] SW Coleman and JC Vassilicos. A unified sweep-stick mechanism to explain particle clustering in two-and three-dimensional homogeneous, isotropic turbulence. *Physics of Fluids*, 21(11): 113301, 2009.

[53] Clayton T Crowe, John D Schwarzkopf, Martin Sommerfeld, and Yutaka Tsuji. *Multiphase Flows with Droplets and Particles.* CRC Press, 2011.

[54] EN da C Andrade and LC Tsien. The velocity-distribution in a liquid-into-liquid jet. *Proceedings of the Physical Society (1926-1948)*, 49(4):381, 1937.

[55] F. Dalla Barba, J. Wang, and F. Picano. Revisiting d2-law for the evaporation of dilute droplets. *Phys. Fluids*, 33(5):051701, 2021.

[56] Federico Dalla Barba. High performance computing of turbulent evaporating sprays. 2016.

[57] Federico Dalla Barba and Francesco Picano. Clustering and entrainment effects on the evaporation of dilute droplets in a turbulent jet. *Phys. Rev. Fluids*, 3(3):034304, 2018.

[58] E James Davis and Gustav Schweiger. *The airborne microparticle: its physics, chemistry, optics, and transport phenomena.* Springer Science & Business Media, 2002.

[59] Julien Delteil, Stéphane Vincent, Arnaud Erriguible, and Pascale Subra-Paternault. Numerical investigations in rayleigh breakup of round liquid jets with vof methods. *Computers & Fluids*, 50(1):10–23, 2011.

[60] J. P. Duguid. The size and the duration of air-carriage of respiratory droplets and droplet-nuclei. *J. Hyg.*, 44(6):471–479, 1946.

[61] John K Eaton and JR1134 Fessler. Preferential concentration of particles by turbulence. *International Journal of Multiphase Flow*, 20:169–209, 1994.

[62] Editorial. COVID-19 transmission — up in the air. *Lancet Respir. Med.*, 8(12):1159, 2020.

[63] H. El-Asrag and S. Menon. Large eddy simulation of soot formation in a turbulent non-premixed jet flame. *Combustion and Flame*, 156(2):385–395, 2009.

[64] S. Elghobashi. On predicting particle-laden turbulent flows. *Appl. Sci. Res.*, 52(4):309–329, 1994.

[65] Said Elgobashi. An updated classification map of particle-laden turbulent flows. In *IUTAM Symposium on Computational Approaches to Multiphase Flow*, pages 3–10. Springer, 2006.

[66] G. M. Faeth. Current status of droplet and liquid combustion. *Prog. Energy Combust. Sci.*, 3(4):191–224, 1977.

[67] G.M Faeth, L.-P Hsiang, and P.-K Wu. Structure and breakup properties of sprays. *Int. J. Multiph. Flow*, 21:99–127, 1995.

[68] A. Favre. Turbulence: Space-time statistical properties and behavior in supersonic flows. *Phys. Fluids*, 26(10):2851, 1983.

[69] Járai-Szabó Ferenc and Zoltán Néda. On the size distribution of poisson voronoi cells. *Physica A: Statistical Mechanics and its Applications*, 385(2):518–526, 2007.

[70] A. Ferrante and S. Elghobashi. On the physical mechanisms of two-way coupling in particle-laden isotropic turbulence. *Phys. Fluids*, 15(2):315–329, 2003.

[71] Jim Ferry and S Balachandar. A fast eulerian method for disperse two-phase flow. *International journal of multiphase flow*, 27(7):1199–1226, 2001.

[72] Jim Ferry and S Balachandar. Equilibrium expansion for the eulerian velocity of small particles. *Powder Technology*, 125(2-3):131–139, 2002.

[73] Jim Ferry, Sarma L Rani, and S Balachandar. A locally implicit improvement of the equilibrium eulerian method. *International journal of multiphase flow*, 29(6):869–891, 2003.

[74] John R Fessler, Jonathan D Kulick, and John K Eaton. Preferential concentration of heavy particles in a turbulent channel flow. *Physics of Fluids*, 6(11):3742–3749, 1994.

[75] Pierre Février, Olivier Simonin, and Kyle D Squires. Partitioning of particle velocities in gas–solid turbulent flows into a continuous field and a spatially uncorrelated random distribution: theoretical formalism and numerical study. *Journal of Fluid Mechanics*, 533:1–46, 2005.

[76] Rodney O Fox, Frédérique Laurent, and Marc Massot. Numerical simulation of spray coalescence in an eulerian framework: direct quadrature method of moments and multi-fluid method. *Journal of Computational Physics*, 227(6):3058–3088, 2008.

[77] S. Gallot-Lavallée and W.P. Jones. Large eddy simulation of spray auto-ignition under egr conditions. *Flow, Turbulence and Combustion*, 96(2):513–534, 2016.

[78] S. Gallot-Lavallée, W.P. Jones, and A.J. Marquis. Large eddy simulation of an ethanol spray flame under mild combustion with the stochastic fields method. *Proceedings of the Combustion Institute*, 36(2):2577–2584, 2017.

[79] Haiwen Ge, Liang Chen, Chunwen Xu, and Xinguang Cui. Large-eddy simulation of droplet-laden cough jets with a realistic manikin model. *Indoor and Built Environment*, page 1420326X211032247, 2021.

[80] William K George. The self-preservation of turbulent flows and its relation to initial conditions and coherent structures. *Advances in turbulence*, 3973, 1989.

[81] Massimo Germano. Turbulence: the filtering approach. *Journal of Fluid Mechanics*, 238: 325–336, 1992.

[82] Bernardus J Geurts and Johannes GM Kuerten. Ideal stochastic forcing for the motion of particles in large-eddy simulation extracted from direct numerical simulation of turbulent channel flow. *Physics of fluids*, 24(8):081702, 2012.

[83] Mathieu Gibert, Haitao Xu, and Eberhard Bodenschatz. Where do small, weakly inertial particles go in a turbulent flow? *Journal of Fluid Mechanics*, 698:160–167, 2012.

[84] G.A.E. Godsave. Studies of the combustion of drops in a fuel spray—the burning of single drops of fuel. *Symp. Combust. Proc.*, 4(1):818–830, 1953.

[85] Jan Gralton, Euan Tovey, Mary-Louise McLaws, and William D Rawlinson. The role of particle size in aerosolised pathogen transmission: a review. *Journal of Infection*, 62(1):1–13, 2011.

[86] Picano Gualtieri, F Picano, and CM Casciola. Anisotropic clustering of inertial particles in homogeneous shear flow. *Journal of Fluid Mechanics*, 629:25–39, 2009.

[87] K Gustavsson and B Mehlig. Statistical models for spatial patterns of heavy particles in turbulence. *Advances in Physics*, 65(1):1–57, 2016.

[88] ZY Han, WG Weng, and QY Huang. Characterizations of particle size distribution of the droplets exhaled by sneeze. *Journal of the Royal Society Interface*, 10(88):20130560, 2013.

[89] Helene Holmgren, Evert Ljungström, Ann-Charlotte Almstrand, Björn Bake, and Anna-Carin Olin. Size distribution of exhaled particles in the range from 0.01 to 2.0 μm. *Journal of Aerosol Science*, 41(5):439–446, 2010.

[90] Abolfazl Irannejad and Farhad Jaberi. Numerical study of high speed evaporating sprays. *International Journal of Multiphase Flow*, 70:58–76, 2015.

[91] Mahesh Jayaweera, Hasini Perera, Buddhika Gunawardana, and Jagath Manatunge. Transmission of covid-19 virus by droplets and aerosols: A critical review on the unresolved dichotomy. *Environ. Res.*, 188:109819, 2020.

[92] Marshall W Jennison. Atomizing of mouth and nose secretions into the air as revealed by high-speed photography. *Aerobiology*, 17:106–128, 1942.

[93] Patrick Jenny, Dirk Roekaerts, and Nijso Beishuizen. Modeling of turbulent dilute spray combustion. *Prog. Energy Combust. Sci.*, 38(6):846–887, 2012.

[94] G. R. Johnson, L. Morawska, Z. D. Ristovski, M. Hargreaves, K. Mengersen, C.Y.H. Chao, M. P. Wan, Y. Li, X. Xie, D. Katoshevski, and S. Corbett. Modality of human expired aerosol size distributions. *J. Aerosol Sci.*, 42(12):839–851, 2011.

[95] W.P Jones and B.E Launder. The prediction of laminarization with a two-equation model of turbulence. *Int. J. Heat Mass Transf.*, 15(2):301–314, 1972.

[96] W.P. Jones and C. Lettieri. Large eddy simulation of spray atomization with stochastic modeling of breakup. *Physics of Fluids*, 22(11), 2010.

[97] WP Jones, S Lyra, and AJ Marquis. Large eddy simulation of evaporating kerosene and acetone sprays. *International Journal of Heat and Mass Transfer*, 53(11-12):2491–2505, 2010.

[98] W.P. Jones, S. Lyra, and S. Navarro-Martinez. Large eddy simulation of a swirl stabilized spray flame. *Proceedings of the Combustion Institute*, 33(2):2153–2160, 2011.

[99] W.P. Jones, S. Lyra, and S. Navarro-Martinez. Numerical investigation of swirling kerosene spray flames using large eddy simulation. *Combustion and Flame*, 159(4):1539–1561, 2012.

[100] W.P. Jones, A.J. Marquis, and K. Vogiatzaki. Large-eddy simulation of spray combustion in a gas turbine combustor. *Combustion and Flame*, 161(1):222–239, 2014.

[101] W.P. Jones, A.J. Marquis, and D. Noh. An investigation of a turbulent spray flame using large eddy simulation with a stochastic breakup model. *Combustion and Flame*, 186:277–298, 2017.

[102] Mrinal Kaushik, Rakesh Kumar, and G Humrutha. Review of computational fluid dynamics studies on jets. *American Journal of Fluid Dynamics*, 5(3A):1–11, 2015.

[103] Ian M. Kennedy. Models of soot formation and oxidation. *Prog. Energy Combust. Sci.*, 23(2): 95–132, 1997.

[104] Ali Khosronejad, Christian Santoni, Kevin Flora, Zexia Zhang, Seokkoo Kang, Seyedmehdi Payabvash, and Fotis Sotiropoulos. Fluid dynamics simulations show that facial masks can suppress the spread of covid-19 in indoor environments. *Aip Advances*, 10(12):125109, 2020.

[105] Won-Wook Kim and Suresh Menon. A new dynamic one-equation subgrid-scale model for large eddy simulations. In *33rd Aerospace Sciences Meeting and Exhibit*, page 356, 1995.

[106] Andrey Nikolaevich Kolmogorov. The local structure of turbulence in incompressible viscous fluid for very large reynolds numbers. *Cr Acad. Sci. URSS*, 30:301–305, 1941.

[107] JGM Kuerten. Subgrid modeling in particle-laden channel flow. *Physics of fluids*, 18(2): 025108, 2006.

[108] JGM Kuerten and AW1187 Vreman. Can turbophoresis be predicted by large-eddy simulation? *Physics of Fluids*, 17(1):011701–011701, 2005.

[109] Johannes GM Kuerten. Point-particle dns and les of particle-laden turbulent flow-a state-of-the-art review. *Flow, turbulence and combustion*, 97(3):689, 2016.

[110] I. Langmuir. The evaporation of small spheres. *Phys. Rev.*, 12(5):368–370, 1918.

[111] P Lavoie, A Pollard, and H Sadeghi. Turbulence and data analytics in the twenty-first century: The round free jet. In *Whither Turbulence and Big Data in the 21st Century?*, pages 119–132. Springer, 2017.

[112] Anthony Leboissetier, Nora Okong'o, and Josette Bellan. Consistent large-eddy simulation of a temporal mixing layer laden with evaporating drops. part 2. a posteriori modelling. *Journal of Fluid Mechanics*, 523:37–78, 2005.

[113] Dyani Lewis. Covid-19 rarely spreads through surfaces. so why are we still deep cleaning? *Nature*, 590(7844):26–28, 2021.

[114] Christian Lieber, Stefanos Melekidis, Rainer Koch, and Hans-Jörg Bauer. Insights into the evaporation characteristics of saliva droplets and aerosols: Levitation experiments and numerical modeling. *Journal of aerosol science*, 154:105760, 2021.

[115] Sung P Lin and Rolf D Reitz. Drop and spray formation from a liquid jet. *Annual review of fluid mechanics*, 30(1):85–105, 1998.

[116] William G Lindsley, Terri A Pearce, Judith B Hudnall, Kristina A Davis, Stephen M Davis, Melanie A Fisher, Rashida Khakoo, Jan E Palmer, Karen E Clark, Ismail Celik, et al. Quantity and size distribution of cough-generated aerosol particles produced by influenza patients during and after illness. *Journal of occupational and environmental hygiene*, 9(7):443–449, 2012.

[117] K Liu, M Allahyari, J Salinas, N Zgheib, and S Balachandar. Investigation of theoretical scaling laws using large eddy simulations for airborne spreading of viral contagion from sneezing and coughing. *Physics of Fluids*, 33(6):063318, 2021.

[118] Li Liu, Jianjian Wei, Yuguo Li, and Andrew Ooi. Evaporation and dispersion of respiratory droplets from coughing. *Indoor air*, 27(1):179–190, 2017.

[119] Yuanqing Liu, Lian Shen, Rémi Zamansky, and Filippo Coletti. Life and death of inertial particle clusters in turbulence. *Journal of Fluid Mechanics*, 902, 2020.

[120] Robert G Loudon and Rena Marie Roberts. Droplet expulsion from the respiratory tract. *American Review of Respiratory Disease*, 95(3):435–442, 1967.

[121] Hao Lu, Christopher J Rutland, and Leslie M Smith. A priori tests of one-equation les modeling of rotating turbulence. *Journal of Turbulence*, (8):N37, 2007.

[122] Frank E Marble. Dynamics of dusty gases. *Annual Review of Fluid Mechanics*, 2(1):397–446, 1970.

[123] Anthony J Marchese and Frederick L Dryer. The effect of liquid mass transport on the combustion and extinction of bicomponent droplets of methanol and water. *Combustion and Flame*, 105(1-2):104–122, 1996.

[124] Cristian Marchioli. Large-eddy simulation of turbulent dispersed flows: a review of modelling approaches. *Acta Mechanica*, 228(3):741–771, 2017.

[125] Cristian Marchioli, Maria Vittoria Salvetti, and Alfredo Soldati. Appraisal of energy recovering sub-grid scale models for large-eddy simulation of turbulent dispersed flows. *Acta mechanica*, 201(1):277–296, 2008.

[126] P. MARMOTTANT and E. VILLERMAUX. On spray formation. *J. Fluid Mech.*, 498:73–111, 2004.

[127] F. Mashayek. Direct numerical simulations of evaporating droplet dispersion in forced low mach number turbulence. *Int. J. Heat Mass Transf.*, 41(17):2601–2617, 1998.

[128] Farzad Mashayek. Droplet–turbulence interactions in low-mach-number homogeneous shear two-phase flows. *Journal of Fluid Mechanics*, 367:163–203, 1998.

[129] M. R. Maxey and J. J. Riley. Equation of motion for a small rigid sphere in a nonuniform flow. *Phys. Fluids*, 26(4):883, 1983.

[130] Martin R Maxey. The gravitational settling of aerosol particles in homogeneous turbulence and random flow fields. *Journal of Fluid Mechanics*, 174:441–465, 1987.

[131] S Menon. Co emission and combustion dynamics near lean-blowout in gas turbine engines. In *Turbo Expo: Power for Land, Sea, and Air*, volume 41669, pages 153–160, 2004.

[132] S. Menon and J.-H. Soo. Simulation of vortex dynamics in three-dimensional synthetic and free jets using the large-eddy lattice boltzmann method. *Journal of Turbulence*, 5, 2004.

[133] Suresh Menon. Multi-scale modeling for les of engineering designs of large-scale combustors. In *42nd AIAA aerospace sciences meeting and exhibit*, page 157, 2004.

[134] Suresh Menon and Nayan Patel. Subgrid modeling for simulation of spray combustion in large-scale combustors. *AIAA journal*, 44(4):709–723, 2006.

[135] WR Michałek, JGM Kuerten, JCH Zeegers, Raoul Liew, J Pozorski, and BJ Geurts. A hybrid stochastic-deconvolution model for large-eddy simulation of particle-laden flow. *Physics of Fluids*, 25(12):123302, 2013.

[136] R. S. Miller, K. Harstad, and J. Bellan. Evaluation of equilibrium and non-equilibrium evaporation models for many-droplet gas-liquid flow simulations. *Int. J. Multiph. Flow*, 24(6): 1025–1055, 1998.

[137] Jean-Pierre Minier. On lagrangian stochastic methods for turbulent polydisperse two-phase reactive flows. *Progress in Energy and Combustion Science*, 50:1–62, 2015.

[138] R. Mittal, R. Ni, and J. H. Seo. The flow physics of covid-19. *J. Fluid Mech.*, 894:317, 2020.

[139] Parviz Moin, Kyle Squires, W Cabot, and Sangsan Lee. A dynamic subgrid-scale model for compressible turbulence and scalar transport. *Physics of Fluids A: Fluid Dynamics*, 3(11): 2746–2757, 1991.

[140] Mohammadreza Momenifar and Andrew D Bragg. Local analysis of the clustering, velocities, and accelerations of particles settling in turbulence. *Physical Review Fluids*, 5(3):034306, 2020.

[141] Romain Monchaux. Measuring concentration with voronoï diagrams: the study of possible biases. *New Journal of Physics*, 14(9):095013, 2012.

[142] Romain Monchaux, Mickaël Bourgoin, and Alain Cartellier. Preferential concentration of heavy particles: a voronoï analysis. *Physics of Fluids*, 22(10):103304, 2010.

[143] Romain Monchaux, Mickael Bourgoin, and Alain Cartellier. Analyzing preferential concentration and clustering of inertial particles in turbulence. *Int. J. Multiph. Flow*, 40:1–18, 2012.

[144] L. Morawska, G. R. Johnson, Z. D. Ristovski, M. Hargreaves, K. Mengersen, S. Corbett, C.Y.H. Chao, Y. Li, and D. Katoshevski. Size distribution and sites of origin of droplets expelled from the human respiratory tract during expiratory activities. *J. Aerosol Sci.*, 40(3): 256–269, 2009.

[145] Harry W Morse. On evaporation from the surface of a solid sphere. preliminary note. In *Proceedings of the American Academy of Arts and Sciences*, volume 45, pages 363–367. JSTOR, 1910.

[146] B. Muralidaran and S. Menon. Large eddy simulation of turbulent reacting jet in cross-flow with adaptive mesh refinement. 2014.

[147] D. D. Joseph N.A. Patankar. Modeling and numerical simulation of particulate fows by the eulerian-lagrangian approach. *Int. J. Multiph. Flow*, 27(10):1659–1684, 2001.

[148] Chong Shen Ng, Kai Leong Chong, Rui Yang, Mogeng Li, Roberto Verzicco, and Detlef Lohse. Growth of respiratory droplets in cold and humid air. *Phys. Rev. Fluids*, 6(5):054303, 2021.

[149] Mark Nicas, William W Nazaroff, and Alan Hubbard. Toward understanding the risk of secondary airborne infection: emission of respirable pathogens. *Journal of occupational and environmental hygiene*, 2(3):143–154, 2005.

[150] JJ Nijdam, SH Stårner, and TAG Langrish. An experimental investigation of droplet evaporation and coalescence in a simple jet flow. *Experiments in Fluids*, 37(4):504–517, 2004.

[151] Christopher Nilsen, Helge I Andersson, and Lihao Zhao. A voronoï analysis of preferential concentration in a vertical channel flow. *Physics of Fluids*, 25(11):115108, 2013.

[152] Nora Okong'o and Josette Bellan. A priori subgrid analysis of temporal mixing layers with evaporating droplets. *Physics of Fluids*, 12(6):1573–1591, 2000.

[153] Nora A Okong'o and Josette Bellan. Consistent large-eddy simulation of a temporal mixing layer laden with evaporating drops. part 1. direct numerical simulation, formulation and a priori analysis. *Journal of Fluid Mechanics*, 499:1–47, 2004.

[154] Yu Pan and Kazuhiko Suga. A numerical study on the breakup process of laminar liquid jets into a gas. *Physics of fluids*, 18(5):052101, 2006.

[155] Chandra Shekhar Pant, Sumit Kumar, and Abhimanyu Gavasane. Mixing at the interface of the sneezing/coughing phenomena and its effect on viral loading. *Physics of Fluids*, 33(11): 115129, 2021.

[156] Dror Parienta, Lidia Morawska, GR Johnson, ZD Ristovski, Megan Hargreaves, Kerrie Mengersen, Stephen Corbett, Christopher YH Chao, Yuguo Li, and David Katoshevski. Theoretical analysis of the motion and evaporation of exhaled respiratory droplets of mixed composition. *Journal of aerosol science*, 42(1):1–10, 2011.

[157] R. Pasumarti, J. Schulz, J. Seitzman, J. Jagoda, and S. Menon. Large eddy simulation of pulsed jets in high speed turbulent crossflow. 2010.

[158] Alec J Petersen, Lucia Baker, and Filippo Coletti. Experimental study of inertial particles clustering and settling in homogeneous turbulence. *Journal of Fluid Mechanics*, 864:925–970, 2019.

[159] F. Picano, F. Battista, G. Troiani, and C. M. Casciola. Dynamics of piv seeding particles in turbulent premixed flames. *Exp. Fluids*, 50(1):75–88, 2011.

[160] Abgail P Pinheiro and João Marcelo Vedovoto. Evaluation of droplet evaporation models and the incorporation of natural convection effects. *Flow, Turbulence and Combustion*, 102(3): 537–558, 2019.

[161] Ugo Piomelli. Large-eddy simulation: achievements and challenges. *Progress in aerospace sciences*, 35(4):335–362, 1999.

[162] Eric Pomraning and Christopher J Rutland. Dynamic one-equation nonviscosity large-eddy simulation model. *AIAA journal*, 40(4):689–701, 2002.

[163] Stephen B. Pope. *Turbulent Flows.* Cambridge University Press, 2000.

[164] Jacek Pozorski and Sourabh V Apte. Filtered particle tracking in isotropic turbulence and stochastic modeling of subgrid-scale dispersion. *International Journal of Multiphase Flow*, 35 (2):118–128, 2009.

[165] B Rabencov and R van Hout. Voronoi analysis of beads suspended in a turbulent square channel flow. *Intl J. Multiphase Flow*, 68:10–13, 2015.

[166] Venkat Raman and Rodney O. Fox. Modeling of fine-particle formation in turbulent flames. *Annu. Rev. Fluid Mech.*, 48(1):159–190, 2016.

[167] Sarma L Rani and S Balachandar. Evaluation of the equilibrium eulerian approach for the evolution of particle concentration in isotropic turbulence. *International journal of multiphase flow*, 29(12):1793–1816, 2003.

[168] MW Reeks. The transport of discrete particles in inhomogeneous turbulence. *Journal of aerosol science*, 14(6):729–739, 1983.

[169] Julien Reveillon and FRANCOIS-XAVIER Demoulin. Effects of the preferential segregation of droplets on evaporation and turbulent mixing. *J. Fluid Mech.*, 583:273–302, 2007.

[170] Osborne Reynolds. Xxix. an experimental investigation of the circumstances which determine whether the motion of water shall be direct or sinuous, and of the law of resistance in parallel channels. *Philosophical Transactions of the Royal society of London*, (174):935–982, 1883.

[171] Osborne Reynolds. Iv. on the dynamical theory of incompressible viscous fluids and the determination of the criterion. *Philosophical transactions of the royal society of london.(a.)*, (186):123–164, 1895.

[172] Lewis Fry Richardson. *Weather prediction by numerical process.* Cambridge university press, 1922.

[173] G. Rocco, F. Battista, F. Picano, G. Troiani, and C. M. Casciola. Curvature effects in turbulent premixed flames of h2/air: a dns study with reduced chemistry. *Flow Turbulence Combust.*, 94(2):359–379, 2015.

[174] Ana Luíza Silva Rocha, Josilene Ramos Pinheiro, Thamilin Costa Nakamura, da Silva, José Domingos Santos, Beatriz Gonçalves Silva Rocha, Raphael Contelli Klein, Alexander Birbrair, and Jaime Henrique Amorim. Fomites and the environment did not have an important role in covid-19 transmission in a brazilian mid-sized city. *Sci. Rep.*, 11(1):15960, 2021.

[175] M. E. Rosti, M. Cavaiola, S. Olivieri, A. Seminara, and A. Mazzino. Turbulence role in the fate of virus-containing droplets in violent expiratory events. *Phys. Rev. Research*, 3(1), 2021.

[176] S Sahu, Y Hardalupas, and AMKP Taylor. Droplet–turbulence interaction in a confined polydispersed spray: effect of turbulence on droplet dispersion. *Journal of Fluid Mechanics*, 794:267–309, 2016.

[177] S Sahu, Y Hardalupas, and AMKP Taylor. Interaction of droplet dispersion and evaporation in a polydispersed spray. *Journal of Fluid Mechanics*, 846:37–81, 2018.

[178] R. Sangras, O. C. Kwon, and G. M. Faeth. Self-preserving properties of unsteady round nonbuoyant turbulent starting jets and puffs in still fluids. *J. Heat Transfer*, 124(3):460–469, 2002.

[179] Vaidyanathan Sankaran and Suresh Menon. Les of spray combustion in swirling flows. *Journal of Turbulence*, 3(1):011, 2002.

[180] Vaidyanathan Sankaran and Suresh Menon. Vorticity-scalar alignments and small-scale structures in swirling spray combustion. *Proceedings of the Combustion Institute*, 29(1):577–584, 2002.

[181] Gaetano Sardina, Francesco Picano, Luca Brandt, and Rodrigo Caballero. Continuous growth of droplet size variance due to condensation in turbulent clouds. *Phys. Rev. Lett.*, 115(18): 184501, 2015.

[182] Ewe Wei Saw, Raymond A Shaw, Sathyanarayana Ayyalasomayajula, Patrick Y Chuang, and Armann Gylfason. Inertial clustering of particles in high-reynolds-number turbulence. *Physical review letters*, 100(21):214501, 2008.

[183] Helmut Schmidt and Ulrich Schumann. Coherent structure of the convective boundary layer derived from large-eddy simulations. *J. Fluid Mech.*, 200:511–562, 1989.

[184] B Shotorban, KKQ Zhang, and F Mashayek. Improvement of particle concentration prediction in large-eddy simulation by defiltering. *International journal of heat and mass transfer*, 50 (19-20):3728–3739, 2007.

[185] Babak Shotorban and S Balachandar. Particle concentration in homogeneous shear turbulence simulated via lagrangian and equilibrium eulerian approaches. *Physics of Fluids*, 18(6):065105, 2006.

[186] Babak Shotorban and Farzad Mashayek. Modeling subgrid-scale effects on particles by approximate deconvolution. *Physics of Fluids*, 17(8):081701, 2005.

[187] Babak Shotorban and Farzad Mashayek. A stochastic model for particle motion in large-eddy simulation. *Journal of Turbulence*, (7):N18, 2006.

[188] WA Sirignano. *Fluid Dynamics and Transport of Droplets and Sprays*. Cambridge University Press, 2010.

[189] J. Smagorinsky. General circulation experiments with the primitive equations. *Mon. Wea. Rev.*, 91(3):99–164, 1963.

[190] Giovanni Soligo, Alessio Roccon, and Alfredo Soldati. Mass-conservation-improved phase field methods for turbulent multiphase flow simulation. *Acta Mechanica*, 230(2):683–696, 2019.

[191] George A Soper. The lessons of the pandemic. *Science*, 49(1274):501–506, 1919.

[192] D. B. Spalding. Combustion of liquid fuels. *Nature*, 165(4187):160, 1950.

[193] DB SPALDING. The combustion of liquid fuels. In *Fourth Symposium (International) on Combustion, Pittsburgh, Penn.(1953)*. The Combustion Institute, 1953.

[194] Dudley Brian Spalding. *Some fundamentals of combustion*, volume 2. Butterworths scientific publications, 1955.

[195] Kyle D Squires and John K Eaton. Particle response and turbulence modification in isotropic turbulence. *Physics of Fluids A: Fluid Dynamics*, 2(7):1191–1203, 1990.

[196] S. Srinivasan, R. Pasumarti, and S. Menon. Large-eddy simulation of pulsed high-speed subsonic jets in a turbulent crossflow. *Journal of Turbulence*, 13:1–21, 2012.

[197] Valentyn Stadnytskyi, Christina E. Bax, Adriaan Bax, and Philip Anfinrud. The airborne lifetime of small speech droplets and their potential importance in sars-cov-2 transmission. *Proc. Natl. Acad. Sci. U.S.A*, 117(22):11875–11877, 2020.

[198] Shankar Subramaniam. Lagrangian–eulerian methods for multiphase flows. *Prog. Energy Combust. Sci.*, 39(2-3):215–245, 2013.

[199] Sholpan Sumbekova, Alain Cartellier, Alberto Aliseda, and Mickael Bourgoin. Preferential concentration of inertial sub-kolmogorov particles: the roles of mass loading of particles, stokes numbers, and reynolds numbers. *Physical Review Fluids*, 2(2):024302, 2017.

[200] Mitsuru Tanaka, Yasushi Maeda, and Yoshimichi Hagiwara. Turbulence modification in a homogeneous turbulent shear flow laden with small heavy particles. *International journal of heat and fluid flow*, 23(5):615–626, 2002.

[201] J. W. Tang, W. P. Bahnfleth, P. M. Bluyssen, G. Buonanno, J. L. Jimenez, J. Kurnitski, Y. Li, S. Miller, C. Sekhar, L. Morawska, L. C. Marr, A. K. Melikov, W. W. Nazaroff, P. V. Nielsen, R. Tellier, P. Wargocki, and S. J. Dancer. Dismantling myths on the airborne transmission of severe acute respiratory syndrome coronavirus-2 (sars-cov-2). *J. Hosp. Infect.*, 110:89–96, 2021.

[202] F Thiesset, RA Antonia, and L Djenidi. Consequences of self-preservation on the axis of a turbulent round jet. *Journal of Fluid Mechanics*, 748, 2014.

[203] Shrey Trivedi, Savvas Gkantonas, Léo CC Mesquita, Salvatore Iavarone, Pedro M de Oliveira, and Epaminondas Mastorakos. Estimates of the stochasticity of droplet dispersion by a cough. *Physics of Fluids*, 33(11):115130, 2021.

[204] Chia C. Wang, Kimberly A. Prather, Josué Sznitman, Jose L. Jimenez, Seema S. Lakdawala, Zeynep Tufekci, and Linsey C. Marr. Airborne transmission of respiratory viruses. *Science*, 373(6558):eabd9149, 2021.

[205] Jietuo Wang, Mobin Alipour, Giovanni Soligo, Alessio Roccon, Marco de Paoli, Francesco Picano, and Alfredo Soldati. Short-range exposure to airborne virus transmission and current guidelines. *Proc. Natl. Acad. Sci. U.S.A*, 118(37), 2021.

[206] Jietuo Wang, Federico Dalla Barba, and Francesco Picano. Direct numerical simulation of an evaporating turbulent diluted jet-spray at moderate reynolds number. *Int. J. Multiph. Flow*, 137:103567, 2021.

[207] Lian-Ping Wang and Martin R Maxey. Settling velocity and concentration distribution of heavy particles in homogeneous isotropic turbulence. *Journal of fluid mechanics*, 256:27–68, 1993.

[208] Qunzhen Wang and Kyle D Squires. Large eddy simulation of particle-laden turbulent channel flow. *Physics of Fluids*, 8(5):1207–1223, 1996.

[209] Jianjian Wei and Yuguo Li. Enhanced spread of expiratory droplets by turbulence in a cough jet. *BUILD. ENVIRON.*, 93:86–96, 2015.

[210] Jianjian Wei and Yuguo Li. Human cough as a two-stage jet and its role in particle transport. *PloS one*, 12(1):e0169235, 2017.

[211] Philipp Weiss, Valentin Giddey, Daniel W Meyer, and Patrick Jenny. Evaporating droplets in shear turbulence. *Physics of Fluids*, 32(7):073305, 2020.

[212] W. F. Wells. On air-borne infection. study ii. droplets and droplet nuclei. *Am. J. Hyg.*, 20: 611–618, 1934.

[213] W. F. Wells. *Airborne Contagion and Air Hygiene. An Ecological Study of Droplet Infections.* Harvard University Press, 1955.

[214] World Health Organization. Coronavirus disease (covid-19): How is it transmitted?, 2020. URL `https://www.who.int/news-room/q-a-detail/coronavirus-disease-covid-19-how-is-it-transmitted`.

[215] X. Xie, Y. Li, A. T. Chwang, P. L. Ho, and W. H. Seto. How far droplets can move in indoor environments – revisiting the wells evaporation–falling curve. *Indoor air*, 17(3):211–225, 2007. ISSN 0905-6947.

[216] Fan Yang, Amir A. Pahlavan, Simon Mendez, Manouk Abkarian, and Howard A. Stone. Towards improved social distancing guidelines: Space and time dependence of virus transmission from speech-driven aerosol transport between two individuals. *Phys. Rev. Fluids*, 5(12), 2020.

[217] MA Yavuz, RPJ Kunnen, GJF Van Heijst, and HJH Clercx. Extreme small-scale clustering of droplets in turbulence driven by hydrodynamic interactions. *Physical review letters*, 120 (24):244504, 2018.

[218] Akira Yoshizawa. Statistical theory for compressible turbulent shear flows, with the application to subgrid modeling. *The Physics of fluids*, 29(7):2152–2164, 1986.

[219] Akira Yoshizawa and Kiyosi Horiuti. A statistically-derived subgrid-scale kinetic energy model for the large-eddy simulation of turbulent flows. *Journal of the Physical Society of Japan*, 54 (8):2834–2839, 1985.

[220] Wenjun Yuan, Lihao Zhao, Helge I Andersson, and Jianqiang Deng. Three-dimensional voronoï analysis of preferential concentration of spheroidal particles in wall turbulence. *Physics of Fluids*, 30(6):063304, 2018.

[221] MC Yuen and La W CHEN. On drag of evaporating liquid droplets. 1976.

[222] AJ Yule, C Ah Seng, PG Felton, A Ungut, and NA Chigier. A study of vaporizing fuel sprays by laser techniques. *Combustion and Flame*, 44(1-3):71–84, 1982.

[223] AJ Yule, PR Ereaut, and A Ungut. Droplet sizes and velocities in vaporizing sprays. *Combustion and Flame*, 54(1-3):15–22, 1983.

[224] Leonid I Zaichik and Vladimir M Alipchenkov. Statistical models for predicting pair dispersion and particle clustering in isotropic turbulence and their applications. *New Journal of Physics*, 11(10):103018, 2009.

[225] Maoying Zhou and Jun Zou. A dynamical overview of droplets in the transmission of respiratory infectious diseases. *Physics of Fluids*, 33(3):031301, 2021.

Appendix A

Paper I

Direct numerical simulation of an evaporating turbulent diluted jet-spray at moderate Reynolds number

Jietuo Wang[1], **Federico Dalla Barba**[1], **Francesco Picano**[1,2]

1. Centro di Ateneo di Studi e Attività Spaziali "Giuseppe Colombo" - CISAS,
University of Padova, Padova, PD 35131, Italy
2. Department of Industrial Engineering, University of Padova,
Padova, PD 35131, Italy

International Journal of Multiphase Flow, 2021, 137, 103567

Abstract: The evaporation of liquid droplets dispersed in jet-sprays is involved in many industrial applications and natural phenomena. Despite the relevance of the problem, a satisfactory comprehension of the mechanisms that regulate the process has still not been achieved. Indeed, a wide range of turbulent scales and an enormous number of droplets are typically involved, causing the numerical and theoretical tackling of the problem to be challenging. In this context, we address the Direct Numerical Simulation (DNS) of a turbulent jet-spray at a bulk Reynolds number $Re = 10{,}000$. We focus on the effect of the jet Reynolds number on the evaporation process and the preferential segregation of droplets. The analysis is conducted by comparing the outcomes of the present DNS with that from a lower Reynolds number one in corresponding conditions, $Re = 6{,}000$. The problem is addressed by employing the point-droplet approximation in the hybrid Eulerian-Lagrangian framework. We present detailed statistical analyses of both the gas and the dispersed phases. We found that the mean droplet vaporization length grows as the bulk Reynolds number is increased from $Re = 6{,}000$ to $Re = 10{,}000$, while keeping all the remaining conditions fixed. We attribute this result to the complex interaction between the inertia of the droplets and the dynamics of the turbulent gaseous phase. In particular, at the higher Reynolds number, the effect of the faster turbulent fluctuations of the jet mixing layer, which tend to fasten the process, is compensated by the slower mass transfer from the liquid droplets to the surrounding environment. We also observe intensive preferential segregation of the dispersed phase that originates from the entrainment of dry environmental air into the mixing layer and is intensified by small-scale clustering in the far-field region. We show how the preferential segregation is responsible for a strongly heterogeneous Lagrangian evolution of the dispersed droplets. All these aspects contribute to the Reynolds-number dependence of the overall droplet evaporation rate. Finally, we discuss the accuracy of the *d-square* law, often used in spray modelling, for present cases. We found that using this law based on environmental conditions leads to a relevant overestimation of the droplet evaporation rate.

Keywords: Turbulent spray, turbulent evaporation, droplet-laden turbulent flows, droplet evaporation, direct numerical simulation

Introduction

Turbulent jet sprays are complex multiphase flows where a dispersed liquid phase is transported by a turbulent gaseous one. The distinguished phases mutually interact by exchanging mass, momentum, and energy in the turbulent regime. These complex flows play a crucial role in many industrial applications, as well as in a large variety of natural and environmental processes. Despite the technical and scientific relevance of the problem, the understanding and modelling of the fundamental mechanisms that regulate the evaporation and the dispersion of droplets in turbulent sprays are still a challenging matter due to the unsteady, multi-scale, and multiphase processes involved in these complex flows[25]. For instance, in the industry, an improved understanding of such processes would contribute significantly to the development of high-efficiency and low-emission internal combustion engines. In these applications, the liquid fuel is directly injected into a hot-temperature and high-pressure combustion chamber and undergoes a phase transition, via primary and secondary atomization, followed by intensive chemical reactions within the turbulent gaseous environment. This complex process completes in very short times inside the combustion chamber and involves different multi-scale, multiphase, and unsteady phenomena. A typical example is the formation of pollutants that is related to fluctuations of temperature and reactant concentrations. In particular, the production of soot occurs through the pyrolysis process in fuel-rich regions where high temperature subsists without enough oxidizer to react[3, 28, 45]. Typically, this phenomenology is observed within droplet clusters, where the concentration of the droplets can be even a thousand times higher than its bulk value giving rise to a peak in the fuel vapour concentration. Furthermore, considered the recent outbreak of the COVID-19 pandemic, an additional instance relies on the transmission of respiratory infections through virus-laden droplets that form in the respiratory tract of an infected person and are expelled from the mouth and nose during spasmodic events, such as coughing and sneezing[5, 12, 39, 40]. Despite the apparent discrepancy between steady-state jet-sprays, which are considered in the present paper, and respiratory flows (e.g. puff-like, different ambient conditions, possible buoyancy effects) the conclusion drawn in presented work could be precious for the future improvements of our understanding and modelling of the basic mechanisms governing the dispersion and evaporation of infectious droplets.

A phenomenological description of the evolution of turbulent jet-sprays can be found in the review of Jenny et al. [25]. The whole process starts with the jet breakup, or atomization, as a high-velocity liquid flow is injected from a duct into a gaseous environment. During the so-called primary atomization, Kelvin-Helmholtz and Rayleigh-Taylor instabilities develop on the gas-liquid interface promoting the jet fragmentation and giving rise to a system of large droplets and liquid ligaments enclosed within the environmental gas[35]. Further downstream, the so-called secondary atomization follows; the aerodynamic forces, arising from the relative inter-phase velocities, cause additional instabilities of the liquid-gas interfaces that lead to a further disintegration of droplets and ligaments[25, 35]. The breakup process occurs in a so-called dense regime and terminates when the surface tension prevails on aerodynamic stresses preventing further fragmentation[25]. At this stage, the so-called dilute regime establishes; the dispersed phase volume fraction is small enough that the droplet mutual interactions, such as collisions and coalescence, can be neglected[19]. Whereas in the dense regime the vaporization rate is negligible, the vaporization process becomes significant in dilute conditions and most of the liquid evaporates at this stage of the turbulent spray evolution[18].

The dilute regime is characterized by the presence of small droplets that preserve a spherical shape due to the dominance of the surface tension on the aerodynamic stresses[17, 19, 25]. Even though the liquid phase still exerts a considerable effect on the flow in terms of mass, momentum, and energy balance, in dilute conditions the droplet size is usually below, or comparable to, the dissipative scale of the turbulent flow. In these conditions, the point-droplet approximation is widely accepted and the hybrid Eulerian-Lagrangian approach is considered suitable and reliable for the numerical description of problem[17]. In this framework, the exchange of mass, momentum, and energy between the Eulerian carrier phase and Lagrangian point-droplets is accounted for by employing distributed sink-source terms in the right-hand sides of the balance equations that govern the Eulerian phase. Concurrently, the droplet kinematic and thermodynamic variables are evolved in the Lagrangian frame[9, 14, 16, 17, 36, 53].

To gain an insight into the fundamental physics of turbulent sprays, various theoretical and numerical studies, which complement traditional experimental investigations, have been conducted. One of the former attempts to describe the vaporization process of spherical droplets dragged by a gaseous flow relies on the well-known *d-square* law, that finds its root in the works of Langmuir [29], Spalding [50], and Godsave [20]. The law states that the surface of a droplet decreases linearly with time in quiescent environments with uniform and fixed thermodynamical properties (temperature, vapour concentration, etc.). Starting from the *d-square* law, Law [32] and Law and Sirignano [33] derived the rapid-mixing model: temperature is assumed to be uniform inside droplets but temporary varying. The model applies well under the assumption that the thermal conductivity of the liquid phase is high enough to permit a rapid stabilization of the droplet internal temperature in response to local changes of the environmental one. Later, Abramzon and Sirignano [2] proposed an improved droplet vaporization model applicable to non-uniform and time-dependent environmental conditions. The model takes into account forced convection, molecular diffusion, and the Stefan flow contribution to the vapour transport from the droplet surface to the neighbouring environment. The author pointed out that the Ranz-Marshall correlations[46] for the Nusselt and Sherwood numbers adopted in the rapid-mixing model and *d-square* law may lead to a physically incorrect super-sensitivity of the transfer rates to the small turbulent velocity fluctuations for the droplet Reynolds number tending to zero. By considering the motion of finite-size spherical particles, or droplets, in turbulent flows, Maxey and Riley [37] derived an equation that accounts for the Stokes drag, added-mass effect, and gravitational force in low-Reynolds number circumstances. All these approaches, among the others reported by the literature, have led to the development of well-established point-droplet equations in the hybrid Eulerian-Lagrangian frame. These models have proved to be effective and reliable in reproducing the evaporation dynamics of liquid droplets both in the Direct Numerical Simulation (DNS) and Large Eddy Simulation (LES) frames[7, 9, 10, 17, 38, 52].

Along with DNS and LES, hybrid Eulerian-Lagrangian approaches based on the Reynolds averaged Navier-Stokes are widely used to perform prediction for industrial applications due to their simplicity and low computational requirements. The main limitation of these methods, which is partially removed in the frame of LES, relies on the impossibility to capture the scales of time-dependent and unsteady motions occurring in turbulent sprays[41]. In contrast, DNS, which resolves all the length and time-scales present in a turbulent flow, has proved its capability to capture the whole physics of the vaporization process in jet-sprays providing accurate insight into the complex phenomena involved. Mashayek [36] conducted one of the first DNS of evaporating droplets in turbulent flows. The author carried out the study under the assumption of incompressible flow and neglected the effect of the dispersed phase on the carrier one (one-way coupling). Bukhvostova et al. [9] addressed the DNS of droplet-laden heated channel flow with phase transition. The authors compared the numerical results obtained with the incompressible formulation of the Navier-Stokes equations with those obtained by using the low-Mach number asymptotic one. In the latter, the effects of changes in the total mass density caused by evaporation of droplets and condensation of water vapour are accounted for. The use of the low-Mach number formulation is found to produce a more reliable quantitative prediction of heat and mass transfer. Reveillon and Demoulin [47] studied the impact of preferential segregation of droplets on the mixture fraction field in one-way coupling conditions. They found that the temporal evolution of the evaporation process has three different stages, each one characterized by a different mode: single droplet mode in the early stage, cluster mode in the intermediate stage and a gaseous mode in the late stage. Recently, Dalla Barba and Picano [16] investigated the dynamics of droplet vaporization within a three dimensional turbulent jet-spray in dilute, non-reacting conditions. The study was carried out in the DNS frame by using the hybrid Eulerian-Lagrangian approach and the point-droplet approximation. The preferential segregation of droplets is found to be driven by two distinct mechanisms: the inertial small-scale clustering in the jet core and the turbulent-non-turbulent dynamics of the jet in the mixing layer, where dry air entrainment occurs.

Although different numerical studies and theoretical exploitation have been already conducted, it is still premature to conclude that a satisfying comprehension of turbulent spray dynamics has been achieved. The capabilities of existing models in reproducing the involved phenomena are not thoroughly confirmed. Moreover, due to the high computational requirements of DNS, most of the numerical dataset and studies available in the literature are limited to relatively low Reynolds numbers. To cover these lacks and to improve the model capabilities for practical applications, it is crucial to improve the availability of data from three-dimensional DNSs of evaporating jet-sprays over a wider range of Reynolds numbers. In this context, the present paper aims to address the numerical study of the basic mechanisms governing the evaporation and preferential segregation of droplets in a three-dimensional turbulent jet-spray at moderate Reynolds number. The problem is addressed via a three-dimensional DNS. The emphasis of the paper is on the effect of the Reynolds number of the jet on different Lagrangian and Eulerian observables, such as evaporation length and droplet size spectrum. A comparison of the present DNS results, $Re=10{,}000$, and those by Dalla Barba and Picano [16] , $Re = 6{,}000$, is provided. In both cases, a similar and strongly inhomogeneous distribution of droplets is observed. Nonetheless, as the Reynolds number is increased from *6,000* to *10,000*, the droplet vaporization length grows while the mean evaporation rate reduces. Several mechanisms that provide an explanation for these differences are discussed in detail. The authors believe that the data reported in this paper could contribute to improve our knowledge about the dynamics of turbulent evaporating jet-sprays, providing at the same time a benchmarking test-case for the future low-order modelling of the phenomena involved.

Numerical methodology

The numerical results reported in this paper have been computed by employing an MPI-parallel code, previously used in other numerical studies, which has undergone an extensive validation and testing campaign [14, 16, 43, 48]. The numerical algorithm is based on a hybrid Eulerian-Lagrangian approach and the point-droplet approximation. The exchanges of mass, momentum and energy between the dispersed phase and the carrier one are accounted for, whereas collisions and coalescence within droplets are neglected in a two-way coupling frame [19]. A brief description of the numerical methodology is provided for the self-consistency of the paper, whereas the reader is referred to the references for additional details [14, 16, 43, 48]. The conservation equations for the gas phase relies on a low-Mach number asymptotic formulation of the Navier-Stokes equations in an open environment:

$$\frac{\partial \rho}{\partial t} + \frac{\partial (\rho u_j)}{\partial x_j} = S_m, \tag{1}$$

$$\frac{\partial (\rho Y_v)}{\partial t} + \frac{\partial (\rho Y_v u_j)}{\partial x_j} = \frac{\partial J_j}{\partial x_j} + S_m, \tag{2}$$

$$\frac{\partial (\rho u_i)}{\partial t} + \frac{\partial (\rho u_i u_j)}{\partial x_j} = \frac{\partial \tau_{ij}}{\partial x_j} - \frac{\partial p}{\partial x_j} + S_{p,i}, \tag{3}$$

$$\frac{\partial u_j}{\partial x_j} = \frac{\gamma - 1}{\gamma} \frac{1}{p_0} \left(\frac{\partial q_j}{\partial x_j} + S_e - L_v^0 S_m \right), \tag{4}$$

$$p_0 = \rho R_w T, \tag{5}$$

with

$$J_i = \rho D \frac{\partial Y_v}{\partial x_i}, \qquad q_i = k \frac{\partial T}{\partial x_i},$$

$$\tau_{ij} = \mu \left(\frac{\partial u_i}{\partial x_j} + \frac{\partial u_j}{\partial x_i} \right) - \frac{2}{3} \mu \frac{\partial u_k}{\partial x_k} \delta_{ij}.$$

The Eulerian fields ρ, u_i, T and p are the density, velocity, temperature and hydrodynamic pressure of the carrier phase, respectively. In the frame of the low-Mach number asymptotic expansion considered in this paper, the thermodynamic pressure, referred to as p_0, results to be spatially uniform and constant in time, due to the open environment conditions Majda and Sethian [34]. The Eulerian field $Y_v = \rho_v / \rho$ is the vapour mass fraction, with ρ_v the partial density of the vapour. The viscous stress tensor is $\tau_{i,j}$, with μ the dynamic viscosity of the carrier phase. The parameter $\gamma = c_p / c_v$ is the specific heat ratio of the carrier mixture, where c_p and c_v are its specific heat capacities at constant pressure and volume, respectively. The flux vectors q_i and J_i represent the thermal and mass diffusion and are computed according to the Fourier's law and Fick's laws, respectively. The parameters k and D are the thermal conductivity of the carrier mixture and the binary diffusivity of the vapour into the gas.

A reference temperature $T_0 = 0\ K$ is fixed and the assumption of calorically perfect chemical species is considered to estimate the sensible enthalpy. Under this hypothesis, L_v^0 is the latent heat of vaporization of the liquid phase evaluated at the reference temperature, T_0. The carrier vapour-gas mixture is assumed to be governed by the state equation for perfect gases (5), where $R_w = \mathcal{R}/W$ is the specific gas constant of the carrier mixture, W its molar mass and $\mathcal{R}$ the universal gas constant. Consistently with previous studies in this field [9, 36], the effect of the dispersed phase on the carrier one is accounted for by employing three sink-source coupling terms in the right-hand side of the mass, momentum, and energy equations, S_m, $S_{p,i}$,and S_e, respectively:

$$S_m = -\sum_k \frac{dm_d^k}{dt}\delta(x_i - x_{d,i}^k), \tag{6}$$

$$S_{p,i} = -\sum_k \frac{d}{dt}(m_d^k u_{d,i}^k)\delta(x_i - x_{d,i}^k), \tag{7}$$

$$S_e = -\sum_k \frac{d}{dt}(m_d^k c_l T_d^k)\delta(x_i - x_{d,i}^k). \tag{8}$$

The Lagrangian variables $x_{d,i}^k$, $u_{d,i}^k$, m_d^k and T_d^k are the position, velocity, mass and temperature of the droplets, respectively, whereas the parameter c_l is the specific heat of the liquid phase. The summations are taken over the whole droplet population located within the domain (index k). The delta function, $\delta(x_i - x_{d_i}^k)$, accounts for the fact that the sink-source terms act only at the Eulerian positions occupied by the point-droplets at a given time. In the numerical algorithm, the Eulerian terms (6)-(8) are calculated, in correspondence of each node of the computational grid, by volume averaging the mass, momentum, and energy sources arising from all the droplets located within the related grid cells.

As mentioned above, the point-droplet approximation is adopted to describe the dispersed phase: the droplets are treated as rigid evaporating spheres and the liquid properties (e.g. temperature) are assumed to be uniform inside each droplet. Since the focus of this paper is on the spray dynamics restricted to dilute conditions, mutual interactions among droplets (e.g. collisions, and coalescence) are neglected. For a discussion about the validity of the preceding assumptions, the reader is referred to [16]. Under these hypotheses, the dynamics of the droplets is completely described by the following Lagrangian equations:

$$\frac{dx_{d,i}}{dt} = u_{d,i}, \tag{9}$$

$$\frac{du_{d,i}}{dt} = \frac{1 + 0.15\ Re_d^{0.687}}{\tau_d}(u_i - u_{d,i}), \tag{10}$$

$$\frac{dm_d}{dt} = -\frac{1}{3\tau_d}\frac{Sh}{Sc}m_d \ln{(1 + B_m)}, \tag{11}$$

$$\frac{dT_d}{dt} = \frac{1}{3\tau_d}\left[\frac{Nu}{Pr}\frac{c_{p,g}}{c_l}(T - T_d) - \frac{Sh}{Sc}\frac{L_v}{c_l}\ln(1 + B_m)\right], \tag{12}$$

where the parameter ρ_l is the density of the liquid phase, $c_{p,g}$ is the heat capacity at constant pressure of the gaseous component of the carrier mixture and L_v the latent heat of vaporization of the liquid phase evaluated at the droplet temperature. The variable τ_d is the droplet relaxation time, $\tau_d = 2\rho_l r_d^2/(9\mu)$, with $Re_d = 2\rho\| u_i - u_{d,i}\| r_d/\mu$ is the droplet Reynolds number. The Schiller-Naumann correlation is adopted in equation (10) to account for the effect of the finite Reynolds number of the droplets on the drag. In equations (11) and (12), the Schmidt number, $Sc = \mu/(\rho D)$, and Prandtl number, $Pr = \mu/(c_p k)$ are employed to compute the mass diffusivity and thermal conductivity, respectively. Besides, the Nusselt number, Nu_0, and Sherwood number, Sh_0, are estimated as a function of the droplet Reynolds number through the Frössling correlation:

$$Nu_0 = 2 + 0.552 Re_d^{\frac{1}{2}} Sc^{\frac{1}{3}}, \tag{13}$$

$$Sh_0 = 2 + 0.552 Re_d^{\frac{1}{2}} Pr^{\frac{1}{3}}. \tag{14}$$

A correction is then applied to Nu_0 and Sh_0 to account for the effect of Stefan flow [2]:

$$Nu = 2 + \frac{Nu_0 - 2}{\ln(1 + B_t)} \frac{B_t}{(1 + B_t)^{0.7}}, \quad B_t = \frac{c_{p,v}}{L_v}(T - T_d) \tag{15}$$

$$Sh = 2 + \frac{Sh_0 - 2}{\ln(1 + B_m)} \frac{B_m}{(1 + B_m)^{0.7}}, \quad B_m = \frac{Y_{v,s} - Y_v}{1 - Y_{v,s}} \tag{16}$$

where $c_{p,v}$ is the specific heat capacity of the pure vapor at constant pressure, Y_v is the vapor mass fraction evaluated at the droplet position, whereas $Y_{v,s}$ is the vapor mass fraction evaluated at the droplet surface. The latter corresponds to the mass fraction of the vapor, in a fully saturated vapor-gas mixture, evaluated at the droplet temperature. In order to estimate $Y_{v,s}$ we employed the Clausius-Clapeyron relation:

$$\chi_{v,s} = \frac{p_{ref}}{p_0} exp\left[\frac{L_v}{R_v}\left(\frac{1}{T_{ref}} - \frac{1}{T_d}\right)\right] \tag{17}$$

where $\chi_{v,s}$ is the vapor molar fraction evaluated at the droplet temperature and p_0 the thermodynamic pressure. The parameter p_{ref} is the saturated vapor pressure evaluated at the reference temperature T_{ref}, whereas $R_v = \mathcal{R}/W_l$ is the specific constant of the vapor. The saturated vapor mass fraction is, then,

$$Y_{v,s} = \frac{\chi_{v,s}}{\chi_{v,s} + (1 - \chi_{v,s})\frac{W_g}{W_l}}. \tag{18}$$

The Eulerian computational domain is a cylinder. The droplet-laden jet-spray is injected through a circular orifice of radius R located at the centre of the lower base of the domain and streams out towards the opposite one. The domain extends for $2\pi \times 20R \times 70R$ in the azimuthal, θ, radial, r and axial, z, directions and is discretized by means of a staggered, cylindrical grid of $N_\theta \times N_r \times N_z = 192 \times 211 \times 1152$ nodes. An Eulerian algorithm advances in time the Eulerian fields by solving the Low-Mach number formulation of the Navier-Stokes equations (1)-(5). Second-order, central finite difference schemes are employed for the spatial discretization, whereas the temporal evolution is performed by a low-storage, third-order Runge-Kutta algorithm. The computational grid is uniform along the azimuthal direction, whereas it is stretched along the radial and axial ones. The grid spacing is maintained of the same order of the Kolmogorov length scale for the whole downstream evolution of the jet-spray. Details about grid resolution and adequacy of grid spacing can be found in [16] for Reynolds number, $Re = U_0 R/\nu = 6,000$. In the present case, the grid spacing has been obtained by a scale-up of the computational grid, previously used in [16], in order to maintain an adequate resolution down to the dissipative length scales, but at a higher Reynolds number, $Re = 10,000$. The ratios between the mean grid spacing of the present and reference case, $\overline{\Delta}_{10,000}/\overline{\Delta}_{6,000}$, are about 0.67 and 0.55 along the azimuthal and axial directions, respectively. Moreover, along these directions, the grid spacing ratio is of the same order of the ratio between the dissipative length-scales $\eta_{10,000}/\eta_{6,000} \simeq (6,000/10,000)^{4/3} \simeq 0.68$. To get benefits from a higher-resolution in the shear layer, a dense, stretched mesh is employed along the radial direction; the mesh is stretched such that the maximum resolution is achieved at the radial position $r/R \simeq 1$, where the mesh spacing is about 0.44 times of the mean one. A convective boundary condition is adopted on the outlet section located on the upper face of the cylindrical domain. An adiabatic, traction-free boundary condition is prescribed at the side boundary of the domain making the entrainment of external fluid possible. The latter, in the present case, consists of dry air. Time-dependent and fully turbulent boundary conditions are prescribed on the inflow section by employing a companion DNS reproducing a fully-developed, periodic pipe flow. A fully turbulent velocity field is assigned on the jet inflow by a Dirichlet condition. This two-dimensional field is computed on a cross-sectional slice of the turbulent pipe. Excluding the circular inflow, the remaining part of the domain base is impermeable and adiabatic. The turbulent pipe extends for $2\pi \times 1R \times 6R$ in the azimuthal, θ, radial, r and axial, z directions. The pipe domain is discretized by using a staggered grid containing $N_\theta \times N_r \times N_z = 192 \times 91 \times 128$ nodes in order to match the corresponding jet-grid nodes at the pipe discharge. The use of a companion pipe simulation makes possible to prescribe fully turbulent inflow conditions, including physically meaningful turbulent fluctuations. On one hand, in applications the flow is usually turbulent even before the inflow, while a top-hat inflow is typical of a strong contraction before the inlet. On the other hand, the use of a fully developed turbulent inflow, instead of a steady top-hat one, avoids the transitional region downstream the inflow, accelerating the establishment of far-field turbulent jet-spray dynamics which weakly depend on inflow condition details.

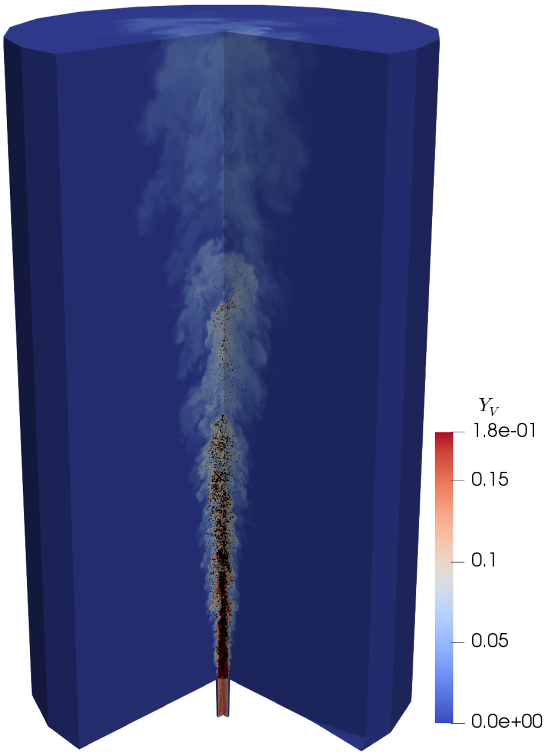

(a) 3D cylindrical domain

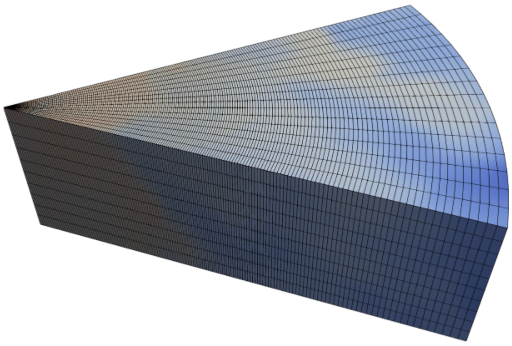

(b) Local mesh structure

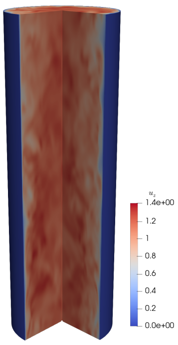

(c) 3D pipe flow

Figure 1: (a) Snapshot of the computational domain and a representative ensemble of the whole droplet population plotted by black points. (b) Sector of the mesh structure centred at $z/R = 20$. (c) Sketch of the turbulent periodic pipe employed to generate fully turbulent boundary conditions at the jet-spray inflow. The colour maps show the vapour mass fraction field, Y_v, within the jet-spray and the axial instantaneous velocity, u_z, in the turbulent pipe, respectively.

A sketch of the cylindrical domain, the mesh structure inside a slice of the domain and the turbulent periodic pipe are shown in figure 1. Concurrently with the Eulerian solver, a synchronous Lagrangian solver evolves the droplet mass, momentum, and temperature laws (9)-(12) by using the same Runge-Kutta scheme adopted for the Eulerian solver. Numerical stability issues, which can arise when the droplet size becomes too small, are avoided by setting a threshold radius $r_{d,th}$ corresponding to a mass-loss due to evaporation of 99.95% of the initial droplet mass. When the radius of a droplet decreases under the fixed stability threshold, the droplet is considered as completely evaporated and is removed from the simulation.

Table 1: Thermodynamic properties of acetone and dry air and simulation parameters.

R	$0.0049\ m$	W_g	$0.0290\ kg/mol$
p_0	$101300\ Pa$	W_l	$0.0581\ kg/mol$
T_0	$275.15\ K$	k_g	$0.0243\ W/(m \cdot K)$
μ	$1.75 \cdot 10^{-5}\ kg/(m\ s)$	k_l	$0.183\ W/(m\ K)$
$c_{p,g}$	$1038\ J/(kg\ K)$	D	$1.1 \cdot 10^{-5}\ m^2/s$
$c_{p,v}$	$1300\ J/(kgK)$	ρ_l	$800\ kg/m^3$
c_l	$2150\ J/(kg\ K)$	L_v	$530000\ J/kg$
U_0	$13.9\ m/s$	r_d	$6 \cdot 10^{-6}\ m$
t_0	$3.5 \cdot 10^{-4}\ s$		

The present paper addresses the numerical simulation of liquid acetone droplets dispersed within a gaseous jet-spray. The jet consists of a mixture of dry air and acetone vapour. The jet streams out from the inflow section into an open environment filled by dry air. The absolute pressure of the environment is $p_0 = 101300\ Pa$, whereas the temperature is set to $T_0 = 275.15\ K$. The radius of the inlet section is set to $R = 4.9 \cdot 10^{-3}\ m$ while the bulk inflow velocity of the jet is $U_0 = 13.9\ m/s$. A monodisperse population of liquid acetone droplets of initial radius $r_{d,0} = 6\ \mu m$ is randomly distributed over the inflow section at each time-step. The injection temperature is fixed to $T_0 = 275.15\ K$ for both the droplets and the carrier mixture. The injection flow rate of the gaseous phase is kept constant by fixing a bulk Reynolds number $Re = 2U_0R/\nu = 10,000$, with $\nu = 1.35 \cdot 10^{-5}\ m^2/s$ the kinematic viscosity. A nearly saturated condition is prescribed at the inflow for the air-acetone vapour mixture, $S = Y_v/Y_{v,s} = 0.99$, with Y_v the actual vapour mass fraction and $Y_{v,s}(p_0, T_0)$ the vapour mass fraction at saturation, evaluated at the actual inflow temperature and thermodynamic pressure. The acetone mass flow rate is set by means of the ratio $\Phi = \dot{m}_{act}/\dot{m}_{air} = 0.28$, where $\dot{m}_{act} = \dot{m}_{act,l} + \dot{m}_{act,v}$ is the sum of the liquid and vapour acetone mass flow rates, while $\dot{m}_{air}$ is the dry-air flow rate. The correspondent bulk volume fraction of the liquid phase is $\Psi = 8.0 \cdot 10^{-5}$. All the thermodynamic and physical properties of the vapour, gas, and liquid phases are reported in table 1. The thermodynamic conditions at the inlet are comparable to that adopted in the well-controlled experiments on dilute coaxial sprays published by the group of Chen et al. [11]. The time step is set to $\Delta t/t_0 = 0.001$ where the reference time-scale t_0 is $t_0 = R/U_0 = 3.5 \cdot 10^{-4} s$. To achieve the prescribed mass flow rate, around 33 acetone droplets are randomly distributed over the inflow section at each step of the temporal integration. The injection velocity of each droplet is set to be equal to the local velocity of the turbulent carrier phase. The simulation was initialized by considering the single-phase jet made of air and acetone vapour until statistically steady conditions have been attained. This process required about 150 time-scales,

$t_0 = R/U_0$. From this step on, droplets were continuously injected and the simulation was run for additional 200 time-scales, $t_0 = R/U_0$, to achieve statistically steady conditions for the two-phase jet-spray before proceeding to the collection of data. All the statistical quantities presented in the present paper are computed by considering 100 non-correlated time levels, separated in time by 1 time-scale, $t_0 = R/U_0$. Concerning the reliability of the simulation, additional information and validation benchmarks about the turbulent periodic pipe, single-phase jet simulations and evaporation model can be found in Ciottoli et al. [14], Dalla Barba and Picano [16].

Results and discussion

In this section, the outcomes from the present DNS case, $Re = 10,000$, are presented and compared with the results from the previous study, $Re = 6,000$ [16]. The essential difference between the two cases relies on the bulk Reynolds number of the injected carrier phase, all of the other parameters being the same. From a physical point of view, we are comparing two jet sprays with different bulk velocities. It is worth noting that, the initial Stokes number of the droplets injected into the domain is larger in the second case, $Re = 10,000$, since

$$St_0 = \frac{2}{9}\frac{\rho_g}{\rho_l}\left(\frac{r_{d,0}}{R_0}\right)^2 Re. \tag{19}$$

In particular, the value of the initial Stokes numbers are $St_0 \simeq 1.04$ and $St_0 \simeq 0.62$ for the $Re = 10,000$ and $Re = 6,000$ cases, respectively.

A macroscopic overview of the structure of turbulent jets can be obtained by visualizing coherent structures and enstrophy. Several methods have been proposed to identify, quantify and visualize the three-dimensional structures in incompressible turbulent flows [13, 24, 26, 55]. We address the visualization of the vortical structures by employing the Q-criterion [24]:

$$Q = \frac{1}{2}(\Omega_{ij}\Omega_{ij} - S_{ij}S_{ij}), \tag{20}$$

with

$$\Omega_{ij} = \frac{1}{2}\left[\frac{\partial u_j}{\partial x_i} - \frac{\partial u_i}{\partial x_j}\right], \quad S_{ij} = \frac{1}{2}\left[\frac{\partial u_j}{\partial x_i} + \frac{\partial u_i}{\partial x_j}\right],$$

where Ω_{ij} and S_{ij} are the vorticity tensor and the rate-of-strain tensor, respectively. By this approach, a vortex is defined as a spatial region where $Q > 0$, e.g. the Euclidean norm of the vorticity tensor dominates that of the rate of strain [22]. In general, larger Q values are associated with more intensive vortexes. Figure 2a shows a comparison of the instantaneous vortical structures of the flow for the two Reynolds numbers, visualized by the iso-surfaces $Q = 1$ and contoured by the magnitude of the Eulerian velocity field. Moving downstream from the inflow section, the vortical structures spread out into the far-field while subjected to a decay process. As the Reynolds number is increased, vortical tubes become denser and smaller, whereas the spread of vortexes is extended in the downstream direction [4]. This aspect is related to a prolonged evolution of the turbulent jet-spray for the higher Reynolds number case. Figure 2b shows a two-dimensional radial-axial snapshot of the instantaneous distribution of droplets and the instantaneous enstrophy

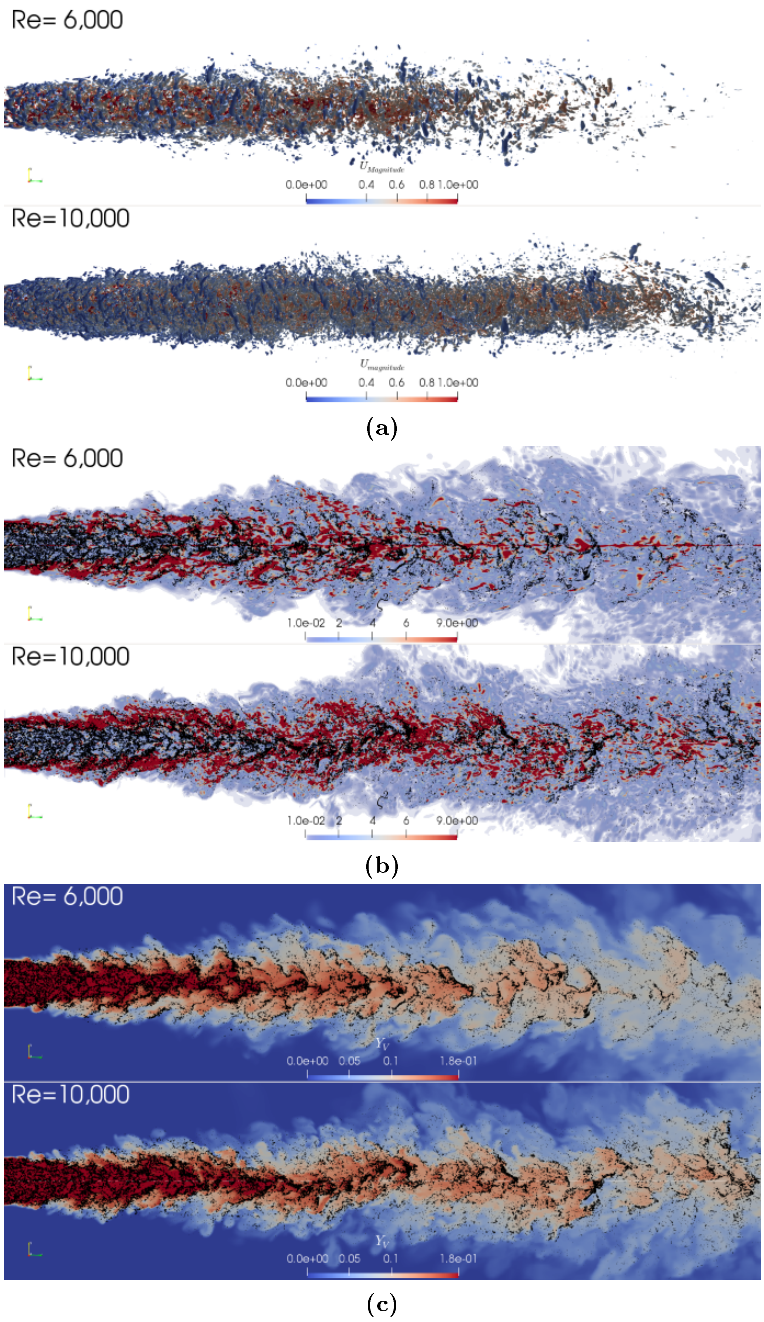

Figure 2: (a) Three-dimensional coherent structures of the flow visualized by the Q-criterion. The iso-surfaces $Q = 1$ are contoured according to the magnitude of the carrier phase velocity. (b) Axial-radial slices of the magnitude of the instantaneous enstrophy field coloured in log scale, $\zeta^2 = \|\nabla \times \overrightarrow{u}\|$. (c) Radial-axial slices of the turbulent sprays at $Re = 10,000$ and $Re = 6,000$. The black points represent a subset of the whole droplet population constituted by droplets located within a distance $\Delta/R = 0.1$ to the slice plane. The size of each point is proportional to the corresponding droplet radius, using a scale factor of 100. The carrier phase is contoured according to the instantaneous vapour mass fraction field, Y_v, which is bounded between 0 and 0.18, the former value corresponding to the dry condition, the latter to the 99% saturation level prescribed at inflow section.

field $\zeta^2 = \|\nabla \times \overrightarrow{u}\|$. As expected, in the near-field high-intensity vorticity regions are mainly located in the shear layer, whereas the vorticity is lower in the jet core. It is worth noting that the considered jets are generated by fully turbulent pipe flows and, thus, velocity fluctuations are present also in the jet cores. Hence, we refer to the *potential core region* as the unperturbed core region where the turbulence statistics remain closer to the ones of the inlet pipe and not to those of jet far-field. Moving downstream, the decay of the jet leads to a different behaviour. The decay dynamics, that is intrinsically related to the physics of turbulent jets, is observed in both cases considered here, the high-Reynolds jet presenting vorticity-related features that are shifted downstream compared to the lower Reynolds number one. It is also worth remarking that, the decay of the turbulent structures of the jet observed in the present paper, is consistent with the experimental observation by [30, 31]. Droplet clustering manifests less frequently in high-vorticity regions, especially in the shear layer. We attribute this effect to two different causes. First, inertial droplets tend to escape from high-vorticity regions, that is a well-established explanation of small-scale clustering [51]. Second, near high-vorticity regions in the shear layer, intensive mixing events occur: dry environmental air, depleted of droplets, is mixed with the inner, saturated gas-vapor mixture laden of droplets. These mixed and non-saturated regions consent a fast evaporation of the droplets that rapidly disappear from these areas. The combination of these two phenomena originates a strong preferential segregation of the dispersed phase. The anti-correlation between the presence of droplets and the saturation level in the carrier phase is highlighted in figure 2c, where the instantaneous vapor mass fraction field and the instantaneous droplet distribution are provided. It is worth noting that, most of the droplets are located in the core regions of the turbulent jets in which a strongly inhomogeneous preferential distribution is observable over the whole downstream evolution of the flows. Nonetheless, in the near-field region, this non-uniform characteristic of droplet dispersion emerges mainly in the mixing layer. This is a source of clustering which propagates also in the downstream evolution. We also emphasize that, in the near-field, a self-preserving core exists with a nearly saturated vapor environment which prevents the droplet to evaporate. In both cases, moving downstream, the inhomogeneous distribution of the droplets becomes more apparent and can be observed both in the near-axis region and in the jet shear layers. Nonetheless, with the bulk Reynolds number increasing from $Re = 6,000$ to $Re = 10,000$, the onset of this intensive preferential segregation of the droplets dispersion appears to be slightly shifted in the downstream direction. Besides, it is worth noting the higher evaporation length for the high-Reynolds number case, where many droplet clusters are still present at a higher distance from the inlet.

Eulerian statistics

Figure 3(a) provides the distribution of the average liquid mass fraction, $\langle \Phi_M \rangle$. The mass fraction is defined as $\Phi_M = m_l/m_g$, where m_l and m_g are the mass of the liquid acetone and the mass of the gaseous phase evaluated inside each mesh cell. A spray vaporization length is defined as the axial distance from the inflow section to where the droplets lost, on average, 99% of their initial mass [16]. According to this definition, the vaporization process ends at about $z/R \simeq 44$ and $z/R \simeq 50$ for $Re = 6,000$ and $Re = 10,000$, respectively. The vaporization length of the high-Reynolds jet is about 13% longer than the one of the low-Reynolds jet. It is worth remarking that the vaporization length defined in the present paper depends on different parameters, such as the environmental conditions and the initial droplet distributions. Hence, its value may vary in conditions different from that considered in the present study. An additional comparison of the spatial distribution of the average liquid mass fraction between the two cases is provided in figure 3b, where the centerline mean liquid mass fraction versus the axial coordinate, z is displayed. The curves exhibit a near-field hump: the liquid mass fraction increases along the jet-axis from the inlet section up to a peak

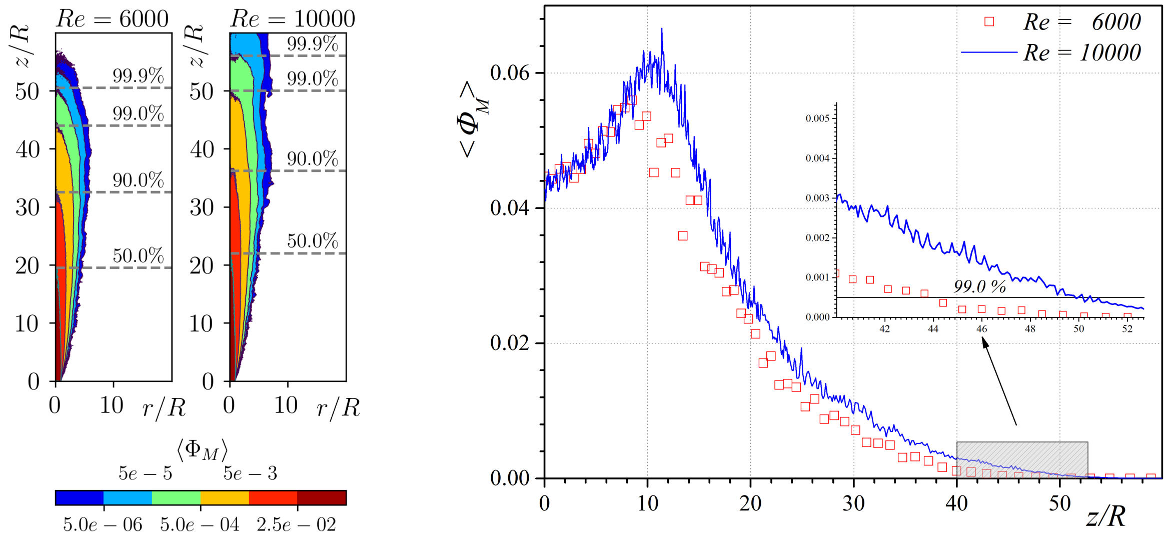

(a) (b)

Figure 3: (a) Averaged Eulerian mass fraction of the liquid phase, $\langle\Phi_M\rangle = \langle m_l/m_g\rangle$, where m_l and m_g are the mean mass of liquid acetone and air computed inside each mesh cell, respectively. The labels show different distances from the jet inlet section, z/R, in correspondence of which the 50%, 90%, 99%, and 99.9% of the overall injected liquid mass is evaporated. (b) Mean liquid mass fraction distribution near the jet-axis within the range $0 < r/R < 0.2$.

located at $z/R \simeq 9$ for $Re = 6,000$ and $z/R \simeq 11$ for $Re = 10,000$. Further downstream, Φ_M reduces along the jet-axis until droplets completely evaporate. The centerline hump of Φ_M reaches a higher value in the $Re = 10,000$ case than in the $Re = 6,000$ one. This behavior is consistent with the observations by [30, 31, 42] in which the centerline concentration of inertial particles is found to increase above the injection value. The phenomenon can be explained by considering the interplay of the droplet/particle inertia and the decay of the mean fluid velocity. The inertia induces

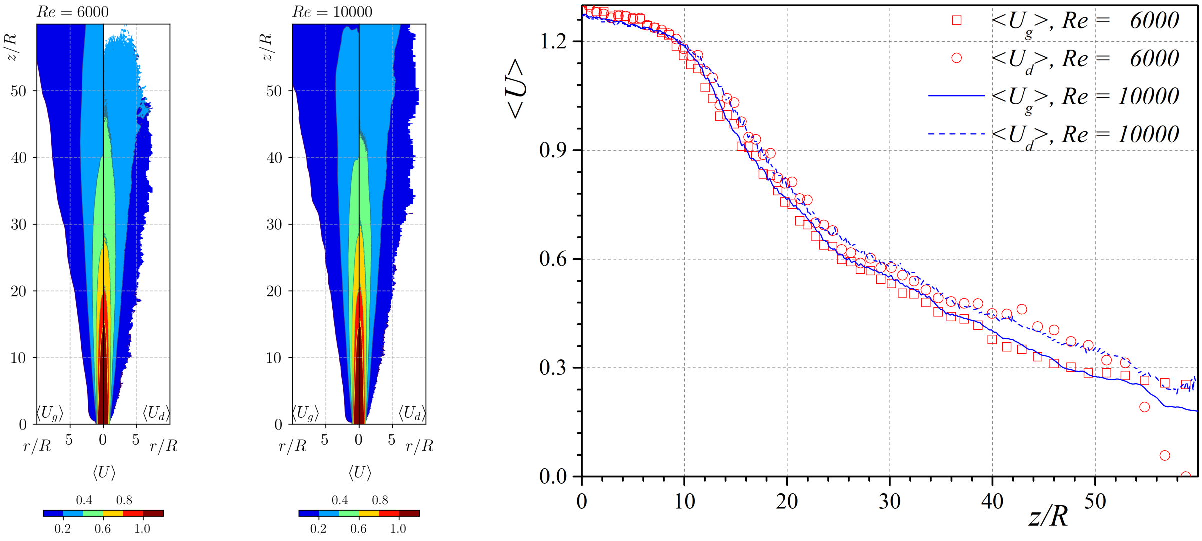

(a) (b) (c)

Figure 4: (a)-(b) Non-dimensional averaged distribution of the gas phase velocity, $\langle U_g\rangle$, and dispersed phase velocity $\langle U_d\rangle$, provided in the left and right sides of the panels, respectively. (c) Mean velocity of two phases near the jet-axis within the range $0 < r/R < 0.2$. The panels provide the data for both the $Re = 6,000$ and the $Re = 10,000$ case.

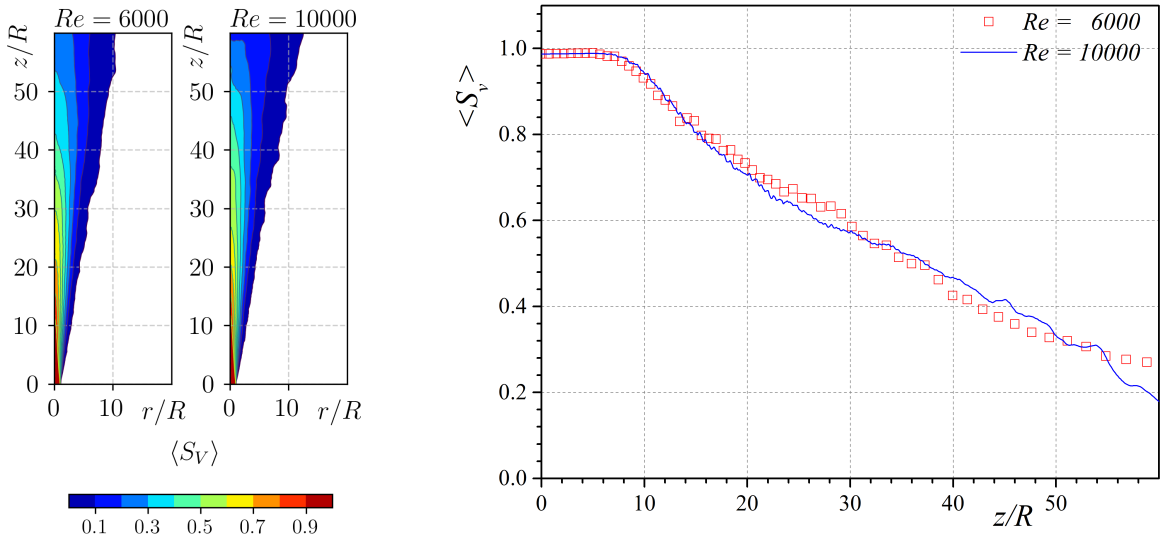

(a)

(b)

Figure 5: (a) Averaged saturation field, $\langle S_v \rangle = \langle Y_v / Y_{v,s} \rangle$, where Y_v is the actual vapour mass fraction and $Y_{v,s} = Y_{v,s}(p_0, T)$ is the value of vapour mass fraction evaluated at local saturation condition. (b) Distribution of the mean vapour saturation near the jet-axis in the range $0 < r/R < 0.2$.

a delay of the particle velocity to adapt to the slower (decayed) flow velocity thus creating a local concentration peak, see Picano et al. [42] for additional details.

The mean velocity of the Eulerian phase and the mean velocity of the droplets are displayed in figure 4. In panels 4a and 4b the mean Eulerian velocity is shown in the half left-side of the image, while the mean droplet velocity in the half right-side, for each of the two cases. The velocity of the dispersed phase is slightly higher than the corresponding Eulerian velocity, but no significant differences emerge by comparing the jets at the two Reynolds numbers. The centerline values of the same quantities, shown in panel 4c, confirm this overall behavior. It follows that the macroscopic dynamics of the flow in the present cases are not affected, in terms of velocity, by the Reynolds number. Thus, the difference found in the evaporation lengths cannot be attributed to a deviation of the gas and particle velocity fields.

In a jet-spray, as the turbulent core spreads and slowly decays, the dry and irrotational environmental air surrounding the jet is continuously entrained. The entrainment of dry air dilutes the vapor concentration and permits the overall vaporization process to advance. The fluid in the inner core does not reach the outer region of the jet and is diluted only by the entrainment. Thus, the centerline region presents a higher saturation level over the whole downstream evolution of the flow. The mean saturation field, $\langle S_v \rangle$, is provided in figure 5a. In both the considered cases, the flow is nearly saturated in the proximity of the inlet section, as prescribed by the inflow conditions. The saturation level gradually decreases in the downstream direction, maintaining a sharp gradient towards the outer jet region. No significant differences between the two cases are observable. Some small discrepancies are present in the intermediate and far-field region, $z/R > 20$. The $Re = 6,000$ case (left panel) shows a relatively higher saturation level in the region $20 < z/R < 30$, whereas the opposite occurs beyond $z/R \simeq 30$. As it will be further discussed in the following, at the lower Reynolds number we observe a faster evaporation rate in the near field, that explains the higher saturation level in this region. Conversely, in the far-field region of the $Re = 10,000$ case, we observe a higher number of dispersed evaporating droplets , such that the higher saturation level is expected. Figure 6 provides a comparison between the mean droplet radius, $\langle r_d \rangle$, in the

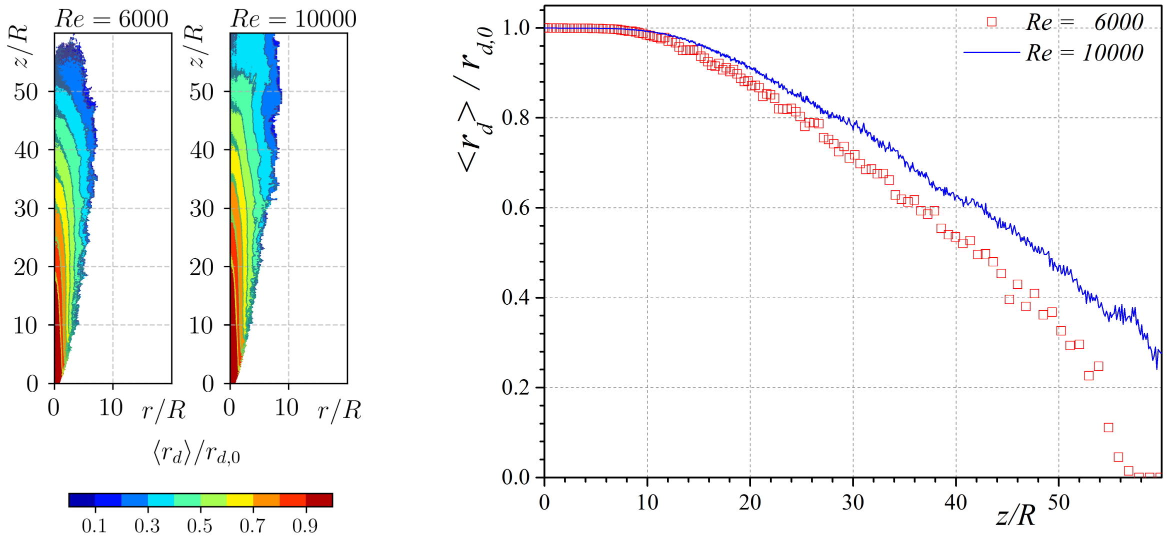

(a) (b)

Figure 6: (a) Average droplet radius, $\langle r_d \rangle$, scaled by the droplet initial radius $r_{d,0} = 6\mu m$. (b) Average droplet radius distribution near the jet-axis computed within the radial region $0 < r/R < 0.2$.

two considered cases. For both the Reynolds numbers, in correspondence of each axial position, z/R, larger droplets are located in the jet core region, whereas smaller droplets can be found in the mixing layer. This behavior is expected since the saturated jet core reduces the vaporization rate of the droplets near the centerline. Actually, the entrainment of environmental dry air dilutes the acetone vapor concentration in the jet mixing layer, enhancing the vaporization process. At the higher Reynolds number, the presence of larger droplets denotes a slower average evaporation rate. A more quantitative view assessing this aspect is provided in figure 6b, which shows the centerline value of the mean droplet radius. The mean droplet evaporation rate, normalized by the flow time-scale, $t_0 = R/U_0$, and the initial droplet mass, $m_{d,0}$, is provided in figure 7a. The evaporation rate peaks in the mixing layer and is stronger in the near-field than in the far-field. This behavior is consistent with the findings on the mean droplet radius, previously discussed. From a quantitative point of view, the high-Reynolds number case shows, on average, lower values of the evaporation rate; this explains the longer evaporation length. The droplet mass transfer is proportional to $1/St \propto 1/Re$, implying a relatively slower mass transport with respect to the advection time-scale. Nonetheless, the dissipative length-scale, as well as the finer length-scales of the turbulent mixing-layer structures, become smaller in the high-Reynolds case. This leads to a faster time-scale of the entrainment process arising in the mixing layer. This peculiar feature makes the (non-dimensional) entrainment, spreading and decay rates of turbulent jets independent of the Reynolds number [44]. Being the dispersed droplets inertial, they are not able to get benefit from these *fast* features and globally show a slower evaporation rate. To better characterize this aspect, we show in figure 7b the mean droplet evaporation rate normalized by the initial droplet relaxation time, $\tau_{d,0} = St \cdot t_0$, and the initial droplet mass, $m_{d,0}$, with $t_0 = R/U_0$. This normalization takes into account the droplet inertia and removes the direct dependence of the evaporation rate from the Reynolds number. Hence, we observe that at the higher Reynolds number the mean (τ_0-dimensionless) evaporation rate appears slightly higher than that of the lower Reynolds number case. The more intensive fluctuations at $Re = 10,000$ fasten the evaporation rate normalized with the droplet-relaxation time, i.e. accounting for the proper droplet time-scale. However, from a physical point of view, this small growth is not sufficient for compensating the faster advection time-scale, $t_0 = R/U_0$, induced by the higher inflow velocity. This dynamics explains the longer jet evaporation length which, nevertheless, does not scale proportionally to the Reynolds number.

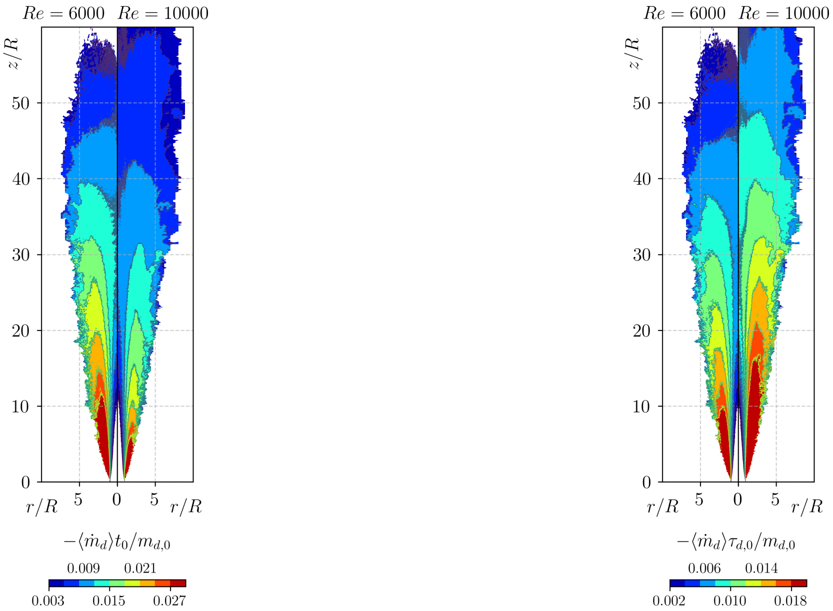

(a) **(b)**

Figure 7: (a) Average droplet vaporization rate, $\langle \dot{m}_d \rangle$ divided by the reference mass-flow-rate scale $\dot{m}_{d,0} = m_{d,0}/t_0$ with $m_{d,0}$ the initial droplet mass and $t_0 = R/U_0$ the reference time-scale of the jet. (b) Average droplet vaporization rate normalized by using the time-scale, $\tau_{d,0}$.

As previously stated, a strong preferential segregation of the dispersed phase arises, both in the low and high Reynolds number cases. Several mechanisms governing the preferential concentration of droplets in a turbulent flow have been proposed, e.g. the small-scale clustering [51], the sweep-stick mechanism [21], the accumulation of droplets along the jet-axis [30, 31, 42] and the intermittent dynamics of the jet mixing layer [16]. Independently from the phenomena giving rise to the observed inhomogeneous and preferentially-segregated spatial distribution of droplets, the local vapor concentration within clusters is significantly higher than its bulk counterpart. Consequently, the evaporation process of the droplets located into a cluster is significantly slowed down. The vaporization may be even locally stopped, if the vapor concentration reaches the saturation level, $Y_{v,s}(p_0, T)$, producing a non-evaporating core surrounding the cluster [47]. Different approaches have been proposed in the literature to measure the intensity of the preferential segregation of the dispersed phase in droplet- or particle-laden multiphase flows [1]. In the present paper, we employ the following clustering index [6, 16]:

$$K = \frac{\overline{(\delta n)^2}}{\overline{n}} - 1. \tag{21}$$

To compute K in the equation above, (21), the Eulerian domain is discretized by employing a uniform and equispaced Cartesian grid of cubic sampling cells. The edge size of the cells is set to $L/R = 0.2$. The variables $\overline{n}$ and $\overline{(\delta n)^2}$ refer to the mean and the variance of the number of droplets located into each sampling cell, respectively. The clustering index, K, is zero for any cell where the distribution of the droplets is purely random (according to a Poisson process), whereas K becomes positive when the variance exceeds the mean value, due to the existence of a preferential concentration of droplets within the considered cell. In this sense, large positive values of K correspond to a strong segregation of the dispersed phase, whereas small values to a uniform spatial distribution of droplets. The results are presented in figure 8a, showing the contour plot of the mean clustering index computed by averaging the instantaneous and local values of K along the azimuthal direction and over time, concurrently. Since no strong differences exist in the spatial distribution of K, at least between the cases considered in this paper, the distribution and the intensity of the preferential segregation of the dispersed phase present only a weak dependence from the bulk Reynolds number of the jet. In the immediate proximity of the inflow section, K assumes positive values mainly in the mixing layer, whereas it is only weakly positive in the core. On the other hand, in the intermediate and far-field, K assumes quite large positive values over the whole jet, both in the core and mixing layer. The peak of the clustering index is located in the jet core, between $z/R \simeq 10$ and $z/R \simeq 20$ in both the low and high Reynolds number cases, the latter presenting a small shift in the downstream direction of the K-peaking-region.

To determine the leading mechanisms that drive the preferential segregation of droplets in different spray regions, we consider the droplet Stokes number evaluated at the dissipative time-scale. Figure 8b provides the trend of the mean Stokes number $\langle St_\eta \rangle$, defined as the ratio of the droplet response time, τ_d, and the characteristic time of the dissipative scale, $\tau_\eta = (\nu/\epsilon)^{1/2}$, computed along the jet-axis and plotted versus z/R. The local dissipative time-scale is evaluated in correspondence of each cell of the computational Eulerian grid, located within the radial range $0 < r/R < 0.2$. Then, the computed time-scale is used to estimate the Stokes number of the droplets located in the correspondent cell. Finally, the mean Stokes number is computed by averaging its instantaneous and local values along the azimuthal direction, within the considered radial range, as well as over time, concurrently. The axial trend of $\langle St_\eta \rangle$ shows a distinct hump around $z/R \simeq 15$, which is followed by a gradually decrease along the streamwise direction until a unity value is achieved around $z/R \simeq 30$ and $z/R \simeq 40$, at $Re = 6,000$ and $Re = 1000$, respectively. The peaks of the Stokes number are achieved in correspondence of the peak of the clustering index. Small-scale inertial clustering arises from the competition between the droplet inertia and the Stokes drag. The drag tends to force the droplets to follow the highly convoluted paths of the turbulent motion, whereas the finite inertia of the droplets prevents them to exactly move along these material-paths. By this mechanism, largest droplets, for which $St_\eta \gg 1$, act as ballistic particles with respect to the smallest scales of turbulence. These droplets move across the smallest turbulent structures being only weakly perturbed and do not tend to accumulate in clusters. On the contrary, the smallest droplets, for which $St_\eta \ll 1$, act as passive tracers which follow exactly the path of the local turbulent motion. These droplets do not contribute significantly to inertial clustering. On the other hand, droplets for which $St_\eta \simeq 1$ manifest an intermediate dynamics. These droplets accumulate into the small-scale interstitial vortical regions and give rise to strong inhomogeneities of the spatial distribution of the dispersed phase. Since the Stokes number keeps values significantly higher than unity in the intermediate field, based on the trend of St_η, we assess that inertial clustering must play a minor role in the preferential segregation of the liquid phase in this region, whereas it becomes dominant in the far-field. A different mechanism, rather than small-scale inertial clustering, should be considered to explain the clustering of droplets in the near and intermediate field of the jet. We attribute the preferential concentration of droplets in these regions to the effect of the intermittent dynamics of the mixing layer of the jet. In the outer-spray region, high-intensity vortical structures separate the turbulent core, populated by droplets, by the dry environment, depleted of droplets. By an Eulerian point of view, this region is characterized by large temporal and spatial fluctuations of the local droplet concentration because of the intermittent dynamics of the turbulent-non-turbulent interface. The entrainment causes the envelopment of dry-air bubbles, depleted of droplets, within the turbulent jet. These dry and droplet-depleted bubbles mix with high-saturated gaseous regions full of droplets, giving rise, instant by instant, to large inhomogeneities of the droplet distributions which are advected downstream. To highlight this source of clustering in the mixing layer, we show in figure 8c the variance of mean vapor mass fraction, $\langle {Y'}_v^2 \rangle$, for the two cases considered in the present paper. It is worth noting that the locations of the peak of K and $\langle {Y'}_v^2 \rangle$ in the near-field region are close to each other. Hence, we assess that the main source of droplet clustering has to be related to the intermittent dynamics of the mixing layer. Clusters created by this mechanism in the

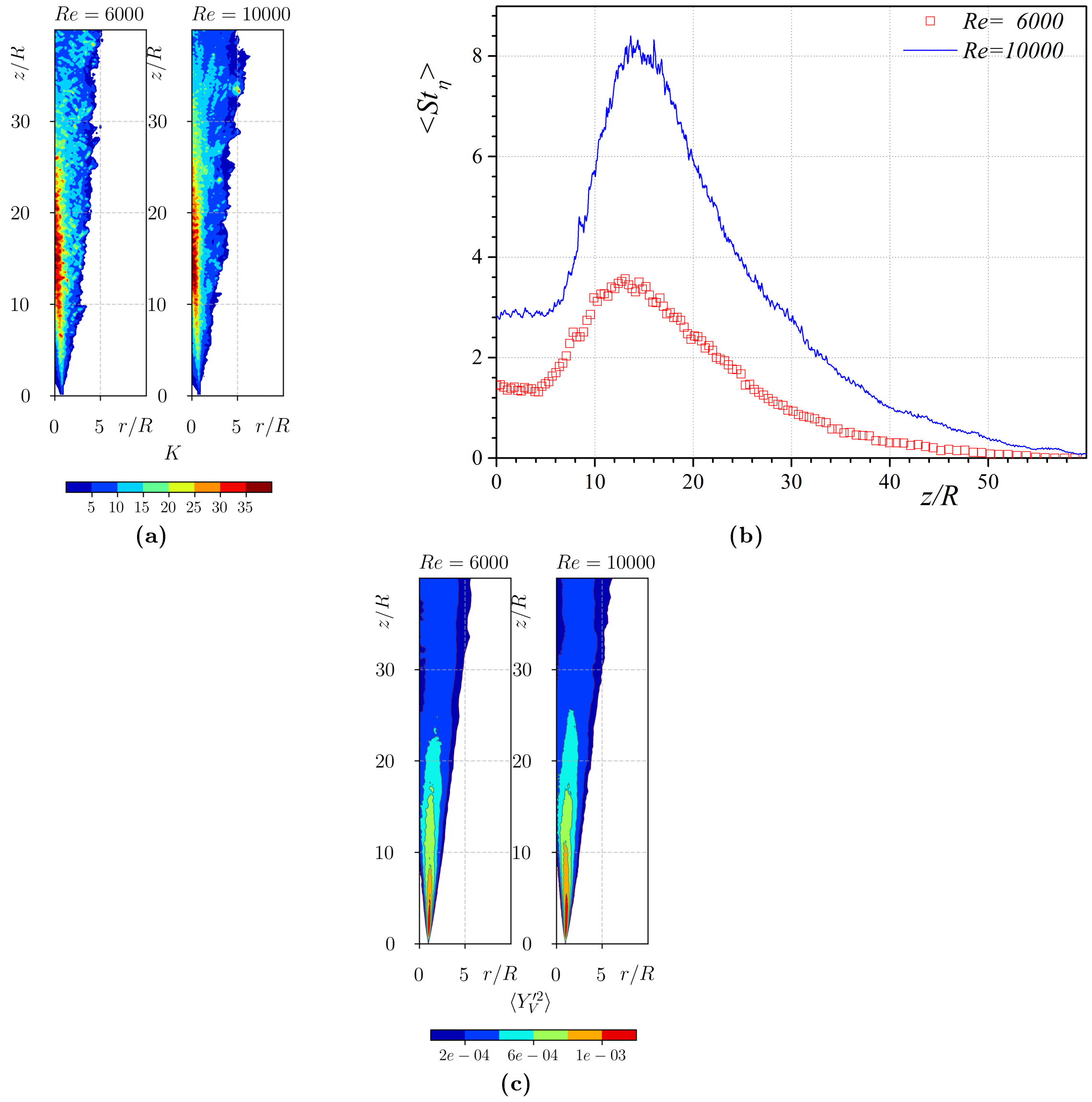

(a)

(b)

(c)

Figure 8: (a) Contour plot of the mean droplet clustering index, K, defined according to equation 21. (b) Evolution along the jet-axis of the mean droplet Stokes number, $\langle St_\eta \rangle$, based on the dissipative time-scale of the carrier phase, $St_\eta = \tau_d/\tau_\eta$. (c) Average distribution of variance of vapor mass fraction,$\langle Y_v'^2 \rangle$.

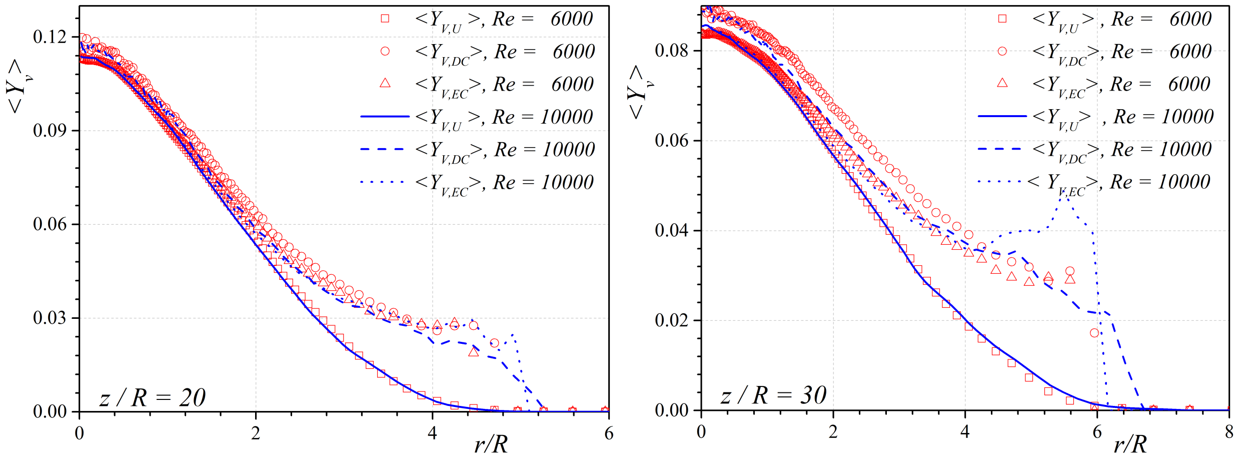

(a) **(b)**

Figure 9: Radial profiles of the average vapor mass fraction field at two different axial distances from the origin: (a) $z/R = 20$, (b) $z/R = 30$. Each plot shows the enstrophy-threshold conditional average, $\langle Y_{V,EC} \rangle$, the droplet-conditional average, $\langle Y_{V,DC} \rangle$, and the unconditional Eulerian average, $\langle Y_{V,U} \rangle$. The enstrophy-conditional average is calculated by sampling the vapor mass fraction only over turbulent core events ($I = 1$), that is, when local enstrophy exceeds a fixed threshold. $\langle Y_{V,DC} \rangle$ is the average vapor mass fraction field conditioned to the presence of droplets at a given point.

near-field are then advected downstream. Then, in the intermediate and far-field regions, inertial clustering becomes more important.

To quantify the importance of the droplet preferential segregation on the evaporation process, we consider different conditional averages of the vapor mass fraction field. We provide a comparison between the conditional mean vapor concentration sampled by the droplets (*droplet-conditional*), $\langle Y_{V,DC} \rangle$, and the unconditional Eulerian one, $\langle Y_{V,U} \rangle$. The latter is computed by averaging the Eulerian vapor mass fraction field along the azimuthal direction and over time, concurrently. The former is defined as the average of the Eulerian vapor mass fraction field, conditioned to the presence of a droplet at a given point. This statistical quantity is computed on the Eulerian grid by associating to each grid cell the mean vapor mass fraction instantaneously sampled by the droplets located within the considered cell. Figure 9 shows the radial profiles of $\langle Y_{V,DC} \rangle$ and $\langle Y_{V,U} \rangle$ at two different axial distances from the jet inflow, $z/R = 20$ and $z/R = 30$, respectively. Globally, the vapor mass fraction sampled by the droplets results to be higher than the correspondent unconditional value, regardless of the Reynolds number. As already reported in [16], this preferential sampling of the vapor mass fraction field actuated by the droplets can be related to different mechanisms. The primary contribution originates from the vapor self-produced by droplets with a tracer-like behavior ($St_\eta \ll 1$). These droplets exactly follow the path of the turbulent motion of the surrounding vapor atmosphere, increasing the local vapor concentration in their surrounding material volume, and hence sampling higher vapor concentration. Secondarily, within a droplet cluster, independently from the mechanisms that drive its formations, a highly-saturated cloud establishes in its proximity. Hence, in the presence of preferential segregation, an oversampling of the vapor concentration field is expected also by the droplets evaporating inside clusters. The radial profiles of the mean vapor concentration are similar inside the jet core, figure 9a, whereas significant differences appear in the mixing layer. In its core, the jet presents a nearly uniform vapor mass fraction field that nullifies the oversampling actuated by the droplets. On the other hand, in the mixing layer, the entrainment of bubbles of dry air depleted of droplets causes the Eulerian unconditional statistics to assume lower values than the conditional one. This aspect is strictly connected to the clustering mechanism previously discussed. Further downstream, the difference between the *droplet-conditional* vapor concentration and the unconditional one gradually increases, even in the jet core, as shown in figure 9b. In the far-field, the inertial small-scale clustering plays a dominant role in the preferential segregation of droplets, as shown in figure 8. This leads to a considerable increment of the vapor mass fraction field sampled by the droplets grouped in clusters with respect to the unconditional statistics. Besides, no evident disagreement is observable for the unconditional mean vapor concentration profiles in the $Re = 10,000$ and $Re = 6,000$ case.

To better analyze the mixing layer of the jet spray, we remind that the inner core and the irrotational outer region are separated by a nearly-sharp fluctuating interface, which is highly convoluted over a wide range of vortical scales [15]. Different approaches can be employed to identify this interface [8, 23, 27, 54]. In the present paper, we consider the local enstrophy, $\zeta^2 = \|\nabla \times \overrightarrow{u}\|$. The inner turbulent core is characterized by large fluctuations of enstrophy, whereas in the outer region the enstrophy is null. Thus, by fixing a threshold, ζ^2_{th}, it is possible to distinguish if a given Eulerian position is located, at a given time instant, in the turbulent jet core or in the outer irrotational environment, by employing the following index:

$$I(\boldsymbol{x}, t) = H[\zeta^2(\boldsymbol{x}, t) - \zeta^2_{th}], \tag{22}$$

with H the Heaviside function. $I = 1$ denotes a turbulent event at the Eulerian position $\boldsymbol{x}$, whereas $I = 0$ an irrotational one. It has been observed that the conditionally averaged profile of the vorticity magnitude in the shear layer is weakly dependent on the threshold vorticity magniture [8, 15]. In Dalla Barba and Picano [16], no relevant differences have been observed on I by changing the value of $\zeta_{th} = 0.6U_0/R$ by a factor 2. Hence, we can assess that the index I, employed in the present paper to distinguish between the rotational jet core and irrotational environment, is weakly dependent from the threshold value ζ_{th}. Thus, we define the *enstrophy-conditional average* of the vapor mass fraction field, $\langle Y_{V,EC}\rangle$, as the average vapor mass fraction obtained by sampling only the instantaneous values of $Y_V(\boldsymbol{x}, t)$ linked to turbulent events, that is for time instants and positions where $I = 1$, only. Figure 9 provides the radial profile of $Y_{V,DC}$, $Y_{V,U}$ and $Y_{V,EC}$. The unconditional and both the conditional statistics are similar in the core at $z/R \simeq 20$. In the mixing layer, the radial profile of $\langle Y_{V,EC}\rangle$ keeps closer to that of $\langle Y_{V,DC}\rangle$, both the statistics assuming higher values than that of $\langle Y_{V,U}\rangle$. This difference, confined to the outer spray regions, confirms the contribution of the intermittent dynamics of the mixing layer to the non-homogeneous spatial distribution of the dispersed phase discussed above. Droplets moving towards the outer region are enclosed by a high concentration vapor cloud which is expelled from the turbulent jet core. Simultaneously, dry air without droplets is engulfed in the core enhancing the fluctuations of the droplet distribution and vapor concentration. Further downstream, $z/R \simeq 30$, the droplet-conditional vapor concentration profile shows the same shape as the enstrophy-conditional one, except for an almost constant offset, both in the core and mixing layer. This confirms how, in the far-field, both the small-scale inertial clustering and the intermittent dynamics of the mixing layer contribute to the oversampling of the vapor mass fraction field actuated by the dispersed phase, the former mechanism becoming the dominant effect in the jet core. The combination of these two mechanisms, leading to the observed oversampling of the vapor concentration, strongly reduces the vaporization rate with respect to the one that would be estimated by employing unconditioned statistics. This phenomenology is similar for both the cases considered in the present study.

Lagrangian statistics

Turbulent fluctuations are responsible for extremely different Lagrangian histories of the evaporating droplets. The Joint Probability Density Function (JPDF) of the droplet vaporization length and time are reported for both cases in figure 10. The vaporization length of a droplet is defined as the axial distance from the inlet, Z_e/R, where the droplet radius is decreased from $r_{d,0}$ to the threshold radius, $r_{d,th} = 0.1 r_{d,0}$ (99.9% of the initial mass is evaporated). The correspondent time is defined as the droplet vaporization time, t_e/t_0, with $t_0 = R/U_0$, being R the reference length scale (inlet radius) and U_0 the bulk inflow velocity. For both cases, a strong linear correlation is found between the droplet vaporization length and time, whereas different slopes are observable. Integrating the JPDFs, we have calculated that half of the ejected droplets are still present around $z_e/R \simeq 32$ for $Re = 6,000$ and $z_e/R \simeq 36$ for $Re = 10,000$, locations where the 90% of the droplet mass is evaporated (see figure 3). Correspondingly, the mean vaporization times are about $t_e/t_0 = 65$ and $t_e/t_0 = 90$ for $Re = 6,000$ and $Re = 10,000$, respectively. Consistently with the previous discussion, we observe a lower average vaporization rate for the higher Reynolds number. It is also worth remarking that the actual droplet vaporization time varies of more than 50% of its mean value (not shown), confirming the extremely heterogeneous dynamics of the vaporization process. Since at $Re = 10,000$ droplets have larger initial Stokes numbers, they tend to remain longer in the nearly saturated turbulent core. This causes an additional delay in the vaporization process in the near-field.

Figure 11(a) compares the Probability Density Function (PDF) of the droplet radius at different axial positions, z/R, for the two Reynolds numbers considered in the present paper. It is worth remarking that, due to numerical stability reasons, droplets with a radius of $r_d < 0.5\mu m$ are removed from the simulation (more than 99.9% of the liquid mass is evaporated before). Thus, all

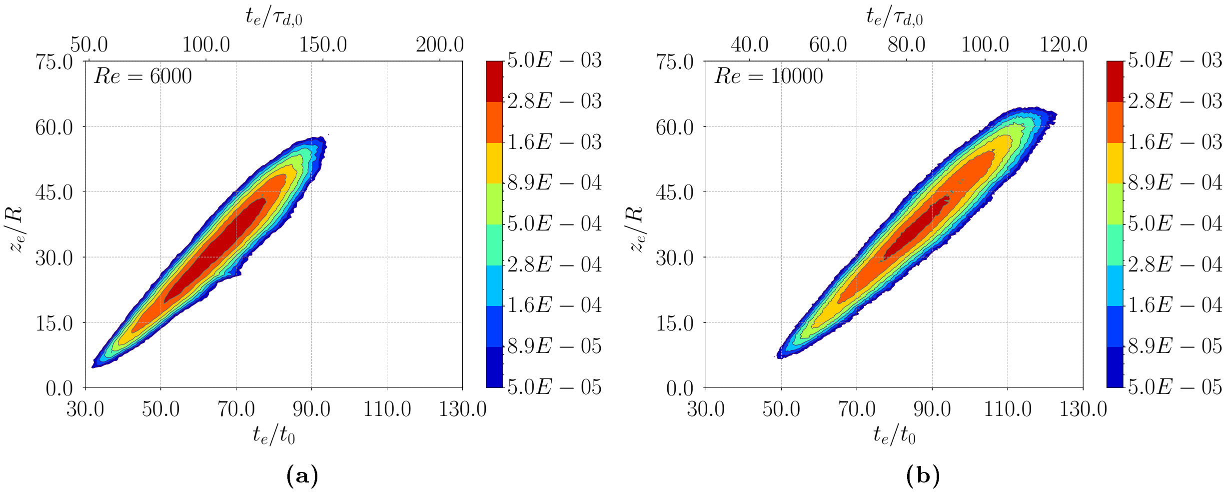

Figure 10: JPDF of the vaporization lengths and times of the injected droplets computed over the whole droplet population. (a) $Re = 6,000$ (b) $Re = 10,000$. The lower axis provides the non-dimensional time, t_e/t_0 with $t_0 = R/U_0$, whereas the secondary top axis provides the non-dimensional time, $t_e/\tau_{d,0}$.

the PDFs sharply terminate. Except for this effect, the PDF clearly shows how fastly polydispersity is promoted in the turbulent jet-spray. Though starting from an identical monodisperse status, the distribution of the droplet radii rapidly spreads over a wide range, even at five jet radii downstream the inlet. We observe this fast growth of polydispersity in both the considered cases, with a slightly narrower PDF at $Re = 10,000$. Further downstream, e.g. $z/R = 20$ and $z/R = 40$, a similar qualitative behaviour is observed: the flat PDFs are related to a nearly constant probability to find droplets of arbitrary sizes. We attribute this fast widening of the droplet size spectrum to the strong inhomogeneous conditions of the vapour concentration. In the mixing layer, the entrainment process creates flow regions with low levels of saturation, which promote fast droplet vaporization. Concurrently, because of clustering, clouds of droplets originating in the jet core maintain slow vaporization rates for a long time. As shown in panel (b) of figure 11, the PDFs of the saturation level of the droplet atmospheres present nearly flat profiles. This reflects in a strongly varying droplet vaporization rate, whose PDFs are shown in panel (c). The droplet vaporization rate is

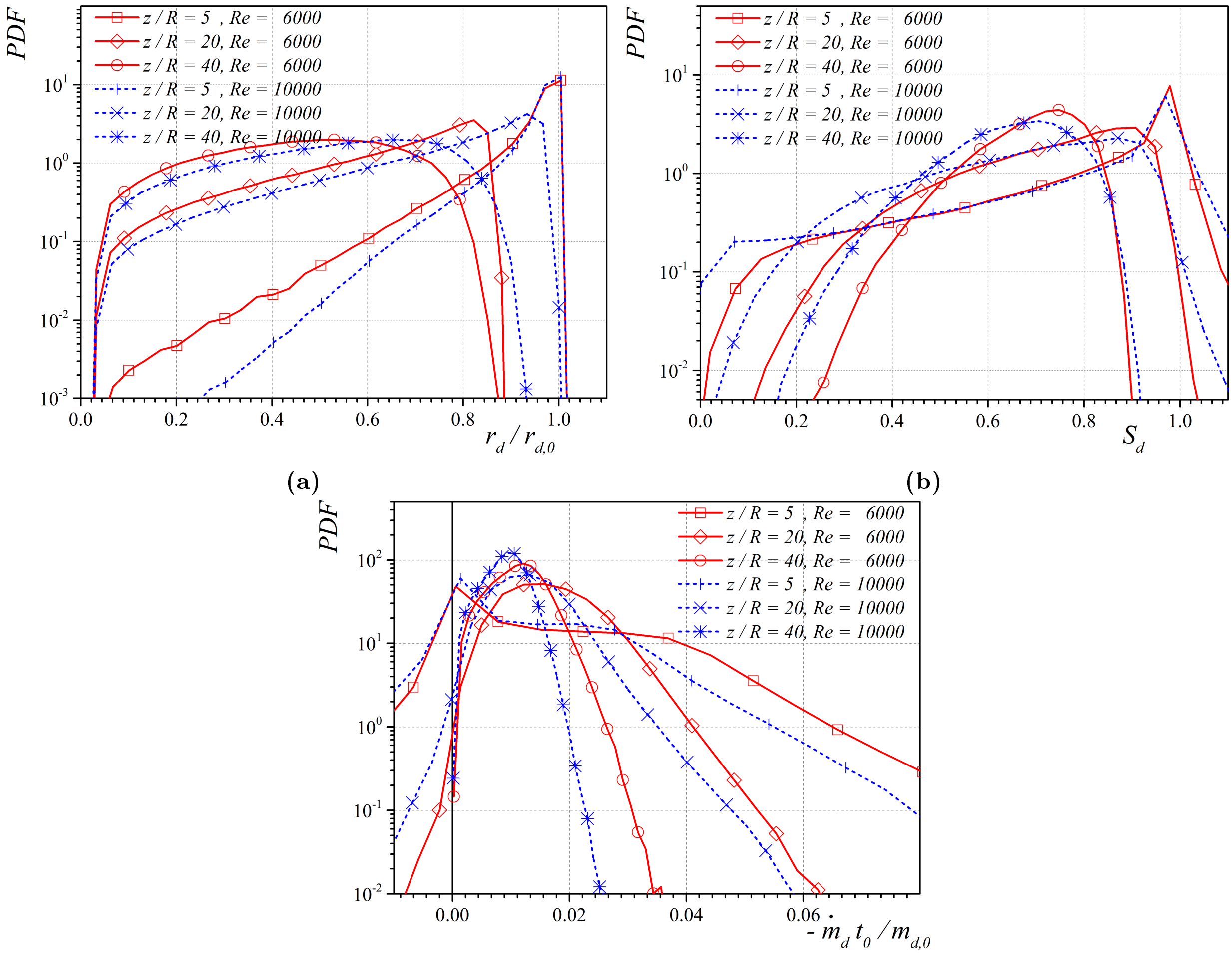

(a)

(b)

(c)

Figure 11: (a) PDF of the non-dimensional droplet radius, $r_d/r_{d,0}$, where $r_{d,0}$ is the initial radius of the injected droplets. (b) PDF of the saturation field evaluated at the droplet surface, $S_d = Y_v/Y_{v,s}$, where $Y_{v,s} = Y_{v,s}(T_d, p)$ is the vapor mass fraction at saturation computed as a function of the droplet actual temperature and the carrier phase thermodynamics pressure,p_0. Y_v is the actual vapor mass fraction in the carrier gaseous mixture evaluated at the droplet position. (c) PDF of the non-dimensional droplet vaporization rate, $-\dot{m}_d t_0/r_{d,0}$, where $t_0 = R/U_0$ and $r_{d,0}$ are the the reference time-scale of the jet and the initial radius of the injected droplets, respectively.

slightly higher for the low Reynolds number case, consistently with the slower jet evaporation length and the previous discussion on the effect of the Reynolds number. Finally, we aim to highlight that in the near and intermediate fields some rare condensation events occur. When the evaporation of a droplet proceeds fast enough, which is more common in the near-field region close to the mixing layer, the droplet temperature decreases. In turn, this results in the establishment of saturation conditions which can block the evaporation even in a region with relatively low values of the vapour concentration field. Then, if the droplet moves into a higher vapour concentration zone due to its inertia, supersaturation conditions could arise. These inertial effects are more worthy of attention for droplets with a higher Stokes number, which is the reason for the relatively broader distribution range of the saturation observed in the $Re = 10,000$ case. The intense polydispersity of the evaporating droplets affects the vaporization length and time of the droplets within the spray.

To predict the temporal evolution of the droplet dynamics, the *d-square* law is often adopted [29]. In this context, a linear behavior for the square diameter of each droplet is expected,

$$\frac{d_d^2}{d_{d,0}^2} \simeq 1 - k\frac{t_f}{t_0}, \tag{23}$$

$$k = \frac{Sh}{Sc}\frac{\rho}{\rho_l}\frac{1}{Re}\left(\frac{R}{r_{d,0}}\right)^2 ln(1 + B_m), \tag{24}$$

where, in many practical and experimental application, the constant k can only be estimated based on the reference environmental state, e.g. bulk vapor concentration. We provide in figure 12 the Joint Probability Density Function (JPDF) of the droplet square diameter and flight time, $D2F(t_f, d_d^2)$. As expected, the droplet square diameter does not follow a linear temporal evolution as predicted by the *d-square* law, otherwise all data should collapse on a single straight line. In the same figure, we also report the average droplet square diameter conditioned to the flight time, $\langle d_d^2/d_{d,0}^2\rangle(t/t_0)$, and the droplets mean flight time conditioned to the square droplet diameter, $\langle t_f/t_0\rangle(d_d^2/d_{d,0}^2)$, for both Reynolds number cases. These two quantities have been directly extracted from the JPDF,

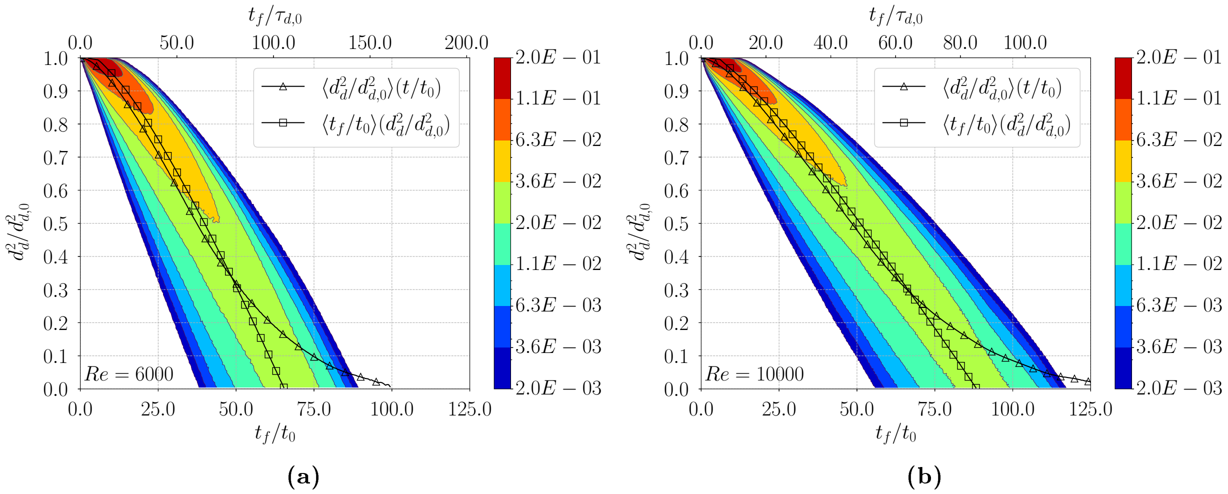

Figure 12: JPDF of the droplet square diameter and flight time, $D2F(t_f, d_d^2)$, for for different Reynolds numbers. The mean square droplet diameter conditioned to the flight time (triangle symbol), $\langle d_d^2/d_{d,0}^2\rangle(t/t_0)$, and the mean droplet flight time conditioned to the square droplet diameter (square symbol), $\langle t_f/t_0\rangle(d_d^2/d_{d,0}^2)$. In the upper abscissa the time is normalized by the initial particle relaxation time, whereas the lower axis provides the non-dimensional time, t_f/t_0.

$D2F$, as:

$$\langle d_d^2 \rangle (t_f) = \frac{\int_0^\infty d_d^2 \;\; D2F(t_f, d_d^2) \; d(d_d^2)}{\int_0^\infty \; D2F(t_f, d_d^2) \; d(d_d^2)} \tag{25}$$

$$\langle t_f \rangle (d_d^2) = \frac{\int_0^\infty t_f \;\; D2F(t_f, d_d^2) \; d(t_f)}{\int_0^\infty \; D2F(t_f, d_d^2) \; d(t_f)}. \tag{26}$$

Although the two quantities are strictly related, their significance is different. The mean square diameter conditioned to the flight time provides the mean square diameter of droplets given a fixed flight time, e.g. after a fixed time since droplet injection. On the other hand, the mean flight time at a given mean square diameter provides the amount of time needed, on average, by droplets to reach a given size. In both the considered cases, the two observables assume similar values for relatively large droplets ($d_d^2/d_{d,0}^2 > 0.25$) and strongly different ones for small droplets. The mean flight time conditioned to the droplet square diameter provides also information about the finite time needed, on average, by the droplets for full evaporation, e.g. $d_d^2/d_{d,0}^2 \to 0$: We name the latter *mean evaporation flight time*, t_f^e. The mean evaporation flight time increases with the Reynolds number when scaled with the advection reference time, being $t_f^e/t_0 \simeq 66$ and $t_f^e/t_0 \simeq 89$, for $Re = 6,000$ and $Re = 10,000$ respectively. We also note that, by scaling the mean flight time with the droplet initial relaxation time, the two cases show closer values, $t_f^e/\tau_{d,0} \simeq 106$ and $t_f^e/\tau_{d,0} \simeq 86$, with a slightly faster evaporation rate for the higher Reynolds number case. This fact confirms that, by increasing the Reynolds number, two different competing effects are present: a stronger turbulence intensity which tends to fasten the evaporation rate and a higher droplet relative inertia which tends to slow down the process. It is worth highlighting that the trends of the two curves, Eq. (25) versus Eq. (26), are extremely different for small droplet sizes. For a time longer than the mean evaporation flight time, t_f^e, a finite average droplet diameter is still observable. This peculiar effect can be explained by considering that droplets in clusters require a very long time to evaporate. Hence, some droplets can survive for a very long time, causing the statistics to display a finite average diameter. The prolonged life-time of droplets could be further extended considering the existence of super-saturation regions controlled by ambient conditions, as showed in the recent high-fidelity simulations about respiratory flows by Chong et al. [12], Ng et al. [40]. Both these aspects could be crucial in the modelling of droplet dispersion in many applications of practical interest.

To better characterize how the *d-square* law is able describe the present cases, we consider the evolution of the droplet square diameter predicted by using the *d-square* law, Eq. (23), and estimating the proportionality constant, k_{env}, by considering the bulk thermodynamic properties of the environment, as usual in many practical applications. Figure 13 provides the trend of the droplet square diameter predicted by using the *d-square* law together with $\langle d_d^2/d_{d,0}^2 \rangle (t/t_0)$ and $\langle t_f/t_0 \rangle (d_d^2/d_{d,0}^2)$. The resulting constants expressed in dimensionless units are $k_{env} \simeq 0.115$ and $k_{env} \simeq 0.069$ for $Re = 6,000$ and $Re = 10,000$, respectively. In both cases the predicted droplet evaporation time is much lower than the actual one, e.g. the estimation of the evaporation rate is much higher than the actual one. We attribute this disagreement to the effects of clustering and preferential sampling of vapor concentration previously discussed, that cannot be accounted for by the *d-square* law. Since the mean flight time computed by Eq. (26) shows a linear behavior for small droplets and long time, we provide also the linear fitting in the form $\langle t_f/t_0 \rangle (d_d^2/d_{d,0}^2) \simeq C - k_{fit}(t_f/t_0)$ restricted

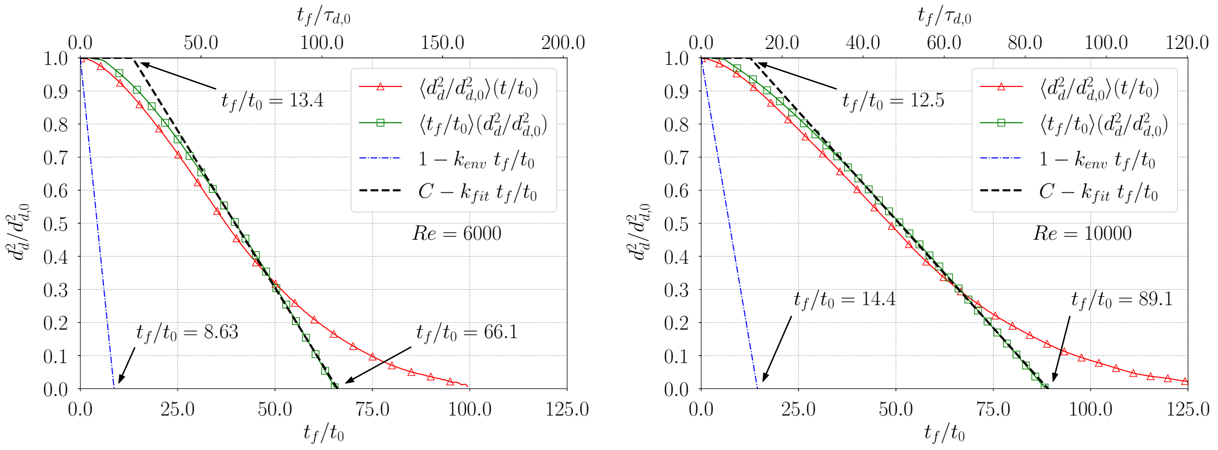

(a) **(b)**

Figure 13: Mean square droplet diameter conditioned to the flight time (triangle symbol), $\langle d_d^2/d_{d,0}^2\rangle(t/t_0)$, and the mean droplet flight time conditioned to the square droplet diameter (square symbol), $\langle t_f/t_0\rangle(d_d^2/d_{d,0}^2)$. In the upper axis the time is normalized by the initial particle relaxation time, $\tau_{d,0}$, whereas in the lower one by the advecting time, t_0. The blue line shows the evolution of droplet square diameter predited by employing the *d-square* law provided in Eq. (23) and by estimating the k constant via the bulk environmental conditions. The black, dashed line provides the linear fitting of $\langle t_f/t_0\rangle(d_d^2/d_{d,0}^2)$ restricted to $t/t_0 > 30$.

to $t_f/t_0 > 30$. In this case the fitting constants are $C \simeq 1.25$ and $k_{fit} \simeq 0.0190$ for $Re = 6000$ whereas $C \simeq 1.164$ and $k_{fit} \simeq 0.0131$ for $Re = 10000$. By using these parameters we can reformulate an effective *d-square* law. We assume that droplets do not evaporate for some time after the injection when they travel in the saturated unperturbed core. Downstream, the droplet square diameter evolves according to an effective *d-square* law. The evaporation delay time, when droplets are assumed to be non-evaporating, is similar for the two cases, e.g. $\sim 13 t_0$, which corresponds to a travelled distance of around 13 jet radii. The estimated values of k_{fit} appear six times lower than those estimated by using the bulk properties of the environment, k_{env}, for both cases. The large discrepancies between the values of k_{env} and k_{fit} confirm the crucial importance of improving bulk spray low-order models accounting for the complex dynamics arising from the strong inhomogeneity of the droplet and the vapor mass fraction distribution in turbulent jet-sprays.

Conclusion

A three-dimensional Direct Numerical Simulation (DNS) is employed to investigate the motion and evaporation of acetone droplets in a moderate Reynolds number turbulent jet-spray (Re = *10,000*) in an open environment and dilute conditions. The gaseous jet-spray is composed of a mixture of dry air and acetone vapour, whereas the surrounding environment is filled with dry air. The problem is numerically tackled by employing the Eulerian-Lagrangian framework and the point-droplet approximation, combined with a two-way coupling concept, including the mass, momentum and energy exchanges between two phases. The simulation reproduces the evaporation of monodisperse acetone droplets, continuously injected within the turbulent gaseous phase at a bulk Reynolds number $Re = 2U_0 R/\nu = 10,000$. After the establishment of statistically-steady conditions for both the phases, a systematic and comprehensive dataset of both instantaneous and average Eulerian and Lagrangian observables was collected. In the present study, the dataset is also compared to a previous DNS dataset concerning a lower Reynolds number case ($Re = 6{,}000$), which, from the physical point of view, corresponds to a lower jet velocity (Dalla Barba and Picano [16]). The effects of the jet Reynolds number on the turbulent evaporation of droplets in dilute jetsprays are investigated. In both the cases considered in the present paper, a strong evaporation rate is observed in the mixing layer, where the entrainment of dry air dilutes the saturated jet core. A longer evaporation length is found for the higher Reynolds number jet-spray. We relate this increment of the evaporation length to the lower average vaporization rate, observed at $Re = 10{,}000$, by scaling the data by the jet advection reference time-scale, $t_0 = R/U_0$. This lower rate is attributed to a higher droplet relative inertia (Stokes number), which slows down the vapour-liquid mass exchange. A strong inhomogeneous and segregated droplet distribution is observed in both the considered cases. This is found to originate in the mixing layer of the jet near-field and propagate in the downstream direction. In the jet mixing layer, we identify different features: entrained bubbles of dry air depleted of droplets and saturated gas clouds full of droplets coming from the saturated core. Since the droplets located in dry regions evaporate fast, whereas the droplets in vapour-saturated clouds cannot evaporate, these dynamics tend to intensify the clustering in the downstream evolution of the jet. Besides, in the far-field, small-scale clustering is also observed. The inhomogeneous distribution of the segregated phase strongly impacts the Lagrangian evolution of the droplets: the droplet size spectrum becomes extremely wide, even starting from a monodisperse distribution. This extreme widening of the droplet size spectrum is associated with a broadening of the probability density functions of the evaporation rate and saturation level sampled by the droplets. These findings could play a role in explaining the fast widening of the droplet spectrum in warm clouds[49]. Finally, we address the evaluation of the accuracy of the well-established *d-square* law in approximating the droplet evolution for the cases considered in the present paper. Firstly, we found that the actual droplet evaporation time varies of more than 50% of its mean value. This highlights how the evolution of the droplet histories strongly deviates from the *d-square* law. Secondly, we observe that, whereas the trend of the mean evaporation (flight) time, t_f^e, can be approximated by a linear law of the droplet mean square diameter, its slope is much lower than the value predicted by considering the bulk thermodynamical properties of the environment. In addition, we show how, after a time much longer than t_f^e , the evaporation process is not still terminated. This peculiar aspect is attributed to clustering dynamics. Aggregates of droplets with a nearly saturated atmospheres may survive for a longer time before fully evaporating. Hence, some droplets may preserve relatively large sizes for long distances and times. Despite the differences between steady-state jet-sprays, which are considered in the present paper, and respiratory flows, this aspect should be considered in the modelling of the evaporation and dispersion of infectious droplets. Indeed, even in these cases, some droplets may persist much longer than what expected using the *d-square* law, especially if its evaluation is based on the bulk thermodynamic properties of the environment. Finally, we believe that dataset and the analysis presented in this study are relevant to improve the knowledge about the dynamics of turbulent evaporating sprays, providing, at the same time, a benchmark test-case for developing more accurate low-order and high-fidelity models.

CRediT authorship contribution statement

Jietuo Wang: Conceptualization, Software, Data curation, Investigation, Formal analysis, Writing - original draft, Visualization. Federico Dalla Barba: Software, Methodology, Validation, Writing - review & editing, Visualization. Francesco Picano: Conceptualization, Methodology, Resources, Formal analysis, Writing - review & editing, Supervision.

ACKNOWLEDGEMENT

This study has been funded by the research project promoted by China Scholarship Council (CSC) Grant #201806250023 . We also thank CINECA for providing computational resources via the ISCRA C project: HiReS (HP10C3YNLC).

Bibliography

[1] Shaw R. A., A. B. Kostinski, and Michael L. Larsen. Towards quantifying droplet clustering in clouds. *Q. J. R. Meteorol. Soc*, 128(582):1043–1057, 2002.

[2] B. Abramzon and W. A. Sirignano. Droplet vaporization model for spray combustion calculations. *Int. J. Heat Mass Transf.*, 32(9):1605–1618, 1989.

[3] Antonio Attili, Fabrizio Bisetti, Michael E. Mueller, and Heinz Pitsch. Formation, growth, and transport of soot in a three-dimensional turbulent non-premixed jet flame. *Combust. Flame*, 161(7):1849–1865, 2014.

[4] Jesse T. Ault, Kevin K. Chen, and Howard A. Stone. Downstream decay of fully developed dean flow. *J. Fluid Mech.*, 777:219–244, 2015.

[5] S. Balachandar, S. Zaleski, A. Soldati, G. Ahmadi, and L. Bourouiba. Host-to-host airborne transmission as a multiphase flow problem for science-based social distance guidelines. *Int. J. Multiph. Flow*, 132:103439, 2020.

[6] F. Battista, F. Picano, G. Troiani, and C. M. Casciola. Intermittent features of inertial particle distributions in turbulent premixed flames. *Phys. Fluids*, 23(12):123304, 2011.

[7] M. BINI and W. P. JONES. Large-eddy simulation of particle-laden turbulent flows. *J. Fluid Mech.*, 614:207–252, 2008.

[8] David K. Bisset, Julian C. R. Hunt, and Michael M. Rogers. The turbulent/non-turbulent interface bounding a far wake. *J. Fluid Mech.*, 451:383–410, 2002.

[9] A. Bukhvostova, E. Russo, J.G.M. Kuerten, and B. J. Geurts. Comparison of dns of compressible and incompressible turbulent droplet-laden heated channel flow with phase transition. *Int. J. Multiph. Flow*, 63:68–81, 2014.

[10] Adrien Chatelier, Benoît Fiorina, Vincent Moureau, and Nicolas Bertier. Large eddy simulation of a turbulent spray jet flame using filtered tabulated chemistry. *J. Combust.*, 2020:1–23, 2020.

[11] Yung-Cheng Chen, Sten H. Stårner, and Assaad R. Masri. A detailed experimental investigation of well-defined, turbulent evaporating spray jets of acetone. *Int. J. Multiph. Flow*, 32(4):389–412, 2006.

[12] Kai Leong Chong, Chong Shen Ng, Naoki Hori, Rui Yang, Roberto Verzicco, and Detlef Lohse. Extended lifetime of respiratory droplets in a turbulent vapor puff and its implications on airborne disease transmission. *Phys. Rev. Lett.*, 126(3):034502, 2021.

[13] M. S. Chong, A. E. Perry, and B. J. Cantwell. A general classification of three–dimensional flow fields. *Phys. Fluids*, 2(5):765–777, 1990.

[14] P. P. Ciottoli, F. Battista, R. Malpica Galassi, F. Dalla Barba, and F. Picano. Direct numerical simulations of the evaporation of dilute sprays in turbulent swirling jets. *Flow Turbulence Combust.*, 106(3):993–1015, 2021.

[15] Carlos B. da Silva, Julian C.R. Hunt, Ian Eames, and Jerry Westerweel. Interfacial layers between regions of different turbulence intensity. *Annu. Rev. Fluid Mech.*, 46(1):567–590, 2014.

[16] Federico Dalla Barba and Francesco Picano. Clustering and entrainment effects on the evaporation of dilute droplets in a turbulent jet. *Phys. Rev. Fluids*, 3(3):034304, 2018.

[17] S. Elghobashi. On predicting particle-laden turbulent flows. *Appl. Sci. Res.*, 52(4):309–329, 1994.

[18] G.M Faeth, L.-P Hsiang, and P.-K Wu. Structure and breakup properties of sprays. *Int. J. Multiph. Flow*, 21:99–127, 1995.

[19] A. Ferrante and S. Elghobashi. On the physical mechanisms of two-way coupling in particle-laden isotropic turbulence. *Phys. Fluids*, 15(2):315–329, 2003.

[20] G.A.E. Godsave. Studies of the combustion of drops in a fuel spray—the burning of single drops of fuel. *Symp. Combust. Proc.*, 4(1):818–830, 1953.

[21] Susumu Goto and J. C. Vassilicos. Sweep-stick mechanism of heavy particle clustering in fluid turbulence. *Phys. Rev. Lett.*, 100(5):054503, 2008.

[22] G. HALLER. An objective definition of a vortex. *J. Fluid Mech.*, 525:1–26, 2005.

[23] M. Holzner, A. Liberzon, N. Nikitin, W. Kinzelbach, and A. Tsinober. Small-scale aspects of flows in proximity of the turbulent/nonturbulent interface. *Phys. Fluids*, 19(7):071702, 2007.

[24] J. C. R. HUNT, A. A. Wray, and P. Moin, editors. *Eddies, streams, and convergence zones in turbulent flows*, 1988. Center for Turbulence Research.

[25] Patrick Jenny, Dirk Roekaerts, and Nijso Beishuizen. Modeling of turbulent dilute spray combustion. *Prog. Energy Combust. Sci.*, 38(6):846–887, 2012.

[26] J. Jeong and F. Hussain. On the identification of a vortex. *J. Fluid Mech.*, 285(1):69, 1995.

[27] JAVIER JIMÉNEZ, SERGIO HOYAS, MARK P. SIMENS, and YOSHINORI MIZUNO. Turbulent boundary layers and channels at moderate reynolds numbers. *J. Fluid Mech.*, 657: 335–360, 2010.

[28] Ian M. Kennedy. Models of soot formation and oxidation. *Prog. Energy Combust. Sci.*, 23(2): 95–132, 1997.

[29] I. Langmuir. The evaporation of small spheres. *Phys. Rev.*, 12(5):368–370, 1918.

[30] Timothy C. W. Lau and Graham J. Nathan. Influence of stokes number on the velocity and concentration distributions in particle-laden jets. *J. Fluid Mech.*, 757:432–457, 2014.

[31] Timothy C. W. Lau and Graham J. Nathan. The effect of stokes number on particle velocity and concentration distributions in a well-characterised, turbulent, co-flowing two-phase jet. *J. Fluid Mech.*, 809:72–110, 2016.

[32] C. K. Law. Unsteady droplet combustion with droplet heating. *Combust. Flame*, 26:17–22, 1976.

[33] C. K. Law and W. A. Sirignano. Unsteady droplet combustion with droplet heating—ii: Conduction limit. *Combust. Flame*, 28:175–186, 1977.

[34] A. Majda and J. Sethian. The derivation and numerical solution of the equations for zero mach number combustion. *Combust. Sci. Technol.*, 42(3-4):185–205, 1985.

[35] P. MARMOTTANT and E. VILLERMAUX. On spray formation. *J. Fluid Mech.*, 498:73–111, 2004.

[36] F. Mashayek. Direct numerical simulations of evaporating droplet dispersion in forced low mach number turbulence. *Int. J. Heat Mass Transf.*, 41(17):2601–2617, 1998.

[37] M. R. Maxey and J. J. Riley. Equation of motion for a small rigid sphere in a nonuniform flow. *Phys. Fluids*, 26(4):883, 1983.

[38] R. S. Miller, K. Harstad, and J. Bellan. Evaluation of equilibrium and non-equilibrium evaporation models for many-droplet gas-liquid flow simulations. *Int. J. Multiph. Flow*, 24(6): 1025–1055, 1998.

[39] R. Mittal, R. Ni, and J. H. Seo. The flow physics of covid-19. *J. Fluid Mech.*, 894:317, 2020.

[40] Chong Shen Ng, Kai Leong Chong, Rui Yang, Mogeng Li, Roberto Verzicco, and Detlef Lohse. Growth of respiratory droplets in cold and humid air. *Phys. Rev. Fluids*, 6(5):054303, 2021.

[41] M. A. Pakhomov and V. I. Terekhov. Rans modeling of flow structure and turbulent heat transfer in pulsed gas-droplet mist jet impingement. *Int. J. Therm. Sci.*, 100:284–297, 2016.

[42] F. Picano, G. Sardina, P. Gualtieri, and C. M. Casciola. Anomalous memory effects on transport of inertial particles in turbulent jets. *Phys. Fluids*, 22(5):051705, 2010.

[43] F. Picano, F. Battista, G. Troiani, and C. M. Casciola. Dynamics of piv seeding particles in turbulent premixed flames. *Exp. Fluids*, 50(1):75–88, 2011.

[44] Stephen B. Pope. *Turbulent Flows.* Cambridge University Press, 2000.

[45] Venkat Raman and Rodney O. Fox. Modeling of fine-particle formation in turbulent flames. *Annu. Rev. Fluid Mech.*, 48(1):159–190, 2016.

[46] W. E. RANZ. Evaporation from drops, parts i & ii. *Chem. Eng. Prog.*, 48:141–146, 1952.

[47] Julien Reveillon and FRANCOIS-XAVIER Demoulin. Effects of the preferential segregation of droplets on evaporation and turbulent mixing. *J. Fluid Mech.*, 583:273–302, 2007.

[48] G. Rocco, F. Battista, F. Picano, G. Troiani, and C. M. Casciola. Curvature effects in turbulent premixed flames of h2/air: a dns study with reduced chemistry. *Flow Turbulence Combust.*, 94 (2):359–379, 2015.

[49] Gaetano Sardina, Francesco Picano, Luca Brandt, and Rodrigo Caballero. Continuous growth of droplet size variance due to condensation in turbulent clouds. *Phys. Rev. Lett.*, 115(18): 184501, 2015.

[50] D. B. Spalding. Combustion of liquid fuels. *Nature*, 165(4187):160, 1950.

[51] Federico Toschi and Eberhard Bodenschatz. Lagrangian properties of particles in turbulence. *Annu. Rev. Fluid Mech.*, 41(1):375–404, 2009.

[52] Philipp Weiss, Valentin Giddey, Daniel W. Meyer, and Patrick Jenny. Evaporating droplets in shear turbulence. *Phys. Fluids*, 32(7):073305, 2020.

[53] Philipp Weiss, Valentin Giddey, Daniel W Meyer, and Patrick Jenny. Evaporating droplets in shear turbulence. *Physics of Fluids*, 32(7):073305, 2020.

[54] J. Westerweel, C. Fukushima, J. M. Pedersen, and J. C. R. HUNT. Mechanics of the turbulent-nonturbulent interface of a jet. *Phys. Rev. Lett.*, 95(17):174501, 2005.

[55] J. ZHOU, R. J. ADRIAN, S. Balachandar, and T. M. KENDALL. Mechanisms for generating coherent packets of hairpin vortices in channel flow. *J. Fluid Mech.*, 387:353–396, 1999.

Appendix B

Paper II

Assessment of the parcel model in evaporating turbulent diluted sprays within a Large-Eddy-Simulation approach

Jietuo Wang[1], **Francesco Picano**[1,2]

1. Centro di Ateneo di Studi e Attività Spaziali "Giuseppe Colombo" - CISAS,
University of Padova, Padova, PD 35131, Italy
2. Department of Industrial Engineering, University of Padova,
Padova, PD 35131, Italy

In preparation

Abstract: The Eulerian-Lagrangian framework has widely used as a dominant scheme in studying dispersed two-phase flows. This strategy has the advantage of explicitly accounting for the continuum dynamics for carrier flows while simultaneously considering the non-continuum physics of a dispersed phase. However, the computational cost related to this method tracking all particles/droplets could be extremely expensive when an enormous number of particles need to be handled. One approach to alleviate this problem is to simply reduce the total number of dispersed particles/droplets tracked in the simulation. Meanwhile, each computation particle/droplet, often mentioned as *parcel*, is treated as a representative of several particles having same properties, e.g. position and size, in the original simulation. However, systematic analyses investigating its soundness within simulations of turbulent flows bearing evaporating droplets is still missing. To fulfil this lack, we address well-resolved Large-eddy Simulations (LESs) of a turbulent diluted acetone jet-spray considering different ratios of computation droplets to physical droplets, i.e. parcel ratio. By benchmarking against a corresponding fully resolved Direct Numerical Simulation (DNS) and a LES both using the total number of droplets, we show to which extent a high parcel ratio is sufficiently accurate in reproducing statistics of the carrier and transported phases. Our numerical results demonstrated the robustness of parcel concept when the ratio between computational and physical particles is carefully implemented. In particular, a too high parcel ratio would leads to a significant underestimation of the evaporation rate. We found that the appropriate parcel ratio should be of the order of the filter width and dissipative length ratio, so similar to the coarse factor of the Eulerian mesh spacing between a resolved DNS and the LES. The authors believe that the findings showed in the present work may contribute to improve capabilities of current models in accurately and efficiently reproducing the flow physics and droplets dynamics in a wide range of problems with scientific and technical interests.

Keywords: Spray dynamics, Lagrangian modeling, LES, parcel model, droplet evaporation

Introduction

Dispersed two-phase flows are frequently found in daily life and in numerous natural and industrial processes, such as sediment transport in rivers, pollutant transport in the air, fuel injection in engines, and spray driers for food processing. These flows are characterized by a carrier phase laden with a dispersed phase in the form of particles, droplets, or bubbles, in which the two distinguished phases interact mutually exchanging mass, momentum and energy often in turbulent conditions. To investigate dispersed multiphase flows, a range of complementary computational approaches have been implemented[8, 9]. If the dimensional scale of dispersed phase is larger than the smallest scale of the carrier flows, a fully resolved method might be applicable to completely resolve all the scales of the ambient fluid and sub-particle scale necessary to capture the fluid/particle interface. The main restriction of this fully resolved approach is the wide range of length and time scales as well as the particle number seeded into the carrier flow that require huge computational resources often still unavailable [7, 10]. The Eulerian approach treating the collection of particles (hereafter we use "particles" to refer both to particles and droplets) as interpenetrating continuum as the carrier one, on the other hand, relaxes the limitation of computational cost[8, 15]. This approximation might not always provide accurate predictions and is not favorable when the particulate phase with extensive variety of sizes are of interest in the particle-laden flows[19]. When restricting the focus on particles smaller than hydrodynamic scales, the Lagrangian method generally applies a *point-particle approximation* to describe individual particles associated with a number of degree of freedom describing their properties like position, size and velocity[16, 35, 36], especially favorable in the context where the polydispersity of dispersed particles introduces a wide range of time and length scales. Each particle is tracked independently along its trajectory by the algorithm and the interactions between particles and surrounding flows are not resolved which indicates the necessity of models to close the evolution equation of particles Maxey and Riley [23]. The computational cost associated to this approach grows linearly with the number of particles [22].

Along with many advantages offered by the Lagrangian point approach, opportunities for improvement in some aspects exist. For instance, in systems with millions, billions and more particles which are not uncommon, an Eulerian-Lagrangian approach to particle-laden flows could be prohibitively expensive for practical applications. A simple reduction in computational cost could be achieved through representing a group of particles with same properties by a single computational particle[3, 6, 16, 17, 24, 26, 30, 31], which is often referred as a concept of *parcel* in the physical system. This technique consists in a lowering of degree of freedom and is analogous to Eulerian corse graining (increase of mesh size) moving from Direct Numerical Simulation (DNS) to Large-eddy Simulation (LES) in turbulent flows. Since the reduction of tracked particles inevitably leads to estimation error[36], implementing such a method always aims to accurately reproduce the *requested* flow statistics. Increasing the number of computational particles will result in a trade-off relationship between the statistic accuracy of the calculation and the computational time and storage.Aiming to evaluated both the Eulerian and Lagrangian approaches in modeling the turbulent evaporating sprays issued by an air-atomizing injector into a still environment, Mostafa and Mongia [24] analyzed the sensitivity of spray dynamics on the parcel concept by progressively increasing the total amount of computational particles until only 3% difference has accrued when using the optimal number and the next higher one. Amsden et al. [3], in the KIVA-II code, associated the number of real particles to the parcel as a numerical weight in the context of droplet coalescence in sprays, which is still the basis of most engine spray CFD modelling package. Sankaran and Menon [31] tracked 10^5 computational particles in performing LESs of spray combustion, and justified this number as being large enough to obtain accurate droplet statistics. Focusing on simulating a temporal mixing layer laden with evaporating droplets under the Eulerian-Lagrangian framework, Okong'o and Bellan [26] evaluated the capability of LES to reproduce the detailed characteristics of DNS. They considered seven parcels-ratio cases in which one computational particle represented *1, 2, 4, 8, 16, 32, 64* physical droplets, respectively, and two reduced flow filed resolutions, i.e. a grid spacing four/eight times larger than that of the DNS. Different models for resolved source terms and unfiltered *sgs* fluxes were also taken into assessment. They reported a complex dependence relationship between filter size and number of computational droplets when comparing the relative error of modeling the unresolved flow filed with the that of parcel concept. Interestingly, a progressive reduction of the computational droplets leads to deteriorated performance of LES models, and finally the modeling error becomes independent of the filter width. Salewski [30] performed LESs of sprays issued into crossflow with *4,500, 11,000, 28,000, and 54,000* computational evaporating droplets. By examining quantities such as the liquid fractional volume and the drop size distribution, they concluded that no remarkable difference between solutions when the number of droplets was increased beyond 11,000. Radhakrishnan and Bellan [28] suspected that the Salewski [30]'s conclusion might not hold for higher order statistics such as scalar fluxes. To quantify the influence of the computational droplet number and filter width on accurately predicting flow statistics and to identify the optimal number of computational drops that provides minimal error in flow prediction, Radhakrishnan and Bellan [28] performed LESs of a mixing layer with evaporating droplets by increasing the computational droplets with a parcel ratio varying from 8 to 128 of physical particles in conjunction with two different filter width, a fine and a coarse mesh grid. They reported the dependence of the second-order flow statistics on both the computational droplet number and the filter size. In particular, they showed that, in the fine-mesh LES, the number of computational droplets tracked in the simulations could be reduced by a factor of no more than *32* as compared to the correspondent DNS without reducing the accuracy of scalar variance and turbulent vapor flux. The coarse mesh LESs provided reasonably accurately predictions for all computational droplets investigated whereas the fine-mesh LES is not as accurate as the coarse-mesh LES when large representation factor of computational droplets was used. They claimed that the number of drops in a computational cell must not be significantly smaller than that in the DNS. Other recent researches employing the parcel concept focused on the breakup or collision of particles, and can be found in Ref. [2, 4, 5, 21, 25].

Though extensive investigations employing the parcel concept have been implemented, a well-established criterion of choosing the representation factor of parcel/computational droplet is still missing. To cover this lack, we address well-resolved Large-eddy Simulations of a turbulent diluted acetone jet-spray considering different ratios of computation particles to physical particles, i.e. parcel ratio. The numerical tool is a validated MPI parallel code which solves the low-Mach number formulation of Navier-Stokes equations on a cylindrical domain coupled with a Lagrangian solver to deal with the position, velocity, radius and temperature of point-droplets. By benchmarking against a corresponding fully resolved Direct Numerical Simulation (DNS) and a LES both using the total number of droplets, we show to which extent a high parcel ratio is sufficiently accurate in reproducing statistics of the carrier and transported phases.

Numerical Methodology

Formulation

In the present work, a hybrid Eulerian-Lagrangian approach was adopted in the numerical algorithm together with the point droplet approximation, which also account for the mutual impact of dispersed phase and carrier gas phase by employing a two-way coupling framework. The velocity, vapor fraction, temperature and density fields of the gaseous phase are described using an Eulerian approach. The governing equations are solved in cylindrical coordinates in an open environment at constant pressure p_0. Under these hypothesis and after applying the Favre-weighted filtering [18] to the asymptotic low-Mach expansion of the Navier-Stokes system, the governing equations can be written as:

$$\frac{\partial \overline{\rho}}{\partial t} + \frac{\partial \overline{\rho} \tilde{u}_i}{\partial x_i} = \overline{S}_m \,, \tag{1}$$

$$\frac{\partial \overline{\rho} \tilde{u}_i}{\partial t} + \frac{\partial \overline{\rho} \tilde{u}_i \tilde{u}_j}{\partial x_j} = -\frac{\partial \overline{p}}{\partial x_i} + \frac{\partial}{\partial x_j}\left[(\mu_g + \mu_{sgs})\left(\frac{\partial \tilde{u}_i}{\partial x_j} + \frac{\partial \tilde{u}_j}{\partial x_i} - \frac{2}{3}\frac{\partial \tilde{u}_i}{\partial x_i}\delta_{ij}\right)\right] + \overline{S}_{p,i} \,, \tag{2}$$

$$\frac{\partial \overline{\rho} \tilde{Y}_v}{\partial t} + \frac{\partial \overline{\rho} \tilde{Y}_v \tilde{u}_i}{\partial x_i} = \frac{\partial}{\partial x_i}\left(\overline{\rho}(\mathcal{D} + \mathcal{D}_{sgs})\frac{\partial \tilde{Y}_v}{\partial x_i}\right) + \overline{S}_m \,, \tag{3}$$

$$\frac{\partial \tilde{u}_i}{\partial x_i} = \frac{\gamma - 1}{\gamma}\frac{1}{p_0}\left[\frac{\partial}{\partial x_i}\left((\kappa_g + \kappa_{sgs})\frac{\partial \tilde{T}}{\partial x_i}\right) + \overline{S}_e - L_v \overline{S}_m\right] , \tag{4}$$

$$p_0 = \tilde{T}\overline{\rho} R_g \,, \tag{5}$$

where $\overline{\rho}$, $\tilde{u}_i$, $\tilde{Y}_v$, $\tilde{T}$, $\overline{p}$ are the density, velocity, vapor mass fraction, temperature and hydrodynamic pressure fields while μ_g is the dynamic viscosity of the gaseous phase, $\mathcal{D}$ the binary mass diffusion coefficient, κ_g the thermal conductivity of the vapor-air mixture and L_v the latent heat of vaporization of the liquid phase. The gaseous phase is assumed to be governed by the equation of state where $R_g = R/W_g$ is the gas constant of the mixture being W_g its molar mass and R the universal gas constant. The ratio $\gamma = c_{p,g}/c_{v,g}$ is the specific heat ratio of the carrier mixture where $c_{p,g}$ and $c_{v,g}$ the gaseous phase specific heat capacity at constant pressure and volume, respectively. The subgrid-scale terms of the Navier-Stokes equations are described using the classical Smagorinsky model [33]:

$$\mu_{sgs} = \overline{\rho}(C_s \Delta)^2 \left\| \frac{1}{2}\left(\frac{\partial \tilde{u}_i}{\partial x_j} + \frac{\partial \tilde{u}_j}{\partial x_i}\right)\right\| , \tag{6}$$

where C_s is a model constant (0.12 in our setup) and $\Delta = [(r\Delta_\theta)\Delta_r \Delta_z]^{1/3}$ is the typical cell size. For the other subgrid-scale fluxes, $\mathcal{D}_{sgs}$ and κ_{sgs}, we adopt the gradient model [32] and their values are assumed proportional to the Smagorinsky eddy-viscosity with a constant turbulent Schmidt and Prandtl numbers equal to $Sc_t = 0.7$ and $Pr_t = 0.7$, respectively.

The effects of the dispersed phase on the gaseous phase are accounted for by three sink-source terms, $\overline{S}_m$, $\overline{S}_{p,i}$ and $\overline{S}_e$:

$$\overline{S}_m = \frac{PR}{\Delta^3}\sum_{k=1}^{n_d} -\frac{dm_k}{dt}\delta(x_i - x_{k,i}) \,, \tag{7}$$

$$\overline{S}_{p,i} = \frac{PR}{\Delta^3}\sum_{k=1}^{n_d} -\frac{d}{dt}(m_k u_{k,i})\delta(x_i - x_{k,i})\,, \tag{8}$$

$$\overline{S}_{e} = \frac{PR}{\Delta^3}\sum_{k=1}^{n_d} -\frac{d}{dt}(m_k c_l T_k)\delta(x_i - x_{k,i})\,, \tag{9}$$

where $x_{k,i}$, m_k and T_k are position, mass, velocity and temperature of the k-th computational particle while c_l is the liquid specific heat. PR indicates the constant number of physical particles represented by a computational particle. The sum is taken over the entire domain parcel population (being n_d the total number of parcels) and, the delta function expresses that the sink-source terms act only at the domain locations occupied by the parcels. These terms are calculated in correspondence of each grid node by volume-averaging the mass, momentum, and energy sources from all parcels located within the cell volume centered around the considered grid point.

The motion of the dispersed phase is described using a Lagrangian approach. In particular, considering the small size of the droplets, these are treated as small rigid evaporating spheres and are approximated as point-wise particles. In addition, the temperature of the liquid phase is assumed to be uniform inside each droplet. As the volume (and mass) fraction of the liquid phase considered in current work is relatively small, the mutual interactions among droplets (i.e collisions, coalescence of droplets) can be neglected. Besides, the effect of the subgrid-scale terms is not taken into consideration. Hence, only the resolved part of the Eulerian fields is used in the equations of the dispersed phase. With these assumptions, the position, velocity, mass and temperature of the droplets are described by the following equations:

$$\frac{dx_{k,i}}{dt} = u_{k,i}\,, \tag{10}$$

$$\frac{du_{k,i}}{dt} = \frac{(\tilde{u}_i - u_{k,i})}{\tau_k}(1 + 0.15Re_k^{0.687}), \tag{11}$$

$$\frac{dr_k^2}{dt} = -\frac{\mu_g}{\rho_l}\frac{Sh}{Sc}\ln\left(1 + B_m\right), \tag{12}$$

$$\frac{dT_k}{dt} = \frac{1}{3\tau_k}\left[\frac{Nu}{Pr}\frac{c_{p,g}}{c_l}(\tilde{T} - T_k) - \frac{Sh}{Sc}\frac{L_v}{c_l}\ln(1 + B_m)\right]\,, \tag{13}$$

where $x_{k,i}$, $u_{k,i}$, r_k and T_k are the position, velocity, radius and temperature of the k-th droplet while ρ_l is the liquid droplet density, $c_{p,g}$ the specific heat capacity of the gaseous phase at constant pressure and L_v the latent heat of vaporization. The droplet relaxation time, τ_k, and the droplet Reynolds number, Re_k, are defined as:

$$\tau_k = \frac{2\rho_l r_k^2}{9\mu_g}\,, \qquad Re_k = \frac{2\rho_l\|\tilde{u}_i - u_{k,i}\|r_k}{\mu_g}\,, \tag{14}$$

while the Schmidt number, Sc, and Prandtl number, Pr, are computed as:

$$Sc = \frac{\mu_g}{\rho_g D}\,, \qquad Pr = \frac{\mu_g c_{p,g}}{k_g}\,, \tag{15}$$

where μ_g and ρ_g are the dynamic viscosity and density of the gaseous phase while $\mathcal{D}$ is the binary mass diffusion coefficient and κ_g the thermal conductivity. The Sherwood number, Sh, and Nusselt number, Nu, are estimated as a function of the droplet Reynolds number using the Frössling correlations [20]:

$$Sh_0 = 2 + 0.552 Re_k^{1/2} Sc^{1/3}\,, \qquad Nu_0 = 2 + 0.552 Re_k^{1/2} Pr^{1/3}\,. \tag{16}$$

The resulting Sherwood and Nusselt numbers are corrected to account for the Stefan flow [1, 14]:

$$Sh = 2 + \frac{Sh_0 - 2}{F_m}\,, \qquad Nu = 2 + \frac{Nu_0 - 2}{F_t}\,. \tag{17}$$

The coefficients F_m and F_t are computed as follows:

$$F_m = \frac{(1+B_m)^{0.7}}{B_m} H_m\,, \qquad F_t = \frac{(1+B_t)^{0.7}}{B_t} H_t, \tag{18}$$

where H_m and H_t are defined as:

$$H_m = \ln(1+B_m)\,, \qquad H_t = \ln(1+B_t)\,, \tag{19}$$

being B_m and B_t the Spalding mass and heat transfer numbers[34]:

$$B_m = \frac{Y_{v,s} - \tilde{Y_v}}{1 - Y_{v,s}}\,, \qquad B_t = \frac{c_{p,v}}{L_v}(\tilde{T} - T_k)\,, \tag{20}$$

where $\tilde{Y_v}$ and $\tilde{T}$ are the vapor mass fraction and temperature fields evaluated at the droplet position, $Y_{v,s}$ is the vapor mass fraction evaluated at droplet surface and $c_{p,v}$ is the vapor specific heat at constant pressure. The vapor mass fraction at the droplet surface corresponds to the mass fraction of the vapor in a saturated vapor-gas mixture at the droplet temperature. To estimate $Y_{v,s}$, we use the Clausius-Clapeyron relation to first compute the vapor molar fraction, $\mathcal{X}_{v,s}$:

$$\mathcal{X}_{v,s} = \frac{p_{ref}}{p_0} \exp\left[\frac{L_v}{R_v}\left(\frac{1}{T_{ref}} - \frac{1}{T_k}\right)\right]\,, \tag{21}$$

where p_{ref} and T_{ref} are arbitrary reference pressure and temperature and $R_v = R/W_l$ is the vapor gas constant. The saturated vapor mass fraction is then computed using the relation:

$$Y_{v,s} = \frac{\mathcal{X}_{v,s}}{\mathcal{X}_{v,s} + (1 - \mathcal{X}_{v,s})\dfrac{W_g}{W_l}}\,, \tag{22}$$

where W_g and W_l are are the molar mass of the gaseous and liquid phases.

Tool and Simulation Setup

The numerical tool, CYCLON[12, 14, 27, 29, 38], is a validated MPI parallel code which consists of two different modules: i) an Eulerian module that solves the governing equations for the gaseous phase (density, velocity, vapor mass fraction and temperature); ii) a Lagrangian module that solves the equations governing the droplet dynamics (position, velocity, mass and temperature). In particular, the governing equations of the gaseous phase are discretized in space using a second-order central finite differences scheme and they are time advanced using a low-storage third-order Runge-Kutta scheme. Likewise, the governing equations of the Lagrangian phase are time integrated using the same Runge-Kutta scheme, and a second-order accurate polynomial interpolation is used to evaluate the Eulerian quantities at the droplet position. More details, benchmarks and tests can be found in [12–14, 38].

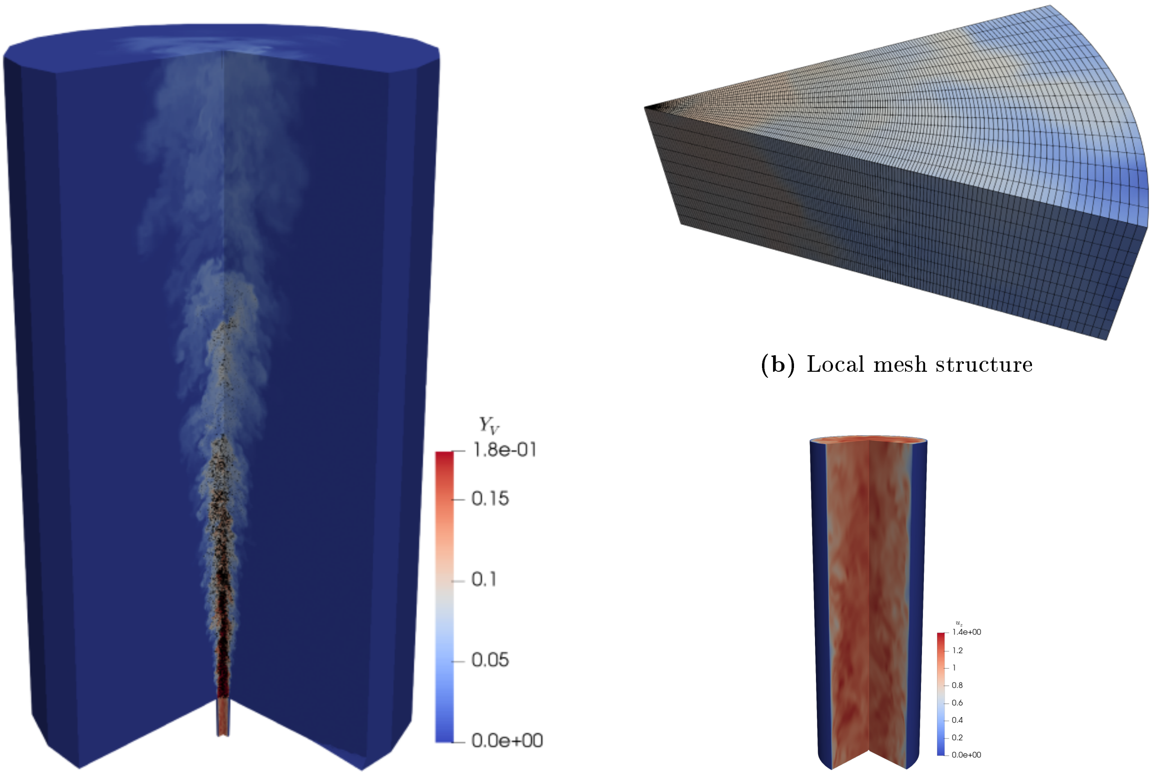

(a) 3D cylindrical domain

(b) Local mesh structure

(c) 3D pipe flow

Figure 1: (a) A sketch of the 3D cylindrical domain where a representative ensemble of the whole droplet population is plotted with black points. (b) A local sector of the mesh structure centered at $z/R = 20$. (c) The turbulent periodic pipe. The colors contour the vapor mass fraction field, Y_v, within the jet and the axial instantaneous velocity, U_z, of the turbulent pipe, respectively[38].

The computational domain, Fig. (1), is a cylinder into which the turbulent jet bearing acetone droplets is injected through a circular orifice of radius $R = 4.9 \times 10^{-3}\ m$ located at the centre of the bottom base. The cylinder dimensions are $L_\theta \times L_r \times L_z = 2\pi \times 20R \times 70R$ along the azimuthal (θ) radial (r) and axial (z) directions. The domain is discretized using a staggered grid with $N_\theta \times N_r \times N_z = 48 \times 54 \times 288$ grid points, which is obtained reducing by a factor 4 in each direction the grid points of the corresponding DNS mesh[38]. The pipe domain, which extends for $2\pi \times 1R \times 6R$ in the azimuthal, θ, radial, r and axial, z,directions, is discretized containing $N_\theta \times N_r \times N_z = 48 \times 22 \times 32$ nodes in order to match the corresponding jet computational grid at the pipe discharge. A convective boundary condition is adopted on the outlet section located on the upper face of the cylindrical domain. An adiabatic, traction-free boundary condition is prescribed at the side boundary of the domain making the entrainment of external fluid possible. The latter, in the present case, consists of dry air. Time-dependent and fully turbulent boundary conditions are prescribed on the inflow section by employing a companion DNS reproducing a fully-developed, periodic pipe flow. A fully turbulent velocity field is assigned on the jet inflow by a Dirichlet condition. This two-dimensional field is computed on a cross-sectional slice of the turbulent pipe. Excluding the circular inflow, the remaining part of the domain base is impermeable and adiabatic.

Table 1: Thermodynamic and physical properties of acetone and dry air.

R_0	0.0049[m]	W_g	0.029[kg/mol]
p_0	101300[Pa]	W_l	0.0581[kg/mol]
T_0	275.15[K]	k_g	0.0243[W/(m · K)]
μ	1.75 E-5[kg/(m · s]	k_l	0.183[W/(m · K)]
$c_{p,g}$	1038[J/(kg · K)]	D	1.1E-5[m^2/s]
$c_{p,v}$	1300[J/(kg · K)]	ρ_l	800[kg/m^3]
c_l	2150[J/(kg ·K)]	L_v	530000[J/kg]
U_0	13.9[m/s]	r_d	6E-6[m]
t_0	3.5E-4[s]		

The present work reproduces the dynamics of liquid acetone droplets dispersed within a turbulent air-acetone vapor jet with a LES approach. The gas-vapor mixture is injected into an open environment through an orifice of radius $R = 5 \times 10^{-3} m$ at a bulk velocity $U_0 = 13.9 m/s$. Liquid acetone mono-disperse phase with an initial radius $r_{d,0} = 6 \mu m$ are randomly distributed over the inflow section. The ambient pressure is set to $p_0 = 101300 Pa$ while the injection temperature is fixed to $T_0 = 275.15 K$ for both the droplets and carrier mixture. The injection flow rate of the gaseous phase is kept constant fixing a bulk Reynolds number $Re = 2U_0 R/\nu = 10000$, with $\nu = 1.35 \times 10^{-5} m^2/s$ the kinematic viscosity. At the inflow section a nearly saturated condition is prescribed for the air-acetone vapor mixture, $S = Y_v/Y_{v,s} = 0.99$, with Y_v the actual vapor mass fraction and $Y_{v,s}(p_0, T_0)$ the vapor mass fraction saturation level evaluated at the actual inflow temperature and thermodynamic pressure. The acetone mass flow rate is set by the mass flow rate ratio $\Phi = \dot{m}_{act}/\dot{m}_{air} = 0.28$, with $\dot{m}_{act} = \dot{m}_{act,l} + \dot{m}_{act,v}$ the sum of liquid and vapor acetone mass flow rates and $\dot{m}_{air}$ the gaseous one. The correspondent bulk volume fraction of the liquid phase is set to $\Psi = 8 \times 10^{-5}$, as previously mentioned. All the thermodynamic and physical properties of the vapor, gas, and liquid phases are reported in Table I. The thermodynamic conditions at the inlet are comparable to that adopted in the well-controlled experiments on dilute coaxial sprays published by the group of Chen et al. [11].

Results and Discussion

We performed a total of six LES simulations adopting the constant parcel ratio (PR) ranging within *1, 4, 16, 64, 256, 1024* which are compared also against a corresponding DNS dataset [38]. All the statistics presented in the following are computed considering around 100 samples separated in time by $R/U_0 = 1$ after reaching a statistical steady condition for the two-phase evaporating flows.

Fig. 2 shows a comparison of the instantaneous fields of vapour mass fraction and the instantaneous droplet distribution between the benchmarking DNS and LESs with *PR = 1, 64, 1024*. It can be seen that, despite small vortical structures of the flow fields not being capably captured in LES cases, the general appearance of levels and structures in all panels looks quite close to each other with no significant deviation between three LESs and the DNS data. The apparent clusters

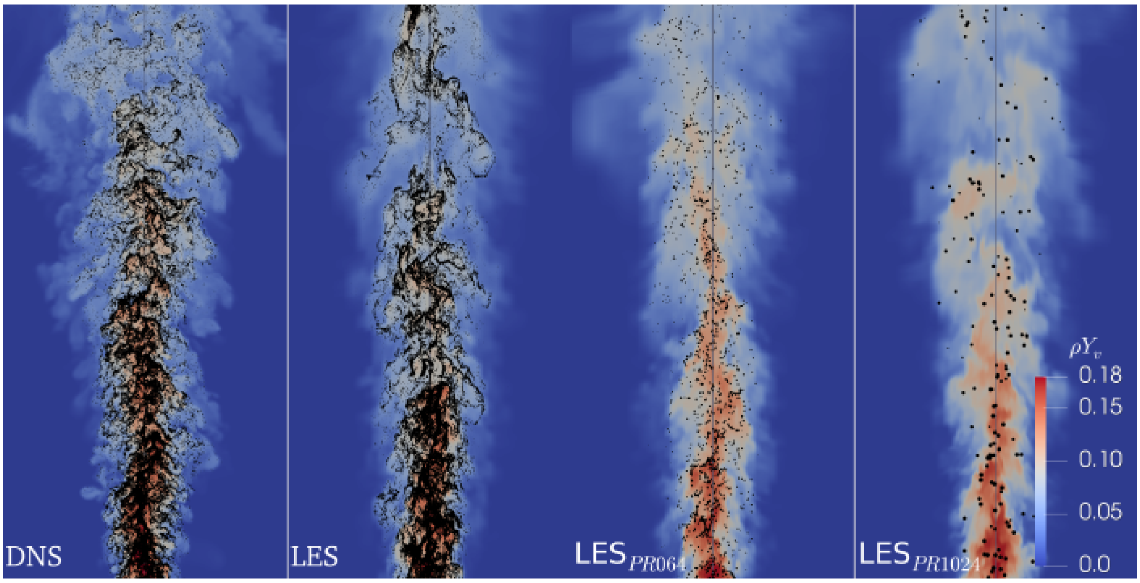

Figure 2: Radial-axial slices of turbulent sprays for DNS and LESs results.The black points represent a subset of the whole droplet population constituted by droplets located within a distance h/R = 0.1 from the slice plane. Each point size in the 1st and 2nd panels is proportional to the corresponding droplet radius (scale factor 100) whereas appropriate enlargements are applied for size of points in 3rd and 4th panels in order to better visualization. The carrier phase is contoured according to the instantaneous vapor mass fraction field, Y_v, which is bounded between 0 and 0.18, the former corresponding to the totally dry air condition and the latter to the 99% saturation level prescribed at inlet. For perspicuity reasons, simulation results with PR = *1, 64, 1024* are showed here.

of evaporating droplets (black points) showed in the DNS panel strongly correlate with regions of high vapour concentration[38], which appears successfully reproduced by the LES case with all physical droplets although at large scales. Moreover, the highly spatial nonuniform distribution of Lagrangian droplets appears progressively missing when a higher PR is adopted, potentially leading to numerical errors as suggested in [36].

As it is less meaningful to compare the instantaneous distribution of single realizations of LESs, more insights about the parcel model can be gained from the statistical moments, e.g. average, joint probability distribution function (JPDF). In Fig. 3a, we compare the average distribution of liquid mass fraction, $\langle\Phi\rangle$, between the benchmarking DNS and LESs with different PRs. The mass fraction is defined as $\Phi = m_l/m_g$, where m_l and m_g are the mass of liquid acetone and of the gaseous phase evaluated inside each mesh cell. A spray vaporization length is defined as the axial distance from the inlet section to where the droplets/parcels lost 99% of their initial mass averagely[14, 37]. According to this definition, the vaporization process completes at about $z/R \sim 52$, $z/R \sim 51$, $z/R \sim 52$, $z/R \sim 50$, $z/R \sim 53$, and $z/R \sim 60$ for LESs with increasing PR whereas the benchmarking DNS is around $z/R \sim 50$. The vaporization length of the LES with highest PR is about 20% longer than that of the benchmarking DNS which is closely predicted by other PR cases. This is because as more physical droplets are represented by a parcel, fewer parcels are available in each cell to form the mesh-based average statistics. Hence, statistical errors, which is inversely proportional to the square root of particle number per cell, would increase[36]. Meanwhile, in LES cases with high PR, each parcel in a cell may impose on carrier flows excessive sources leading to localized regions with high vapor concentrations which eventually slows down the evaporation process of parcels. An additional comparison of the spatial distribution of the average liquid mass fraction is provided in

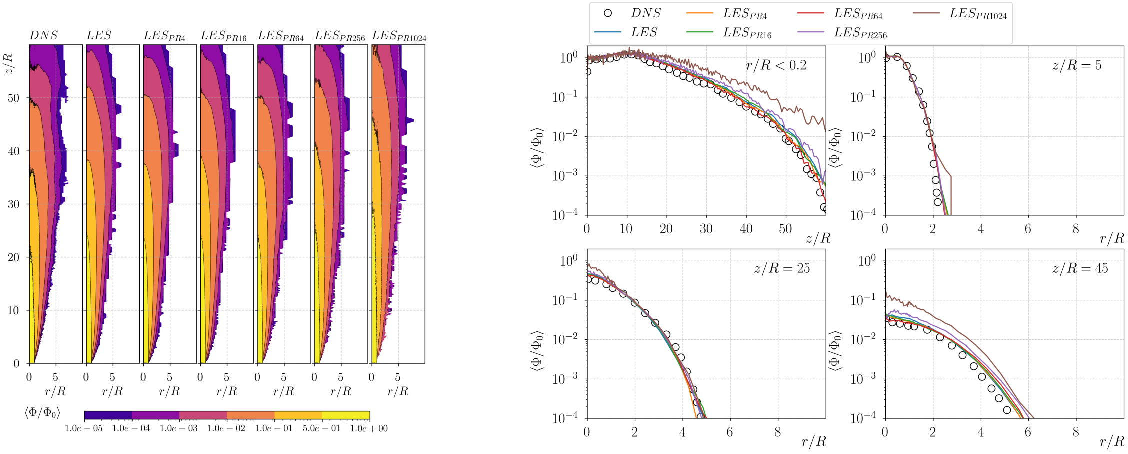

(a) **(b)**

Figure 3: (a)Mean liquid mass fraction, $\Phi = m_l/m_g$ normalized by the initial value Φ_0, where m_l and m_g are the mean mass of liquid acetone and air inside each mesh cell, respectively. (b) shows the Φ distribution along center axis and three different z/R positions. (Both DNS and LESs with different parcel ratio are present)

Fig. 3b, where the center-line mean liquid mass fraction, as well as the radial distribution at three different axial positions, i.e. $z/R = 5, 25, 45$, are displayed. It is evident that, for all cases presented, the general trend is the same. For instance, in the center-line plot that the liquid mass fraction increases along the jet-axis from the inflow section up to a peak located at $z/R \simeq 11$. Further downstream, Φ reduces along the jet-axis until droplets/parcels completely evaporate. However, significant deviations based on the benchmarking DNS results appear in intermediate- and far-fields if a large *PR* is adopted, i.e. *PR= 256 & 1024* in the present work. Far from the origin all the errors induced by the parcel representation can sum up and appear as inaccurate statistics.

To assess Lagrangian statistics of evaporating droplets/parcels, in Fig. (4a-4g), we provide the Joint Probability Density Function (*JPDF*) of the normalized droplet square diameter, $d_d^2/d_{d,0}^2$, and normalized flight time, t_f/t_0 for the benchmarking DNS and LESs at different *PRs*. In each subfigure, conditioned average as also reported: The mean square droplet diameter as a function of the flight time, $\langle d_d^2/d_{d,0}^2\rangle(t/t_0)$, and the mean droplet flight time as a function of the square droplet diameter, $\langle t/t_0\rangle(d_d^2/d_{d,0}^2)$ which are directly extracted from the JPDF statistics. Although the two quantities are strictly related, their meaning is different. The mean square diameter conditioned to the flight time provides the mean square diameter of droplets given a fixed flight time, e.g. after a fixed time since droplet injection. On the other hand, the mean flight time at a given mean square diameter provides the amount of time needed, on average, by the droplets to reach a given size. As shown in the Fig. (4a-4g) all LES results show a consistent trend as the benchmarking DNS does, whereas both the contour map and plots shift rightward by increasing the *PR* value, indicating a slower evaporation process when large *PR* is used. This could be attributed to the error induced both from LES and from the parcel ratio. The former can be quantified by the LES with all droplets ($PR = 1$). Concerning the latter, when too less parcels are present in the simulation domain, the proper non-uniform distribution behaviors of dispersed droplets could not be reproduced, e.g. clustering. In addition, as previously discussed, the coupling source terms imposed on the carrier flows can suddenly saturate local vapour phase in a computational cell at high *PR*. To better quantify the influence of parcel model on the average fate of droplets, we extract both

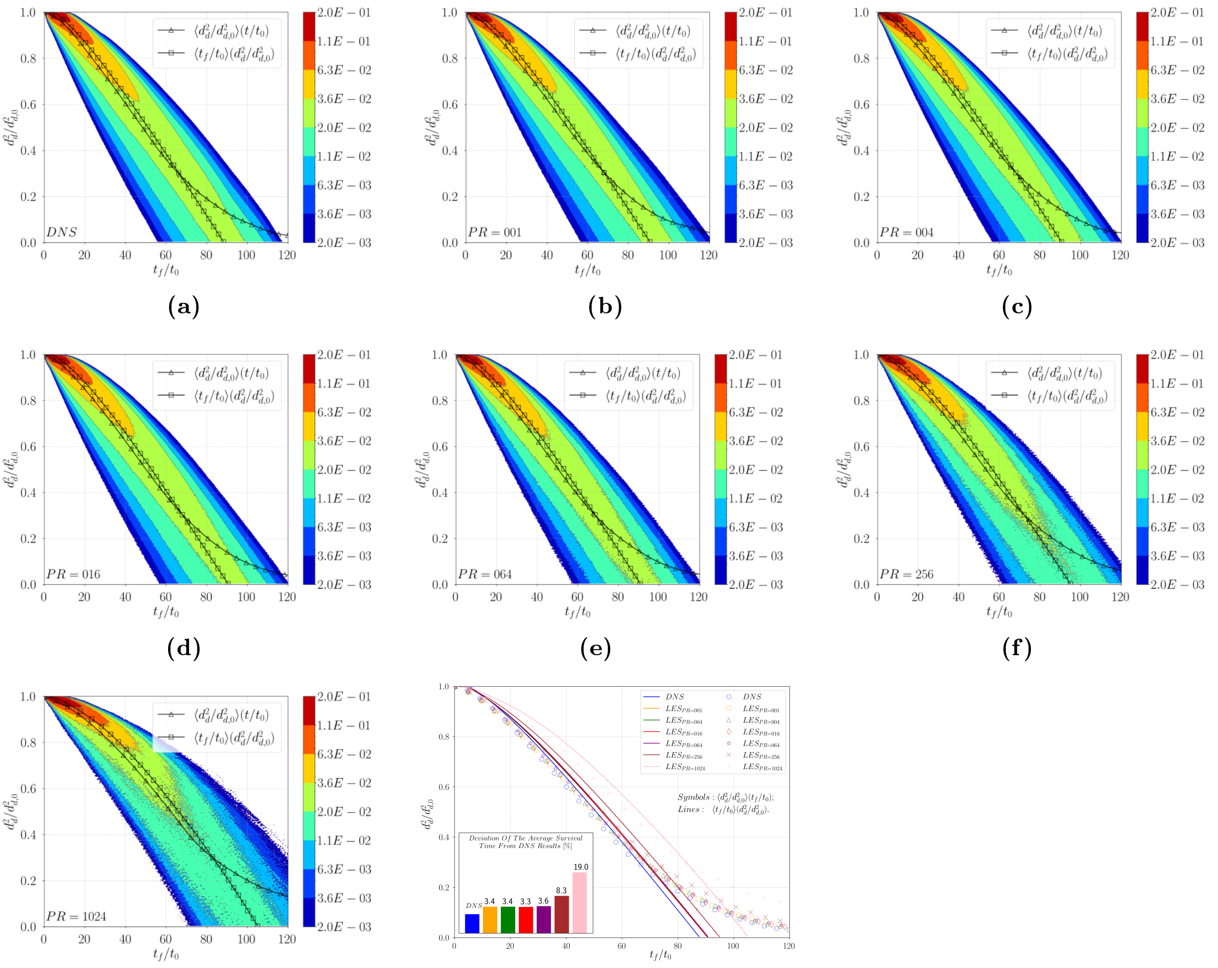

(a) **(b)** **(c)**

(d) **(e)** **(f)**

(g) **(h)**

Figure 4: (a-g) shows JPDF of the normalized droplet square diameter, $d_d^2/d_{d,0}^2$, and normalized flight time, t_f/t_0 for benchmarking DNS and LESs with different PRs. The mean square droplet diameter as a function of the flight time, $\langle d_d^2/d_{d,0}^2\rangle(t/t_0)$, and the mean droplet flight time as a function of the square droplet diameter, $\langle t/t_0\rangle(d_d^2/d_{d,0}^2)$,are also displayed for each case. (h) shows comparisons of both $\langle d_d^2/d_{d,0}^2\rangle(t/t_0)$ and $\langle t/t_0\rangle(d_d^2/d_{d,0}^2)$.

conditional quantities from each figure and show comparisons in Fig. 4h. The inset panel reports the relative deviation of the average survival time for parcels from each LES case based on the DNS restuls. It is clear that a robust result can be achieved with PR up to *64* where the error appears unaffected by PR, while increases at higher PR.

We aim to remark that the reduction the degree of freedom from DNS to LES, i.e. the overall reduction of cell number is 64. Hence, we propose as criterion that the Parcel Ratio PR should scales with the Eulerian reduction of the degree of freedom, and so with the mesh size global coarsening. This criterion can be generalized considering that the typical mesh size in DNS Δ_{DNS} is of the order of the dissipative Kolmogorov length η, so $PR \leq \Delta_{LES}/\Delta_{DNS} \simeq PR \leq \Delta_{LES}/\eta$. In other words, in a general LES approach the parcel ratio should be set evaluating the ratio between typical mesh size Δ_{LES} over the typical dissipativel Kolmogorov length η.

Conclusion

The computational cost related to Lagrangian method tracking all particles/droplets could be extremely expensive when an enormous number of particles/droplets need to be handled in two-phase fluid system. One approach to alleviate this problem is to simply lower the total number of dispersed particles tracked in the simulation by representing a cluster of droplet having same properties with a computational particle, also called parcel. In this paper, we address the well-resolved Large-eddy Simulations (LESs) of a turbulent diluted acetone jet-spray considering different ratios of computation particles to physical particles, i.e. parcel ratio.

All thermodynamical and physical properties as well as simulation parameters in this work are the same as that in a corresponding DNS [38], except for a coarse mesh dedicated to the LES approach and the parcel concept. In particular, the cylindrical domain is discretized by a coarse factor 4 in each direction the grid points of the corresponding DNS mesh reported in [38]. To assess the robustness of the parcel concept, five parcel ratios were used together with a case presenting all physical particles, namely PR = 1, 4, 16, 64, 256, and 1024. By benchmarking against the corresponding fully resolved DNS and the LES with the total number of droplets, the present work showed to which extent the parcel ratio does not cause a significant change in statistics of the gasesous and droplet phases.

Numerical results demonstrated the robustness of parcel concept when the ratio between computational and physical particles is carefully implemented. In particular, an appropriate parcel ratio, which keeps same number of computational particle per cell as its DNS counterpart, e.g. 64 in the present work, could provide robust results on mean statistics of droplets. From this information we extrapolate a criterion that in a general LES approach the parcel ratio should be set of the order of the ratio between typical mesh size Δ_{LES} over the typical dissipative Kolmogorov length η. Further increasing the parcel ratio would lead to a significant underestimation of the mean behaviors of droplets evaporation for two reasons which are the statistical errors introduced by grid-based estimate of average field variables, and the inaccurate spatial distribution of parcels. We believe that the findings showed in the present study may contribute to improve capabilities of current models in accurately and efficiently reproducing the flow physics and particle dynamics in a wide range of problems with scientific and technical interests.

Bibliography

[1] B. Abramzon and W. A. Sirignano. Droplet vaporization model for spray combustion calculations. *Int. J. Heat Mass Transf.*, 32(9):1605–1618, 1989.

[2] Falah Alobaid. A particle–grid method for euler–lagrange approach. *Powder Technology*, 286: 342–360, 2015.

[3] A. A. Amsden, P. J. O'Rourke, and T. D. Butler. Kiva-ii: A computer program for chemically reactive flows with sprays.

[4] S. V. Apte, M. Gorokhovski, and P. Moin. Les of atomizing spray with stochastic modeling of secondary breakup. *Int. J. Multiph. Flow*, 29(9):1503–1522, 2003.

[5] Sourabh V. Apte, Krishnan Mahesh, Michael Gorokhovski, and Parviz Moin. Stochastic modeling of atomizing spray in a complex swirl injector using large eddy simulation. *Proc. Combust. Inst.*, 32(2):2257–2266, 2009.

[6] SV Apte, Mikhael Gorokhovski, and Parviz Moin. Les of atomizing spray with stochastic modeling of secondary breakup. *International Journal of Multiphase Flow*, 29(9):1503–1522, 2003.

[7] Mehdi Niazi Ardekani, Pedro Costa, Wim Paul Breugem, and Luca Brandt. Numerical study of the sedimentation of spheroidal particles. *International Journal of Multiphase Flow*, 87: 16–34, 2016.

[8] S. Balachandar and John K. Eaton. Turbulent dispersed multiphase flow. *Annu. Rev. Fluid Mech.*, 42(1):111–133, 2010.

[9] Luca Brandt and Filippo Coletti. Particle-laden turbulence: Progress and perspectives. *Annual Review of Fluid Mechanics*, 54, 2021.

[10] Tristan M Burton and John K Eaton. Fully resolved simulations of particle-turbulence interaction. *Journal of Fluid Mechanics*, 545:67–111, 2005.

[11] Yung-Cheng Chen, Sten H. Stårner, and Assaad R. Masri. A detailed experimental investigation of well-defined, turbulent evaporating spray jets of acetone. *Int. J. Multiph. Flow*, 32(4):389–412, 2006.

[12] P. P. Ciottoli, F. Battista, R. Malpica Galassi, F. Dalla Barba, and F. Picano. Direct numerical simulations of the evaporation of dilute sprays in turbulent swirling jets. *Flow Turbulence Combust.*, 106(3):993–1015, 2021.

[13] F. Dalla Barba, J. Wang, and F. Picano. Revisiting d2-law for the evaporation of dilute droplets. *Phys. Fluids*, 33(5):051701, 2021.

[14] Federico Dalla Barba and Francesco Picano. Clustering and entrainment effects on the evaporation of dilute droplets in a turbulent jet. *Phys. Rev. Fluids*, 3(3):034304, 2018.

[15] OA Druzhinin and S Elghobashi. Direct numerical simulations of bubble-laden turbulent flows using the two-fluid formulation. *Physics of Fluids*, 10(3):685–697, 1998.

[16] J. K. Dukowicz. A particle-fluid numerical model for liquid sprays. *J. Comput. Phys.*, 35(2): 229–253, 1980.

[17] S. Elghobashi. On predicting particle-laden turbulent flows. *Appl. Sci. Res.*, 52(4):309–329, 1994.

[18] A. Favre. Turbulence: Space-time statistical properties and behavior in supersonic flows. *Phys. Fluids*, 26(10):2851, 1983.

[19] Rodney O Fox, Frédérique Laurent, and Marc Massot. Numerical simulation of spray coalescence in an eulerian framework: direct quadrature method of moments and multi-fluid method. *Journal of Computational Physics*, 227(6):3058–3088, 2008.

[20] N. Froessling. On the evaporation of falling drops. *Army Biological Labs Frederick MD*, 1968.

[21] Perry L. Johnson. Predicting the impact of particle-particle collisions on turbophoresis with a reduced number of computational particles. *Int. J. Multiph. Flow*, 124:103182, 2020.

[22] Perry L Johnson. Predicting the impact of particle-particle collisions on turbophoresis with a reduced number of computational particles. *International Journal of Multiphase Flow*, 124: 103182, 2020.

[23] M. R. Maxey and J. J. Riley. Equation of motion for a small rigid sphere in a nonuniform flow. *Phys. Fluids*, 26(4):883, 1983.

[24] AA Mostafa and HC Mongia. On the modeling of turbulent evaporating sprays: Eulerian versus lagrangian approach. *International Journal of Heat and Mass Transfer*, 30(12):2583–2593, 1987.

[25] D. D. Joseph N.A. Patankar. Modeling and numerical simulation of particulate fows by the eulerian-lagrangian approach. *Int. J. Multiph. Flow*, 27(10):1659–1684, 2001.

[26] Nora A Okong'o and Josette Bellan. Consistent large-eddy simulation of a temporal mixing layer laden with evaporating drops. part 1. direct numerical simulation, formulation and a priori analysis. *Journal of Fluid Mechanics*, 499:1–47, 2004.

[27] F. Picano, G. Sardina, P. Gualtieri, and C. M. Casciola. Anomalous memory effects on transport of inertial particles in turbulent jets. *Phys. Fluids*, 22(5):051705, 2010.

[28] Senthilkumaran Radhakrishnan and Josette Bellan. Influence of computational drop representation in les of a mixing layer with evaporating drops. *Computers & fluids*, 58:15–26, 2012.

[29] G. Rocco, F. Battista, F. Picano, G. Troiani, and C. M. Casciola. Curvature effects in turbulent premixed flames of h2/air: a dns study with reduced chemistry. *Flow Turbulence Combust.*, 94 (2):359–379, 2015.

[30] Mirko Salewski. *LES of jets and sprays injected into crossflow*. Lund University, 2006.

[31] Vaidyanathan Sankaran and Suresh Menon. Les of spray combustion in swirling flows. *Journal of Turbulence*, 3(1):011, 2002.

[32] Helmut Schmidt and Ulrich Schumann. Coherent structure of the convective boundary layer derived from large-eddy simulations. *J. Fluid Mech.*, 200:511–562, 1989.

[33] J. Smagorinsky. General circulation experiments with the primitive equations. *Mon. Wea. Rev.*, 91(3):99–164, 1963.

[34] D. B. Spalding. Combustion of liquid fuels. *Nature*, 165(4187):160, 1950.

[35] Kyle D Squires and John K Eaton. Particle response and turbulence modification in isotropic turbulence. *Physics of Fluids A: Fluid Dynamics*, 2(7):1191–1203, 1990.

[36] Shankar Subramaniam. Lagrangian–eulerian methods for multiphase flows. *Prog. Energy Combust. Sci.*, 39(2-3):215–245, 2013.

[37] Jietuo Wang, Mobin Alipour, Giovanni Soligo, Alessio Roccon, Marco de Paoli, Francesco Picano, and Alfredo Soldati. Short-range exposure to airborne virus transmission and current guidelines. *Proc. Natl. Acad. Sci. U.S.A*, 118(37), 2021.

[38] Jietuo Wang, Federico Dalla Barba, and Francesco Picano. Direct numerical simulation of an evaporating turbulent diluted jet-spray at moderate reynolds number. *Int. J. Multiph. Flow*, 137:103567, 2021.

Appendix C

Paper III

Short-range exposure to airborne virus transmission and current guidelines

Jietuo Wang[1], Mobin Alipour[2,4], Giovanni Soligo[3], Alessio Roccon[2,4], Marco De Paoli[2], Francesco Picano[1,5], Alfredo Soldati[2,4]

1. Centro di Ateneo di Studi e Attività Spaziali "Giuseppe Colombo" - CISAS, University of Padova, 35131, Padova, Italy
2. Institute of Fluid Mechanics and Heat Transfer, TU Wien, Vienna, 1060, Austria
3. Complex Fluids and Flows Unit, OIST, 1919-1 Tancha, Onna-son, Okinawa 904-0495, Japan
4. Polytechnic Department, University of Udine, 33100, Udine, Italy
5. Department of Industrial Engineering, University of Padova, 35131, Padova, Italy

Proceedings of the National Academy of Sciences of the United States of America, 2021, 118 (37), e2105279118

Abstract: After the Spanish flu pandemic, it was apparent that airborne transmission was crucial to spreading virus contagion, and research responded by producing several fundamental works like the experiments of Duguid [J. Hyg. 44:6, 1946] and the model of Wells [Am. J. Hyg., 20:611–18,1934]. These seminal works have been pillars to past and current guidelines published by health organizations. However, in about one century, understanding of turbulent aerosol transport by jets and plumes has enormously progressed and it is now time to use this body of developed knowledge. In this work, we use detailed experiments and accurate computationally-intensive numerical simulations of droplet-laden turbulent puffs emitted during sneezes in a wide range of environmental conditions. We consider the same emission – number of drops, drop size distribution and initial velocity – and we change environmental parameters as temperature and humidity, and we observe strong variation in droplets evaporation or condensation in accordance with their local temperature and humidity microenvironment. We assume that 3% of the initial droplet volume is made of non-volatile matter. Our systematic analysis confirms that droplets lifetime is always about one order of magnitude larger compared to previous predictions, in some cases up to 200 times. Finally, we have been able to produce original virus exposure maps, which can be a useful instrument for health scientists and practitioners to calibrate new guidelines to prevent short-range airborne disease transmission.

Keywords: COVID-19, airborne, infectious disease, SARS-CoV-2, public health

Introduction

Respiratory viruses can be transmitted among human subjects via three main routes. First, direct contact and fomites, where a healthy individual comes into direct contact with an infected person (direct contact) or touches a contaminated surface (fomites). Second, through the droplet transmission that occurs in the proximity of an infected person, who exhales large and small respiratory droplets containing the virus. Third, through the airborne transmission of smaller droplets and particles (droplet nuclei), which remain airborne over a much longer time, traveling farther distances than droplet transmission. While the latest research suggests that direct contact and fomites are unlikely to be a major source of infection for SARS-CoV-2 [20, 25], understanding the role played by the latter two contributions is crucial to design effective guidelines for pathogens transmission prevention.

Conventionally, and according to WHO guidelines [58], droplets larger than 5 μm in diameter are referred to as respiratory droplets (droplet transmission), while those smaller than 5 μm in diameter are defined as droplets nuclei (airborne transmission). This threshold has been widely used to define public health guidelines and to design infection control interventions for healthcare workers [10]. The current pandemic, however, highlighted the limitations of these guidelines and made it clear that new research should be embraced to revise these recommendations. Indeed, the threshold used to distinguish between droplet transmission and airborne transmission and its scientific rationale are highly questionable [56, 60]: the aerodynamic behavior of droplets, ballistic for respiratory droplets and aerosol-like for droplet nuclei, strongly depends on the local flow conditions. Recent works suggest that a much larger threshold (100 μm) [17, 54] better differentiates between large and small droplets dynamics. Likewise, the better understanding of turbulence gained in the last 50 years, has shown how the evaporation process is extremely complex [13, 21, 31] and cannot be captured with simplified models, like those employed by Wells [55]. Finally, from a medical perspective, it is evident how the distinction between large droplets and small droplets (airborne) diseases and its connection with the short- and long-range transmission is rather weak and for many respiratory infections the predominant route depends on the specific setting [35, 48].

A key step towards understanding the routes of pathogens transmission must rely on the study of the fluid dynamics as it plays a crucial role in almost every aspect of disease spreading [31, 40]. Thanks to recent experimental and numerical advancements, we can have access to detailed time- and space-resolved quantities. In this work, using the most recent experimental and numerical methodologies, we investigate the evaporation and dispersion dynamics of the respiratory droplets released during a sneeze in four different ambient conditions (temperature and relative humidity). Although sneezing is not a known symptom of covid-19, it can significantly contribute to the spreading of diseases as it is a powerful event that generates thousand of virus-laden droplets and which is also common of many diseases and allergies [15]. Then, building on these results, and using virological data, we evaluate the transport of the viral copies providing graphical visualizations of the infection risk at close distance from an infected subject. Our findings suggest that predictions based on the models adopted in current guidelines are largely unsatisfactory, leading to a dangerous underestimation of the infection risk. In particular, current guidelines underestimate the infectious potential associated with the short-range airborne route [12, 26, 60], i.e. the infection risk associated with small droplets and droplet nuclei that remain airborne in the proximity of an infected individual and that may readily penetrate and deposit in the upper and lower respiratory tract [52].

Materials and Methods

We summarize here the numerical and experimental methodologies used. Further details on the numerical method, experimental setup and additional tests can be found in *SI Appendix.*

Simulations

The numerical simulations are based on an hybrid Eulerian-Lagrangian framework [53]. An Eulerian Large-Eddy-Simulation approach is used to describe the velocity, density, vapor and temperature fields, while the motion, mass and temperature of the droplets are described using a Lagrangian approach. The computational domain consists of a horizontal cylinder into which the droplet-laden sneezing jet is injected via a circular orifice of radius $R = 1\ cm$ that mimics the mouth opening [22]. The cylinder has dimensions $L_\theta \times L_r \times L_z = 2\pi \times 150R \times 300R = 2\pi \times 150\ cm \times 300\ cm$ along the azimuthal, radial and axial directions. A total mass of liquid equal to $m_l = 8.08 \times 10^{-6}\ kg$ is ejected together with the sneezing jet. The resulting volume fraction is $\Phi_v = 4.55 \times 10^{-6}$, in agreement with previous measurements [6, 14]. The inflow velocity profile is obtained from a gamma-probability-distribution function [8] and the overall duration of the injection stage is about 0.6 seconds. The jet has a temperature of $T_j = 308\ K$ and a relative humidity equal to $RH_j = 90\%$ [6, 19, 32], while its peak velocity is $u_{z,j} = 20\ m/s$ [7, 59]. Please note that in the simulation used to compare numerical and experimental results, we consider a jet having the same temperature and humidity of the ambient. For the liquid phase, for each respiratory droplet, its initial diameter is assumed to follow a log-normal distribution with geometric mean equal to 12 μm and geometric standard deviation equal to 0.7 [5]. The ambient is assumed quiescent and characterized by a uniform temperature and relative humidity and constant thermodynamic pressure. We consider four ambient conditions: two temperatures, $T = 5\ °C$ and $T = 20\ °C$, and two relative humidities, $RH = 50\%$ and $RH = 90\%$. To simulate the presence of non-volatile elements such as salt, protein and pathogens in the respiratory liquid [51], the minimum size that a droplet can attain has been limited to 3% of the initial volume ($\simeq$ 30% of the initial diameter) [5, 11, 46, 47]. Additional simulations, which detailed discussion can be found in the *SI Appendix*, have been also performed to test the results sensitivity to multiple sneezing events and initial droplet size distribution.

Experiments

The experimental setup has been designed to obtain a repeatable droplets-laden jet having properties (jet duration, flow rate) analogous to those considered in the numerical simulations. To prevent exposure of human beings to the potentially harmful laser light, a dummy head is used. The flow is generated by a compressor-based system and is controlled with the aid of an electromagnetic valve. The air stream is seeded with non evaporating, tracer-like droplets (average size 2 μm, Stokes number $St \ll 1$) and finally emitted through a circular opening (radius $R = 1\ cm$) located on the front of the head. The seeding solution is kept at ambient temperature. We observed that the droplets remain suspended in the ambient for long time, without any apparent effect of sedimentation. We performed 94 experiments, consisting of a series of 7 recordings with high speed cameras and 87 velocity measurements with hot-wire anemometry. Further experiments, not listed above and discussed in *SI Appendix*, have been performed to analyse the effect of face-covering devices. All the experiments are performed in the same flow conditions (fluids temperature, jet duration, flow velocity). We use high-speed imaging system (acquisition rate 0.8 kHz) to record the evolution of the flow on a 4 mm thick vertical plane. The main components of the imaging system are a double-pulse laser (25 mJ per pulse), and a high-speed camera (sensor size of 2560×1600 pixel at 0.8 kHz) looking perpendicularly to the laser sheet and located at a distance of 2 m from the laser plane. The droplet distribution (see inset panels in figure 1) is processed to identify the relevant flow quantities, such as the front and opening angle of the jet. Finally, we employ hot-wire anemometry technique (acquisition rate 1 kHz) to characterize the axial flow evolution, i.e. we measure the time- and space-dependent flow axial velocity at different z locations. This measurements are also used to verify that the flow generated is highly repeatable.

Results and Discussion

We start by comparing the behavior predicted by our experiments and simulations of a violent expiratory event. In particular, we consider the sneeze ejected from a human subject without any face covering (please refer to *SI Appendix* for a discussion on face covering). The results obtained are benchmarked against theoretical scaling laws available for the two phases characterizing the expiratory event: jet and puff [1, 6, 41]. Then, high-fidelity simulations are used to characterize the dispersion and evaporation of the respiratory droplets in different ambient conditions. These results are compared with the predictions obtained from models currently employed in public health guidelines. Finally, we try to bridge fluid dynamics and virological data on SARS-CoV-2 to characterize the virus exposure discussing the risk associated with droplets of different sizes.

Sneezing event: simulations and experiments

To assess the reliability of numerical simulations in accurately reproducing a sneezing event, we start by benchmarking simulation results against those obtained from the experiments performed in the TU Wien laboratory. Due to the impossibility of performing experiments in which temperature, vapor mass fraction and velocity fields are recorded simultaneously, we focus on the ability of simulations and experiments to accurately capture the flow structures and the dynamics of the sneeze. As in this section we do not investigate the evaporation process, we consider a neutrally buoyant jet having the same temperature and humidity of the ambient ($T = 22\ ^{\circ}C$ and $RH = 50\%$). The jet is seeded with tracers (mono-dispersed silicone oil droplets having a diameter equal to 2 μm), which are used for flow visualization and specifically to track the advancement of the the jet front. For simulations, the inflow condition is obtained from a gamma-probability-distribution function [8], which mimics the airflow generated by a sneezing event. Likewise, experiments have been designed to reproduce an inlet condition that is repeatable and similar to that adopted in the simulations. Please refer to *Materials and Methods* and *SI Appendix* for further details.

To quantitatively compare the results, we consider the time evolution of the jet front. Results are also benchmarked against the theoretical scaling laws available in the literature [1, 6, 41]. In particular, considering the finite duration of a sneezing event (and consequently the finite time during which momentum is injected in the environment), we can distinguish between two different phases: *i*) jet phase, linked to the early jet evolution when momentum is continuously provided (constant momentum flux); *ii*) puff phase, linked to the late evolution where momentum injection ceases and the jet momentum remains constant. Using the self-similarity hypothesis, two scaling laws for the distance traveled by the jet front can be derived [43]; for the starting jet phase (constant momentum flux), the distance traveled by the jet front L grows over time as $L \propto t^{1/2}$, while for the puff phase (constant momentum), the penetration distance grows as $L \propto t^{1/4}$.

Figure 1 shows the evolution of the front of the jet obtained from simulations (red points) and experiments (blue points with error bars). As reference, the theoretical scaling laws for the jet and puff phase are reported with two dashed lines. For the jet phase, we observe a very good agreement between experiments and simulations. In particular, the resulting least-squares power-law fits are: $L(t) = 1.51 \times t^{0.51}$ for the experiments and $L(t) = 1.38 \times t^{0.51}$ for the simulations. Present results are

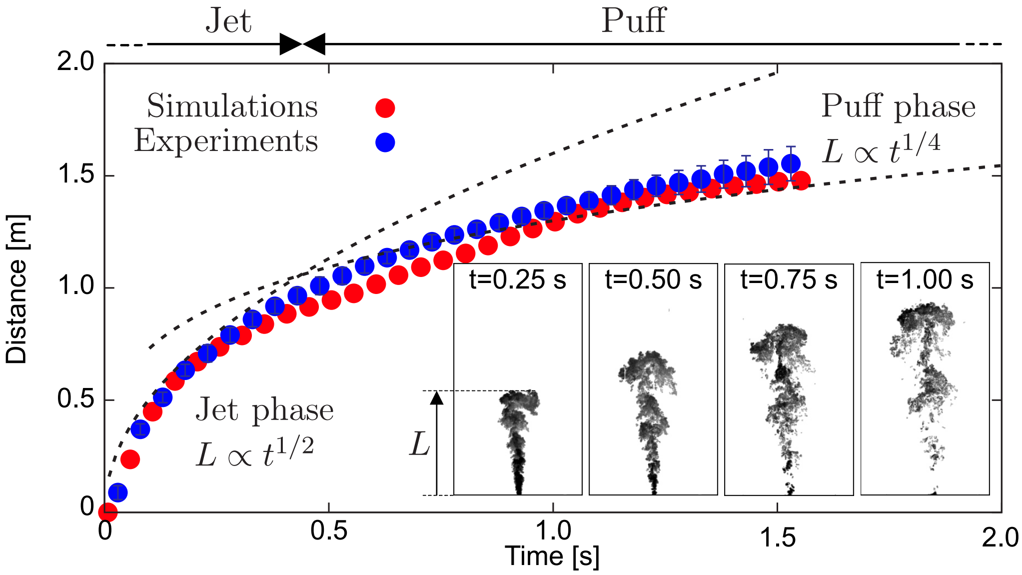

Figure 1: Distance traveled by the front of the jet: comparison between simulations (red dots) and experiments (blue dots). For experiments, data are obtained from 7 independent realizations and error bars corresponding to the standard deviation are also shown. The two stages that characterize the sneezing event, jet (early stage) and puff (late stage) are clearly visible; the scaling laws for the jet, $L \propto t^{1/2}$, and puff phase, $L \propto t^{1/4}$, are reported as reference with black dashed lines. Both simulations and experiments exhibit a very similar behavior and are in excellent agreement. Qualitative visualizations obtained from experiments showing the instantaneous tracers concentration (black-high; white-low) at different times ($t = 0.25\ s$, $t = 0.50\ s$, $t = 0.75\ s$ and $t = 1.00\ s$, respectively) are reported as representative of the jet/puff evolution.

also in good agreement with the analytical scaling law. A detailed quantification on the goodness of the fittings proposed is presented in *SI Appendix*. The very small discrepancy observed between our results and the theoretical scaling law can be traced back to the constant momentum flux hypothesis used to derive the scaling. This assumption is only partially satisfied as in the very first stage of the sneeze ($t < 0.1\ s$), there is a rapid, but not instantaneous, increase of the inlet velocity and thus of the momentum flux. Moving to the puff phase, there is a remarkable decrease of the momentum flux and the distance traveled by the jet front deviates from the jet scaling law and approaches the puff scaling law. Even in this later stage, an overall good agreement is observed between experiments and simulations. For both curves (experiments and simulations), the exponent of the power-law least-squares fitting approaches the value 1/4, as suggested by the theoretical scaling law. To further compare simulations and experiments, we measured the semi-cone angle of the jet obtaining very similar values among experiments ($\alpha = 8.5°$) and simulations ($\alpha = 8°$). These findings are also in agreement with previous investigations on human respiratory activities [1]. Additional comparisons between simulations and experiments are available in the *SI Appendix*.

Sneezing event simulations

Once assessed the reliability of the numerical framework, we use numerical simulations to study the dispersion and evaporation of respiratory droplets resulting from a sneeze. We study four different ambient conditions: two temperatures ($T = 5\ °C$ and $T = 20\ °C$) and two relative humidities ($RH = 50\%$ and $RH = 90\%$). These simulations are performed using the same numerical setup discussed before (see *Materials and Methods* and *SI Appendix* for details).

Figure 2 shows a graphical representation of the sneezing event reproduced by the simulations;

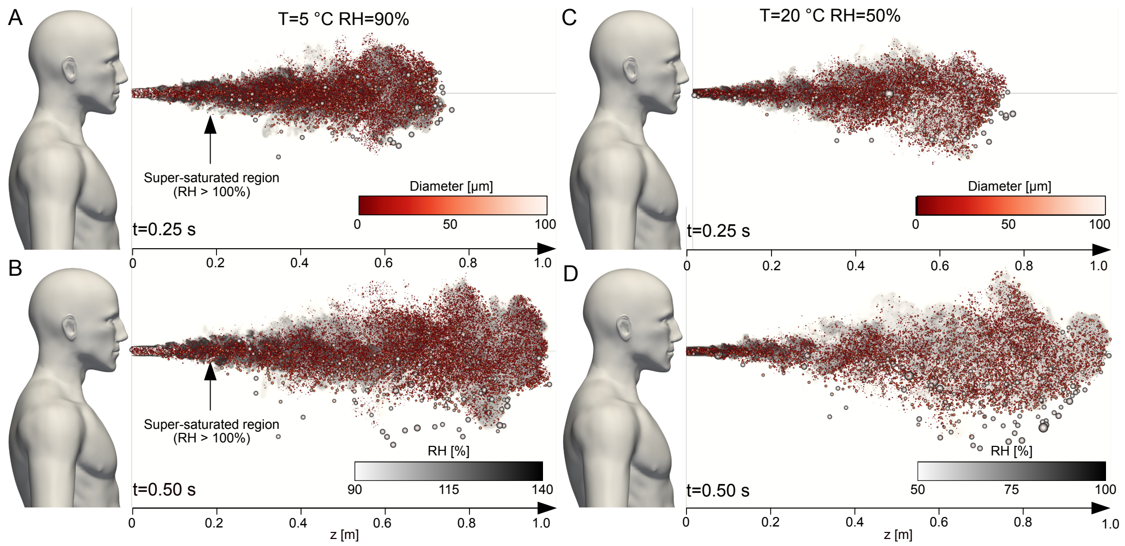

Figure 2: Snapshots of the sneezing event at: $t = 0.25\ s$ (A, C) and $t = 0.50\ s$ (B, D), where $t = 0$ represents the beginning of the respiratory event. The left column refers to $T = 5\ °C$ and $RH = 90\%$, while the right column to $T = 20\ °C$ and $RH = 50\%$. The background shows the local value of the relative humidity (white-low; black-high). The respiratory droplets are displayed rescaled according to their size (not in real scale) and are also colored according to their size (red-small; white-large). We can appreciate how most droplets move together with the turbulent gas cloud generated by the sneezing jet. This cloud is characterized by a much larger value of the RH with respect to the ambient. In addition, for $T = 5\ °C$ and $RH = 90\%$ (left column), a wide region is characterized by supersaturated conditions ($RH > 100\%$).

the left column (A and B) refers to the $T = 5\ °C$ and $RH = 90\%$ case while the right column (C, D) refers to the $T = 20\ °C$ and $RH = 50\%$. For each case, two different time instants, $t = 0.25\ s$ and $t = 0.50\ s$, are shown; the background is colored by the local RH (white-low; black-high), while the dimension (not in scale) and color of the respiratory droplets correspond to their diameter (red-small; white-large). At the beginning (A, C), for both cases, most of the droplets are within the turbulent saturated cloud emitted by the sneezing jet. Only few droplets, with diameter larger than 100 μm (white), located in the front of the jet leave the cloud. Later in time (B, D), the largest droplets start to settle down and thus to significantly move along the vertical direction. On the contrary, most of the other droplets remain suspended in the vapor cloud generated by the sneezing jet as their settling time is longer (e.g. 600 s for a 10 μm droplet) [55]. The effect of buoyancy is also apparent. Since the jet is characterized by a higher temperature (smaller density) than the environment, the cloud starts to move upwards carrying small droplets as well. This effect is more evident for the low temperature cases. Finally, it is worth to observe that already after 0.5 s the front of the jet with the transported droplets has already travelled about 1 m away from the infected individual.

Evaporation of respiratory droplets

To evaluate the infection risk associated with droplets of different sizes, we first evaluate the lifetime of the respiratory droplets. To this aim, we compute the time required by each droplet to complete the evaporation process, reaching its terminal size determined by the presence of non-volatile elements. Indeed, since respiratory liquid contains salt and proteins [5, 11, 46, 47], droplets evaporate until they reach a critical size forming droplet nuclei (water and non-volatile evaporation residua), which may remain suspended. The volume fraction of non-volatile elements varies between individuals and is on average about 3% in volume [5, 11, 39, 46, 47], which correspond to a dry nuclei size of about 30% of the initial droplet diameter. Figure 3 shows the resulting evaporation times for the different ambient conditions tested (A-D). The evaporation times are reported according to the initial droplet diameter and, for each class of diameters, we compute the probability of obtaining a given evaporation time. The sample plot on the left side of the figure guides the reading of the other four panels. For any given initial diameter, the leftmost part of the distribution marks the shortest evaporation time, while the rightmost part of the distribution marks the longest evaporation time; empty black circles identify the mean evaporation time for each initial diameter. The distribution is colored by the probability of each evaporation time (blue-low probability; yellow-high probability). Present results have been compared with the evaporation time predicted by the constant temperature model [23, 55], which is currently employed in most public health guidelines. This model, assuming an isolated droplet at constant ambient temperature, leads to the so-called d^2-law, which predicts that the evaporation time is proportional to the initial diameter squared (and thus to the initial droplet surface). The predicted evaporation time (or more precisely the time required for a droplet to shrink down to 30% of its initial diameter) is reported with a red solid line as a function of the diameter: according to the d^2-law, small droplets evaporate almost immediately, while a much longer time is required for larger droplets. We highlight how the evaporation process obtained from simulations is different from that predicted by the model. Indeed, according to the d^2-law, only droplet nuclei should be present beyond the red line, which marks the evaporation time predicted with the constant temperature model. However, simulations show a completely different picture with most of the droplets completing the evaporation process well beyond the predicted time. The slower evaporation dynamics of respiratory droplets is very pronounced for the high relative humidity cases (B,D), where only droplets smaller than 20 μm fully evaporate within 2.5 s. It is worth mentioning that for the $T = 5\ ^{\circ}C$ and $RH = 90\%$ case, the presence of a supersaturated region induced by the warm humid exhaled air (see figure 2A-B), produces an initial condensation of smaller droplets. Hence, in the first phase, droplets grow in size [13, 34] instead of evaporating and shrinking.

A similar trend, but less marked, can be observed for the low humidity cases, where for the most favorable case (C), almost all droplets with a size smaller than 40 μm reach their final size. The resulting mean evaporation times obtained from simulations are thus larger (by at least one order of magnitude) than those predicted from the constant temperature model, as also observed in recent studies [13, 34]. This dramatic slowdown of the evaporation process traces back to the motion of the droplets and to the local thermodynamic conditions they sample. Indeed, most of the droplets are exposed to the warmer and more humid conditions that characterize the exhaled cloud [6, 59] and to their fluctuations produced by turbulence [41]. As the evaporation rate of the droplets is determined by the local humidity value at the droplet position, which is much higher than the expected environmental value, this results in a much slower evaporation (i.e. a much longer evaporation time). Although the resulting evaporation times are much larger than d^2-law predictions, it is worth observing that the d^2-law scaling seems to still bear some universality. Indeed, for the high-temperature cases (C, D), the mean evaporation times seem to follow a similar scaling (but with a different pre-factor). However, when low temperatures and high humidities are considered (A, B), the presence of condensation in the early stages of the expiratory event extensively modifies the evaporation dynamics and the d^2-law scaling does not hold anymore.

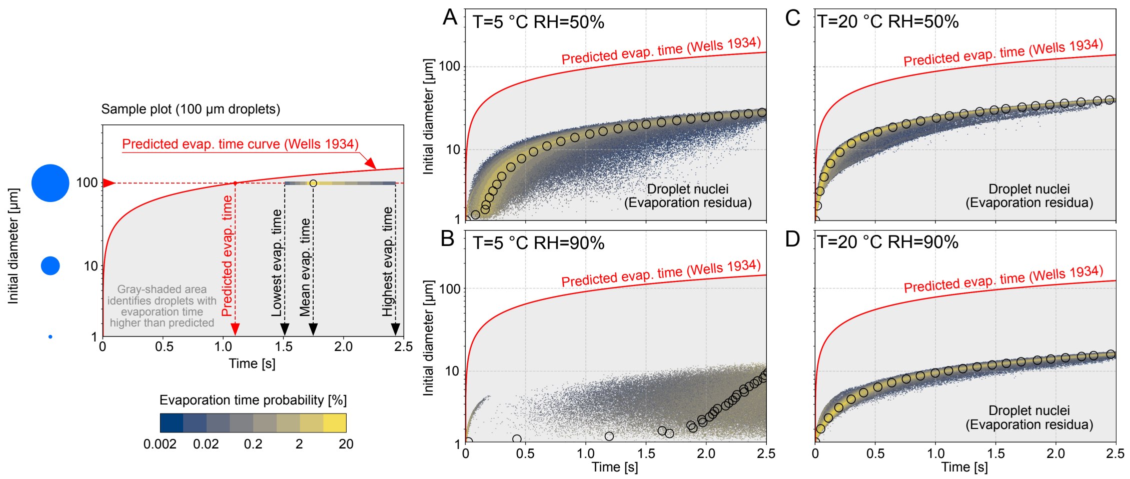

Figure 3: Time required by the respiratory droplets to complete the evaporation process in the four ambient conditions tested: $T = 5°C$ and $RH = 50\% - 90\%$ (A and B) and $T = 20°C$ and $RH = 50\% - 90\%$ (C, D). The sample plot on the left provides at a glance guidance on how to read the main panels. In particular, for any given initial diameter, the leftmost side of the distribution indicates the shortest evaporation time, while the rightmost side of the distribution marks the longest evaporation time observed for droplets with a certain initial diameter. The color of the distribution represents the probability (blue-low; yellow-high) of having a certain evaporation time. Empty black dots represent the mean evaporation time obtained from the simulation data. The predicted evaporation time obtained from the d^2-law, a model currently employed for the definition of public health guidelines, is reported with a solid red line as a function of the droplet diameter. According to the model prediction, all droplets should evaporate within the time prescribed by the red line, thus the gray-shaded area below the red line should be empty (i.e. droplets should have already evaporated to dry nuclei). Simulations results, however, show a completely different picture and for all ambient conditions, droplets evaporate well beyond the predicted time. This reflects the action of turbulence and of moist air released during the sneeze, which largely slows down the evaporation. These effects are very pronounced for the low temperature/high humidity case (B), where only a fraction of droplets smaller than 10 μm completely evaporates to a dry nucleus within $2.5s$. For the other cases (A, C and D), small droplets (less than 20 to 40 μm) complete the evaporation process, and the formation of droplet-nuclei can be appreciated.

Besides, the formation of the droplet-nuclei can be also appreciated. For any given diameter, evaporated droplets shrink down to the critical size determined by the presence of non-volatile matter (30% of the initial diameter). The dispersion of these nuclei is critical in disease transmission as they carry a relatively large amount of bacteria and viruses [33, 48], which may remain infectious for a considerable amount of time, traveling long distances (e.g. for SARS-CoV-2, the half-life in aerosol is $\simeq 1\ h$). The presence of droplet nuclei is observed in those cases characterized by a faster evaporation dynamics (A, C and D), while for the case $T = 5$ °C and $RH = 90\%$ (D), nuclei formation is strongly delayed as the evaporation process is hindered by the higher local relative humidity.

Virus exposure maps

To evaluate the infection risk, we present the virus exposure maps. Specifically, we compute the cumulative number of virus copies that go past a control area in different domain locations. This type of evaluation requires precise information on the viral load for the SARS-CoV-2 virus. However, in archival literature, this information is characterized by large uncertainty and the reported viral loads differ by several orders of magnitude [2, 3, 27, 36, 42, 49, 57]. Indeed, viral load measurements are not only influenced by the method used to test the swab, but viral load exhibits also strong variations during the different stages of the infection [9, 49, 57], being influenced by the severity of symptoms [18, 24, 38] and many other factors as well, among which age, sex and droplet size [29, 44, 49]. To bypass this uncertainty, we present our results in a dimensionless form, normalized by the total number of virus copies ejected and assuming a uniform viral load across all droplets at the time of their ejection. The dimensional concentration of virions can be calculated by multiplying the data from the normalized virus exposure maps for the viral load (an indicative value is 7×10^6 $copies/mL$ for an individual with severe symptoms) [27, 57] and the ejected liquid volume ($\simeq 0.01$ mL). As the time scale of present simulations (3 s) is much smaller than the half-time life [4, 50] in aerosol of SARS-CoV-2 (about 1 h), we do not consider any viral load decay.

Figure 4 shows the virus exposure obtained from the four ambient conditions tested (A-D), which are calculated counting the cumulative number of virus copies (contained inside the droplets) passing through a control area. For all simulated cases, we observe a core-region (green) characterized by a rather uniform value of exposure and some hotspots characterized by larger values of exposure, up to ten times more. This behavior is attributed to the contemporary presence of droplets of very different sizes. Large droplets (more than 100 μm) carry a high number of virus copies (proportional to the initial droplet volume) and produce hotspots of virus concentration as their number is low; by opposite, small droplets (less than 100 μm) carry a lower number of virus copies and produce a more uniform exposure level as their number is higher and they disperse more uniformly. The presence of exposure hotspots (and thus of droplets larger than 100 μm) extends up to 1.25 m. Indeed, these larger droplets follow almost ballistic trajectories and soon settle to the ground. The core region is surrounded by an outer region characterized by a smaller level of exposure, that extends farther in space. This outer region is generated by smaller droplets and droplet nuclei, which reach this outer region later in time ($t > 1$ s) when the majority of the larger droplets have already settled to the ground and most of the smallest ones have completed the evaporation process (see figure 3).

Overall, although for smaller droplets the probability of containing a virus copy is lower due to their initial small volume, we can observe how their large population leads to a remarkable level of virus exposure in the core region (hundreds of thousands of virions per square meter for a viral load of 7×10^6 $copies/mL$) as well as in the outer region (thousands of virions per square meter for the same viral load). As the independent action hypothesis, which states that each pathogen individual has a non-zero probability of causing host infection, seems to apply for SARS-CoV-2, the virus exposure produced by these small droplets poses a significant risk for airborne transmission. It is interesting to observe that the risk of infection via small droplets (i.e. via the airborne route) is significant in the long-range (beyond 1 m from the source), but is even more important in the short-range where a remarkable level of exposure can be addressed to small droplets. This observation suggests that the airborne route has an important, if not dominant, role also in the short-range transmission, and it is not limited to the long-range route, as commonly assumed in most of the current guidelines. The potential of these small droplets in causing infections in the long-range is of difficult estimation as it depends on the virus viability in the droplet nuclei [50] and to the specific environmental conditions (e.g. wind, ventilation). However, considering the relatively high density of virus copies present in these small droplets and droplet nuclei, the risk of infection via the airborne route also in the long-range cannot be neglected. This risk is particularly pronounced in closed places where air dilution is low, as also documented by the large number of outbreaks that occurred in closed spaces [28, 30, 37, 45].

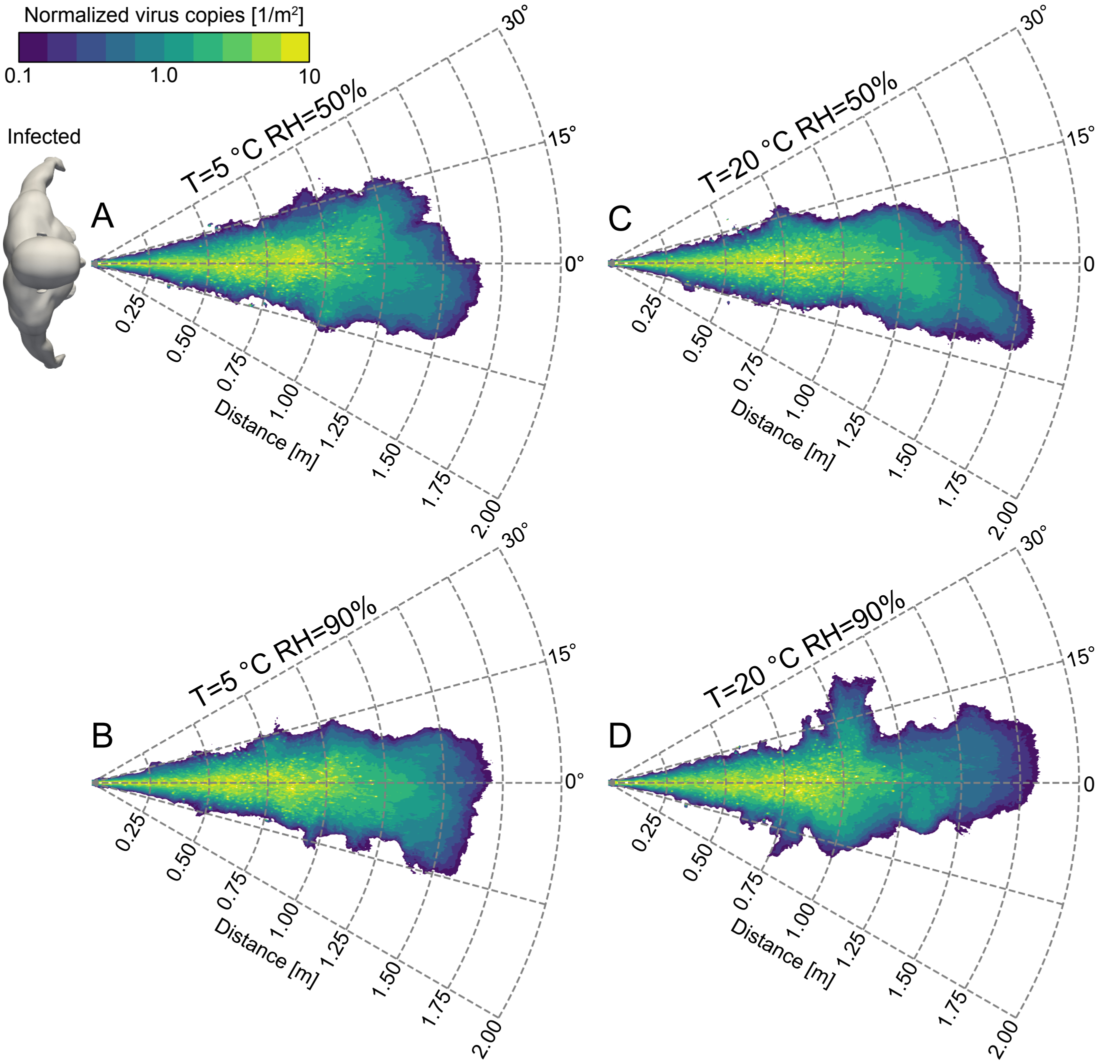

Figure 4: Virus exposure (violet-low; green-high) for the four ambient conditions simulated: $T = 5°C$ and $RH = 50\% - 90\%$ (A-B) and $T = 20°C$ and $RH = 50\% - 90\%$ (C-D). Exposure is defined as the number of virus copies (virions) that go past a control area in different locations of the domain. The results are shown normalized by the total number of virus copies ejected during a sneeze. The dimensional concentration of virus copies can be obtained by multiplying the normalized exposure data for the viral load and the ejected liquid volume ($\simeq 0.01\ mL$ in the present simulations). We can observe the presence of a core region characterized by a high level of virus exposure, which is mainly determined by the large droplets (100 microns or more). These droplets follow almost ballistic paths and settle to the ground within $\simeq 1.25\ m$. This core region is surrounded by a wider region characterized by a lower level of virus exposure. Although in this outer region the value of exposure is smaller, a susceptible individual is still exposed to thousands of virus copies (here we consider an average viral load for SARS-CoV-2 of $7 \times 10^6\ copies/mL$). According to the independent action hypothesis, the presence of thousands of virus copies in the small droplets and droplet nuclei poses a significant threat on both the short- and long-range airborne transmission routes of SARS-CoV-2.

Conclusion

In this study, with the help of finely time- and space-resolved experiments and simulations, we provide evidence that current guidelines, which rely on recommendations based on seminal works [16, 55], present several flaws. A first flaw is identified in the standard prediction of the evaporation times: models currently used in public health guidelines grossly underestimate by at least one order of magnitude the actual evaporation times. A second flaw is represented by the threshold used to differentiate between large and small droplets; while this definition can be meaningful in healthcare environments where the term aerosol refers to a specific group of operations, from a fluid dynamics perspective, this criterium is questionable as the behavior of droplets is influenced by the local flow conditions (e.g. breath/cough/sneeze) and even large droplets (60/100 μm, considered as ballistic in most guidelines) stay suspended in the environment for a considerable amount of time. These flaws lead to a consistent underestimation of the infection risk: formation of droplet-nuclei is delayed with respect to predictions and droplets remain in the most infectious condition (liquid) for a much longer time. In addition, the flow conditions generated by violent expiratory events (sneeze), allow 60/100 μm droplets to remain airborne for a significant amount of time. As highlighted by the virus exposure maps, this leads to a remarkable risk of infection via airborne particles also in the short-range transmission. In light of the present findings, we believe that mitigation of the infection risk via the short-range airborne route [12, 26, 60] must be addressed in current guidelines.

ACKNOWLEDGEMENT

Consorzio Interuniversitario per il Calcolo Automatico (CINECA supercomputing center, Bologna, Italy) is gratefully acknowledged for generous allowance of computer resources under Grant HP10C1XSJU. We gratefully acknowledge the financial support from the Marie Skłodowska-Curie Innovative Training Networks, European Industrial Doctorates (MSCA-ITN-EID, Grant 813948), project next-generation Computational Methods for Enhanced Multiphase Flow Processes (COMETE), from Progetti di Ricerca di Interesse Nazionale (PRIN, project "Advanced computations and experiments in turbulent multiphase flow," Grant 2017RSH3JY), and from the research project promoted by China Scholarship Council (Grant 201806250023).

Bibliography

[1] Manouk Abkarian, Simon Mendez, Nan Xue, Fan Yang, and Howard A. Stone. Speech can produce jet-like transport relevant to asymptomatic spreading of virus. *Proc. Natl. Acad. Sci. U.S.A*, 117(41):25237–25245, 2020.

[2] Carmen Alonso, Peter C. Raynor, Peter R. Davies, and Montserrat Torremorell. Concentration, size distribution, and infectivity of airborne particles carrying swine viruses. *PloS one*, 10(8): e0135675, 2015.

[3] S. Anand and Y. S. Mayya. Size distribution of virus laden droplets from expiratory ejecta of infected subjects. *Sci. Rep.*, 10(1):21174, 2020.

[4] Sima Asadi, Nicole Bouvier, Anthony S. Wexler, and William D. Ristenpart. The coronavirus pandemic and aerosols: Does covid-19 transmit via expiratory particles? *Aerosol Sci. Technol.*, 0(0):1–4, 2020.

[5] S. Balachandar, S. Zaleski, A. Soldati, G. Ahmadi, and L. Bourouiba. Host-to-host airborne transmission as a multiphase flow problem for science-based social distance guidelines. *Int. J. Multiph. Flow*, 132:103439, 2020.

[6] Dehandschoewercker E. & Bush J. W. Bourouiba, L. Violent expiratory events: on coughing and sneezing. *J. Fluid Mech.*, 745:537–563, 2014.

[7] L. Bourouiba. Turbulent gas clouds and respiratory pathogen emissions: Potential implications for reducing transmission of covid-19. *JAMA*, 323(18):1837–1838, 2020.

[8] Giacomo Busco, Se Ro Yang, Joseph Seo, and Yassin A. Hassan. Sneezing and asymptomatic virus transmission. *Phys. Fluids*, 32(7):073309, 2020.

[9] Muge Cevik, Krutika Kuppalli, Jason Kindrachuk, and Malik Peiris. Virology, transmission, and pathogenesis of sars-cov-2. *Brit. Med. J.*, 371:m3862, 2020.

[10] Y Chartier and CL Pessoa-Silva. Natural ventilation for infection control in health-care settings. 2009.

[11] Swetaprovo Chaudhuri, Saptarshi Basu, Prasenjit Kabi, Vishnu R. Unni, and Abhishek Saha. Modeling the role of respiratory droplets in covid-19 type pandemics. *Phys. Fluids*, 32(6): 063309, 2020.

[12] Wenzhao Chen, Nan Zhang, Jianjian Wei, Hui-Ling Yen, and Yuguo Li. Short-range airborne route dominates exposure of respiratory infection during close contact. *BUILD. ENVIRON.*, 176:106859, 2020.

[13] Kai Leong Chong, Chong Shen Ng, Naoki Hori, Rui Yang, Roberto Verzicco, and Detlef Lohse. Extended lifetime of respiratory droplets in a turbulent vapor puff and its implications on airborne disease transmission. *Phys. Rev. Lett.*, 126(3):034502, 2021.

[14] Talib Dbouk and Dimitris Drikakis. On coughing and airborne droplet transmission to humans. *Phys. Fluids*, 32(5):053310, 2020.

[15] Rajiv Dhand and Jie Li. Coughs and sneezes: Their role in transmission of respiratory viral infections, including sars-cov-2. *Am. J. Respir. Crit. Care Med.*, 202(5):651–659, 2020.

[16] J. P. Duguid. The size and the duration of air-carriage of respiratory droplets and droplet-nuclei. *J. Hyg.*, 44(6):471–479, 1946.

[17] Editorial. COVID-19 transmission — up in the air. *Lancet Respir. Med.*, 8(12):1159, 2020.

[18] Jesse Fajnzylber, James Regan, Kendyll Coxen, Heather Corry, Colline Wong, Alexandra Rosenthal, Daniel Worrall, Francoise Giguel, Alicja Piechocka-Trocha, Caroline Atyeo, Stephanie Fischinger, Andrew Chan, Keith T. Flaherty, Kathryn Hall, Michael Dougan, Edward T. Ryan, Elizabeth Gillespie, Rida Chishti, Yijia Li, Nikolaus Jilg, Dusan Hanidziar,

Rebecca M. Baron, Lindsey Baden, Athe M. Tsibris, Katrina A. Armstrong, Daniel R. Kuritzkes, Galit Alter, Bruce D. Walker, Xu Yu, and Jonathan Z. Li. Sars-cov-2 viral load is associated with increased disease severity and mortality. *Nat. Commun.*, 11(1):5493, 2020.

[19] G. A. Ferron, B. Haider, and W. G. Kreyling. Inhalation of salt aerosol particles—i. estimation of the temperature and relative humidity of the air in the human upper airways. *J. Aerosol Sci.*, 19(3):343–363, 1988.

[20] Emanuel Goldman. Exaggerated risk of transmission of covid-19 by fomites. *Lancet Infect. Dis.*, 20(8):892–893, 2020.

[21] F. K. A. Gregson, J. F. Robinson, R. E. H. Miles, C. P. Royall, and J. P. Reid. Drying kinetics of salt solution droplets: Water evaporation rates and crystallization. *J. Phys. Chem. B*, 123 (1):266–276, 2019.

[22] J. K. Gupta, C-H Lin, and Q. Chen. Flow dynamics and characterization of a cough. *Indoor air*, 19(6):517–525, 2009. ISSN 0905-6947.

[23] I. Langmuir. The evaporation of small spheres. *Phys. Rev.*, 12(5):368–370, 1918.

[24] Enrico Lavezzo, Elisa Franchin, Constanze Ciavarella, Gina Cuomo-Dannenburg, Luisa Barzon, Claudia Del Vecchio, Lucia Rossi, Riccardo Manganelli, Arianna Loregian, Nicolò Navarin, Davide Abate, Manuela Sciro, Stefano Merigliano, Ettore de Canale, Maria Cristina Vanuzzo, Valeria Besutti, Francesca Saluzzo, Francesco Onelia, Monia Pacenti, Saverio G. Parisi, Giovanni Carretta, Daniele Donato, Luciano Flor, Silvia Cocchio, Giulia Masi, Alessandro Sperduti, Lorenzo Cattarino, Renato Salvador, Michele Nicoletti, Federico Caldart, Gioele Castelli, Eleonora Nieddu, Beatrice Labella, Ludovico Fava, Matteo Drigo, Katy A. M. Gaythorpe, Alessandra R. Brazzale, Stefano Toppo, Marta Trevisan, Vincenzo Baldo, Christl A. Donnelly, Neil M. Ferguson, Ilaria Dorigatti, and Andrea Crisanti. Suppression of a sars-cov-2 outbreak in the italian municipality of vo'. *Nature*, 584(7821):425–429, 2020.

[25] Dyani Lewis. Covid-19 rarely spreads through surfaces. so why are we still deep cleaning? *Nature*, 590(7844):26–28, 2021.

[26] L. Liu, Y. Li, P. V. Nielsen, J. Wei, and R. L. Jensen. Short-range airborne transmission of expiratory droplets between two people. *Indoor air*, 27(2):452–462, 2017. ISSN 0905-6947.

[27] Yang Liu, Li-Meng Yan, Lagen Wan, Tian-Xin Xiang, Aiping Le, Jia-Ming Liu, Malik Peiris, Leo L. M. Poon, and Wei Zhang. Viral dynamics in mild and severe cases of covid-19. *Lancet Infect. Dis.*, 20(6):656–657, 2020.

[28] Jianyun Lu, Jieni Gu, Kuibiao Li, Conghui Xu, Wenzhe Su, Zhisheng Lai, Deqian Zhou, Chao Yu, Bin Xu, and Zhicong Yang. Covid-19 outbreak associated with air conditioning in restaurant, guangzhou, china, 2020. *Emerg. Infect. Dis.*, 26(7):1628–1631, 2020.

[29] Jianxin Ma, Xiao Qi, Haoxuan Chen, Xinyue Li, Zheng Zhang, Haibin Wang, Lingli Sun, Lu Zhang, Jiazhen Guo, Lidia Morawska, et al. Covid-19 patients in earlier stages exhaled millions of sars-cov-2 per hour. *Clin. Infect. Dis.*, 2020.

[30] Shelly L. Miller, William W. Nazaroff, Jose L. Jimenez, Atze Boerstra, Giorgio Buonanno, Stephanie J. Dancer, Jarek Kurnitski, Linsey C. Marr, Lidia Morawska, and Catherine Noakes. Transmission of sars-cov-2 by inhalation of respiratory aerosol in the skagit valley chorale superspreading event. *Indoor air*, 2020. ISSN 0905-6947.

[31] R. Mittal, R. Ni, and J. H. Seo. The flow physics of covid-19. *J. Fluid Mech.*, 894:317, 2020.

[32] L. Morawska, G. R. Johnson, Z. D. Ristovski, M. Hargreaves, K. Mengersen, S. Corbett, C.Y.H. Chao, Y. Li, and D. Katoshevski. Size distribution and sites of origin of droplets expelled from the human respiratory tract during expiratory activities. *J. Aerosol Sci.*, 40(3):256–269, 2009.

[33] Edward A. Nardell. Transmission and institutional infection control of tuberculosis. *Cold Spring Harb. Perspect. Med.*, 6(2):a018192, 2015.

[34] Chong Shen Ng, Kai Leong Chong, Rui Yang, Mogeng Li, Roberto Verzicco, and Detlef Lohse. Growth of respiratory droplets in cold and humid air. *Phys. Rev. Fluids*, 6(5):054303, 2021.

[35] Mark Nicas and Rachael M. Jones. Relative contributions of four exposure pathways to influenza infection risk. *Risk Anal.*, 29(9):1292–1303, 2009.

[36] Yang Pan, Daitao Zhang, Peng Yang, Leo L. M. Poon, and Quanyi Wang. Viral load of sars-cov-2 in clinical samples. *Lancet Infect. Dis.*, 20(4):411–412, 2020.

[37] Shin Young Park, Young-Man Kim, Seonju Yi, Sangeun Lee, Baeg-Ju Na, Chang Bo Kim, Jung il Kim, Hea Sook Kim, Young Bok Kim, Yoojin Park, In Sil Huh, Hye Kyung Kim, Hyung Jun Yoon, Hanaram Jang, Kyungnam Kim, Yeonhwa Chang, Inhye Kim, Hyeyoung Lee, Jin Gwack, Seong Sun Kim, Miyoung Kim, Sanghui Kweon, Young June Choe, Ok Park, Young Joon Park, and Eun Kyeong Jeong. Coronavirus disease outbreak in call center, south korea. *Emerg. Infect. Dis.*, 26(8):1666–1670, 2020.

[38] Elisabet Pujadas, Fayzan Chaudhry, Russell McBride, Felix Richter, Shan Zhao, Ania Wajnberg, Girish Nadkarni, Benjamin S. Glicksberg, Jane Houldsworth, and Carlos Cordon-Cardo. Sars-cov-2 viral load predicts covid-19 mortality. *Lancet Respir. Med.*, 8(9):e70, 2020.

[39] John Redrow, Shaolin Mao, Ismail Celik, J. Alejandro Posada, and Zhi gang Feng. Modeling the evaporation and dispersion of airborne sputum droplets expelled from a human cough. *BUILD. ENVIRON.*, 46(10):2042–2051, 2011.

[40] M. E. Rosti, S. Olivieri, M. Cavaiola, A. Seminara, and A. Mazzino. Fluid dynamics of covid-19 airborne infection suggests urgent data for a scientific design of social distancing. *Sci. Rep.*, 10 (1):22426, 2020.

[41] M. E. Rosti, M. Cavaiola, S. Olivieri, A. Seminara, and A. Mazzino. Turbulence role in the fate of virus-containing droplets in violent expiratory events. *Phys. Rev. Research*, 3(1), 2021.

[42] Camilla Rothe, Mirjam Schunk, Peter Sothmann, Gisela Bretzel, Guenter Froeschl, Claudia Wallrauch, Thorbjörn Zimmer, Verena Thiel, Christian Janke, Wolfgang Guggemos, Michael Seilmaier, Christian Drosten, Patrick Vollmar, Katrin Zwirglmaier, Sabine Zange, Roman Wölfel, and Michael Hoelscher. Transmission of 2019-ncov infection from an asymptomatic contact in germany. *N. Engl. J. Med.*, 382(10):970–971, 2020.

[43] R. Sangras, O. C. Kwon, and G. M. Faeth. Self-preserving properties of unsteady round nonbuoyant turbulent starting jets and puffs in still fluids. *J. Heat Transfer*, 124(3):460–469, 2002.

[44] Joshua L. Santarpia, Danielle N. Rivera, Vicki L. Herrera, M. Jane Morwitzer, Hannah M. Creager, George W. Santarpia, Kevin K. Crown, David M. Brett-Major, Elizabeth R. Schnaubelt, M. Jana Broadhurst, James V. Lawler, St Patrick Reid, and John J. Lowe. Aerosol and surface contamination of sars-cov-2 observed in quarantine and isolation care. *Sci. Rep.*, 10(1):12732, 2020.

[45] Ye Shen, Changwei Li, Hongjun Dong, Zhen Wang, Leonardo Martinez, Zhou Sun, Andreas Handel, Zhiping Chen, Enfu Chen, Mark H. Ebell, Fan Wang, Bo Yi, Haibin Wang, Xiaoxiao Wang, Aihong Wang, Bingbing Chen, Yanling Qi, Lirong Liang, Yang Li, Feng Ling, Junfang Chen, and Guozhang Xu. Community outbreak investigation of sars-cov-2 transmission among bus riders in eastern china. *JAMA Intern. Med.*, 180(12):1665–1671, 2020.

[46] Scott H. Smith, G. Aernout Somsen, Cees van Rijn, Stefan Kooij, Lia van der Hoek, Reinout A. Bem, and Daniel Bonn. Aerosol persistence in relation to possible transmission of sars-cov-2. *Phys. Fluids*, 32(10):107108, 2020.

[47] Valentyn Stadnytskyi, Christina E. Bax, Adriaan Bax, and Philip Anfinrud. The airborne lifetime of small speech droplets and their potential importance in sars-cov-2 transmission. *Proc. Natl. Acad. Sci. U.S.A*, 117(22):11875–11877, 2020.

[48] Raymond Tellier, Yuguo Li, Benjamin J. Cowling, and Julian W. Tang. Recognition of aerosol transmission of infectious agents: a commentary. *BMC Infect. Dis.*, 19(1):101, 2019.

[49] Kelvin Kai-Wang To, Owen Tak-Yin Tsang, Wai-Shing Leung, Anthony Raymond Tam, Tak-Chiu Wu, David Christopher Lung, Cyril Chik-Yan Yip, Jian-Piao Cai, Jacky Man-Chun Chan, Thomas Shiu-Hong Chik, Daphne Pui-Ling Lau, Chris Yau-Chung Choi, Lin-Lei Chen, Wan-Mui Chan, Kwok-Hung Chan, Jonathan Daniel Ip, Anthony Chin-Ki Ng, Rosana Wing-Shan Poon, Cui-Ting Luo, Vincent Chi-Chung Cheng, Jasper Fuk-Woo Chan, Ivan Fan-Ngai Hung, Zhiwei Chen, Honglin Chen, and Kwok-Yung Yuen. Temporal profiles of viral load in posterior oropharyngeal saliva samples and serum antibody responses during infection by sars-cov-2: an observational cohort study. *Lancet Infect. Dis.*, 20(5):565–574, 2020.

[50] Neeltje van Doremalen, Trenton Bushmaker, Dylan H. Morris, Myndi G. Holbrook, Amandine Gamble, Brandi N. Williamson, Azaibi Tamin, Jennifer L. Harcourt, Natalie J. Thornburg, Susan I. Gerber, James O. Lloyd-Smith, Emmie de Wit, and Vincent J. Munster. Aerosol and surface stability of sars-cov-2 as compared with sars-cov-1. *N. Engl. J. Med.*, 382(16): 1564–1567, 2020.

[51] Eric P. Vejerano and Linsey C. Marr. Physico-chemical characteristics of evaporating respiratory fluid droplets. *J. R. Soc. Interface*, 15(139), 2018.

[52] James H. Vincent. Health-related aerosol measurement: a review of existing sampling criteria and proposals for new ones. *J. Environ. Monit.*, 7(11):1037–1053, 2005.

[53] Jietuo Wang, Federico Dalla Barba, and Francesco Picano. Direct numerical simulation of an evaporating turbulent diluted jet-spray at moderate reynolds number. *Int. J. Multiph. Flow*, 137:103567, 2021.

[54] Jianjian Wei and Yuguo Li. Enhanced spread of expiratory droplets by turbulence in a cough jet. *BUILD. ENVIRON.*, 93:86–96, 2015.

[55] W. F. Wells. On air-borne infection. study ii. droplets and droplet nuclei. *Am. J. Hyg.*, 20: 611–618, 1934.

[56] Nick Wilson, Stephen Corbett, and Euan Tovey. Airborne transmission of covid-19. *BMJ*, 370: m3206, 2020.

[57] Roman Wölfel, Victor M. Corman, Wolfgang Guggemos, Michael Seilmaier, Sabine Zange, Marcel A. Müller, Daniela Niemeyer, Terry C. Jones, Patrick Vollmar, Camilla Rothe, Michael Hoelscher, Tobias Bleicker, Sebastian Brünink, Julia Schneider, Rosina Ehmann, Katrin Zwirglmaier, Christian Drosten, and Clemens Wendtner. Virological assessment of hospitalized patients with covid-2019. *Nature*, 581(7809):465–469, 2020.

[58] World Health Organization. *Infection prevention and control of epidemic- and pandemic-prone acute respiratory infections in health care: WHO Guidelines*. World Health Organization, 2014.

[59] X. Xie, Y. Li, A. T. Chwang, P. L. Ho, and W. H. Seto. How far droplets can move in indoor environments – revisiting the wells evaporation–falling curve. *Indoor air*, 17(3):211–225, 2007. ISSN 0905-6947.

[60] Nan Zhang, Wenzhao Chen, Pak-To Chan, Hui-Ling Yen, Julian Wei-Tze Tang, and Yuguo Li. Close contact behavior in indoor environment and transmission of respiratory infection. *Indoor air*, 30(4):645–661, 2020. ISSN 0905-6947.

Supplementary Information for Short-range exposure to airborne virus transmission and current guidelines

Proceedings of the National Academy of Sciences of the United States of America, 2021, 118 (37), e2105279118

Methods: Numerical simulations

Numerical simulations are based on an hybrid Eulerian-Lagrangian framework. An Eulerian approach is used to describe the gaseous phase while a Lagrangian approach is used to track the motion of the respiratory droplets. In the following, the numerical framework, the parameters and the initial and boundary conditions adopted for the simulations will be detailed.

Description of the gaseous phase

The velocity, vapor fraction, temperature and density fields of the gaseous phase are described using an Eulerian approach. The governing equations are solved in cylindrical coordinates in an open environment at constant pressure p_0. Considering the larger Reynolds number that characterizes a sneezing event (with respect to a cough), a large eddy simulation (LES) approach is employed. Although the choice of a LES approach may reduce the accuracy of the simulations, a posteriori analysis showed that the results obtained are in excellent agreement with those obtained from direct numerical simulations (DNS). Indeed, for the present configuration and considering the grid resolutions employed for the LES, the regions characterized by high values of the viscous dissipation are extremely localized and their contribution to the overall system dynamics is negligible. Under these hypothesis and after applying the Favre-weighted filtering [15] to the asymptotic low-Mach expansion of the Navier-Stokes system, the governing equations read as follows:

$$\frac{\partial\overline{\rho}}{\partial t}+\frac{\partial\overline{\rho}\tilde{u}_i}{\partial x_i}=\overline{S}_m\,, \tag{1}$$

$$\frac{\partial\overline{\rho}\tilde{u}_i}{\partial t}+\frac{\partial\overline{\rho}\tilde{u}_i\tilde{u}_j}{\partial x_j}=-\frac{\partial\overline{p}}{\partial x_i}+\frac{\partial}{\partial x_j}\left[(\mu_g+\mu_{sgs})\left(\frac{\partial\tilde{u}_i}{\partial x_j}+\frac{\partial\tilde{u}_j}{\partial x_i}-\frac{2}{3}\frac{\partial\tilde{u}_i}{\partial x_i}\delta_{ij}\right)\right]+(\overline{\rho}-\rho_g)g_i+\overline{S}_{p,i}\,, \tag{2}$$

$$\frac{\partial\overline{\rho}\tilde{Y}_v}{\partial t}+\frac{\partial\overline{\rho}\tilde{Y}_v\tilde{u}_i}{\partial x_i}=\frac{\partial}{\partial x_i}\left(\overline{\rho}(D+D_{sgs})\frac{\partial\tilde{Y}_v}{\partial x_i}\right)+\overline{S}_m\,, \tag{3}$$

$$\frac{\partial\tilde{u}_i}{\partial x_i}=\frac{\gamma-1}{\gamma}\frac{1}{p_0}\left[\frac{\partial}{\partial x_i}\left((k_g+k_{sgs})\frac{\partial\tilde{T}}{\partial x_i}\right)+\overline{S}_e-L_v\overline{S}_m\right]\,, \tag{4}$$

$$\tilde{T}=\frac{p_0}{\overline{\rho}R_g}\,, \tag{5}$$

where $\overline{\rho}$, $\tilde{u}_i$, $\tilde{Y}_v$, $\tilde{T}$, $\overline{p}$ are the density, velocity, vapor mass fraction, temperature and hydrodynamic pressure fields while μ_g is the dynamic viscosity of the gaseous phase, D the binary mass diffusion coefficient, k_g the thermal conductivity of the vapor-air mixture and L_v the latent heat of vaporization of the liquid phase. The gaseous phase is assumed to be governed by the equation of state where $R_g = R/W_g$ is the gas constant of the mixture being W_g its molar mass and R the universal gas constant. The ratio $\gamma = c_{p,g}/c_{v,g}$ is the specific heat ratio of the carrier mixture where $c_{p,g}$ and $c_{v,g}$ the gaseous phase specific heat capacity at constant pressure and volume, respectively. In the Navier-Stokes equations, the relative buoyancy force of the jet is accounted via the term $(\overline{\rho} - \rho_g)g_i$ being ρ_g the density of the ambient humid air and g_i the i-th component of the gravity acceleration. The subgrid-scale terms of the Navier-Stokes equations are described using the classical Smagorinsky model [30]:

$$\mu_{sgs} = \overline{\rho}(C_s\Delta)^2 \left\| \frac{1}{2}\left(\frac{\partial \tilde{u}_i}{\partial x_j} + \frac{\partial \tilde{u}_j}{\partial x_i}\right) \right\| , \tag{6}$$

where C_s is a model constant (0.12 in our setup) and $\Delta = [(r\Delta_\theta)\Delta_r\Delta_z]^{1/3}$ is the typical cell size. For the other subgrid-scale fluxes, D_{sgs} and k_{sgs}, we adopt the gradient model [29] and their value are assumed proportional to the Smagorinsky eddy-viscosity with a constant turbulent Schmidt and Prandtl numbers equal to $Sc_t = 0.66$ and $Pr_t = 0.78$, respectively.

The effects of the dispersed phase on the gaseous phase are accounted for by three sink-source terms, $\overline{S}_m$, $\overline{S}_{p,i}$ and $\overline{S}_e$:

$$\overline{S}_m = -\sum_{k=1}^{n_d} \frac{dm_k}{dt}\delta(x_i - x_{k,i}) , \tag{7}$$

$$\overline{S}_{p,i} = -\sum_{k=1}^{n_d} \frac{d}{dt}(m_k u_{k,i})\delta(x_i - x_{k,i}) , \tag{8}$$

$$\overline{S}_e = -\sum_{k=1}^{n_d} \frac{d}{dt}(m_k c_l T_k)\delta(x_i - x_{k,i}) , \tag{9}$$

where $x_{k,i}$, m_k and T_k are k-th droplet position, mass, velocity and temperature while c_l is the liquid specific heat. The sum is taken over the entire domain droplet population (being n_d the total number of droplets) and, the delta function expresses that the sink-source terms act only at the domain locations occupied by the droplets. These terms are calculated in correspondence of each grid node by volume averaging the mass, momentum, and energy sources from all droplets located within the cell volume centered around the considered grid point.

Description of the respiratory droplets

The motion of the respiratory droplets is described using a Lagrangian approach. In particular, considering the small size of the droplets, these are treated as small rigid evaporating spheres and are approximated as point-wise particles. In addition, the temperature of the liquid phase is assumed to be uniform inside each droplet. As the volume (and mass) fraction of the fluid phase in real coughs and sneezes is relatively small [4, 14, 20], the mutual interactions among droplets (i.e collisions, coalescence of droplets) can be neglected. Besides, the effect of the subgrid-scale terms is not taken into consideration. Hence, only the resolved part of the Eulerian fields is used in the equations of the dispersed phase. With these assumptions, the position, velocity, mass and temperature of the droplets are described by the following equations:

$$\frac{dx_{k,i}}{dt} = u_{k,i}\,, \tag{10}$$

$$\frac{du_{k,i}}{dt} = \frac{(\tilde{u}_i - u_{k,i})}{\tau_k}(1 + 0.15Re_k^{0.687}) + (1 - \frac{\overline{\rho}}{\rho_l})g_i\,, \tag{11}$$

$$\frac{dr_k^2}{dt} = -\frac{\mu_g}{\rho_l}\frac{Sh}{Sc}\ln(1 + B_m)\,, \tag{12}$$

$$\frac{dT_k}{dt} = \frac{1}{3\tau_k}\left[\frac{Nu}{Pr}\frac{c_{p,g}}{c_l}(\tilde{T} - T_k) - \frac{Sh}{Sc}\frac{L_v}{c_l}\ln(1 + B_m)\right]\,, \tag{13}$$

where $x_{k,i}$, $u_{k,i}$, r_k and T_k are the position, velocity, radius and temperature of the k-th droplet while ρ_l is the liquid droplet density, $c_{p,g}$ the specific heat capacity of the gaseous phase at constant pressure and L_v the latent heat of vaporization. The droplet relaxation time, τ_k, and the droplet Reynolds number, Re_k, are defined as:

$$\tau_k = \frac{2\rho_l r_k^2}{9\mu_g}\,, \qquad Re_k = \frac{2\rho_l\|\tilde{u}_i - u_{k,i}\|r_k}{\mu_g}\,, \tag{14}$$

while the Schmidt number, Sc, and Prandtl number, Pr, are computed as:

$$Sc = \frac{\mu_g}{\rho_g D}\,, \qquad Pr = \frac{\mu_g c_{p,g}}{k_g}\,, \tag{15}$$

where μ_g and ρ_g are the dynamic viscosity and density of the gaseous phase while D is the binary mass diffusion coefficient and k_g the thermal conductivity. The Sherwood number, Sh, and Nusselt number, Nu, are estimated as a function of the droplet Reynolds number using the Frössling correlations [17]:

$$Sh_0 = 2 + 0.552Re_k^{1/2}Sc^{1/3}\,, \qquad Nu_0 = 2 + 0.552Re_k^{1/2}Pr^{1/3}\,. \tag{16}$$

The resulting Sherwood and Nusselt numbers are corrected to account for the Stefan flow [1, 9]:

$$Sh = 2 + \frac{Sh_0 - 2}{F_m}\,, \qquad Nu = 2 + \frac{Nu_0 - 2}{F_t}\,. \tag{17}$$

The coefficients F_m and F_t are computed as follows:

$$F_m = \frac{(1 + B_m)^{0.7}}{B_m}H_m\,, \qquad F_t = \frac{(1 + B_t)^{0.7}}{B_t}H_t, \tag{18}$$

where H_m and H_t are defined as:

$$H_m = \ln(1 + B_m)\,, \qquad H_t = \ln(1 + B_t)\,, \tag{19}$$

being B_m and B_t the Spalding mass and heat transfer numbers:

$$B_m = \frac{Y_{v,s} - \tilde{Y}_v}{1 - Y_{v,s}}\,, \qquad B_t = \frac{c_{p,v}}{L_v}(\tilde{T} - T_k)\,, \tag{20}$$

where $\tilde{Y}_v$ and $\tilde{T}$ are the vapor mass fraction and temperature fields evaluated at the droplet position, $Y_{v,s}$ is the vapor mass fraction evaluated at droplet surface and $c_{p,v}$ is the vapor specific heat at constant pressure. The vapor mass fraction at the droplet surface corresponds to the mass fraction of the vapor in a saturated vapor-gas mixture at the droplet temperature. To estimate $Y_{v,s}$, we use the Clausius-Clapeyron relation to first compute the vapor molar fraction, $\mathcal{X}_{v,s}$:

$$\mathcal{X}_{v,s} = \frac{p_{ref}}{p_0} \exp\left[\frac{L_v}{R_v}\left(\frac{1}{T_{ref}} - \frac{1}{T_k}\right)\right]\,, \tag{21}$$

where p_{ref} and T_{ref} are arbitrary reference pressure and temperature and $R_v = R/W_l$ is the vapor gas constant. The saturated vapor mass fraction is then computed using the relation:

$$Y_{v,s} = \frac{\mathcal{X}_{v,s}}{\mathcal{X}_{v,s} + (1 - \mathcal{X}_{v,s})\dfrac{W_g}{W_l}}\,, \tag{22}$$

where W_g and W_l are are the molar mass of the gaseous and liquid phases.

Numerical method

The numerical code consists of two different modules: i) an Eulerian module that solves the governing equations for the gaseous phase (density, velocity, vapor mass fraction and temperature); ii) a Lagrangian module that solves the equations governing the droplet dynamics (position, velocity, mass and temperature). In particular, the governing equations of the gaseous phase are discretized in space using a second-order central finite differences scheme and they are time advanced using a low-storage third-order Runge-Kutta scheme. Likewise, the governing equations of the droplets are time integrated using the same Runge-Kutta scheme, and a second-order accurate polynomial interpolation is used to evaluate the Eulerian quantities at the droplet position. Please refer to previous works [9, 23, 26] for additional validations and tests of the numerical method.

Simulation setup

The computational domain, figure 1, is a cylinder into which the droplet-laden sneezing jet is injected through a circular orifice of radius $R = 1\ cm$ located at the centre of the left base that mimics the average mouth opening for females and males subjects [4, 19]. The cylinder dimensions are $L_\theta \times L_r \times L_z = 2\pi \times 150R \times 300R$ along the azimuthal (θ) radial (r) and axial (z) directions. The domain is discretized using a staggered grid with $N_\theta \times N_r \times N_z = 96 \times 223 \times 1024$ grid points. The calibration of the numerical parameters (e.g. domain size, grid resolution) is based on previous works [9, 37]. In these works, which rely on a very similar model and setup, numerical results have been benchmarked against analytic and experimental results. In addition, further validation tests (e.g. evaporation of an isolated droplet) have been performed and results obtained compared against analytic solutions.

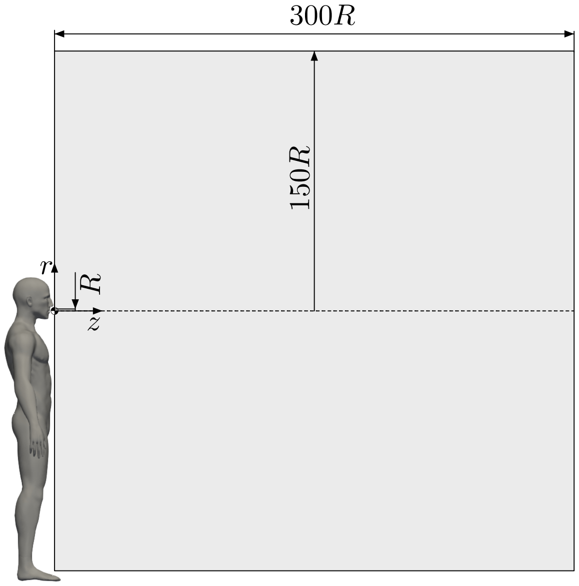

Figure 1: Sketch of the simulation setup used for the simulations. The computational domain is a cylinder having dimensions $L_\theta \times L_r \times L_z = 2\pi \times 150R \times 300R$ being $R = 1\ cm$ the radius of the circular orifice that mimics the mouth opening. The sneezing jet, together with the respiratory droplets, are injected from the left side of the domain (through the orifice). The domain is initially quiescent (zero velocity) and characterized by a uniform value of temperature, humidity.

A total mass of liquid equal to $m_l = 8.08 \times 10^{-6}\ kg$ is ejected together with the sneezing jet; the mass of the ejected gaseous phase is equal to $m_g = 2.00 \times 10^{-3}\ kg$. The resulting mass fraction is equal to $\Phi_m = 4.04 \times 10^{-3}$ while the volume fraction is equal to $\Phi_v = 4.55 \times 10^{-6}$ conforming to previous experimental studies [4, 11, 12, 14, 20].

The inflow velocity profile of the sneezing jet (figure 2) is obtained from a gamma-probability-distribution function [6] and a simple conversion from dynamic pressure to velocity is implemented based on Bernoulli's principle. The overall duration of the injection stage (sneezing jet and droplets) is about 0.6 s [6]. The sneezing jet is characterized by a temperature of $T_j = 308\ K$ and a relative humidity $RH_j = 90\%$ [4, 16, 22] and its peak velocity is $u_{z,j} = 20\ m/s$ [5, 38]. Although the values of these parameters, which define the inlet/injection conditions, can sensitively influence the first stage of the sneezing event, their effect in the latter stages of the simulations is expected to be marginal as the ambient conditions are the dominant factors in the evaporation process. From the temperature and relative humidity of the sneezing jet, the density and vapor mass fraction of the jet are obtained from the revised formula reported in Picard *et al.* (2008)[24]. The other thermo-physical and transport properties are estimated from Tsilingiris (2008) [34], see table 2 for details.

Considering now the liquid phase (respiratory droplets), for each droplet injected in the computational domain, its initial diameter is assumed to follow a log-normal distribution with geometric mean equal to 12 μm and geometric standard deviation (GSD) equal to 0.7 [3]. Albeit being an important parameter, the droplet size distribution is expected to have a minor influence on the final results in terms of suspension and/or deposition of the respiratory droplets, as also shown by previous works [27], see also the section *Sensitivity of simulations to other physical parameters* for further discussion. The above mentioned distribution is generated using a Gaussian random number generator based on a Ziggurat method [21]. The initial velocity of the droplets is obtained through interpolation of the velocity field of the gaseous phase in the inlet region, while the initial temperature of the droplets is set to $T = 308\ K$. To mimic the presence of salt, protein and virus dissolved in the respiratory droplets [35], the droplets have a non-volatile core and thus they cannot completely evaporate. This leads to the formation of the so-called droplet nuclei, i.e. the residual part of the respiratory droplets that does not evaporate. In agreement with previous studies [3, 7, 13, 25, 31, 32], we consider that the non-volatile core of each droplet represents the 3% of the droplet volume. In terms of droplets size, this means that a droplet can shrink down to $\simeq 30\%$ of its initial diameter. Due to numerical stability issues [9], all generated droplets with an initial size smaller than a critical radius of $0.65\ \mu m$ will be treated as tracers. Likewise, if a droplet, due to the evaporation, becomes smaller than the critical radius, it will be treated as a tracer.

The ambient is assumed quiescent (i.e. all velocity components are initially set to zero) and is characterized by a uniform value of temperature, humidity and constant thermodynamic pressure. The density of the gaseous phase is obtained from the gas equation of state, while the vapor mass fraction is obtained through the Clausius–Clapeyron relation using the sneezing jet conditions as reference.

We perform a total of 7 simulations: a benchmark simulation used for the comparison with the experiments (case S0 in table 2), four production simulations (cases S1-4 in table 2) and two additional simulations used to test the sensitivity of the results (case S5-6 in table 2). The benchmark case considers mono-dispersed non-evaporating droplets (diameter of $2\ \mu m$) released in a sneezing jet having the same temperature of the ambient: $T = 295\ K$ ($22\ °C$) and humidity: $RH = 50\%$ (TU Wien laboratory conditions). The production simulations investigate the effects of ambient temperature and relative humidity on the evaporation process (main results presented in the manuscript). Indeed, considering the constitutive equations of the evaporation process, these two variables are expected to be the physical parameters with the most important effects on the evaporation/condensation process. These simulations consider four different ambient conditions: two different temperatures, $T = 278\ K$ ($5\ °C$) and $T = 293\ K$ ($20\ °C$), and two relative humidity values, $RH = 50\%$ and $RH = 90\%$. The latter two simulations investigate the sensitivity of the results obtained from simulations S1-4 to two specific parameters: the occurrence of multiple sneezing events and the initial droplet size distribution. Specifically, the first simulation considers a case in which a second sneeze follows two seconds after the initial sneeze, while the second considers a case with a different initial size distribution of the injected droplets, namely a Pareto distribution. For these latter cases, the ambient conditions have been kept fixed to $T = 293\ K$ and $RH = 50\%$.

A detailed summary of the simulation parameters and thermo-physical properties adopted for the different simulations is reported in table 1-2.

Methods: Experiments

We set up a laboratory experiment to investigate the dynamics of droplets-laden jets. We used a compressor-based system to supply the flow with air, which is seeded with micrometrical droplets by a liquid seeder. Measurements consist of flow velocity (point wise) and drops distribution (two-dimensional distribution). Details are provided in the following.

Table 1: Summary of the simulation parameters and thermophysical properties.

Parameter	Symbol	Value	Unit of measurement
Inlet radius	R	1.00×10^{-2}	m
Sneezing jet temperature	T_j	308	K
Sneezing jet relative humidity	RH_j	90%	-
Maximum sneezing jet velocity	$u_{z,j}$	20	m/s
Droplets temperature	T_k	308	K
Mass injected liquid phase	m_l	8.08×10^{-6}	kg
Mass injected gaseous phase	m_g	2.00×10^{-3}	kg
Liquid mass fraction	Φ_m	4.04×10^{-3}	-
Liquid volume fraction	Φ_v	4.55×10^{-6}	-
Environment temperature	T	278 and 293	K
Environment relative humidity	RH	50% and 90%	-
Environment thermodynamic pressure	p_0	1.01×10^5	Pa
Dynamic viscosity gaseous phase	μ_g	1.99×10^{-5}	Pa s
Thermal conductivity gaseous phase	k_g	2.63×10^{-2}	W/(m*K)
Latent heat of vaporization	L_v	2.41×10^6	J/kg
Universal gas constant	R	2.87×10^2	J/(kg*K)
Molar mass of the gaseous phase	W_g	2.89×10^{-2}	kg/mol
Gas constant gaseous phase	R_g	2.92×10^2	J/(kg*K)
Specific heat capacity at constant pressure gaseous phase	$c_{p,g}$	1.03×10^3	J/(kg*K)
Specific heat capacity at constant volume gaseous phase	$c_{v,g}$	7.42×10^2	J/(kg*K)
Specific heat ratio gaseous phase	γ	1.39	-
Vapor specific heat capacity at constant pressure	$c_{p,v}$	1.88×10^3	J/(kg*K)
Vapor phase gas constant	R_v	4.61×10^2	J/(kg*K)
Binary mass diffusion coefficient	D	2.67×10^{-5}	m^2/s
Molar mass liquid phase	W_l	1.80×10^{-2}	kg/mol
Density liquid phase	ρ_l	1.00×10^3	kg/m^3
Specific heat liquid phase	c_l	4.18×10^3	J/(kg*K)
Volume fraction non-volatile material droplet	Φ_v^c	3%	-
Prandtl number	Pr	0.782	-
Schmidt number	Sc	0.663	-

Table 2: Summary of the main simulation parameters

Case -	Temperature T [K]	Relative humidity RH [%]	Density ρ_g [kg/m^3]	Vapor mass fraction Y_g	Sneezing events -	Size distribution -
S0	295	50	1.174	8.22×10^{-3}	Single	Monodispersed
S1	278	50	1.245	2.82×10^{-3}	Single	Log-normal
S2	278	90	1.245	5.09×10^{-3}	Single	Log-normal
S3	293	50	1.181	7.42×10^{-3}	Single	Log-normal
S4	293	90	1.181	1.34×10^{-2}	Single	Log-normal
S5	293	50	1.181	7.42×10^{-3}	Double	Log-normal
S6	293	50	1.181	7.42×10^{-3}	Single	Pareto

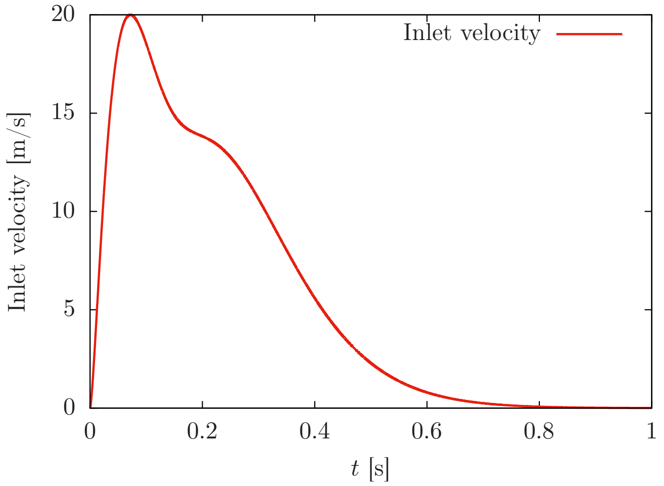

Figure 2: Inflow velocity of the sneezing jet used in the simulations. The inlet velocity is obtained from a gamma-probability-distribution function [6]. The duration of the sneezing event is $\simeq 0.6$ s and the peak velocity is 20 m/s.

Experimental setup

The main components of the system are shown in figure 3(a). To produce repeatable flow conditions, we designed a system in which the flow parameters (pressure, duration) can be carefully controlled. The flow generated by the compressor (pressure 6.5 bar) is controlled by an electromagnetic valve (Parker 4818653D D5L F). The valve is activated by a timer (Finder, relays type 94.02 and plug-in timer 85.02), which is set to maintain the valve open for 0.15 s. We verified *a-posteriori* via hot-wire measurements that the flow is highly repeatable.

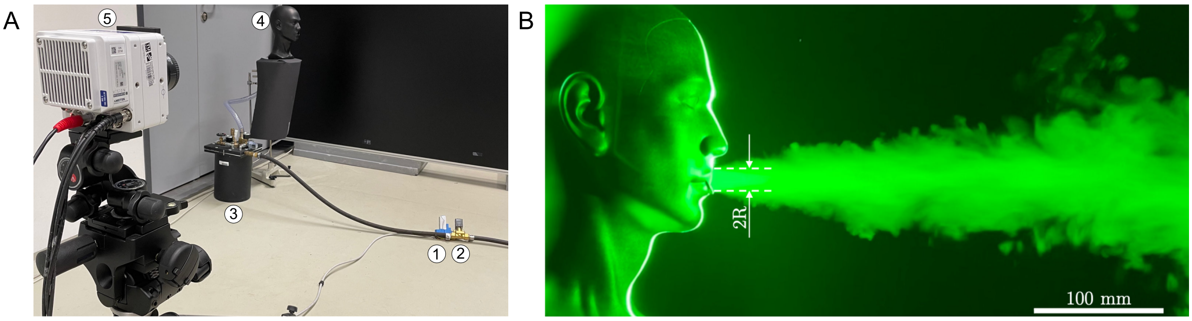

Figure 3: Panel A shows the experimental setup used. The setup is composed by the compressor (not shown), timer (1), electromagnetic valve (2), liquid seeder (3) and dummy head (4). A laser is used to illuminate the micro-metric droplets. Image acquisition is preformed by a high-speed camera (5). Panel B shows the dummy head used to perform the experiments ($R = 1$ cm).

The compressor is connected to a seeding generator (9010F0031 Liquid Seeder, type FT700CE), which produces droplet with size falling in the range 1-3 μm, with an average droplets size of 2 μm, as reported in figure 4. To seed the flow with neutrally-buoyant and non-evaporating drops, an aqueous and non-toxic solution (Safex - Inside Nebelfluid, Dantec Dynamics) is used. The solution is kept at the ambient temperature. We observed that the drops remain suspended in the ambient for long time, without any apparent effect of sedimentation. The droplets Stokes number, St, is defined as $St = \rho_l r_l^2 \bar{u}_{z,j}/(R\mu_g)$, being $r_l = 1$ μm averaged droplets radius and $\bar{u}_{z,j} \leq 20$ m/s the reference velocity. For the present case, we obtain $St \leq 0.1$ and we consider the droplets as flow tracers [33].

We used a dummy head to avoid exposure of human beings to the potentially harmful laser light. The droplet-laden jet is emitted through the mouth of the dummy, which is mimicked by a circular opening of radius $R = 1$ cm, see figure 3(B). The mouth is directly connected to the fog generator through a tube of length 100 *cm* and inner diameter $2R$. The temperature of environment (T), jet (T_j) and droplets (T_k) is constant and equal to $T = T_j = T_k = 295$ K, therefore buoyancy plays no role in the dynamics of the jet, in agreement with the observations of [40]. The relative humidity of the air is $RH = 50\%$.

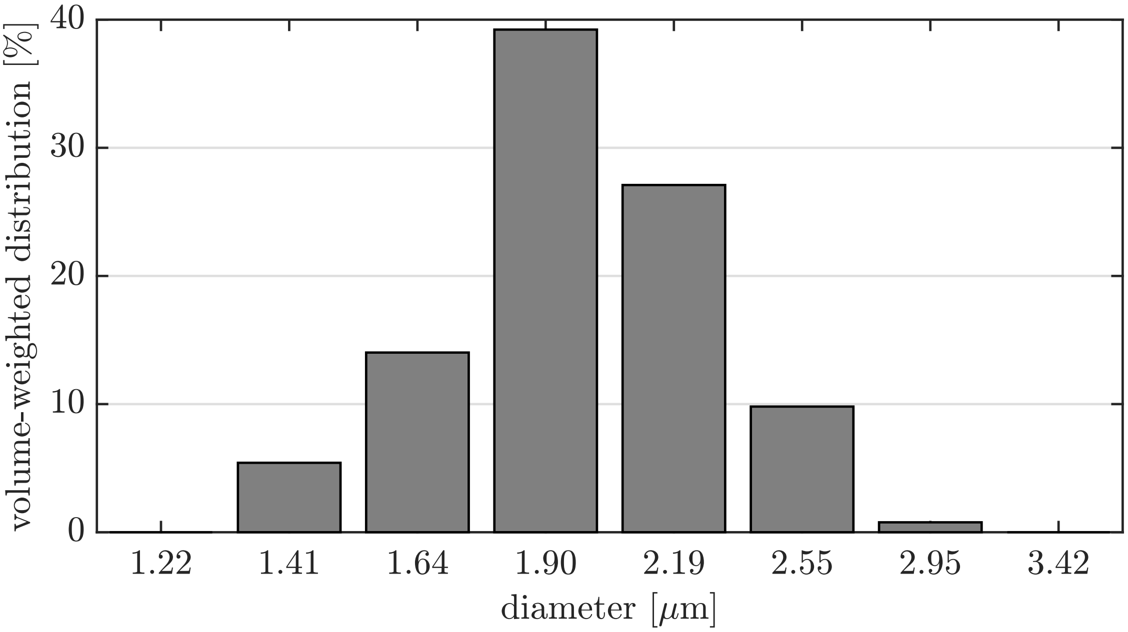

Figure 4: Volume-weighted droplets distribution [%] as a function of the diameter of the droplets produced [10].

Imaging system

A high-speed laser is used to create a sheet (thickness 4 *mm*) in which the experimental measurements are performed. The laser consists of a double-pulse laser (Litron LD60-532 PIV, 25 mJ per pulse) illuminating the measurement region at frequency 0.8 kHz. To record the evolution of the flow, we used a Phantom VEO 340L (sensor size of 2560 × 1600 pixel at 0.8 kHz) equipped with lenses having focal length 35 *mm*, looking perpendicularly to the laser sheet at a distance of 200 *cm*. Camera and laser are controlled via a high-speed synchroniser (PTU X, LaVision GmbH, Germany). Images are collected with DAVIS 10 (LaVision GmbH, Germany) and processed in MATLAB to compute the extension of the front of the jet.

As the jet propagates along the axial direction (z), particles concentration reduces. As a result, the light intensity recorded by the cameras drops significantly with z, making the detection of the front of the jet hard to obtain. To perform the edge-detection process, we applied subsequent image processing steps (subtracting background noise, binarization, median filter). After image preprocessing, the boundary of the jet is found by Moore-Neighbor tracing algorithm [18] and finally the edge, the maximum horizontal coordinate of the boundary, is determined and tracked in time. In figure 5 (and as well in the manuscript), the evolution of the front of the jet, L, is reported as a function of time. The mean (red solid line) and standard deviation (error bars) are obtained from 7 independent experiments.

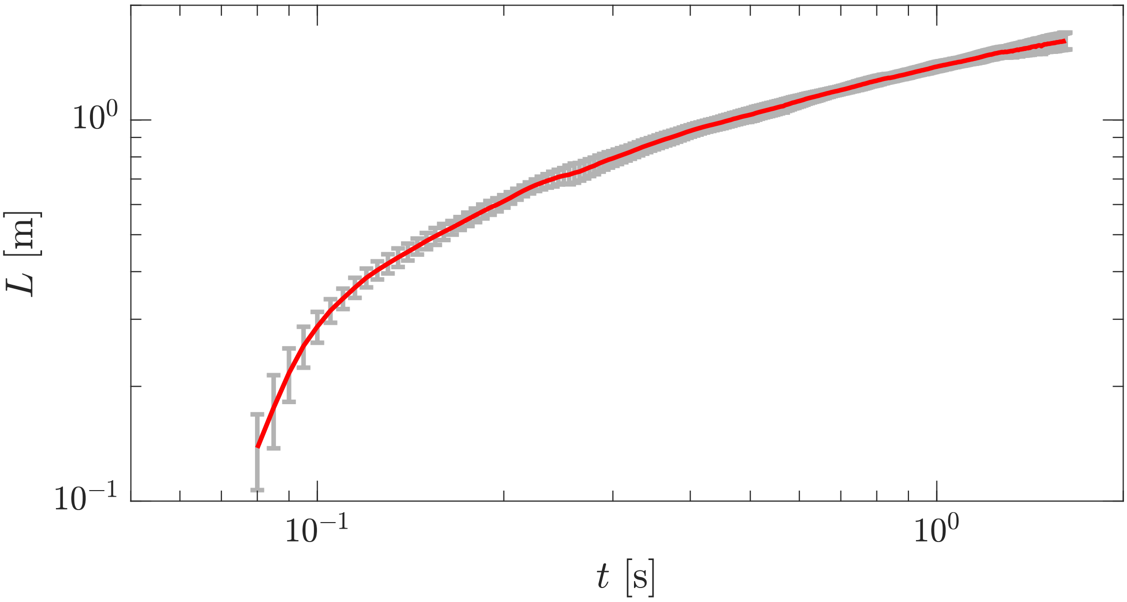

Figure 5: Evolution of the front of the jet, L, as a function of time, t. Mean (red solid line) and standard deviation (error bars) are obtained from 7 independent experiments. The acquisition rate is 0.8 kHz and we show here one every 4 instants.

Hot-wire anemometry

We used a hot-wire anemometry system (acquisition rate 1 kHz, probe type Dantec 55P11) to measure the axial velocity of the flow and thus to calibrate the inflow velocity profile. Figure 6 shows the axial velocity measured along the centerline of the jet ($r = 0$) at a distance $z = 20$ mm from the mouth as a function of time, t. To characterise the inlet condition, we performed 11 independent experiments. In each experiment, the instantaneous velocity measurements (u_1, grey data) are averaged over a moving window of 20 ms to obtain u_{20} (blue solid line). Then results of all experiments are averaged to obtained the ensemble averaged flow velocity (u, red solid line). The excellent agreement observed between the ensemble average (u) and the single experiment (u_{20}) confirms the repeatability of the flow generated. Finally, the mean value of velocity computed for $0 \leq t \leq 0.7$ s ($\overline{u}$, dashed line) is also shown, and it is used for further comparison with the results obtained from the numerical simulations.

Comparison between simulations and experiments

We provide here a quantitative comparison of the experimental and numerical results obtained. The results are analyzed in terms of jet properties in time (distance travelled by the jet) and in space (average jet velocity at different positions). We compute the best-fitting exponent and the corresponding least-squares power-law fit for the two phases of the sneezing event (i.e. jet and puff). Finally, we compare numerical and experimental measurements of the jet velocity at increasing distance from the inlet.

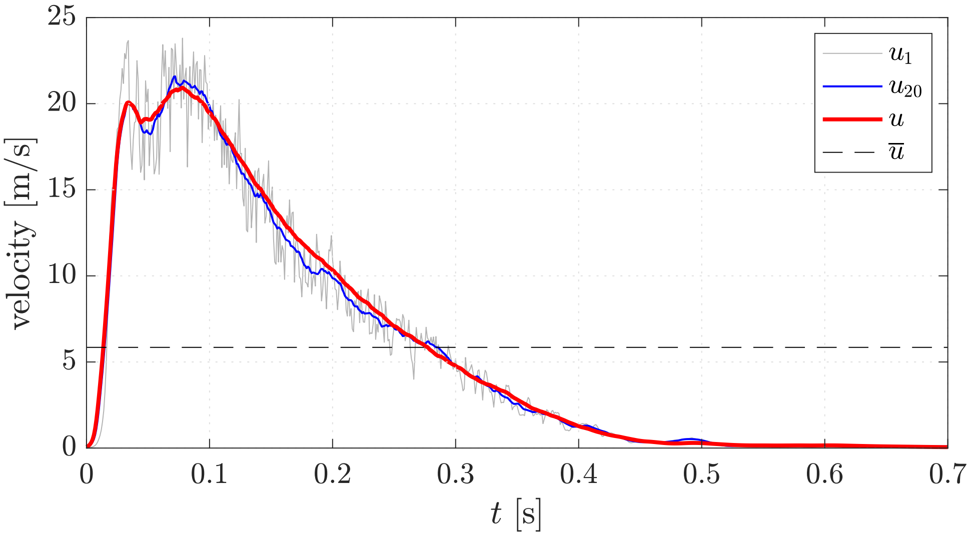

Figure 6: Time-dependent evolution of the axial velocity measured at the centerline ($r = 0$) at distance $z = 20$ mm from the mouth. Instantaneous velocity measurements (u_1, grey line) as well as the velocity averaged over a moving window of 20 ms (u_{20}, blue line) are shown here for one experiment. Then results of 11 experiments are used to obtained the ensemble averaged flow velocity (u, red solid line). Finally, the mean value computed for $0 \leq t \leq 0.7$ s is shown ($\overline{u}$, dashed line).

We consider first the initial growth of the jet ($t < 0.6$ s), in which the momentum flux is constant. Indeed, for $t > 0.6$ s the flow-rate at the inlet is negligible, see figure 6. As a result, the expected jet growth obtained using the self-similarity hypothesis [28] is $L \sim t^{1/2}$. Assuming that the initial stage is defined for $0 \leq t \leq 0.6$ s and fitting the results within this time interval, we obtain that the least-squares power-law fits are (with 95% confidence bounds):

- $L(t) = (1.51 \pm 0.03) \times t^{0.51 \pm 0.02}$, with root mean squared error of RMSE $= 0.03$ for the experiments.
- $L(t) = (1.38 \pm 0.04) \times t^{0.51 \pm 0.03}$, with root mean squared error of RMSE $= 0.05$ for the numerical simulations.

The resulting exponents of the power-law scalings obtained numerically and experimentally are in excellent agreement, and match also the theoretical (self-similar) predictions, as shown in figure 7.

We consider now the asymptotic scaling exponent ($t > 0.6$ s). During this phase, the flow behaves like a puff and is characterized by constant momentum. The penetration distance, obtained again using the hypothesis of self-similarity [28], evolves as $L \sim t^{1/4}$. Since this phase is longer than the jet phase, we can provide an accurate quantification of the scaling exponent for $t > 0.6$ s. In particular, assuming that $L \sim t^n$, the scaling exponent can be estimated by examining the local slopes, $\frac{d \log (L/R)}{d \log (t/T_0)}$. We use the inlet radius $R = 0.01$ m to make the penetration distance dimensionless. Similarly, we use $T_0 = R/u_{z,j}$ to rescale the time, with $u_{z,j} = 20$ m/s the maximum sneezing jet velocity. Please note that the quantities used to make the variables dimensionless do not have any effect on the estimate of the scaling exponent. Results of experiments and simulation (symbols) are shown in figure 8 and suggest that, also in this phase, the self-similar solution is attained for long times ($L \sim t^{1/4}$, dashed line).

Finally, to further benchmark experimental results against numerical results, we also investigate the evolution of the time-averaged jet velocity, $\overline{u}$, along the axial direction (z axis). The time interval

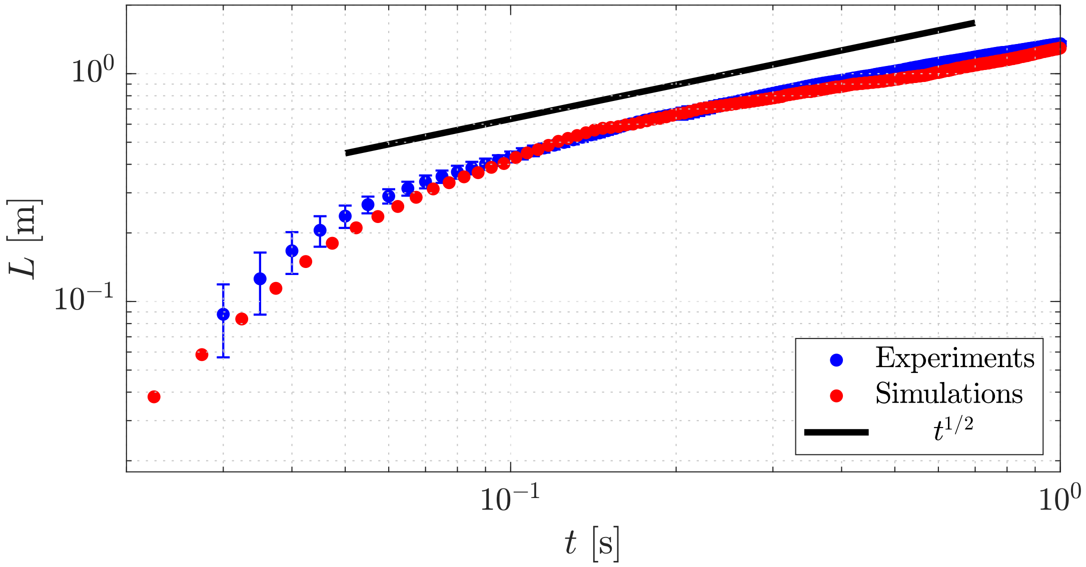

Figure 7: Distance travelled by the front of the jet in the early-stage of the process (first second of the simulation). Results obtained experimentally (symbols, blue) and numerically (symbols, red) are in excellent agreement with the theoretical (self-similar) predictions ($t^{1/2}$, black solid line).

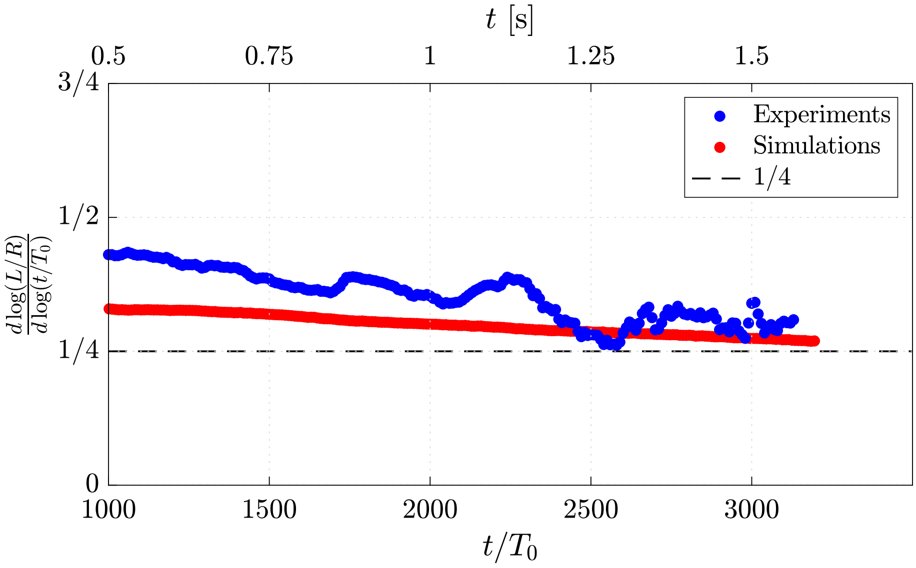

Figure 8: Evolution in time of the scaling exponent, evaluated by the local slope, $\frac{d\log(L/R)}{d\log(t/T_0)}$ in the late stages of the simulations. We use the inlet radius R to make the penetration distance dimensionless, and $T_0 = R/u_{z,j}$ to rescale the time, being $u_{z,j}$ the maximum sneezing jet velocity. Results of experiments (0.1 s moving average, blue dots) and simulations (red dots) indicate that, for long times, the self-similar solution ($L \sim t^{1/4}$, dashed line) is attained.

used for the average spans from $t = 0\ s$ up to $t = 0.6\ s$. Concerning the experiments, 76 independent realizations are used to determine $\overline{u}(z)$, which is defined as described above. Measurements are performed along the centerline at 76 equally-spaced z positions. For simulations, data are obtained from the Eulerian grid used to compute the velocity fields and then averaged in time. Results are shown in figure 9 for simulations (red dots) and experiments (blue dots). The velocity profiles are reported normalized by $\overline{u}_0$, i.e. the first velocity value (closest point to the inlet position). The scaling law, $\overline{u} \propto 1/x$, is also reported as a reference [39] with a black, dashed line. As can be appreciated from the figure, experiments and simulations are in excellent agreement over the entire axis span. In addition, both experimental and numerical results well match with the analytic scaling law.

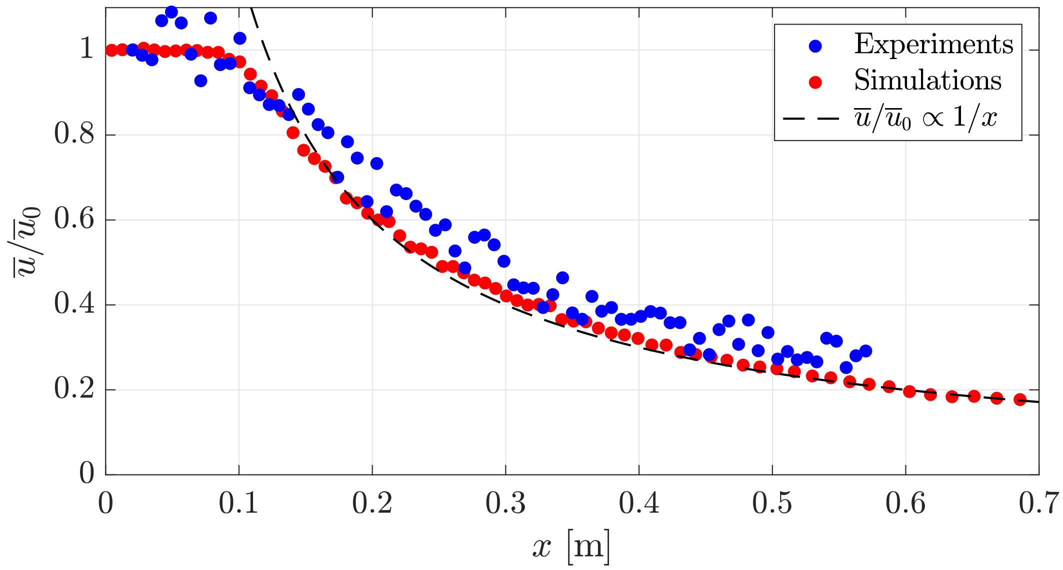

Figure 9: Time-averaged axial velocity, $\overline{u}$, measured at the jet centerline and normalised by the velocity at the closet point to the inlet position ($\overline{u}_0$), is reported as a function of the distance from the mouth, z. Experimental results are represented using blue dots while simulations results with red dots. As a reference, the scaling law $\overline{u}/\overline{u}_0 \propto 1/x$ (dashed, black line) is also reported.

Sensitivity of simulations to other physical parameters

We present here the results obtained from simulations S5-6. These simulations have been used to assess the sensitivity of the results obtained from simulations S1-4 to two additional factors: the occurrence of multiple sneezing event and the initial droplet size distribution.

Multiple sneezing events

We start by discussing the sensitivity of the results to multiple sneezing events analyzing the results obtained from simulation S5. This simulation considers a second sneeze that occurs two seconds after the initial sneeze. First, we analyze the resulting evaporation times of the droplets, which are shown in figure 10.

Panel (A) refers to a single sneeze while panel (B) to a double sneeze. For both cases, the evaporation time is calculated starting from the time at which the droplet is injected in the domain up to the time when the dry nuclei size is reached (i.e. considering the droplet flight time). We observe how the distribution of the evaporation times obtained from the two cases are almost identical. We can thus infer that the first sneeze does not influence the evaporation times of the droplets released during the second sneeze. This behavior can be traced back to the motion of the droplets. Indeed, most droplets are characterized by a small diameter (less than 100 microns) and, as a consequence, their velocity is similar to that of the gaseous phase they are entrained in. Therefore, these droplets are unlikely to sample the conditions of the turbulent gas cloud of moist air released during the first sneeze (located much farther in space and already partially mixed with

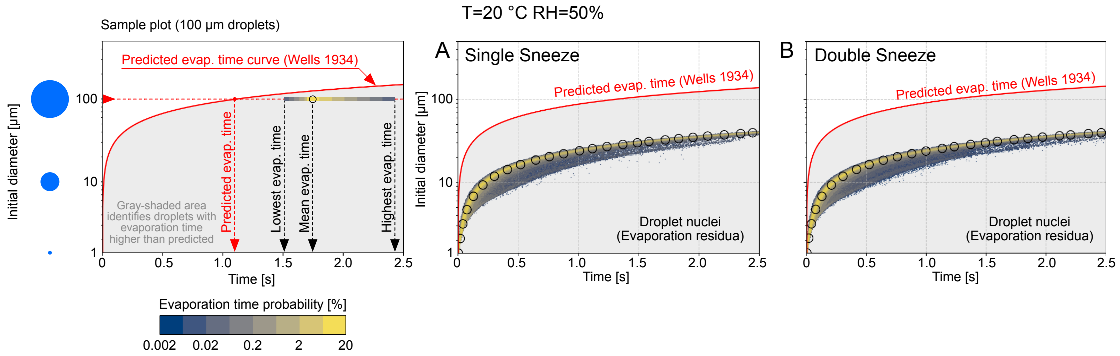

Figure 10: Distribution of droplets evaporation times for a single sneeze (A) and a double sneeze (B). For any initial diameter, the leftmost side of the distribution indicates the shortest evaporation time, while the rightmost side of the distribution marks the longest evaporation time. Color identifies the probability (blue-low; yellow-high) of having a certain evaporation time. Empty black dots represent the mean evaporation time. The predicted evaporation (d^2-law) is reported with a solid red line.

the ambient air), but instead, they will sample the thermodynamics conditions of the turbulent gas cloud generated by the second sneeze.

Second, we evaluate the dispersion of the droplets analyzing the resulting exposure maps, figure 11.

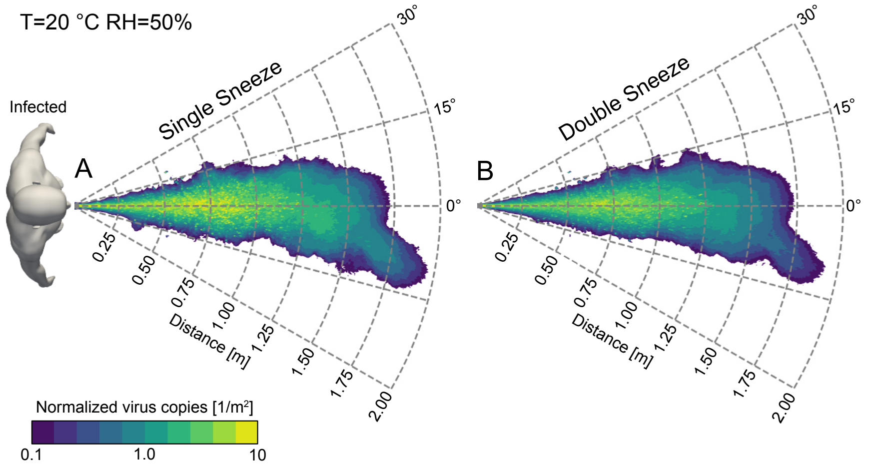

Figure 11: Virus exposure maps obtained considering a single sneezing event (A) and multiple sneezing events (B). Results are shown normalized by the total number of virus copies ejected during the single sneeze (A) or the two sneezes (B). Results refer to $T = 20°C$ and $RH = 50\%$.

As in the manuscript, exposure maps are computed counting the cumulative number of virus copies that go past a control area in different locations of the domain; data for the exposure maps is collected over a time interval of 4 seconds for both cases. These maps are then normalized dividing by the total number of virions ejected (double for this new case considered). Similar dispersion and spreading in the forward horizontal direction are observed between the single sneeze and the double sneeze case, indicating indeed that the presence on a cloud of warm and moist air emitted during the first sneeze does not particularly affect the evolution of the second sneeze and the dispersion of the droplets emitted. Thus, similarly to the evaporation times, also the virus exposure maps are not significantly influenced by the second sneezing event. Please note that since the results are normalized by the total number of virus copies ejected, for the same value of exposure the dimensional concentration of virus copies is double when a sequence of two sneezes is considered.

Initial droplet size distribution

We move now to discuss the results obtained from simulation S6. This simulation considers the case in which the size of the injected droplets follows a Pareto distribution. We start by analyzing the resulting evaporation times of the droplets, which are reported in figure 12.

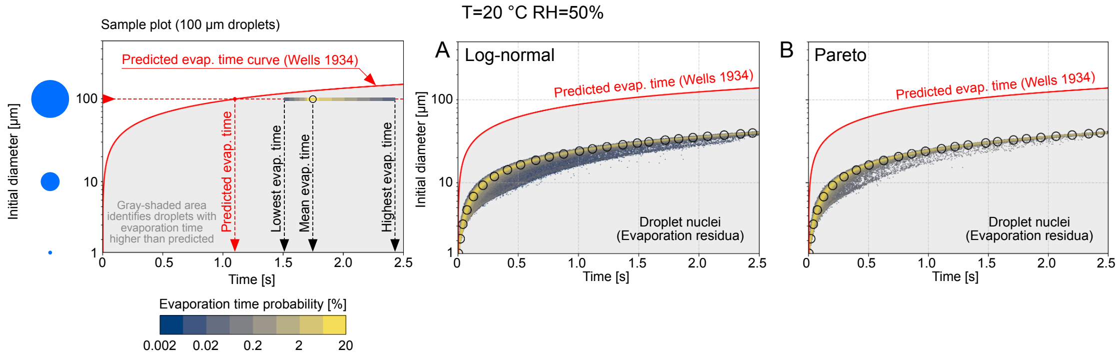

Figure 12: Distribution of droplets evaporation times when a log-normal (A) and a Pareto (B) distribution are used. For any initial diameter, the leftmost side of the distribution indicates the shortest evaporation time, while the rightmost side of the distribution marks the longest evaporation time. Color identifies the probability (blue-low; yellow-high) of having a certain evaporation time. Empty black dots represent the mean evaporation time. d^2-law predictions are reported with a solid red line.

Looking at the plots, we can observe how the two resulting distributions are very similar. Being the initial size distribution different, marginal difference can be noticed in the number of samples present in the different diameter classes. Overall, this indicates that the evaporation times are not significantly influenced by the prescribed initial size distribution. This behavior can be somehow expected as we are in a dilute regime (low volume fractions).

We move now to the virus exposure maps, which are shown in figure 13.

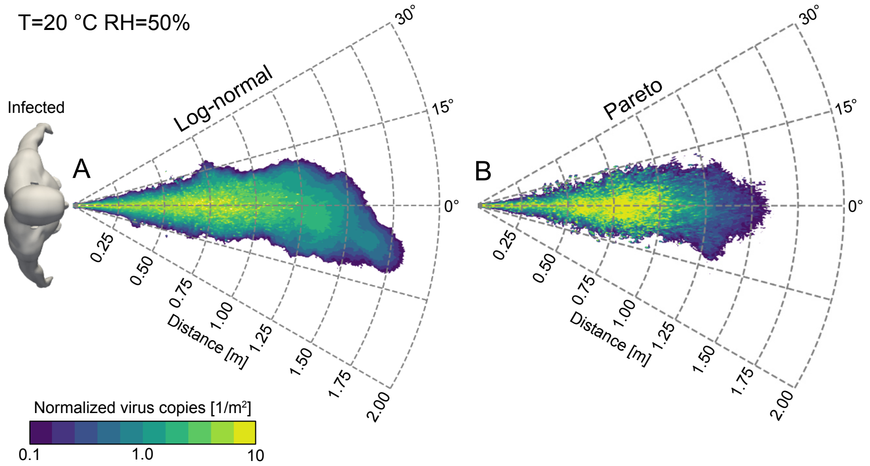

Figure 13: Virus exposure maps obtained assuming a log-normal distribution (A) and a Pareto distribution (B). Results are shown normalized by the total number of virus copies ejected during the single sneeze (almost the same for both cases). Both simulations consider $T = 20°C$ and $RH = 50\%$.

Panel A refers to the simulation performed using a log-normal distribution (as in the manuscript), while panel B refers to the simulation performed using a Pareto distribution. We can observe that the general picture offered by the exposure map is similar and for both cases there is a core region characterized by a high-level of virus exposure surrounded by an outer region characterized by a lower level of virus exposure. As well, the extension (and thus the dispersion pattern) of the respiratory droplets is similar and for both cases the front of the jet reaches the distance of about 1.65 m. Some differences can be noticed in the transitions between the different levels of virus exposure, which are smoother when a log-normal distribution is used. These difference can be traced back to the lower number of 10 to 15 μm droplets present in the simulation that uses a Pareto distribution. As the liquid mass ejected is the same for both cases, the lack of smaller droplets in the Pareto distribution simulation is balanced out by the presence of larger droplets, which generate hotspots of viral load (and consequently a higher local exposure value), and thus a noisier exposure map.

Effect of face covering

With the aim of briefly discussing the effect of face covering, we performed a series of additional experiments in which different types of protecting devices are adopted. We use advanced imaging techniques to qualitatively evaluate the action of protective devices against droplets spread. In particular, we examine qualitatively the capability of protective devices to prevent the possibility of host-to-host direct contagion. By direct contagion we mean here the exposure to the direct emission of droplets ejected from the mouth or to the droplets carried by the puff propelled forward by the emitter during normal breathing, coughing, sneezing, talking etc. [3]. The following configurations have been considered:

- No face-covering device;
- Surgical mask Level I/Type I, conforming to norm ASTM F2100 for US, to EN 14683 for EU and YY-0469 for China (figure 14A);
- Respirator mask N95/FFP2/KN95, conforming to norm NIOSH 42 for US, to EN 149 for EU and GB2626 for China (figure 14B);
- Face shield, conforming to EN 166 for EU (figure 14C).

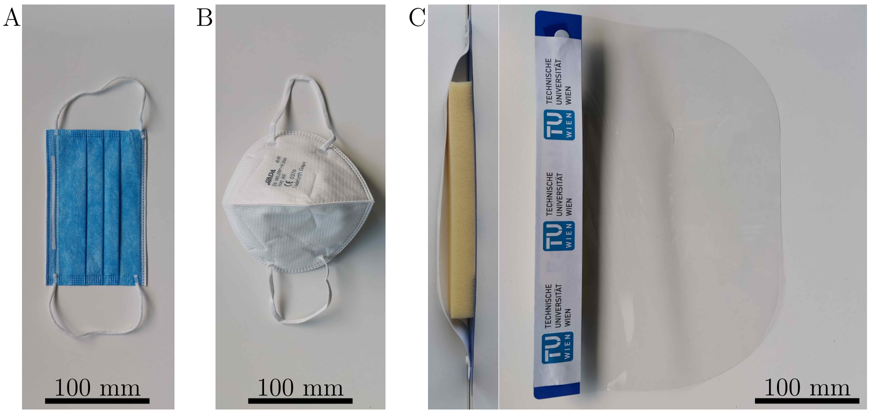

Figure 14: Face covering devices tested: surgical mask level I/Type I (A), respirator mask N95/FFP2/KN95 (B) and face shield (C, top and front view).

In these experiments, the inlet velocity condition is the same described in figure 6. We show in figure 15 the light intensity distribution recorded using different types of face covering devices. The color indicates the light intensity recorded, from low (white) to high (black) values. The amount of light scattered by the airborne drops and recorded by the cameras is proportional to the local number of drops. Therefore, on a qualitative basis, the light intensity distribution corresponds to the concentration distribution of droplets. The instant considered is the same for all cases shown and corresponds to time $t = 0.15$ s, being $t = 0$ the instant at which the flow starts. One comparative movie (Movie S5) representing the time-dependent evolution of the flow in all configurations considered is also available in the electronic supplementary material[36]. Although these visualizations represent just a qualitative picture of the distribution of droplets emitted, it is possible to analyze the effect of protective devices on the spread of the droplets. We observe in figure 15(B-D) that for all devices considered and in the time window investigated, the advection-diffusion process of the droplets in the horizontal forward direction is decreased with respect to the case without protective devices, shown in figure 15(A). Moreover, we also note that the breathing puffs are mainly evacuated from the venting located at the gaps between the protective devices rims and the face of the dummy. For the face shield, puffs are mainly evacuated downward (i.e. towards the neck of the dummy), whereas for surgical and respiratory masks, a much reduced flow-rate of puffs is evacuated downward/backward towards the neck of the dummy. However, the numbers of droplets emitted from the upper rim (i.e. in the nasal bridge area) is much larger than the number of droplets emitted towards the neck. Eventually the droplets carried by the rising plume are observed to slowly propagate few centimeters in forward direction. From our qualitative analysis, we observe that the action produced by protective devices against droplets spread is effective to prevent host-to-host direct contagion. However, to provide detailed and quantitative information about the impact of the devices on the amount of droplets suspended, further analysis are required. Please also refer to recent works [2, 8] for a detailed discussion on face-covering devices.

Bibliography

[1] B. Abramzon and W. A. Sirignano. Droplet vaporization model for spray combustion calculations. *Int. J. Heat Mass Transf.*, 32(9):1605–1618, 1989.

[2] G. Bagheri, B. Thiede, B. Hejazi, O. Schlenczek, and E. Bodenschatz. An upper bound on one-to-one exposure to infectious human respiratory particles. *Proc. Natl. Acad. Sci. USA*, 118 (49):e2110117118, 2021.

[3] S. Balachandar, S. Zaleski, A. Soldati, G. Ahmadi, and L. Bourouiba. Host-to-host airborne transmission as a multiphase flow problem for science-based social distance guidelines. *Int. J. Multiph. Flow*, 132:103439, 2020.

[4] Dehandschoewercker E. & Bush J. W. Bourouiba, L. Violent expiratory events: on coughing and sneezing. *J. Fluid Mech.*, 745:537–563, 2014.

[5] L. Bourouiba. Turbulent gas clouds and respiratory pathogen emissions: Potential implications for reducing transmission of covid-19. *JAMA*, 323(18):1837–1838, 2020.

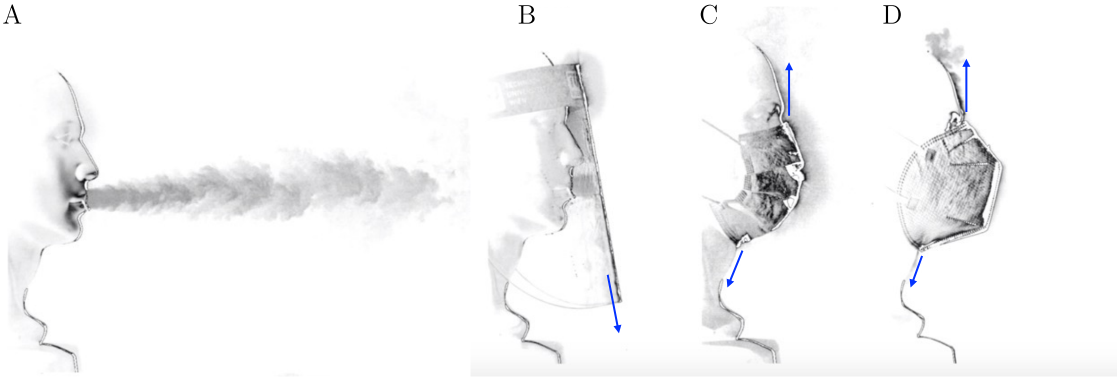

Figure 15: Comparison of the effect of different type of face covering. “Still” frame taken at $t = 0.15$ s from Movie S5[36]. Experimental measurements are reported in four flow configurations: no face-covering device (A), surgical mask level I/Type I (B), respirator mask N95/FFP2/KN95 (C) and face shield (D). The color indicates the light intensity recorded, from low (white) to high (black) values. On a qualitative basis, the light intensity distribution corresponds to the concentration distribution of droplets. In the configurations considered and in the time window investigated, the advection-diffusion process of the droplets in horizontal forward direction is decreased with respect to the case without protective devices. The breathing puffs are mainly evacuated from the venting occurring at the gaps between the protective devices rims and the face of the dummy.

[6] Giacomo Busco, Se Ro Yang, Joseph Seo, and Yassin A. Hassan. Sneezing and asymptomatic virus transmission. *Phys. Fluids*, 32(7):073309, 2020.

[7] Swetaprovo Chaudhuri, Saptarshi Basu, Prasenjit Kabi, Vishnu R. Unni, and Abhishek Saha. Modeling the role of respiratory droplets in covid-19 type pandemics. *Phys. Fluids*, 32(6): 063309, 2020.

[8] Yafang Cheng, Nan Ma, Christian Witt, Steffen Rapp, Philipp S. Wild, Meinrat O. Andreae, Ulrich Pöschl, and Hang Su. Face masks effectively limit the probability of sars-cov-2 transmission. *Science*, 372(6549):1439–1443, 2021.

[9] Federico Dalla Barba and Francesco Picano. Clustering and entrainment effects on the evaporation of dilute droplets in a turbulent jet. *Phys. Rev. Fluids*, 3(3):034304, 2018.

[10] *Seeding Generator for LDA and PIV.* Dantec Dynamics, 2009.

[11] Talib Dbouk and Dimitris Drikakis. On coughing and airborne droplet transmission to humans. *Phys. Fluids*, 32(5):053310, 2020.

[12] Talib Dbouk and Dimitris Drikakis. On respiratory droplets and face masks. *Phys. Fluids*, 32 (6):063303, 2020.

[13] Santanu De, K. N. Lakshmisha, and Robert W. Bilger. Modeling of nonreacting and reacting turbulent spray jets using a fully stochastic separated flow approach. *Combustion flame*, 158 (10):1992–2008, 2011.

[14] J. P. Duguid. The size and the duration of air-carriage of respiratory droplets and droplet-nuclei. *J. Hyg.*, 44(6):471–479, 1946.

[15] A. Favre. Turbulence: Space-time statistical properties and behavior in supersonic flows. *Phys. Fluids*, 26(10):2851, 1983.

[16] G. A. Ferron, B. Haider, and W. G. Kreyling. Inhalation of salt aerosol particles—i. estimation of the temperature and relative humidity of the air in the human upper airways. *J. Aerosol Sci.*, 19(3):343–363, 1988.

[17] N. Froessling. On the evaporation of falling drops. *Army Biological Labs Frederick MD*, 1968.

[18] Rafael C Gonzalez, Steven L Eddins, and Richard E Woods. *Digital image publishing using MATLAB*. Prentice Hall, 2004.

[19] J. K. Gupta, C-H Lin, and Q. Chen. Flow dynamics and characterization of a cough. *Indoor air*, 19(6):517–525, 2009. ISSN 0905-6947.

[20] G. R. Johnson, L. Morawska, Z. D. Ristovski, M. Hargreaves, K. Mengersen, C.Y.H. Chao, M. P. Wan, Y. Li, X. Xie, D. Katoshevski, and S. Corbett. Modality of human expired aerosol size distributions. *J. Aerosol Sci.*, 42(12):839–851, 2011.

[21] George Marsaglia and Wai Wan Tsang. The ziggurat method for generating random variables. *J. Stat. Soft.*, 5(8):1–7, 2000.

[22] L. Morawska, G. R. Johnson, Z. D. Ristovski, M. Hargreaves, K. Mengersen, S. Corbett, C.Y.H. Chao, Y. Li, and D. Katoshevski. Size distribution and sites of origin of droplets expelled from the human respiratory tract during expiratory activities. *J. Aerosol Sci.*, 40(3):256–269, 2009.

[23] F. Picano, F. Battista, G. Troiani, and C. M. Casciola. Dynamics of piv seeding particles in turbulent premixed flames. *Exp. Fluids*, 50(1):75–88, 2011.

[24] A. Picard, R. S. Davis, M. Gläser, and K. Fujii. Revised formula for the density of moist air (cipm-2007). *Metrologia*, 45(2):149–155, 2008.

[25] John Redrow, Shaolin Mao, Ismail Celik, J. Alejandro Posada, and Zhi gang Feng. Modeling the evaporation and dispersion of airborne sputum droplets expelled from a human cough. *BUILD. ENVIRON.*, 46(10):2042–2051, 2011.

[26] G. Rocco, F. Battista, F. Picano, G. Troiani, and C. M. Casciola. Curvature effects in turbulent premixed flames of h2/air: a dns study with reduced chemistry. *Flow Turbulence Combust.*, 94 (2):359–379, 2015.

[27] M. E. Rosti, S. Olivieri, M. Cavaiola, A. Seminara, and A. Mazzino. Fluid dynamics of covid-19 airborne infection suggests urgent data for a scientific design of social distancing. *Sci. Rep.*, 10 (1):22426, 2020.

[28] R. Sangras, O. C. Kwon, and G. M. Faeth. Self-preserving properties of unsteady round nonbuoyant turbulent starting jets and puffs in still fluids. *J. Heat Transfer*, 124(3):460–469, 2002.

[29] Helmut Schmidt and Ulrich Schumann. Coherent structure of the convective boundary layer derived from large-eddy simulations. *J. Fluid Mech.*, 200:511–562, 1989.

[30] J. Smagorinsky. General circulation experiments with the primitive equations. *Mon. Wea. Rev.*, 91(3):99–164, 1963.

[31] Scott H. Smith, G. Aernout Somsen, Cees van Rijn, Stefan Kooij, Lia van der Hoek, Reinout A. Bem, and Daniel Bonn. Aerosol persistence in relation to possible transmission of sars-cov-2. *Phys. Fluids*, 32(10):107108, 2020.

[32] Valentyn Stadnytskyi, Christina E. Bax, Adriaan Bax, and Philip Anfinrud. The airborne lifetime of small speech droplets and their potential importance in sars-cov-2 transmission. *Proc. Natl. Acad. Sci. U.S.A*, 117(22):11875–11877, 2020.

[33] Cameron Tropea, Alexander L. Yarin, and John F. Foss. *Springer Handbook of Experimental Fluid Mechanics.* 2007.

[34] P. T. Tsilingiris. Thermophysical and transport properties of humid air at temperature range between 0 and 100°c. *Energy Convers. Manag.*, 49(5):1098–1110, 2008.

[35] Eric P. Vejerano and Linsey C. Marr. Physico-chemical characteristics of evaporating respiratory fluid droplets. *J. R. Soc. Interface*, 15(139), 2018.

[36] Jietuo Wang, Mobin Alipour, Giovanni Soligo, Alessio Roccon, Marco de Paoli, Francesco Picano, and Alfredo Soldati. Short-range exposure to airborne virus transmission and current guidelines. *Proc. Natl. Acad. Sci. U.S.A*, 118(37), 2021.

[37] Jietuo Wang, Federico Dalla Barba, and Francesco Picano. Direct numerical simulation of an evaporating turbulent diluted jet-spray at moderate reynolds number. *Int. J. Multiph. Flow*, 137:103567, 2021.

[38] X. Xie, Y. Li, A. T. Chwang, P. L. Ho, and W. H. Seto. How far droplets can move in indoor environments – revisiting the wells evaporation–falling curve. *Indoor air*, 17(3):211–225, 2007. ISSN 0905-6947.

[39] C. Xu, P. V. Nielsen, G. Gong, L. Liu, and R. L. Jensen. Measuring the exhaled breath of a manikin and human subjects. *Indoor air*, 25(2):188–197, 2015. ISSN 0905-6947.

[40] Fan Yang, Amir A. Pahlavan, Simon Mendez, Manouk Abkarian, and Howard A. Stone. Towards improved social distancing guidelines: Space and time dependence of virus transmission from speech-driven aerosol transport between two individuals. *Phys. Rev. Fluids*, 5(12), 2020.

Appendix D

Paper IV

Revisiting $\mathcal{D}^2$-law for the evaporation of dilute droplets

Federico Dalla Barba[1], **Jietuo Wang**[2], **Francesco Picano**[1,2]

1. Department of Industrial Engineering, University of Padova,
35131, Padova, Italy
2. Centro di Ateneo di Studi e Attività Spaziali "Giuseppe Colombo" - CISAS,
University of Padova, 35131, Padova, Italy

Physics of fluid, 2021, 33(5), 051701.

Abstract: In a wide range of applications, the estimate of droplet evaporation time is based on the classical $\mathcal{D}^2$-law, which, assuming a fast mixing and fixed environmental properties, states that the droplet surface decreases linearly with time at a determined rate. However, in many cases the predicted evaporation rate is overestimated. In this Letter, we propose a revision of the $\mathcal{D}^2$-law capable to accurately determine droplet evaporation rate in dilute conditions by a proper estimate of the asymptotic droplet properties. Besides a discussion of the main assumptions, we tested the proposed model against data from direct numerical simulations finding an excellent agreement for predicted droplet evaporation time in dilute turbulent jet-sprays.

The prediction of droplet evaporation in turbulent flows is crucial in science and applications, e.g. in internal combustion engines [2] or respiratory flows [12]. The outbreak of COVID-19 pandemic is highly increasing the scientific relevance of this topic [3, 6, 14]: Virus-laden droplets dispersed into the environment by an infected person spread the disease [16], but their dispersion range, although at the base of health guidelines, is still scientifically debated [3, 6, 12, 14]. For practical estimates, the prediction of droplet dispersion is still based on the work of Wells [20], which is founded on the $\mathcal{D}^2$-law to compute droplet evaporation rate. The $\mathcal{D}^2$-law, proposed in the seminal works of Langmuir [11] and others [9, 17], states that the surface of an evaporating droplet decreases linearly with time, at a rate fixed by the ambient properties. Although deviations from the classical $\mathcal{D}^2$-law have been observed in some peculiar conditions, e.g. for droplet sizes of the order of the mean vapor's free path [15], trans-critical evaporation of nano/micro-droplets [21] and multi-component droplets [10, 13], a linear decrease of the droplet surface is usually observed for single-component micro/millimetric droplets. Nonetheless, recent studies on respiratory events [6, 14] found that droplet lifetime may increase even 150 times as compared to the Wells's estimate; although a linear decrease of the droplet surface could still be observed, the evaporation rate is found to be much lower than that predicted by the $\mathcal{D}^2$-law. Considering that the temperature of an evaporating droplet tends to a value lower than the environmental one, we propose a revision of the $\mathcal{D}^2$-law for single component, millimetric/micrometric droplets. This effect, caused by the balance between heat flux and latent enthalpy, is not accounted for in the classical formulation of the $\mathcal{D}^2$-law, which assumes a fast mixing of the gas around the droplet. We show that, by including this effect in a revised $\mathcal{D}^2$-law, the droplet evaporation time can be accurately estimated in dilute conditions. To this purpose, the revised and the classical $\mathcal{D}^2$-laws are compared to reference data obtained from Direct Numerical Simulations (DNS) under a hybrid Eulerian-Lagrangian framework and the point-droplet approximation [1, 5, 19]. For droplets smaller than the smallest flow length-scale, the temporal evolution can be Lagrangianly described using the so-called *point-droplet approximation* [1, 19]. Indeed, droplet temperature and radius equations read,

$$\frac{dT_d}{dt} = \frac{1}{3\tau_d}\left[\frac{Nu}{\bar{Pr}}\frac{\bar{c_p}}{c_l}(T_m - T_d) - \frac{Sh}{\bar{Sc}}\frac{\Delta H_v}{c_l}H_m\right], \tag{1}$$

$$\frac{dr_d^2}{dt} = -\frac{Sh}{\bar{Sc}}\frac{\bar{\rho}}{\rho_l}\bar{\nu}H_m, \tag{2}$$

where T_d is the droplet temperature, r_d the radius and T_m the temperature of the carrier mixture evaluated at the droplet center. The variable $\tau_d = 2\rho_l r_d^2/(9\bar{\rho}\bar{\nu})$ is the droplet relaxation time, whereas the Schmidt and Prandtl number are $\bar{Sc} = \bar{\nu}/D_{g,v}$ and $\bar{Pr} = \bar{\nu}\bar{\rho}\bar{c_p}/\bar{k}$, with $\bar{\nu}$ the kinematic viscosity, $\bar{\rho}$ the density, $\bar{c}_p$ the isobaric specific heat capacity and $\bar{k}$ the thermal conductivity of the gas. The mass diffusivity is $D_{g,v}$, c_l and ρ_l are the specific heat capacity and density of the liquid, and ΔH_v is the latent heat of vaporization (over-bars refer to Eulerian quantities evaluated at droplet centers). In the model a fast conductivity is implicitly assumed, i.e. the liquid thermal conductivity is assumed to be much higher than that of the carrier gas (low Biot number [4]), such that the temperature inside a droplet is uniform, but time-varying. In analogy with $(T_m - T_d)$, which is the forcing term for convective heat transfer, the term H_m drives the mass transfer rate:

$$H_m = ln\left(\frac{1 - Y_{v,m}}{1 - Y_{v,d}}\right), \tag{3}$$

with $Y_{v,m}(\chi_{v,m})$ the vapor mass fraction evaluated at the droplet center and $Y_{v,d}(\chi_{v,d})$ the mass fraction of a saturated gas-vapor mixture evaluated at the temperature of the droplet, T_d. The mass fractions depend on the vapor molar fractions which, in turn, are related to the vapor pressure as:

$$\chi_{v,m} = RH_m\,\frac{p_{sv}(T_m)}{p_a}, \quad \chi_{v,d} = 1.0\,\frac{p_{sv}(T_d)}{p_a}, \tag{4}$$

where p_a is the ambient pressure, $p_{sv}(T)$ the saturated vapor pressure evaluated at T, and RH_m the relative humidity of the moist carrier evaluated at the point-droplet center. The saturated vapor pressure, $p_{sv}(T)$, depends on temperature and pressure and can be calculated by using the Clausius-Clapeyron equation. Finally, the Nusselt and Sherwood numbers are correlated to the droplet Reynolds number via the Frössling correlations, see e.g. Wang et al. [18] for details.

Based on Eq. (1)- (2), for an isolated droplet in an environment at temperature $T_m = T_a$ and relative humidity $RH_m = RH_a$, the classical formulation of $\mathcal{D}^2$-law [11] can be derived by assuming a fast mixing of the droplet atmosphere with the environment. Under this hypothesis, the quantities regulating the evaporation of the droplet are set by the bulk thermodynamic state of the ambient ($\bar{\rho} = \rho_a$, $\bar{\nu} = \nu_a$, $\bar{Sc} = Sc_a$ and $\bar{Pr} = Pr_a$). With the droplet temperature fixed to $T_d = T_a$, Eq. (2) can be exactly integrated as:

$$r_d^2 = r_{d,0}^2 - K\ t, \tag{5}$$

where $r_{d,0}$ is the initial droplet radius and K is a function of the bulk properties of the ambient T_a,

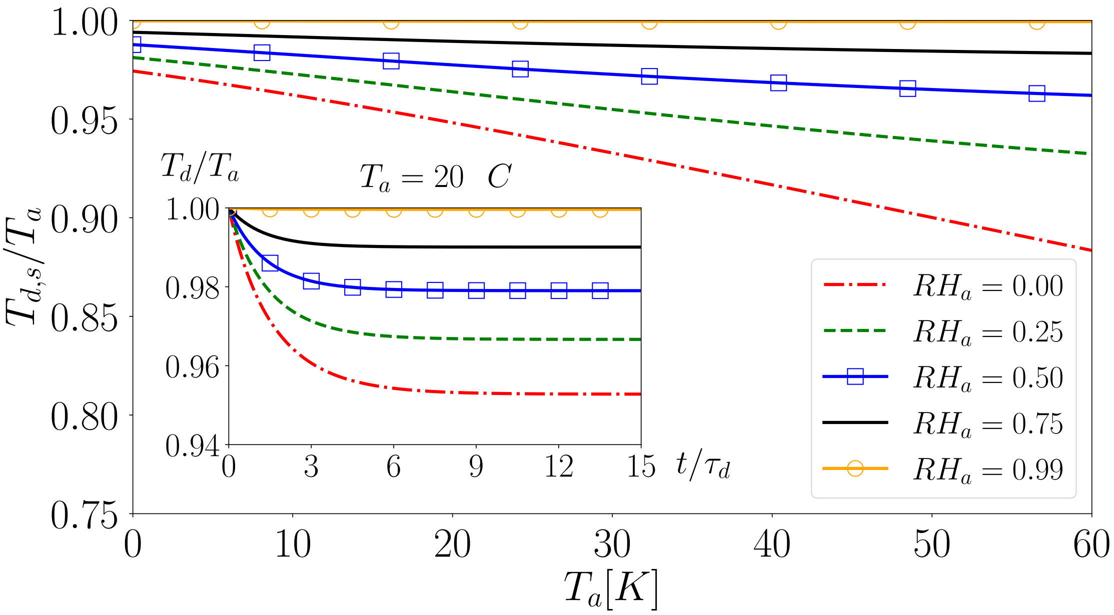

Figure 1: Ratio between the droplet asymptotic temperature, $T_{d,s}$, and ambient one, T_a, versus ambient temperature for isolated water droplets. Inset: temporal evolution of the temperature of evaporating water droplets; the time is normalized by τ_d. Data are obtained by the numerical solution of Eq. (1) and Eq. (2).

p_a and RH_a:

$$K = \frac{\rho_a}{\rho_l}\frac{Sh}{Sc_a}\nu_a H_m(T_a, p_a, RH_a). \tag{6}$$

Then, the droplet evaporation time can be estimated as $t_{d,e} = r_{d,0}^2/K$. Eq. (5) is historically referred to as $\mathcal{D}^2$-law since it predicts a quadratic temporal evolution of the droplet diameter. It assumes that the droplet temperature is fixed and equal to the environmental one, $T_d \simeq T_a$; in turn, this condition implicitly assumes that the convective heat transfer term in the droplet temperature equation, Eq. (1), dominates the latent heat term. Nonetheless, in real cases, this condition is valid only for a short time, whose duration scales with the droplet relaxation time as sketched in the inset of Fig. 1. After a time $t \simeq 6\tau_{d,0}$, the droplet temperature sets to a constant value, $T_{d,s}$, which is lower than the environmental temperature, T_a. The ratio between T_a and $T_{d,s}$, determined by the balance between convective heat transfer and latent heat absorption, depends on the ambient temperature itself and relative humidity, as shown in Fig. 1. The droplet temperature is similar to the ambient one only for $t \ll \tau_{d,0}$, whereas, for the major part of the vaporization process, it keeps closer to the asymptotic temperature, $T_{d,s}$. Since the prediction of the droplet lifetime using the $\mathcal{D}^2$-law is highly sensitive to the droplet temperature, the latter may induce a significant overestimation of the evaporation rate [6, 18]. Hence, we propose to revise the $\mathcal{D}^2$-law assuming a constant droplet temperature equal to the droplet asymptotic temperature and not to the ambient one: $T_d \simeq T_{d,s}$. In these conditions, Eq. (1) and Eq. (3) become:

$$T_{d,s} + \frac{Pr_a}{Sc_a}\frac{Sh}{Nu}\frac{\Delta H_v}{c_{p,a}} H_m(T_a, p_a, RH_a, T_{d,s}) - T_a = 0, \tag{7}$$

$$H_m = ln\left(\frac{1 - Y_{v,a}(T_a, p_a, RH_a)}{1 - Y_{v,d}(T_{d,s}, p_a)}\right), \tag{8}$$

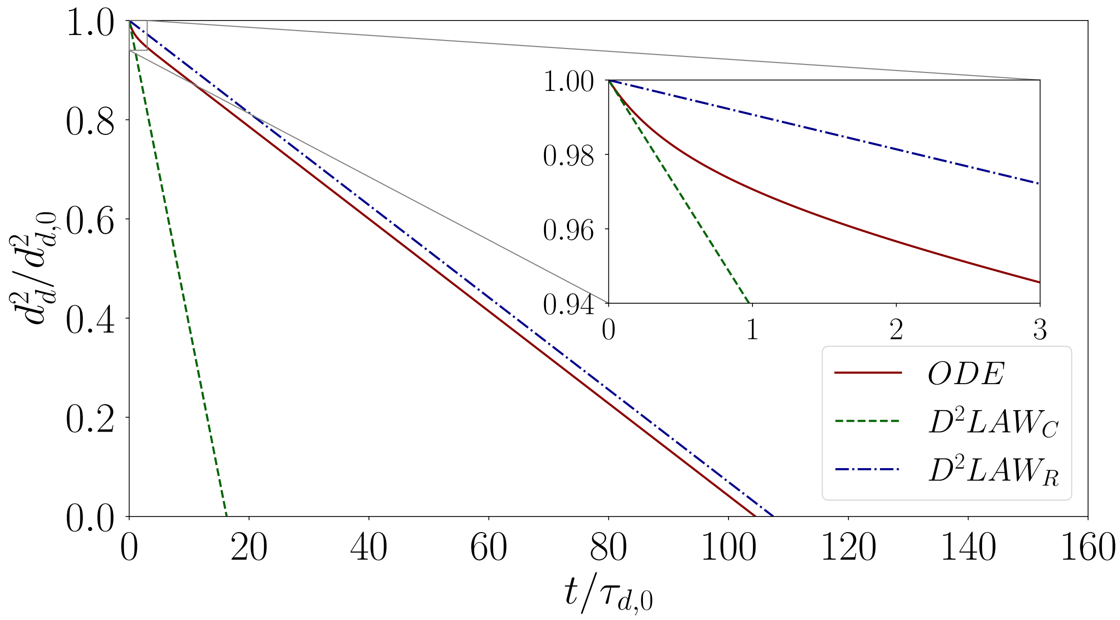

Figure 2: Temporal evolution of the square diameter, $d_d^2/d_{d,0}^2$, of a water droplet in a quiescent environment at temperature $T_a = 50\ ^\circ C$ and relative humidity $RH_a = 0$, with $d_{d,0}$ the initial droplet diameter. Exact solution of Eq. (1) and Eq. (2) (ODE), classical $\mathcal{D}^2$-law (D^2LAW_C) and revised formulation (D^2LAW_R).

which can be easily solved for $T_{d,s}$. The latter can be employed to compute a revised decay constant, K_r,

$$K_r = \frac{\rho_a}{\rho_l}\frac{Sh}{Sc_a}\nu_a H_m(T_a, p_a, RH_a, T_{d,s}), \tag{9}$$

$$r_d^2 = r_{d,0}^2 - K_r\ t, \tag{10}$$

leading to a revised evaporation time, $t_{d,e} = r_{d,0}^2/K_r$. Fig. 2 shows the temporal evolution of the square diameter of a water droplet in a quiescent environment at $T_a = 50\ ^\circ C$ and $RH_a = 0$, providing the numerical solution of Eq. (2) and the predictions by the classical and revised $\mathcal{D}^2$-laws. In the initial evaporation phase, $t \ll \tau_{d,0}$, since $T_d \simeq T_a$, the vaporization rate predicted by the classical $\mathcal{D}^2$-law is close to the reference one (numerical solution of Eq. (2)). Nonetheless, for $t \gg \tau_{d,0}$, the behavior predicted using the revised $\mathcal{D}^2$-law guarantees a much better agreement with the reference data. Fig. 3 shows the value of the decay constants K and K_r for water droplets versus ambient temperature at different relative humidities. The relative difference between K_r and K increases with T_a and reduces with RH_a. It is worth remarking that this difference spans over nearly one order of magnitude, leading to a significant mismatch in the evaporation rates estimated by using the bulk ambient temperature or the droplet asymptotic temperature.

To test the proposed revision of the $\mathcal{D}^2$-law, we consider a turbulent evaporating jet-spray. The well-established framework of the point-droplet equations is used to predict the temporal evolution of droplet temperature and radius (Eq. 1-Eq. 2) together with the Lagrangian equations of motion [8, 18, 19]. The droplet equations are coupled with the low-Mach number asymptotic expansion of the Navier-Stokes equations, which are directly solved to reproduce the dynamics of the carrier flow. A fully developed turbulent jet, generated from a companion DNS of a turbulent pipe flow [8] at $Re_0 = 2U_0\, R_0/\nu = 6000$, is injected into an open, quiescent environment ($U_0 = 9.3\, m/s$ and

$R_0 = 4.9 \cdot 10^{-3}\, m$ the pipe bulk velocity and radius). Both the jet and the environment gases consist of dry air at temperature $T_a = 20°C$. The computational domain is a cylinder extending for $2\pi \times 22R_0 \times 70R_0$ in the azimuthal, θ, radial, r and axial, z, directions and is discretized by a staggered grid of $N_\theta \times N_r \times N_z = 128 \times 223 \times 640$ nodes. A convective boundary condition is prescribed at the outlet section and a traction-free boundary condition is imposed on the domain side boundary to allow entrainment. A monodisperse population of water droplets of initial radius $r_{d,0} = 4\mu m$ and temperature $T_{d,0} = T_a = 20°C$ is randomly distributed over the inflow section at each time-step. Four simulations have been performed changing the liquid mass fraction at the inflow: $\psi_0 = m_l/m_g = 0.0007; 0.0028; 0.0058; 0.01$, with m_l and m_g the mass of the liquid and gas injected per unit time, which correspond to 8.7×10^{-7}; 3.5×10^{-6}; 7.0×10^{-6}; 1.2×10^{-5} in volume fraction, respectively. Additional two simulations were conducted suppressing the numerical integration of equation Eq. (1) and Eq. (2): In the former, the classical formulation of the $\mathcal{D}^2$-law, Eq. (5), is used to evolve the droplet radius; in the latter, the revised $\mathcal{D}^2$-law is used, Eq. (10). In all cases, the position and velocity of droplets are numerically integrated according to the standard equation of point-droplet [8, 18]. For a detailed description of the methodology and tests the reader is referred to references [7, 8, 18]. It is worth remarking that droplet number density, mass and volume fractions are related parameters to characterize the spray dilution, governing the droplet collision/coalescence rate, mutual interaction via emitted vapor and droplet momentum back-reaction. Since the mass fraction is the parameter which mainly controls the vapor concentration and determines the balance between heat and latent enthalpy fluxes during evaporation, we select this parameter to characterize the spray dilution in present study. Fig. 4 provides the contours of the normalized mean liquid mass fraction and mean droplet diameter in the spray for the simulations based on the classical $\mathcal{D}^2$-law, the revised one, and on the full model for the most dilute case, $\psi_0 = 0.0007$. The average is computed considering a time range of $100t_0$ (200 independent snapshots) after the establishment of a statistically steady regime [8], with $t_0 = R_0/U_0$ the jet advection time scale. Both the distributions

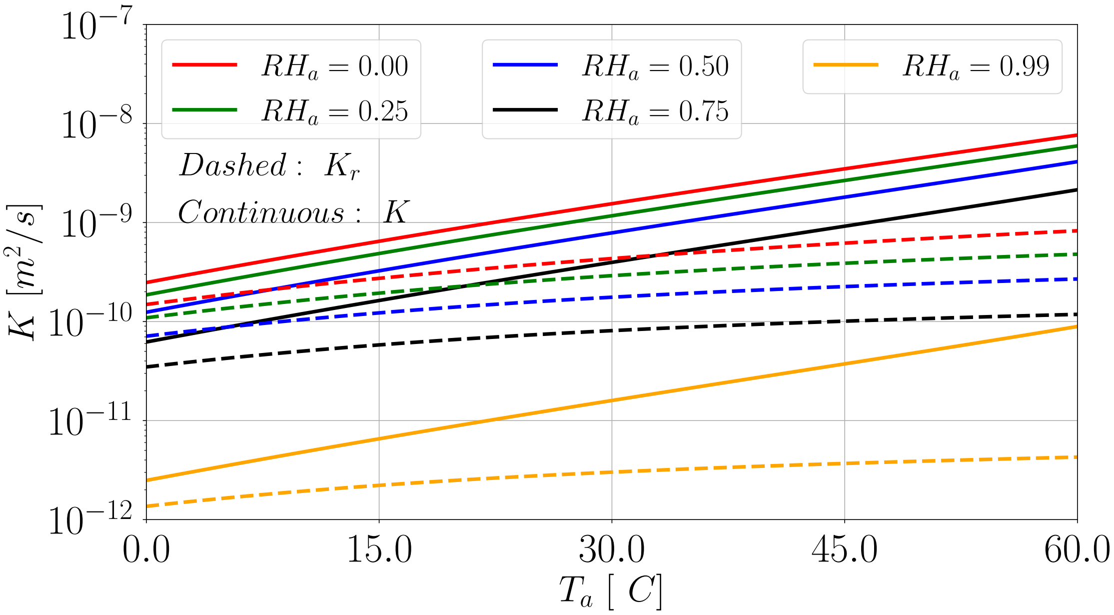

Figure 3: Constant K (Eq. (6); continuous line) and K_r (Eq. (9); dashed lines) for water droplets versus ambient temperature, T_a, for different values of the relative humidity, RH_a.

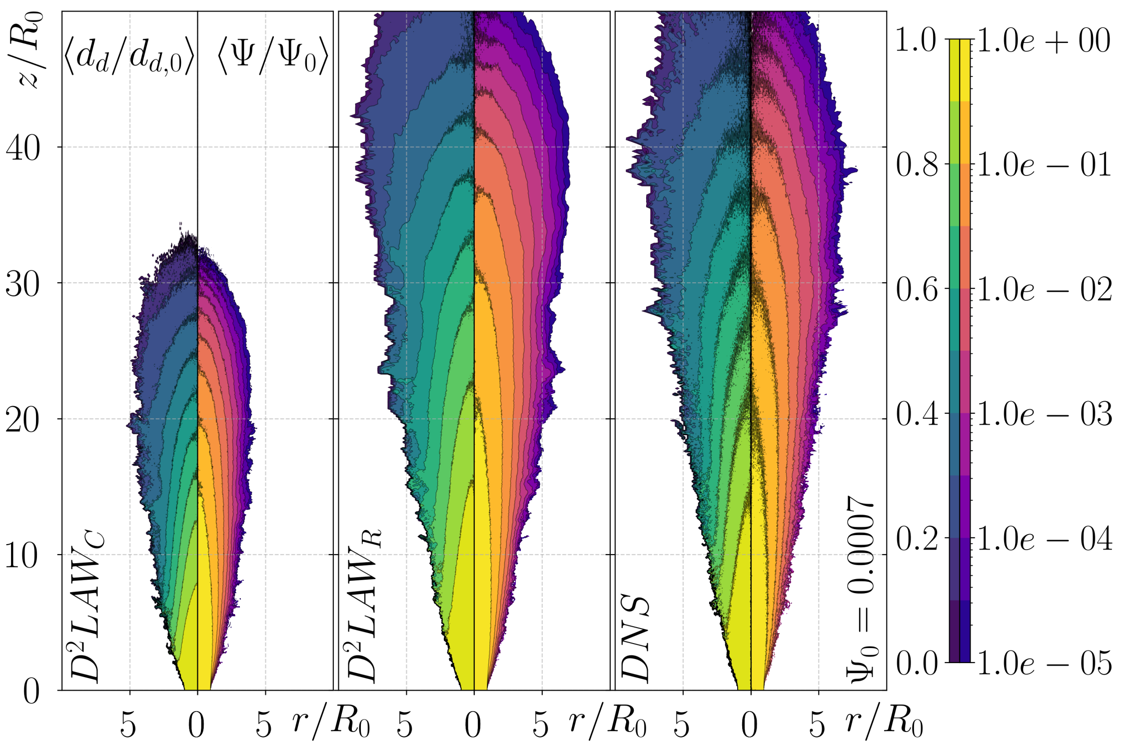

Figure 4: Contour of the mean liquid mass fraction (right-half) and mean droplet diameter (left-half) for $\psi_0 = 0.0007$.

of the mean mass fraction and diameter computed using the revised $\mathcal{D}^2$-law model are in excellent agreement with the reference data. Besides, the classical $\mathcal{D}^2$-law results in a much shorter spray evaporation length, due to the overestimation of the vaporization rate. The evaporation length of a turbulent jet-spray, z_e, can be defined as the distance from the inflow where the 99% of the injected liquid mass has evaporated. This distance corresponds to a mass fraction level of $\psi/\psi_0 = 10^{-2}$ and, hence, to a mean droplet radius $r_{d,99}/r_{d,0} \simeq (\psi/\psi_0)^{1/3} \simeq 10^{-2/3}$. By neglecting possible two-way coupling effects, an estimate of the evaporation length can be obtained by considering the self-similar behavior of the mean jet centerline velocity, $U_{z,c}$ and supposing that the droplet mean axial velocity is approximately $u_{z,d} \simeq U_{z,c}$,

$$\frac{U_{z,c}}{U_0} = \frac{2B}{\frac{z}{R_0} - \frac{z_0}{R_0}} \qquad \Longrightarrow \qquad \frac{R_0}{U_0}\frac{d}{dt}\left(\frac{z_d}{R_0}\right) = \frac{2B}{\frac{z_d}{R_0} - \frac{z_0}{R_0}}, \tag{11}$$

with $B \simeq 6$ a universal constant, z_0 the so-called jet virtual origin [8] and z_d the droplet position along the jet axis. Then, by assuming a vanishing virtual origin, $z_0/R \simeq 0$, and considering that, according to Eq. (5) and Eq. (10), the time required for a droplet to reduce its radius from $r_{d,0}$ to $r_{d,99}$ is $t_{d,e} = (r_{d,0}^2 - r_{d,99}^2)/K$, the integration of Eq. (11) along z leads to:

$$\frac{z_e}{R_0} \simeq 2\sqrt{\frac{B}{\frac{K}{R_0 U_0}}\left[\left(\frac{r_{d,0}}{R_0}\right)^2 - \left(\frac{r_{d,99}}{R_0}\right)^2\right]}, \tag{12}$$

where K is either the decay rate defined according to Eq. (6) or K_r defined in Eq. (9). By using Eq. (12), the resulting evaporation lengths are $z_e/R_0 \simeq 28$ and $z_e/R_0 \simeq 46$, computed by using

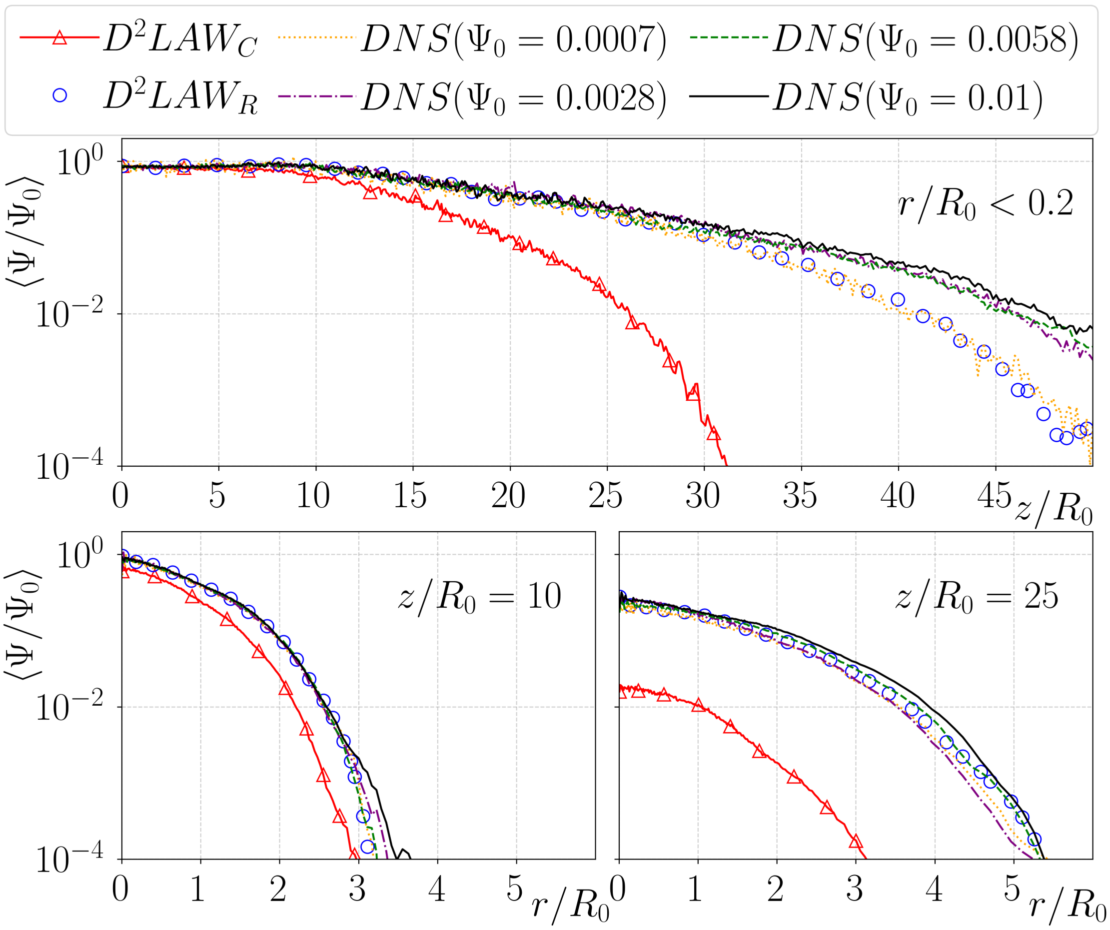

Figure 5: Upper panel: mean liquid mass fraction along the centerline of the jet computed for $r/R_0 < 0.2$. Lower panels: mean liquid mass fraction along the radial direction for two different distances from the inflow, $z/R_0 = 10$ (left) and $z/R_0 = 25$ (right).

K and K_r, respectively. These values are consistent with the axial locations where the 99% of the injected liquid mass has evaporated according to Fig. 4 ($\psi/\psi_0 \simeq 10^{-2}$) showing the superior estimate of the proposed model. To better quantify the evaporation length, the upper panel of Fig. 5 provides the mean liquid mass fraction computed along the jet centerline. In the near-field, up to 10 jet radii away from the inlet, all the curves are close to each other. In this region the actual droplet temperature is close to the environmental one, $T_d \simeq T_a$; being the droplet and ambient temperature similar, the actual evaporation rate is close to the one imposed by the environmental conditions. Moving downstream, the droplet temperature decreases and the classical $\mathcal{D}^2$-law underestimates the mean liquid mass fraction, since droplets evaporate at a constant rate driven by the ambient temperature. On the other hand, the simulation based on the revised $\mathcal{D}^2$-law better approximates the actual droplet temperature, providing a more accurate estimate of the mean evaporation rate and axial evolution of the mean mass fraction. For the latter, the agreement with all the reference simulations is excellent, except for the far-field of the higher mass fraction cases, $\psi_0 > 0.0028$. In non-dilute cases, the mutual droplet interactions, via the emitted vapor, cause a deviation of the local evaporation rate from the one predicted by the $\mathcal{D}^2$-laws. Similar results are obtained for the radial profiles of the mean mass fraction provided in the lower panel of Fig. 5 and computed at $z/R_0 = 10$ and $z/R_0 = 25$. At $z/R_0 = 10$ all curves are still similar, although the simulation

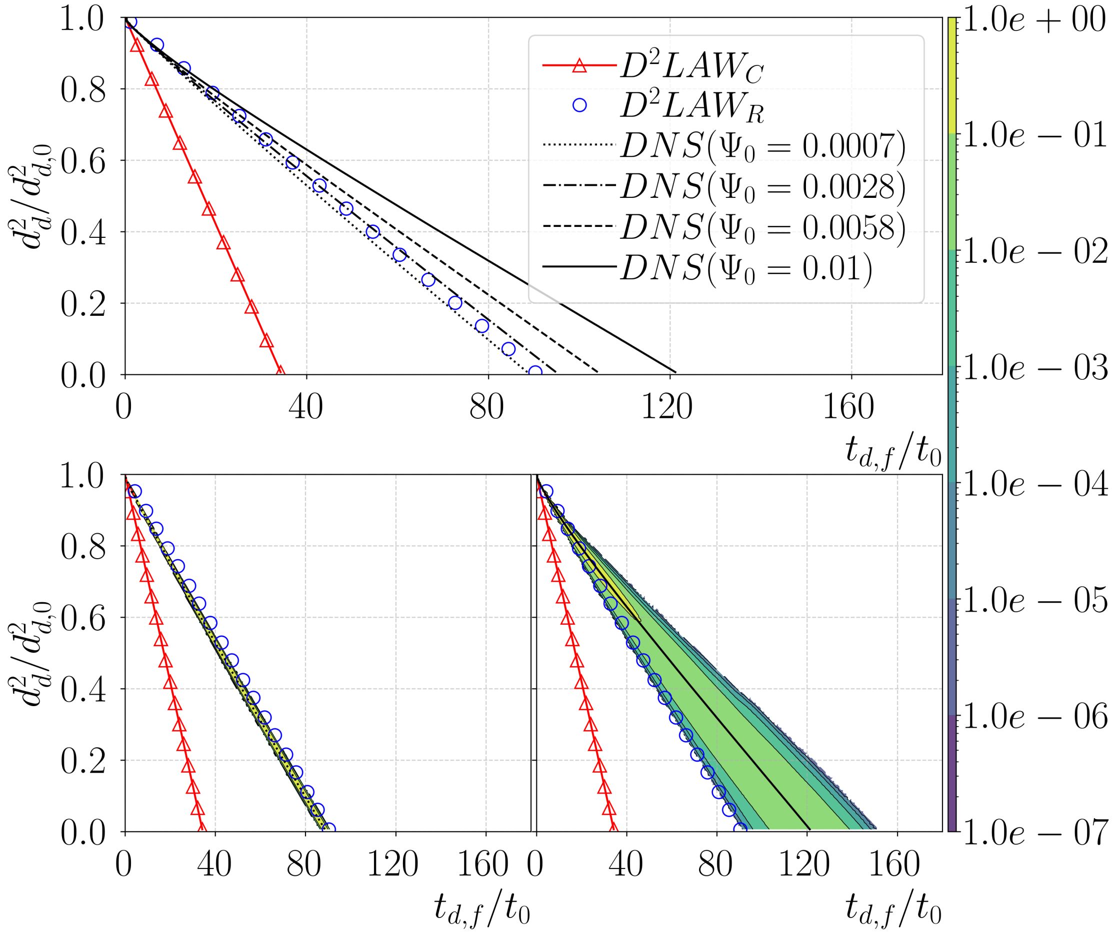

Figure 6: Upper panel: mean droplet square diameter, $d_d^2/d_{d,0}^2$ versus mean droplet flight time, $t_{d,f}/t_0$. Lower panel: joint probability density functions of the droplet square diameter versus flight time for $\psi_0 = 0.0007$ (left) and $\psi_0 = 0.01$ (right).

employing the classical $\mathcal{D}^2$-law shows differences with respect to reference data. Moving downstream, the underestimation of the liquid mass fraction resulting from the classical $\mathcal{D}^2$-law is more apparent, whereas the revised $\mathcal{D}^2$-law still provides an excellent estimate.

Considering Lagrangian statistics, the top panel of Fig. 6 shows the mean droplet square diameter, $d_d^2/d_{d,0}^2$ versus the flight time, $t_{d,f}/t_0$, computed since the injection. In all cases, the evolution of $d_d^2/d_{d,0}^2$ computed from full DNSs are compared with the estimates from the classical and revised $\mathcal{D}^2$-laws. The predictions obtained from the proposed revised model appear much more accurate with respect to the classical formulation. For mass fraction equal, or below, to $\psi_0 = 0.0028$ the agreement is excellent, whereas the classical $\mathcal{D}^2$-law predicts an evaporation time shorter than the half with respect to the reference DNS. Increasing the injected mass fraction, the mutual interactions of droplets slow down the evaporation. From the figure, we conclude that the proposed revised $\mathcal{D}^2$-law optimally describe droplet evaporation in dilute conditions up to mass fractions of the order of $\psi_0 \sim 10^{-3}$. The effect of the mutual interactions of the evaporating droplets is better highlighted in the lower panels of Fig. 6, which provides the Joint Probability Density Functions (JPDF) of $d_d^2/d_{d,0}^2$ vs $t_{d,f}/t_0$ for the lowest and highest mass fraction cases, $\psi_0 = 0.0007$ and $\psi_0 = 0.01$. It is worth noting that, in the most dilute conditions the JPDF is superimposed on the straight line determined by the revised $\mathcal{D}^2$-law: Each droplet evaporates as an isolated one, which is perfectly

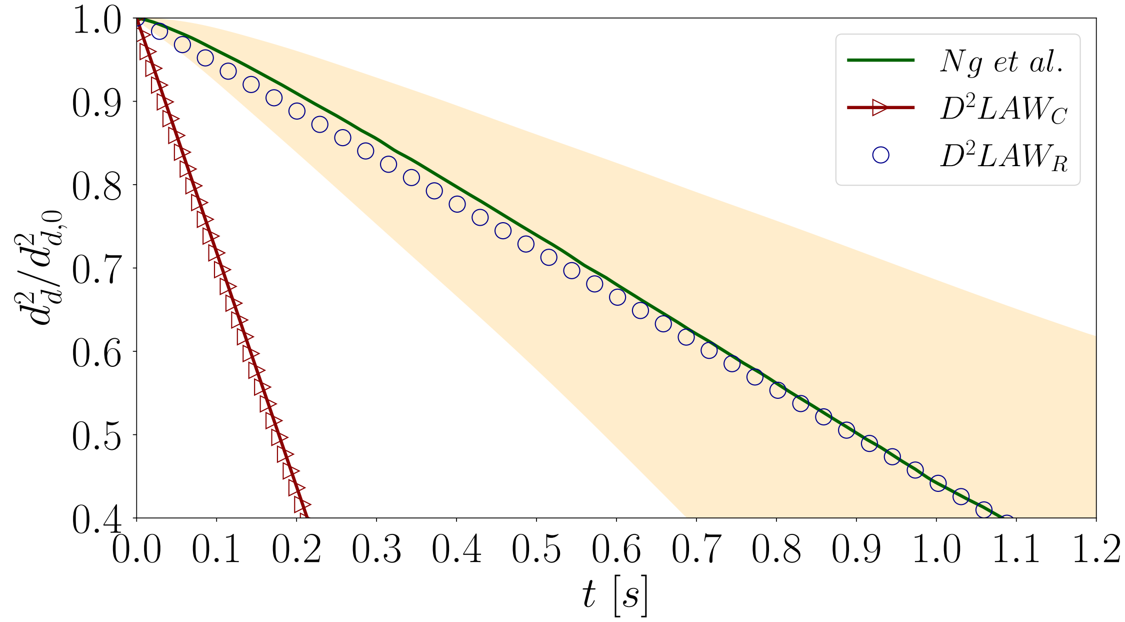

Figure 7: Mean droplet square diameter, $d_d^2/d_{d,0}^2$ versus flight time. Green line data, by Ng et al. [14]; the highlighted area represents the distribution range of the droplet diameters observed.

described by the proposed model. On the contrary, for the highest mass fraction, the JPDF spreads over a wider range and the evaporation times are longer than that predicted by the proposed model (around 35% in mean). This indicates that droplets exhibit different Lagrangian histories and, as expected, the proposed model cannot account for this complex interaction, typical of non-dilute conditions.

To highlight the generality of present study, we employed our model against the dataset from recent independent works [6, 14] on respiratory droplets evaporation. We focus on their numerical simulation on droplets expelled in a turbulent respiratory puff (cough) at $T_a = 30°C$ and $RH_a = 90\%$. The authors observed a linear decrease of the droplet surface but found an evaporation rate much lower than that estimated by the classical $\mathcal{D}^2$-law. In Fig. 7 we compare the mean droplet square diameter, $d_d^2/d_{d,0}^2$, versus mean droplet flight time obtained by Ng et al. [14] with that predicted by using the classical and the revised $\mathcal{D}^2$-laws. Our revised formulation accurately reproduces the temporal evolution of mean square droplet diameter, whereas the classical prediction strongly overestimates the vaporization rate, leading to shorter evaporation times. It is worth noting that the additional cases presented in Ng et al. [14] pertain to conditions where the emitted gaseous jet strongly differs from the environmental ones, so the present model cannot be directly applied.

Summarizing the applicability limits of present model, the droplet size should be smaller than the smallest flow length scales (point-droplet approximation) and well above the non-continuum length-scales, i.e. nano-droplets [15]. Hence, we can state the model is applicable for droplet size below millimeters and above a micrometer. In addition, beyond a dilute mass fraction ($\psi_0 < 10^{-2}$), the basic assumptions behind the presented revision of the $\mathcal{D}^2$-law requires the thermodynamic ambient conditions to be sufficiently homogeneous and similar to that of the gaseous jet. These assumptions are also at the base of the classical $\mathcal{D}^2$-law.

To conclude, the present study demonstrates that reformulating the $\mathcal{D}^2$-law by using the asymptotic temperature of isolated, evaporating droplets instead of the ambient one, allows a superior description of the evaporation of dilute, millimetric/micrometric and single component droplets in turbulent flows with respect to the classical $\mathcal{D}^2$-law. An excellent agreement of the predictions by our revised model against reference DNS is found for jet-sprays up to a liquid mass fraction of the order of $\psi_0 \sim 10^{-3}$, whereas the agreement is still acceptable up to $\psi_0 \sim 10^{-2}$. The authors believe that the proposed revision of the $\mathcal{D}^2$-law will contribute to improve practical estimates of droplet evaporation times. In the context of respiratory droplet dispersion, we expect that present findings could be significant for a revision of the Wells theory [20], which is based on the classical $\mathcal{D}^2$-law.

Acknowledgement. J.W. is grateful to the China Scholarship Council (CSC) for supporting this research (201806250023).

Bibliography

[1] B. Abramzon and W. A. Sirignano. Droplet vaporization model for spray combustion calculations. *Int. J. Heat Mass Transf.*, 32(9):1605–1618, 1989.

[2] M. Al Qubeissi, S. S. Sazhin, J. Turner, S. Begg, C. Crua, and M. R. Heikal. Modelling of gasoline fuel droplets heating and evaporation. *Fuel*, 159:373–384, 2015. ISSN 0016-2361.

[3] S. Balachandar, S. Zaleski, A. Soldati, G. Ahmadi, and L. Bourouiba. Host-to-host airborne transmission as a multiphase flow problem for science-based social distance guidelines. *Int. J. Multiph. Flow*, 132:103439, 2020.

[4] A. Bukhvostova, E. Russo, J.G.M. Kuerten, and B. J. Geurts. Comparison of dns of compressible and incompressible turbulent droplet-laden heated channel flow with phase transition. *Int. J. Multiph. Flow*, 63:68–81, 2014.

[5] A. Bukhvostova, J.G.M. Kuerten, and B. J. Geurts. Heat transfer in droplet-laden turbulent channel flow with phase transition in the presence of a thin film of water. *Int. J. Heat Fluid Flow*, 61:256–271, 2016.

[6] Kai Leong Chong, Chong Shen Ng, Naoki Hori, Rui Yang, Roberto Verzicco, and Detlef Lohse. Extended lifetime of respiratory droplets in a turbulent vapor puff and its implications on airborne disease transmission. *Phys. Rev. Lett.*, 126(3):034502, 2021.

[7] P. P. Ciottoli, F. Battista, R. Malpica Galassi, F. Dalla Barba, and F. Picano. Direct numerical simulations of the evaporation of dilute sprays in turbulent swirling jets. *Flow Turbulence Combust.*, 106(3):993–1015, 2021.

[8] Federico Dalla Barba and Francesco Picano. Clustering and entrainment effects on the evaporation of dilute droplets in a turbulent jet. *Phys. Rev. Fluids*, 3(3):034304, 2018.

[9] G. M. Faeth. Current status of droplet and liquid combustion. *Prog. Energy Combust. Sci.*, 3 (4):191–224, 1977.

[10] Yifei Gong, Guowei Xiao, Xiao Ma, Kai Hong Luo, Shijin Shuai, and Hongming Xu. Phase transitions of multi-component fuel droplets under sub- and supercritical conditions. *Fuel*, 287: 119516, 2021. ISSN 0016-2361.

[11] I. Langmuir. The evaporation of small spheres. *Phys. Rev.*, 12(5):368–370, 1918.

[12] R. Mittal, R. Ni, and J. H. Seo. The flow physics of covid-19. *J. Fluid Mech.*, 894:317, 2020.

[13] Rasoul Nasiri and Kai H. Luo. Specificity switching pathways in thermal and mass evaporation of multicomponent hydrocarbon droplets: A mesoscopic observation. *Sci. Rep.*, 7(1):5001, 2017.

[14] Chong Shen Ng, Kai Leong Chong, Rui Yang, Mogeng Li, Roberto Verzicco, and Detlef Lohse. Growth of respiratory droplets in cold and humid air. *Phys. Rev. Fluids*, 6(5):054303, 2021.

[15] A. S. Rana, D. A. Lockerby, and J. E. Sprittles. Lifetime of a nanodroplet: Kinetic effects and regime transitions. *Phys. Rev. Lett.*, 123(15):154501, 2019.

[16] Leonardo Setti, Fabrizio Passarini, Gianluigi de Gennaro, Pierluigi Barbieri, Maria Grazia Perrone, Massimo Borelli, Jolanda Palmisani, Alessia Di Gilio, Prisco Piscitelli, and Alessandro Miani. Airborne transmission route of covid-19: Why 2 meters/6 feet of inter-personal distance could not be enough. *Int. J. Environ. Res. Public Health*, 17(8):2932, 2020.

[17] D. B. Spalding. Combustion of liquid fuels. *Nature*, 165(4187):160, 1950.

[18] Jietuo Wang, Federico Dalla Barba, and Francesco Picano. Direct numerical simulation of an evaporating turbulent diluted jet-spray at moderate reynolds number. *Int. J. Multiph. Flow*, 137:103567, 2021.

[19] Philipp Weiss, Valentin Giddey, Daniel W Meyer, and Patrick Jenny. Evaporating droplets in shear turbulence. *Physics of Fluids*, 32(7):073305, 2020.

[20] W. F. Wells. On air-borne infection. study ii. droplets and droplet nuclei. *Am. J. Hyg.*, 20: 611–618, 1934.

[21] Guowei Xiao, Kai H. Luo, Xiao Ma, and Shijin Shuai. A molecular dynamics study of fuel droplet evaporation in sub- and supercritical conditions. *Proc. Combust. Inst.*, 37(3):3219–3227, 2019.

Appendix E

Paper V

Modelling the direct virus exposure risk associated with respiratory events

Jietuo Wang[1], **Federico Dalla Barba**[2], **Alessio Roccon**[3,4], **Gaetano Sardina**[5], **Alfredo Soldati**[3,4], **Francesco Picano**[1,2]

1. Centro di Ateneo di Studi e Attività Spaziali - CISAS, University of Padova, Padova, 35131, Italy
2. Department of Industrial Engineering, University of Padova, Padova, 35131, Italy
3. Institute of Fluid Mechanics and Heat Transfer, TU Wien, Vienna, 1060, Austria
4. Polytechnic Department, University of Udine, 33100, Udine, Italy
5. Department of Mechanics and Maritime Sciences, Chalmers University of Technology, 41296, Gothenburg, Sweden

Journal of The Royal Society Interface, 2021, In press.

Abstract: The outbreak of the COVID-19 pandemic highlighted the importance of accurately modeling the pathogen transmission via droplets and aerosols emitted while speaking, coughing and sneezing. In this work, we present an effective model for assessing the direct contagion risk associated with these pathogen-laden droplets. In particular, using the most recent studies on multi-phase flow physics, we develop an effective yet simple framework capable of predicting the infection risk associated with different respiratory activities in different ambient conditions. We start by describing the mathematical framework and benchmarking the model predictions against well-assessed literature results. Then, we provide a systematic assessment of the effects of physical distancing and face coverings on the direct infection risk. The present results indicate that the risk of infection is vastly impacted by the ambient conditions and the type of respiratory activity, suggesting the non-existence of a universal safe distance. Meanwhile, wearing face masks provides excellent protection, effectively limiting the transmission of pathogens even at short physical distances, i.e. 1 meter.

Keywords: infectious diseases, airborne, virus transmission, low-order model

---

Introduction

Since the COVID-19 pandemic outbreak in the spring of 2020, extensive researches have been done to significantly advance our understanding of different scientific problems ranging from the transmission pathways of respiratory diseases to mitigation strategies for reducing the infection risk [37]. The SARS-CoV-2 virus, like many other respiratory viruses, spreads from an infected individual to other susceptible individuals through virus-laden droplets emitted while breathing, speaking, singing, coughing and sneezing. The size of these droplets span over a wide range of diameters: from large drops, $\mathcal{O}(1\ mm)$, to small droplets, $\mathcal{O}(1\ \mu m)$ [7, 12, 22, 38, 66]. These droplets, released together with a puff/jet of buoyant moist turbulent air, are then dispersed in the surrounding ambient and exposure or inhalation of these droplets leads to a potential risk of infection [9, 10, 12]. Investigating the transport and deposition of these droplets is thus of fundamental importance to design effective guidelines for disease transmission prevention.

The transport and deposition of respiratory droplets is controlled by the competition among gravitational forces, drag forces and, evaporation. Depending on the outcome of this competition, we can distinguish among three infection routes. The first route can be identified in the fomites: droplets that settle along their trajectories can contaminate surfaces, and a susceptible individual, touching the contaminated surface, can get infected [55, 65]. The other two possible routes of infection can be linked to the inhalation and subsequent deposition of pathogen-laden droplets in the respiratory mucosa: droplet direct transmission and airborne transmission. The key differentiating factor between these two routes is the aerodynamics behavior of the pathogen-laden droplets. Droplet transmission [27] refers to the infection propagation associated with large droplets, which motion is governed by gravity, and that behave ballistically. By opposite, airborne transmission [23, 53, 57] refers to the spread of the disease associated with smaller droplets, which motion is governed by aerodynamic drag and evaporation, and that behave as aerosols, i.e. droplets/particles that remain airborne and can spread for long distances.

As the latest research suggests that fomites are unlikely to be a major source of infection for SARS-CoV-2 [23, 31, 44], understanding the role played by the two latter infection routes is crucial to establish effective guidelines for pathogens transmission prevention. One of the first seminal works in this direction was written by Wells [62] who hypothesised that the interplay of evaporation and gravity determines the lifetime of respiratory droplets. In the picture described by Wells, there is a critical size (about $100\mu m$) for each specific environmental condition that dichotomises particles that would fall to the ground and droplets that would evaporate out at the same time. Wells theory is pioneering in differentiating droplet and airborne transmission, also corroborated by the fact that small droplets could evolve into droplet nuclei by evaporation [63], micro-metric particles of non-volatile materials (e.g. mucus) that can potentially carry the virus contributing to the spread of the disease. This framework is so concise, readable and expressive that, since reported, it has been largely used in most public health guidelines [7, 10]. The Wells model, however, presents a major weakness [7, 10, 17, 39, 58, 66]: the evaporation time of the droplets is estimated using the classical D^2-law [29] (or constant temperature model) which states that the droplet surface reduces linearly over time at a rate determined by ambient conditions. This evaporation model ignores the presence of a turbulent cloud of moist air, which, as recently demonstrated in recent studies, plays a crucial role in the fate of respiratory droplets [37, 45], as well as the presence of the surrounding droplets. This leads to wrong estimates of the evaporation times and results in much shorter predicted droplet lifetimes [39, 58].

To overcome these limitations, Xie et al. [66] developed an improved model capable of describing the evaporation and motion of droplets exhaled during respiratory events in different conditions (relative humidity, air velocity, and respiratory jets). The model is composed of a detailed mathematical framework that describes droplets motion using non-linear differential equations coupled with a low-order description of the buoyant turbulent puff. The model developed by Xie et al. [66], although more solid and accurate than Wells theory, inevitably loses the conciseness advantage of the latter. With the aim of developing an effective yet simple model able to accurately predict droplet evaporation times, it is worthwhile noticing that an interesting picture emerges from recent studies on respiratory droplets evaporation [17, 39, 58]: although the resulting droplets lifetimes are much larger than classical D^2-law predictions, the D^2-law scaling seems still to bear some universality [58, 59]. Specifically, the mean evaporation times seem to follow a D^2-law-like scaling but with a different pre-factor. Inspired by this observation, a revised version of the D^2-law has been recently proposed by Dalla Barba et al. [18]: using a proper estimate of the asymptotic droplet temperature, the evaporation rate of dilute droplets in sprays, jets and puffs can be accurately determined. Even if more accurate than the classical formulation, it should be remarked that the performance of the revised D^2-law is affected by low-temperature and high relative humidity environmental conditions. In particular, the non-monotonic time behavior of the droplet surface, reported in Ng et al. [39] for these extreme conditions, cannot be fully captured even by the revised model.

In light of the most recent understanding of respiratory events, we use this body of developed knowledge to move away from the isolated drop emission to the turbulent, multi-phase puff model [7, 9, 37]. In this paper, we establish a comprehensive theoretical framework capable of accurately describing the evaporation and dispersion behavior of pathogen-laden droplets emitted during expiratory events. The model revises the outdated Wells theory with the most recent knowledge on turbulent droplet transport by jets or plumes, as well as the state-of-the-art understanding of respiratory activities. The proposed model, although mathematically simple, provides a general assessment of the direct contagion risk during different respiratory activities and ambient conditions.

We start by assessing the accuracy of the revised D^2-law [18] in evaluating the evaporation of respiratory droplets. Building on this, we propose a revision of the traditional Wells theory, including an effective correction to the classical Stokes drag needed for relatively large droplets. We show that the proposed model can accurately predict the evaporation-falling curve of droplets when compared to previous reference data [66]. Coupling the latest research on turbulent jets and puffs [1, 9, 35, 48, 58, 61, 66], we proceed by proposing an integrated framework able to describe the evaporation-falling dynamics of respiratory droplets for different environmental conditions and respiratory activities. Then, using the theoretical model and available data on respiratory events (e.g. droplet initial size distribution [7, 22, 58], viral load measurements [54, 64]), we quantify the direct virus exposure as a function of either the physical distancing or face covering. Descriptions of more complex phenomena, e.g. droplet condensation [17, 39, 58] and the upward movement of buoyant puffs [9, 10, 58, 66], are not considered in the proposed model, but their importance should be critical for the indirect airborne contagion and would be our future focus.

Methodology and Validation

To evaluate the lifetime of the respiratory droplets, t_l, our model considers both evaporation and settling dynamics of the droplets. Once the droplet lifetime is evaluated, the horizontal distance travelled by the droplets, L_d, can be also calculated. A graphical representation of these model parameters is provided in figure 1. From a mathematical point of view, the model formulation can

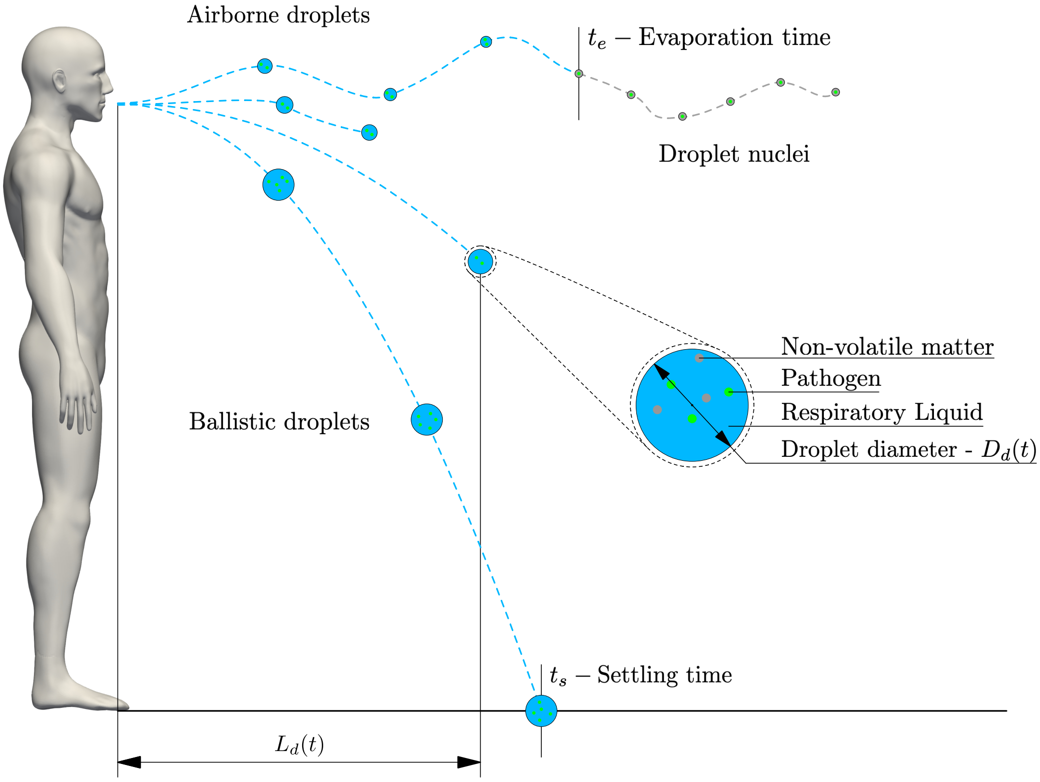

Figure 1: Sketch showing the main parameters of the model. For large ballistic droplets, the droplet lifetime is the settling time, t_s, while for smaller airborne droplets, the droplet lifetime is the evaporation time, t_e. The horizontal distance travelled by the respiratory droplets, $L_d(t)$, is also shown. The close-up view shows the droplet dimension and highlights the presence of the pathogens and other non-volatile components in the respiratory liquid. For visualization purposes, the sketch is not in scale.

be summarized as follows:

$$t_l = \min(t_e, t_s) \; ; \tag{1}$$

$$t_e = \frac{D_{d,0}^2}{k} \; ; \tag{2}$$

$$t_s = \frac{D_{d,0}^2 - \sqrt{D_{d,0}^4 - 9\frac{4k\mu}{(\rho_d-\rho)gf}H_d}}{k} \; ; \tag{3}$$

$$L_d = \begin{cases} L_{d,1} = \sqrt{4BU_0R_0}t_l^{\frac{1}{2}} & \text{when} \quad t_l \leq t_{inj} \; ; \\ L_{d,2} = \sqrt{4BU_0R_0}t_{inj}^{\frac{1}{4}}t_l^{\frac{1}{4}} & \text{when} \quad t_l > t_{inj} \; ; \end{cases} \tag{4}$$

where μ, ρ and ρ_d are the dynamic viscosity and density of the ambient air and the droplet density, respectively, with k being the surface evaporation rate estimated by the thermodynamic properties of the droplet and environment [18]. The inertial Reynolds number of droplets with initial diameter $D_{d,0}^2$ is taken into account for the Stokes law with a fixed drag correction factor f. The initial height of droplets away from the ground is defined as H_d and U_0 is the velocity of respiratory puff ejected from a mouth with characteristic size R_0. g represents the gravity acceleration and B the universal jet velocity-decay constant [42]. The lifetime of a respiratory droplet, t_l, is determined by equation (1). Following the Wells formalism, a respiratory droplet can either evaporate or settle on the ground. Hence, the lifetime t_l corresponds to the minimum between the evaporation time, t_e, expressed by equation (2), and the settling time, t_s, determined by equation (3). Given the droplet lifetime, it is possible to predict the horizontal distance travelled by the droplet. This length is defined by $L_{d,1}$ when the droplet lifetime is smaller than t_{inj}, where t_{inj} identifies the duration of the jet phase of the respiratory event (i.e. the time during which momentum is injected in the ambient). By opposite, if the droplet lifetime is larger than t_{inj}, the horizontal distance travelled by the droplets is determined by $L_{d,2}$. Indeed, once the jet-phase is terminated, the flow behaves as a turbulent puff [35, 45].

In the following, a brief description of each sub-part of the model is presented, whereas additional details are provided in the Supplementary Material. Equation (2) describes the evaporation time, t_e, necessary for a droplet to dry out by assuming a linear reduction in time of its surface and a constant droplet temperature. The variable $D_{d,0}$ represents the initial droplet diameter, whereas k is the surface evaporation rate estimated by the thermodynamic properties of the droplet and environment (see also Supplementary Material for details). A similar evaporation model, the so-called $\mathcal{D}^2$-law, was introduced by Langumir's pioneering work [29] and then adopted in the Wells theory [62]. Recently, it has been revised in Dalla Barba et al. [18] for the determination of k where the asymptotic evaporation temperature of isolated, evaporating droplets is used instead of the initial one to calculate the evaporation rate. This revised $\mathcal{D}^2$-law provides more accurate predictions for the evaporation of dilute droplets (See Supplementary Material for details and validations against experimental data); for additional details, readers are referred to Dalla Barba et al. [18].

To further assess the accuracy of the revised $\mathcal{D}^2$-law in predicting the evaporation times for respiratory droplets, we compare in figure 2 the predictions of the evaporation time of water droplets obtained from three different models: *i*) the original Wells theory; *ii*) the revised $\mathcal{D}^2$-law evaporation model; *iii*) the evaporation times obtained from high-fidelity simulations of sneezing events performed using a setup similar to that adopted by Wang et al. [58]. Each of the four plots refers to a different combination of temperature and relative humidity (RH) values. In each sub-figure, for a given initial diameter $D_{d,0}$, red-solid lines identify the predictions based on the Wells theory (classical $\mathcal{D}^2$-law), i.e. assuming that the droplet temperature is constant and equal to the initial jet temperature. Likewise, blue-dashed lines identify the predictions obtained from the revised $\mathcal{D}^2$-law with the decay constant computed from the ambient temperature. Meanwhile, for the high-fidelity simulations, for any given initial diameter $D_{d,0}$ the mean evaporation time is shown with empty black circles. A blue-yellow colour map shows the probability of obtaining a certain evaporation time.

The revised $\mathcal{D}^2$-law is capable of predicting the mean evaporation behaviors of respiratory droplets accurately. However, for the low-temperature and high RH case, e.g. $T = 5°\mathrm{C}$ RH=90% (panel B), good results are observed only for long times, i.e. $t > 2.5$ s. In low-temperature and high-RH conditions, where the emitted respiratory jet strongly differs from the ambient, the local micro-environments are critical in determining the temporal evolution of droplet dynamics [58] which differ from a linear decay of the droplet surface. Ng et al. [39] observed that, in these conditions, air could not contain much moisture. Therefore, the warm and humid exhaled vapor puff becomes supersaturated when entering in the cold ambient air, so the droplets carried by the puff tend to experience vapor condensation before evaporating at long time. Colder the ambient air, the more important this non-monotonic behavior is [19, 39]. To improve the accuracy of the evapora-

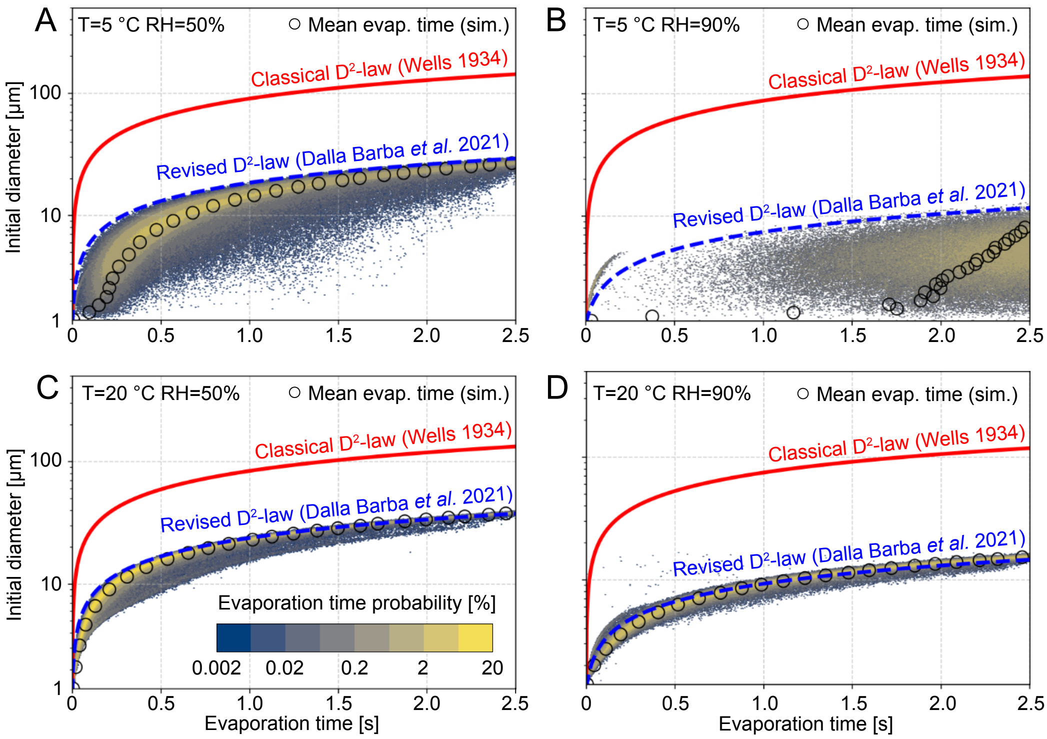

Figure 2: Comparisons of the evaporation time, t_e, of water droplets of different initial diameters estimated by different models: Wells theory [62] (red line), revised $\mathcal{D}^2$-law [18] (blue line) and high-fidelity simulations of sneezing jet [58] (empty black circles). For the high-fidelity simulations, in addition to the mean evaporation time (black circles), the probability density function of the evaporation times for any given initial diameter is shown with a blue-yellow map. Each panel refers to a different combination of temperature and relative humidity values: $T = 5°\mathrm{C}$ and RH=50% and 90% (A and B), $T = 20°\mathrm{C}$ and RH=50% and 90% (C and D).

tion model, especially for short time evolution, we propose here a minor improvement of the revised $\mathcal{D}^2$-law. In particular, as reported in Dalla Barba et al. [18], a small transient is necessary for the droplet temperature to collapse on its asymptotic value starting from its initial one. This transient time has been observed to be few droplet relaxation times, $\tau_{d,0} = \rho_d D^2_{d,0}/18\mu$, corresponding to the typical inertial timescale of the droplet in a viscous flow (ρ_d the droplet density and μ the air viscosity). To account for this, we introduce a two-stage evaporation model: in the initial step of the evaporation process, i.e. $t < 6\tau_{d,0}$, the droplets evaporate with a rate k determined by the initial droplet temperature, as in the classical $\mathcal{D}^2$-law; then, the evaporation rate k is computed using the asymptotic droplet temperature, as in the revised $\mathcal{D}^2$-law (see Supplementary Material for details).

Moving to the settling dynamic, equation (3) predicts the settling time t_s, i.e. the time needed to reach the ground from a specific falling height H_d, here fixed to 2 meters consistently with previous studies [62, 66]. In the Wells theory, the settling time is estimated using the Stokes drag law, which holds for tiny droplets at small droplet Reynolds number $Re_d = \rho u_s D_d/\mu \ll 1$, i.e. in the viscous dominated regime, with ρ and μ being density and dynamic viscosity of the air respectively. This hypothesis is realistic for small respiratory droplets whose Reynolds number, Re_d, is supposed to be sub-unitary. However, for large droplets (200 microns or more), the Reynolds number based on settling speed could be around ten or more. As reported in Seinfeld [50], the Stokes law may overestimate the settling speed by 60% for these large droplets. To account for finite (small) Reynolds number effects, we propose a correction of the Stokes law by a fixed drag correction factor

f, which we show to provide good predictions for respiratory droplets (see Supplementary Material for details). In particular, to avoid a non-linear model, we define the drag correction factor using an average constant droplet Reynolds number $Re_d^* = \rho u_s D_d^*/\mu$, where D_d^* is an average droplet diameter and $u_s = (\rho_d - \rho)gD_d^{*2}/18/\mu$ is the Stokes terminal velocity:

$$f = \frac{1}{1 + 0.15 Re_d^{*0.687}}; \tag{5}$$

$$Re_d^* = \frac{1}{18}\frac{\rho_d - \rho}{\mu^2} g\rho D_d^{*3}; \tag{6}$$

$$D_d^{*3} = \frac{D_{d,0}^3 + D_{d,t}^3}{2} \simeq \frac{D_{d,0}^3}{2}; \tag{7}$$

where $D_{d,0}$ and $D_{d,t}$ are the initial and terminal droplet diameters. Figure 3 compares the droplet lifetime predicted by the Wells theory [62] (continuous line) and the model here proposed (dashed lines) against the Xie *et al.* model [66] (empty circles) for different droplet initial diameters. As highlighted from the sample plot reported on the left, the droplet lifetime is the minimum between the evaporation time (lifetime for small droplets) and the falling time (lifetime for large droplets), as also illustrated in equation (1). Colors are used to distinguish among the different humidity values considered: RH=90% (black), 70% (gray), 50% (blue), 30%(yellow), 0% (red). The initial temperature of droplets and ambient air are $T_{d,0} = 33$°C and $T = 18$°C, respectively. It is worthwhile to note that, in Xie et al. [66], a detailed (Lagrangian) description of the droplet dynamics was employed together with an (Eulerian) model for the spatial-temporal evolution of respiratory jets. The complete model results in a system of non-linear differential equations that must be numerically integrated for any fixed environmental condition. Hence, this complex framework produces accurate data that can be used as a benchmark. From figure 3, we can observe how the Wells model largely underestimates the droplet lifetime even by more than one order of magnitude for middle-size droplets (upper right part of the plot). On the contrary, the algebraic model proposed

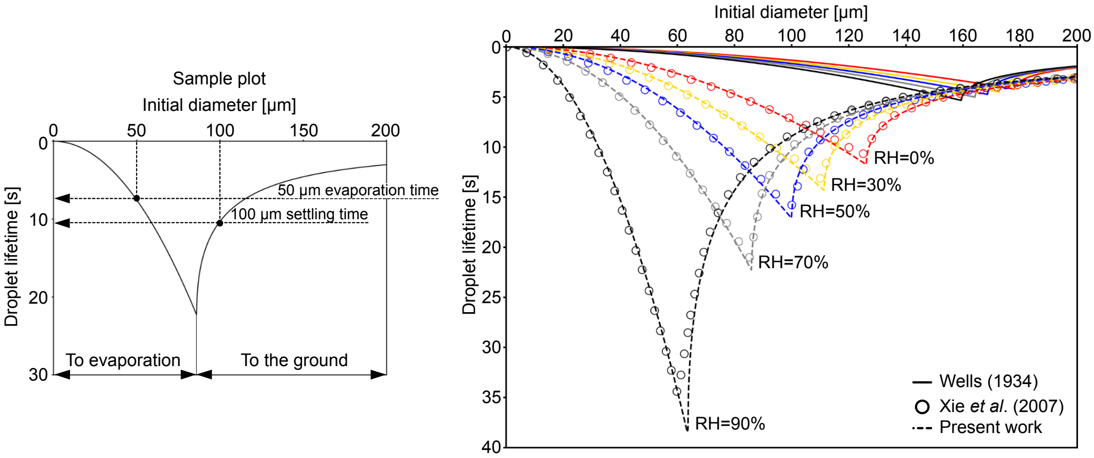

Figure 3: The right panel shows the comparison of the predicted droplet lifetime of water droplets having different diameters obtained from different models: Wells [62] (solid lines), Xie et al. [66] (symbols) and the present model (dashed line). The sample plot on the left guides the reading of the main panel: for small droplets diameters, the lifetime is determined by evaporation (left branch of the plot; to evaporation) while, for larger droplets diameters, the lifetime is determined by the settling dynamics (right branch of the plot; to the ground). The plot refers to an ambient temperature equal to $T = 18$ °C and different relative humidities values are considered: RH=90% (black), 70% (gray), 50% (blue), 30% (yellow), 0% (red).

here can accurately capture the droplet lifetime in both the evaporating (left, t_e) and falling (right, t_s) branches of the plot for all ambient conditions considered. In addition, the present results are in excellent agreement with the reference data of Xie et al. [66].

Using this simple and effective model, it is also possible to estimate the horizontal distances travelled by the respiratory droplets during different respiratory events. Indeed, all the different respiratory flows (e.g. speaking, coughing, and sneezing) can be modelled as a jet phase, during which the exhaled gas is emitted, followed by a puff phase [7, 9, 45]. On this ground, equation (4) determines the horizontal travelling distance of respiratory droplets, where $B \simeq 6$, U_0, and R_0 indicate the universal jet velocity-decay constant [42], the ejection velocity and the inlet radius (i.e. a characteristic size of the mouth), respectively. Equation (4) has been derived assuming that the droplet velocity is equal to the gas phase velocity in the geometric center of the inlet and assuming a two-phase propagation process of the expelled air. In particular, we consider a turbulent jet phase having duration t_{inj}, followed closely by a puff phase after the ending of the ejection phase. For details on the two-phase propagation theory of turbulent puffs, readers are referred to the following references Abkarian et al. [1], Bourouiba [9], Sangras et al. [48], Wang et al. [58], Wei and Li [61], Xie et al. [66].

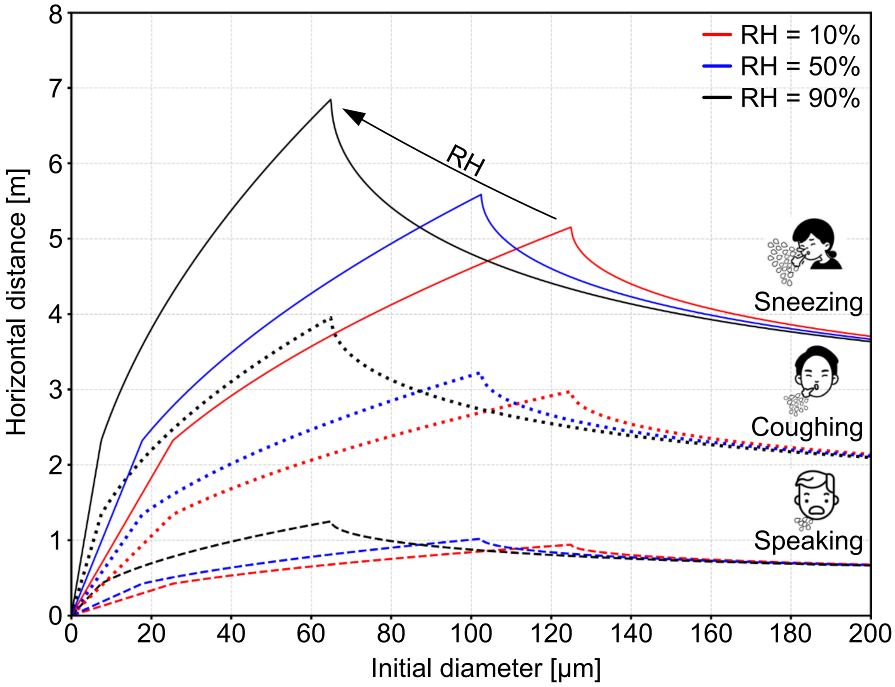

Figure 4: Comparison of the predicted horizontal distances travelled by the respiratory droplets, L_d, for different ambient conditions: RH=10% (red), RH=50% (blue), and RH=90% (black) as a function of the initial droplet diameter. Each respiratory event is reported with a different line style: speaking (dashed), coughing (dotted), and sneezing (continuous). Present results are obtained considering an ambient temperature equal $T = 20°$ C and an initial droplet temperature of $T_{d,0} = 35°$ C. The characteristic velocity of the different respiratory events is assumed equal to: 1m/s (speaking), 10 m/s (coughing), and 30 m/s (sneezing).

Results

Using the proposed model and considering different respiratory events [49, 56, 66], we can estimate the horizontal distance travelled by the droplets as a function of the initial diameter for different ambient conditions, as illustrated in figure 4. We can observe droplets emitted during different respiratory events reach different distances before evaporating or falling depending also on the ambient relative humidity (RH=10% - red, RH=50% - blue, and RH=90%-black). In particular, considering the most violent respiratory act (sneeze), 60 microns droplets can reach a distance of nearly 7 meters. This prediction is consistent with the experimental findings reported in Bourouiba [11, 12]. Droplets of similar size, emitted when speaking, can reach a distance slightly longer than one meter, in agreement with Abkarian et al. [1]. Reducing the relative humidity, droplets with a larger initial size reach shorter maximum distances: evaporation dynamic becomes faster and for 60-100 microns droplets the lifetime decreases. Overall, our model estimates indicate that respiratory droplets can reach a maximum distance between 5 and 7 meters when sneezing, 3 to 4 meters when coughing, and $\simeq 1$ meter when speaking.

Once the distance traveled by the respiratory droplets and their lifetime are known, assuming an initial droplet size distribution (e.g. a log-normal distribution [7, 59]), and a certain viral load, we can estimate the virus exposure. As viral load is characterized by large uncertainty [2, 3, 33, 40, 46, 54, 64] and exhibits strong variations during the different infection stages [14, 54, 64], we compute the exposure in a dimensionless form [58]. The dimensionless virus exposure is defined as the ratio of the cumulative initial volume of droplets survived at distance L_d to the total volume of droplets at the beginning. This definition is based on three hypotheses: 1) a uniform viral load across all droplets, i.e. the virus copies inside each droplet are directly proportional to the droplet initial volume; 2) no viral load decay, i.e. the number of virus copies is fixed by the initial droplet size; 3) the virus exposure becomes null when a droplet reaches the ground or completely evaporates. By assuming that all respiratory events are initially characterized by the same droplet size distribution, we provide virus exposure maps normalized by the total amount of virus copies emitted during the most violent respiratory event (sneezing). Since each respiratory event has been experimentally characterized by a different average droplet number [22], i.e. 1000.000, 5.000, and 250 for sneezing, coughing and speaking, respectively; the initial number of emitted virus copies is different, and so is the virus exposure at time t. However, it is worth noting that the droplet number for speaking obtained from Duguid experiments [22] does not correspond to a single event but counts during “speaking loudly one hundred words”, since its definition is not as distinct as coughing or sneezing events. Chao et al. [15] estimated the total number of droplets expelled during speaking ranged from 112 to 6720 by counting 1-100 numbers. Asadi et al. [5] reported that the droplet emission rate during normal speech is positively correlated with the loudness of vocalization, ranging from approximately 1 s^{-1} to 50 s^{-1} particles for low to high amplitudes, regardless of the language spoken. However, more recent studies [4, 51] by visualizing small speech droplets with an intense sheet of laser light revealed mean droplet emission rates of $1,000\ s^{-1}$ with peak emission rates as high as $10,000\ s^{-1}$, indicating a higher total integrated volume than previous results [5, 15, 22, 38]. Overall, the droplet number employed here to compute the initial virus exposure related to speaking events could be a conservative estimate, is at least a reasonable value.

Using these assumptions, we show in figure 5 the spatial evolution of the virus exposure for

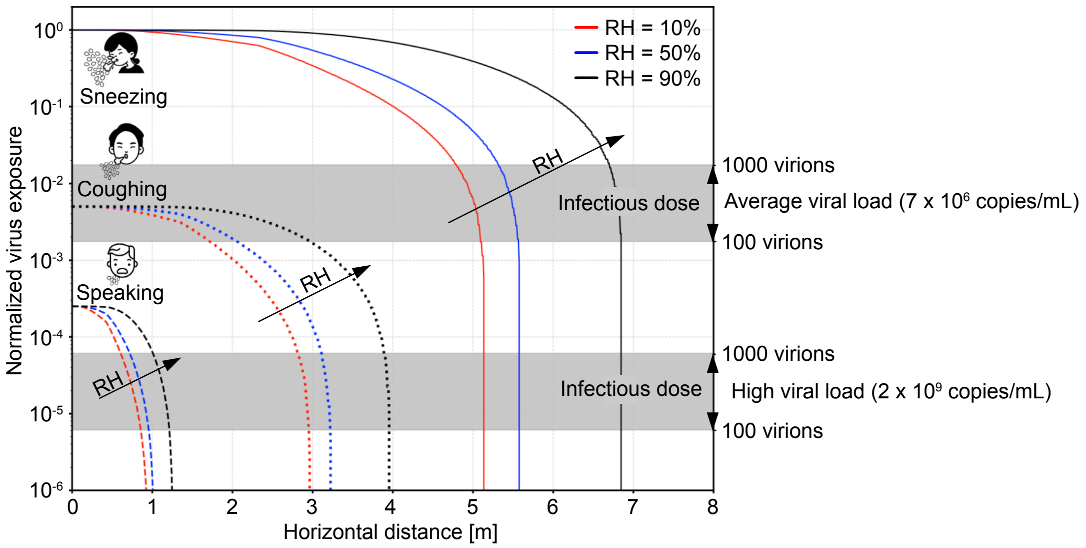

Figure 5: Normalized virus exposure as a function of the horizontal distance from an infected individual for different ambient conditions: RH=10% (red), RH=50% (blue), and RH=90% (black). Three distinct respiratory events are considered with the same initial droplets size distribution, i.e. a log-normal distribution with $\widehat{\mu} = \ln(12\ \mu m)$ and $\widehat{\sigma} = 0.7$ [7]. Present results are obtained considering an ambient temperature equal $T = 20°$ C and an initial droplet temperature of $T_{d,0} = 35°$C. The characteristic velocity of the respiratory events considered is assumed equal to 1m/s (speaking), 10 m/s (coughing) and 30 m/s (sneezing). As a reference, the infectious dose (which ranges from 100 to 1000 virions [28, 41]) is reported with two gray bands for two viral loads: an average case (7×10^6 copies/mL)[33, 64] and an extreme case (2×10^9 copies/mL)[64].

different respiratory events and ambient conditions: RH=10% (red), RH=50% (blue), and RH=90% (black). An important picture emerges from the virus exposure maps: a well-defined *safe distance* is not only related to the respiratory events but also determined by the ambient conditions. These results imply that it is impossible to define a universal standard safe distance. In particular, the safe distance should be extended when the ambient relative humidity is high. A 1-meter social distance might be enough when people talk, but not when coughing, especially in high relative humidity conditions. It is also true that coughs and sneezes are less frequent than standard talking among groups of people, so policymakers may consider this aspect to evaluate a global infection risk. We believe that, rather than a single safe distance, it is possible to evaluate a quantitative reduction of the infection risk as a function of the social distance and different relative humidity values. Policymakers may exploit these maps to determine the impact of a different social distance prescription on reducing the direct infection risk. To provide also an indication of the infection risk associated with the different respiratory events, the infectious dose for SARS-CoV-2 (from 100 to 1000 virions [28, 41]) is reported with a gray band for two different viral load values: an average case (7×10^6 copies/mL)[33, 64] and an extreme case (2×10^9 copies/mL)[64] (given the droplet number and distribution in a respiratory event, the overall liquid emitted is fixed, e.g. 0.0081ml for a sneeze). An exhaustive discussion on the infection risk in relation to these thresholds is however difficult: viral loads (and thus the position of these bands) are characterized by a large variability and depend on many different factors (e.g. disease severity, infection stage, vaccination status, etc.). From present model, it appears that, in case of high viral load, it is possible to be directly infected when talking at one meter of distance for around one minute. In addition, it should noted that overall virus exposure depends also on the indirect transmission route and so on the exposure time (i.e. the overall time in the proximity of an infected individual, especially in closed environments).

The use of face masks against SARS-CoV-2 transmissions substantially increased since the outbreak of the COVID-19 pandemic, though significant controversy on its effectiveness existed and recommendations on this measurement varied across countries [24]. More recently, wearing face masks has been widely accepted as a well-established protective measurement, providing both "inward" protection by filtering virus-laden aerosolized particles that would be inhaled by an uninfected person and "outward" protection by trapping virus-laden droplets expelled by an infected person [37]. Recent studies [6, 16, 20, 25, 30, 58] have provided evidence that supports the ability of face masks in reducing pathogen transmission. We focus here on the "outward" protection provided by two standard face coverings, i.e. surgical and N95 masks, and take into account two effects: a lower jet velocity and a trapping of virus-laden droplets. The first aspect is implemented by simply assuming a reduction of the emitted flow velocity induced by the mask presence, which is estimated from the experimental data reported in Prasanna Simha and Mohan Rao [43]. In particular, we assume that the velocity of the expelled puffs reduces to 1/4 times its *original* value when using a surgical mask and 1/8 for an N95 mask. The second aspect is accounted for by following Cheng et al. [16] study in which the size-dependent particle penetration rate of surgical and N95 masks based on the past literature [26, 60] is calculated. Additional findings on face mask efficiency can be found in the experimental study of Bagheri et al. [6] and in the theoretical one of Mao and Hosoi [34], with the latter mainly focused on airborne aerosols with size smaller than 1 μm. As it is known that the breathing airflow could escape from the edge area due to improper mask fit [21, 58] so, for each type of mask, we also consider a case in which leakages of respiratory droplets occur. Using the data provided in Cheng et al. [16], we treat leakage as reduced efficiency in the size-dependent droplet mask filtering. In other words, we consider the leakage as a higher number of droplets passing through the mask. Although not perfect, this model assumes the worst scenario where the leaked droplets are totally carried by the jet flow.

Figure 6 shows the normalized virus exposure obtained with different types of face-covering: no mask (continuous line), surgical mask (empty squares), surgical mask with leakage (empty circles), N95 mask (cross), N95 mask with leakage (empty diamonds). Colours are used to identify the different respiratory events: speaking (red), coughing (blue) and sneezing (black). For simplicity, only one ambient condition is considered: $T = 20°\text{C}$ and RH=50%. From figure 6, it appears that wearing masks is a very effective measure in reducing virus exposure and N95 shows a superior protection performance. In particular, at close distances, the virus exposure associated with an infected person wearing a surgical mask is about three orders of magnitude lower than its correspondent value without the mask. Likewise, properly wearing an N95 mask could further decrease the exposure to an almost vanishing level, i.e. $O(10^{-6})$. This observation can be traced back to the ability of masks in blocking large droplets, which load more virus copies than smaller droplets (assuming a uniform viral load across all droplets diameters). Indeed, experimental data recently published showed that masks are highly effective in blocking respiratory droplets larger than about 20 microns [6, 16]. Besides, the suppressing effect of masks on airflow velocity results also in a shorter propagation distance for droplets, effectively limiting the infection risk even near an infected person, i.e. 1 meter. Considering both these mechanisms – the blocking effect of masks on respiratory droplets larger than 20 microns and the suppressing effect on airflow velocity – it is clear that wearing masks significantly reduces the spreading of infectious droplets and provides excellent

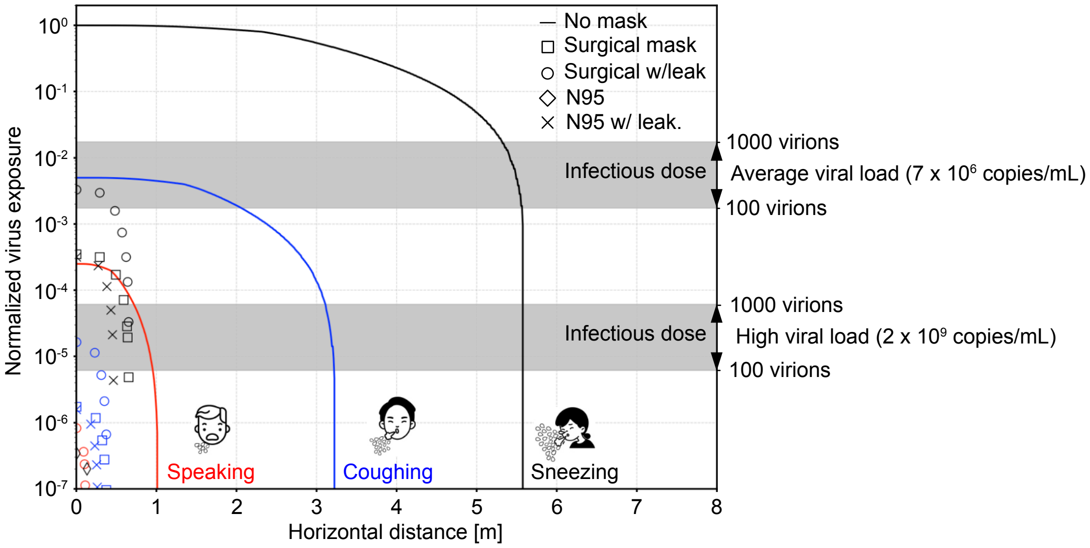

Figure 6: Normalized virus exposure maps for different face coverings: no mask (continuous line), surgical mask (empty squares), surgical mask with leakage (empty circles), N95 mask (cross), N95 mask with leakage (empty diamonds). Colors are used to distinguish among the different respiratory events: sneezing (black), coughing (red) and speaking (red). We assume that the puff velocity decays to 1/4 (or 1/8) times its initial value after passing a surgical mask (or N95) [43]. For perspicuity reasons, only one ambient condition ($T = 20°$C and RH=50%) is considered. As a reference, the infectious dose (from 100 to 1000 virions [28, 41]) is reported with a gray band for two viral load values: an average case (7×10^6 copies/mL)[33, 64] and an extreme case (2×10^9 copies/mL)[64]

.

'outward' protection.

Concluding the discussion, the proposed model presents the great potential of predicting the evaporation and dispersion of infectious droplets, leading to reasonable estimates of the direct virus exposure. Hence, it could be considered a revision of the seminal Wells model that incorporates the latest knowledge on multiphase flow modeling applied to respiratory flows. In any case, considering the aim of the present study, this cannot be applied to estimate the indirect transmission route dominated by aerosolized droplets carried out by the environmental flows. On this point, several recent models have been proposed. E.g. Yang et al. [67] incorporated the results of high-fidelity simulations on speech jets [1], and proposed a simplified dose-response model to quantify the spatio-temporal dependence of virus infection risk driven by speech-generated-aerosols between two speakers. This model assumes the continuous speaking activities as quasi-steady, jet-like flows and fast aerosolization of speech droplets. They showed that both physical distancing and exposure time should be imposed to control the infection probability. In particular, speakers should keep the contact time below 8 minutes for a physical distancing of 1 m and 16 minutes for 2 m. Recently, Bazant and Bush [8] developed a theoretical model of long-term airborne transmission considering the number of occupants and their time spent in an enclosed space. Their model adopts the well-mixed assumption and quantified the extent to which infection risk could be impacted by practical parameters, like ventilation, room volume, the penetration rate of face masks, and disease transmission tolerance. They suggested that less vigorous respiratory activities, using face masks and large rooms with high air exchange rates, could effectively mitigate the transmission risk related to aerosolized virions. Other models recently proposed for the indirect route can be found in the references [13, 36, 47, 52]. The authors would like to note that the aforementioned models focus on the indirect airborne virus transmission, whereas the mathematical framework presented in this paper focuses on the direct exposure (short-range airborne and droplets). Hence, the present model is complementary to the those since both transmission routes are concurrently active.

Conclusion

Droplets released during respiratory events play a crucial role in transmitting respiratory diseases (e.g. SARS-CoV-2) from an infected host to a susceptible individual. In this study, we developed a simple physical model to predict the evaporation-falling-travelling performance of droplets expelled during respiratory activities in different ambient conditions. The proposed model revises the outdated Wells theory exploiting the better knowledge on turbulent droplets transport by jets or plumes developed in the last few decades, as well as the state-of-the-art understanding of respiratory ejections. The model relies on a simple algebraic formulation and, without the need of solving complex systems of non-linear differential equations, it is capable of accurately estimating the dispersion, evaporation, and settling behaviors of droplets within a turbulent multiphase jet/puff. The model can take into account different respiratory events (speaking, coughing, sneezing) and different ambient conditions (temperature and relative humidity) except for very cold and humid environments where droplet surface time decay would not be simply characterized by a linear behavior [39]. Reference data from well-recognized model [66], high-fidelity simulations [39, 58] and latest experimental investigations [32] have been used to benchmark the present model. Using the proposed framework, we systematically assess the effects of physical distancing and face coverings on virus exposure maps and thus on the infection risk. We show that the infection risk is vastly impacted by the ambient conditions and respiratory event considered, indicating the non-existent of a universal safe distance. Finally, using the proposed model and exploiting experimental data on the penetration of respiratory droplets through face masks [16, 26, 43, 60], we assess the effects of face masks on the infection risk. We confirm that face masks provide excellent "outward" protection, effectively reducing the infection risk near an infected person. Overall, we believe that the present model represents a substantial improvement of older models [62, 66] and, thanks to its simple but effective mathematical background, can be widely used by policymakers to design effective guidelines for the prevention of direct contagion.

ACKNOWLEDGEMENT

Authors gratefully acknowledge the financial support from the MSCA-ITN-EID project “COMETE” (813948), from PRIN project “Advanced computations and experiments in turbulent multiphase flow” (2017RSH3JY), from FISR project PURITY (FISR2020IP_02809), from the Research project promoted by China Scholarship Council (201806250023) and from the Swedish Research Council grant no. VR 2020-05861.

Bibliography

[1] Manouk Abkarian, Simon Mendez, Nan Xue, Fan Yang, and Howard A. Stone. Speech can produce jet-like transport relevant to asymptomatic spreading of virus. *Proc. Natl. Acad. Sci.*

U.S.A, 117(41):25237–25245, 2020.

[2] Carmen Alonso, Peter C. Raynor, Peter R. Davies, and Montserrat Torremorell. Concentration, size distribution, and infectivity of airborne particles carrying swine viruses. *PloS one*, 10(8): e0135675, 2015.

[3] S. Anand and Y. S. Mayya. Size distribution of virus laden droplets from expiratory ejecta of infected subjects. *Sci. Rep.*, 10(1):21174, 2020.

[4] Philip Anfinrud, Valentyn Stadnytskyi, Christina E. Bax, and Adriaan Bax. Visualizing speech-generated oral fluid droplets with laser light scattering. *N. Engl. J. Med.*, 382(21):2061–2063, 2020.

[5] Sima Asadi, Anthony S. Wexler, Christopher D. Cappa, Santiago Barreda, Nicole M. Bouvier, and William D. Ristenpart. Aerosol emission and superemission during human speech increase with voice loudness. *Sci. Rep.*, 9(1):2348, 2019.

[6] G. Bagheri, B. Thiede, B. Hejazi, O. Schlenczek, and E. Bodenschatz. An upper bound on one-to-one exposure to infectious human respiratory particles. *Proc. Natl. Acad. Sci. USA*, 118 (49):e2110117118, 2021.

[7] S. Balachandar, S. Zaleski, A. Soldati, G. Ahmadi, and L. Bourouiba. Host-to-host airborne transmission as a multiphase flow problem for science-based social distance guidelines. *Int. J. Multiph. Flow*, 132:103439, 2020.

[8] M.Z. Bazant and J.W.M. Bush. A guideline to limit indoor airborne transmission of COVID-19. *Proc. Natl. Acad. Sci. USA*, 118(17), 2021.

[9] Dehandschoewercker E. & Bush J. W. Bourouiba, L. Violent expiratory events: on coughing and sneezing. *J. Fluid Mech.*, 745:537–563, 2014.

[10] L. Bourouiba. Turbulent gas clouds and respiratory pathogen emissions: Potential implications for reducing transmission of covid-19. *JAMA*, 323(18):1837–1838, 2020.

[11] Lydia Bourouiba. Images in clinical medicine. a sneeze. *N. Engl. J. Med.*, 375(8):e15, 2016.

[12] Lydia Bourouiba. The fluid dynamics of disease transmission. *Annu. Rev. Fluid Mech.*, 53(1), 2021.

[13] G. Buonanno, L. Stabile, and L. Morawska. Estimation of airborne viral emission : Quanta emission rate of SARS-CoV-2 for infection risk assessment. *Environ. Int.*, 141:105794, 2020.

[14] Muge Cevik, Krutika Kuppalli, Jason Kindrachuk, and Malik Peiris. Virology, transmission, and pathogenesis of sars-cov-2. *Brit. Med. J.*, 371:m3862, 2020.

[15] C. Y. H. Chao, M. P. Wan, L. Morawska, G. R. Johnson, Z. D. Ristovski, M. Hargreaves, K. Mengersen, S. Corbett, Y. Li, X. Xie, and D. Katoshevski. Characterization of expiration air jets and droplet size distributions immediately at the mouth opening. *J. Aerosol Sci.*, 40 (2):122–133, 2009.

[16] Yafang Cheng, Nan Ma, Christian Witt, Steffen Rapp, Philipp S. Wild, Meinrat O. Andreae, Ulrich Pöschl, and Hang Su. Face masks effectively limit the probability of sars-cov-2 transmission. *Science*, 372(6549):1439–1443, 2021.

[17] Kai Leong Chong, Chong Shen Ng, Naoki Hori, Rui Yang, Roberto Verzicco, and Detlef Lohse. Extended lifetime of respiratory droplets in a turbulent vapor puff and its implications on airborne disease transmission. *Phys. Rev. Lett.*, 126(3):034502, 2021.

[18] F. Dalla Barba, J. Wang, and F. Picano. Revisiting d2-law for the evaporation of dilute droplets. *Phys. Fluids*, 33(5):051701, 2021.

[19] Federico Dalla Barba and Francesco Picano. Clustering and entrainment effects on the evaporation of dilute droplets in a turbulent jet. *Phys. Rev. Fluids*, 3(3):034304, 2018.

[20] Talib Dbouk and Dimitris Drikakis. On coughing and airborne droplet transmission to humans. *Phys. Fluids*, 32(5):053310, 2020.

[21] Talib Dbouk and Dimitris Drikakis. On respiratory droplets and face masks. *Phys. Fluids*, 32 (6):063303, 2020.

[22] J. P. Duguid. The size and the duration of air-carriage of respiratory droplets and droplet-nuclei. *J. Hyg.*, 44(6):471–479, 1946.

[23] Editorial. COVID-19 transmission — up in the air. *Lancet Respir. Med.*, 8(12):1159, 2020.

[24] Shuo Feng, Chen Shen, Nan Xia, Wei Song, Mengzhen Fan, and Benjamin J. Cowling. Rational use of face masks in the covid-19 pandemic. *Lancet Respir. Med.*, 8(5):434–436, 2020.

[25] Emma P. Fischer, Martin C. Fischer, David Grass, Isaac Henrion, Warren S. Warren, and Eric Westman. Low-cost measurement of face mask efficacy for filtering expelled droplets during speech. *Sci. Adv.*, 6(36):eabd3083, 2020.

[26] Sergey A. Grinshpun, Hiroki Haruta, Robert M. Eninger, Tiina Reponen, Roy T. McKay, and Shu-An Lee. Performance of an n95 filtering facepiece particulate respirator and a surgical mask during human breathing: two pathways for particle penetration. *J. Occup. Environ. Hyg.*, 6(10):593–603, 2009.

[27] Mahesh Jayaweera, Hasini Perera, Buddhika Gunawardana, and Jagath Manatunge. Transmission of covid-19 virus by droplets and aerosols: A critical review on the unresolved dichotomy. *Environ. Res.*, 188:109819, 2020.

[28] S. Karimzadeh, R. Bhopal, and H.N. Tien. Review of infective dose, routes of transmission and outcome of covid-19 caused by the sars-cov-2: comparison with other respiratory viruses. *Epidemiol. Infect.*, 149:e96, 2021.

[29] I. Langmuir. The evaporation of small spheres. *Phys. Rev.*, 12(5):368–370, 1918.

[30] Nancy H. L. Leung, Daniel K. W. Chu, Eunice Y. C. Shiu, Kwok-Hung Chan, James J. McDevitt, Benien J. P. Hau, Hui-Ling Yen, Yuguo Li, Dennis K. M. Ip, J. S. Malik Peiris, Wing-Hong Seto, Gabriel M. Leung, Donald K. Milton, and Benjamin J. Cowling. Respiratory virus shedding in exhaled breath and efficacy of face masks. *Nat. Med.*, 26(5):676–680, 2020.

[31] Dyani Lewis. Covid-19 rarely spreads through surfaces. so why are we still deep cleaning? *Nature*, 590(7844):26–28, 2021.

[32] C. Lieber, S. Melekidis, R. Koch, and H.J. Bauer. Insights into the evaporation characteristics of saliva droplets and aerosols: Levitation experiments and numerical modeling. *J. Aerosol Sci.*, 154:105760, 2021.

[33] Yang Liu, Li-Meng Yan, Lagen Wan, Tian-Xin Xiang, Aiping Le, Jia-Ming Liu, Malik Peiris, Leo L. M. Poon, and Wei Zhang. Viral dynamics in mild and severe cases of covid-19. *Lancet Infect. Dis.*, 20(6):656–657, 2020.

[34] X. Mao and A.E. Hosoi. Estimating the filtration efficacy of cloth masks. *Phys. Rev. Fluids*, 6 (11):114201, 2021.

[35] A. Mazzino and M.E. Rosti. Unraveling the secrets of turbulence in a fluid puff. *Phys. Rev. Lett.*, 127(9):094501, 2021.

[36] R. Mittal, C. Meneveau, and W. Wu. A mathematical framework for estimating risk of airborne transmission of COVID-19 with application to face mask use and social distancing. *Phys. Fluids*, 32(10):101903, 2020.

[37] R. Mittal, R. Ni, and J. H. Seo. The flow physics of covid-19. *J. Fluid Mech.*, 894:317, 2020.

[38] L. Morawska, G. R. Johnson, Z. D. Ristovski, M. Hargreaves, K. Mengersen, S. Corbett, C.Y.H. Chao, Y. Li, and D. Katoshevski. Size distribution and sites of origin of droplets expelled from the human respiratory tract during expiratory activities. *J. Aerosol Sci.*, 40(3):256–269, 2009.

[39] Chong Shen Ng, Kai Leong Chong, Rui Yang, Mogeng Li, Roberto Verzicco, and Detlef Lohse. Growth of respiratory droplets in cold and humid air. *Phys. Rev. Fluids*, 6(5):054303, 2021.

[40] Yang Pan, Daitao Zhang, Peng Yang, Leo L. M. Poon, and Quanyi Wang. Viral load of sars-cov-2 in clinical samples. *Lancet Infect. Dis.*, 20(4):411–412, 2020.

[41] A. Popa, J.W. Genger, M.D. Nicholson, T. Penz, D. Schmid, S.W. Aberle, B. Agerer, A. Lercher, L. Endler, H. Colaço, et al. Genomic epidemiology of superspreading events in austria reveals mutational dynamics and transmission properties of sars-cov-2. *Sci. Transl. Med.*, 12(573), 2020.

[42] Stephen B. Pope. *Turbulent Flows.* Cambridge University Press, 2000.

[43] Padmanabha Prasanna Simha and Prasanna Simha Mohan Rao. Universal trends in human cough airflows at large distances. *Phys. Fluids*, 32(8):081905, 2020.

[44] Ana Luíza Silva Rocha, Josilene Ramos Pinheiro, Thamilin Costa Nakamura, da Silva, José Domingos Santos, Beatriz Gonçalves Silva Rocha, Raphael Contelli Klein, Alexander Birbrair, and Jaime Henrique Amorim. Fomites and the environment did not have an important role in covid-19 transmission in a brazilian mid-sized city. *Sci. Rep.*, 11(1):15960, 2021.

[45] M. E. Rosti, M. Cavaiola, S. Olivieri, A. Seminara, and A. Mazzino. Turbulence role in the fate of virus-containing droplets in violent expiratory events. *Phys. Rev. Research*, 3(1), 2021.

[46] Camilla Rothe, Mirjam Schunk, Peter Sothmann, Gisela Bretzel, Guenter Froeschl, Claudia Wallrauch, Thorbjörn Zimmer, Verena Thiel, Christian Janke, Wolfgang Guggemos, Michael Seilmaier, Christian Drosten, Patrick Vollmar, Katrin Zwirglmaier, Sabine Zange, Roman Wölfel, and Michael Hoelscher. Transmission of 2019-ncov infection from an asymptomatic contact in germany. *N. Engl. J. Med.*, 382(10):970–971, 2020.

[47] B.R. Rowe, A. Canosa, J.M. Drouffe, and J.B.A. Mitchell. Simple quantitative assessment of the outdoor versus indoor airborne transmission of viruses and covid-19. *Environ. Res.*, 198: 111189, 2021.

[48] R. Sangras, O. C. Kwon, and G. M. Faeth. Self-preserving properties of unsteady round nonbuoyant turbulent starting jets and puffs in still fluids. *J. Heat Transfer*, 124(3):460–469, 2002.

[49] B. E. Scharfman, A. H. Techet, J. W. M. Bush, and L. Bourouiba. Visualization of sneeze ejecta: steps of fluid fragmentation leading to respiratory droplets. *Exp. Fluids*, 57(2):24, 2016.

[50] John H. Seinfeld. *Atmospheric chemistry and physics: from air pollution to climate change.* John Wiley & Sons, Inc, 2016.

[51] Valentyn Stadnytskyi, Christina E. Bax, Adriaan Bax, and Philip Anfinrud. The airborne lifetime of small speech droplets and their potential importance in sars-cov-2 transmission. *Proc. Natl. Acad. Sci. U.S.A*, 117(22):11875–11877, 2020.

[52] C. Sun and Z. Zhai. The efficacy of social distance and ventilation effectiveness in preventing covid-19 transmission. *Sustain. Cities Soc.*, 62:102390, 2020.

[53] J. W. Tang, W. P. Bahnfleth, P. M. Bluyssen, G. Buonanno, J. L. Jimenez, J. Kurnitski, Y. Li, S. Miller, C. Sekhar, L. Morawska, L. C. Marr, A. K. Melikov, W. W. Nazaroff, P. V. Nielsen, R. Tellier, P. Wargocki, and S. J. Dancer. Dismantling myths on the airborne transmission of severe acute respiratory syndrome coronavirus-2 (sars-cov-2). *J. Hosp. Infect.*, 110:89–96, 2021.

[54] Kelvin Kai-Wang To, Owen Tak-Yin Tsang, Wai-Shing Leung, Anthony Raymond Tam, Tak-Chiu Wu, David Christopher Lung, Cyril Chik-Yan Yip, Jian-Piao Cai, Jacky Man-Chun Chan, Thomas Shiu-Hong Chik, Daphne Pui-Ling Lau, Chris Yau-Chung Choi, Lin-Lei Chen, Wan-Mui Chan, Kwok-Hung Chan, Jonathan Daniel Ip, Anthony Chin-Ki Ng, Rosana Wing-Shan Poon, Cui-Ting Luo, Vincent Chi-Chung Cheng, Jasper Fuk-Woo Chan, Ivan Fan-Ngai Hung, Zhiwei Chen, Honglin Chen, and Kwok-Yung Yuen. Temporal profiles of viral load in posterior oropharyngeal saliva samples and serum antibody responses during infection by sars-cov-2: an observational cohort study. *Lancet Infect. Dis.*, 20(5):565–574, 2020.

[55] US Centers for Disease Control and Prevention. Covid-19 and your health, 2021. URL `https://www.cdc.gov/coronavirus/2019-ncov/prevent-getting-sick/how-covid-spreads.html`.

[56] Meg VanSciver, Shelly Miller, and Jean Hertzberg. Particle image velocimetry of human cough. *Aerosol Sci. Technol.*, 45(3):415–422, 2011.

[57] Chia C. Wang, Kimberly A. Prather, Josué Sznitman, Jose L. Jimenez, Seema S. Lakdawala, Zeynep Tufekci, and Linsey C. Marr. Airborne transmission of respiratory viruses. *Science*, 373(6558):eabd9149, 2021.

[58] Jietuo Wang, Mobin Alipour, Giovanni Soligo, Alessio Roccon, Marco de Paoli, Francesco Picano, and Alfredo Soldati. Short-range exposure to airborne virus transmission and current guidelines. *Proc. Natl. Acad. Sci. U.S.A*, 118(37), 2021.

[59] Jietuo Wang, Federico Dalla Barba, and Francesco Picano. Direct numerical simulation of an evaporating turbulent diluted jet-spray at moderate reynolds number. *Int. J. Multiph. Flow*, 137:103567, 2021.

[60] A. Weber, K. Willeke, R. Marchloni, T. Myojo, R. Mckay, J. Donnelly, and F. Liebhaber. Aerosol penetration and leakae characteristics of masks used in the health care industry. *Am. J. Infect. Control*, 21(4):167–173, 1993.

[61] Jianjian Wei and Yuguo Li. Human cough as a two-stage jet and its role in particle transport. *PloS one*, 12(1):e0169235, 2017.

[62] W. F. Wells. On air-borne infection. study ii. droplets and droplet nuclei. *Am. J. Hyg.*, 20: 611–618, 1934.

[63] W. F. Wells. *Airborne Contagion and Air Hygiene. An Ecological Study of Droplet Infections.* Harvard University Press, 1955.

[64] Roman Wölfel, Victor M. Corman, Wolfgang Guggemos, Michael Seilmaier, Sabine Zange, Marcel A. Müller, Daniela Niemeyer, Terry C. Jones, Patrick Vollmar, Camilla Rothe, Michael Hoelscher, Tobias Bleicker, Sebastian Brünink, Julia Schneider, Rosina Ehmann, Katrin Zwirglmaier, Christian Drosten, and Clemens Wendtner. Virological assessment of hospitalized patients with covid-2019. *Nature*, 581(7809):465–469, 2020.

[65] World Health Organization. Coronavirus disease (covid-19): How is it transmitted?, 2020. URL `https://www.who.int/news-room/q-a-detail/coronavirus-disease-covid-19-how-is-it-transmitted`.

[66] X. Xie, Y. Li, A. T. Chwang, P. L. Ho, and W. H. Seto. How far droplets can move in indoor environments – revisiting the wells evaporation–falling curve. *Indoor air*, 17(3):211–225, 2007. ISSN 0905-6947.

[67] Fan Yang, Amir A. Pahlavan, Simon Mendez, Manouk Abkarian, and Howard A. Stone. Towards improved social distancing guidelines: Space and time dependence of virus transmission from speech-driven aerosol transport between two individuals. *Phys. Rev. Fluids*, 5(12), 2020.

Supplementary Material of Modeling the direct virus exposure risk associated to respiratory events

Journal of The Royal Society Interface, 2021, In press.

Formula Derivation

The temporal evolution of the position, velocity, size and temperature of an evaporating droplet, whose size is smaller than the smallest scales of the turbulent carrier flow, can be described in the framework of the so-called *point-droplet approximation* [8]. In this framework, an evaporating droplet is modelled as a rigid point-wise sphere whose dynamics is described by the following Lagrangian equations [1, 6, 11, 15]:

$$\frac{du_d}{dt} = \frac{1}{f}\frac{\bar{u}-u_d}{\tau_d} + \frac{\rho_d-\bar{\rho}}{\rho_d}g, \quad f = \frac{1}{1+0.15{Re_d}^{0.687}}, \tag{1}$$

$$\frac{dD_d^2}{dt} = -4\frac{Sh}{\bar{Sc}}\frac{\bar{\rho}}{\rho_d}\bar{\nu}H_m, \tag{2}$$

$$\frac{dT_d}{dt} = \frac{1}{3\tau_d}\left[\frac{Nu}{\bar{Pr}}\frac{\bar{c_p}}{c_d}\left(\bar{T}-T_d\right) - \frac{Sh}{\bar{Sc}}\frac{\Delta H_v}{c_d}H_m\right], \tag{3}$$

where u_d is the droplet velocity, D_d is the droplet diameter, and T_d is the temperature of the droplet. The over-bar notation refers to Eulerian quantities, describing the carrier flow, evaluated at the instantaneous position of the point-droplet. Equation (1) is the one-dimensional governing equation of a sphere in viscous flow. The variable $\bar{u}$ is the velocity of the moist airflow carrying the droplet evaluated at the position of the droplet itself and $\bar{\rho}$ its density. Gravitational acceleration, g, and buoyancy forces are accounted for by the second right-hand side term of equation (1). The parameter τ_d is called droplet relaxation time, $\tau_d = \rho_d D_d^2/(18\bar{\mu})$, with ρ_d the water droplet density and $\bar{\mu}$ the dynamic viscosity of the airflow. A factor f is used to account for droplet finite inertia, which is a function of the droplet Reynolds number, $Re_d = ||\bar{u} - u_d||D_d/\bar{\nu}$, with $\bar{\nu}$ the kinematic viscosity of the carrier flow. Equation (2) governs the evolution of the droplet diameter, whereas equation (3) describes the temporal evolution of the droplet temperature. The variable $\bar{T}$ is the temperature of the moist air flow that carries the droplets. The parameters $\bar{Sc} = \bar{\nu}/D_{a,v}$ and $\bar{Pr} = \bar{\mu}\bar{c_p}/\bar{k}$ are the Schmidt and Prandtl numbers, respectively, with $\bar{c}_p$ the isobaric specific heat capacity of the moist air flow, and $\bar{k}$ its thermal conductivity. The parameter $D_{g,v}$ is the mass diffusivity of water vapor into air, whereas c_d and ΔH_v are the specific heat capacity of liquid droplet and its latent heat of vaporization, respectively. As $(\bar{T} - T_d)$ is the forcing term for convective heat transfer, the term H_m drives the mass transfer rate:

$$H_m = ln\left(\frac{1-\bar{Y}_v}{1-Y_{v,d}}\right), \tag{4}$$

with $\bar{Y}_v(\bar{\chi}_v)$ the vapor mass fraction in the carrier flow evaluated at the droplet center and $Y_{v,d}(\chi_{v,d})$ the mass fraction of a saturated gas-vapor mixture evaluated at the temperature of the droplet, T_d.

The vapor mass fractions depend on the vapor molar fractions:

$$\bar{Y}_v = \frac{\bar{\chi}_v}{\bar{\chi}_v + (1-\bar{\chi}_v)\frac{W_a}{W_d}}, \quad Y_{v,d} = \frac{\chi_{v,d}}{\chi_{v,d} + (1-\chi_{v,d})\frac{W_a}{W_d}}, \tag{5}$$

which, in turn, are related to the vapor pressure:

$$\bar{\chi}_v = \bar{RH}\,\frac{p_{sv}(\bar{T})}{p_a}, \quad \chi_{v,d} = 1.0\,\frac{p_{sv}(T_d)}{p_a}, \tag{6}$$

where p_a is the ambient pressure, $p_{sv}(\bar{T})$ the saturated vapor pressure evaluated at $\bar{T}$, $\bar{RH}$ the relative humidity of the moist carrier, W_a and W_d the molar weight of air and liquid water, respectively. The saturated vapour pressure depends on temperature and pressure and can be calculated by using the Clausius-Clapeyron equation. Finally, the Nusselt number, Nu, and Sherwood number, Sh, are correlated to the droplet Reynolds number via the Frössling correlations, see e.g. **?**] for details.

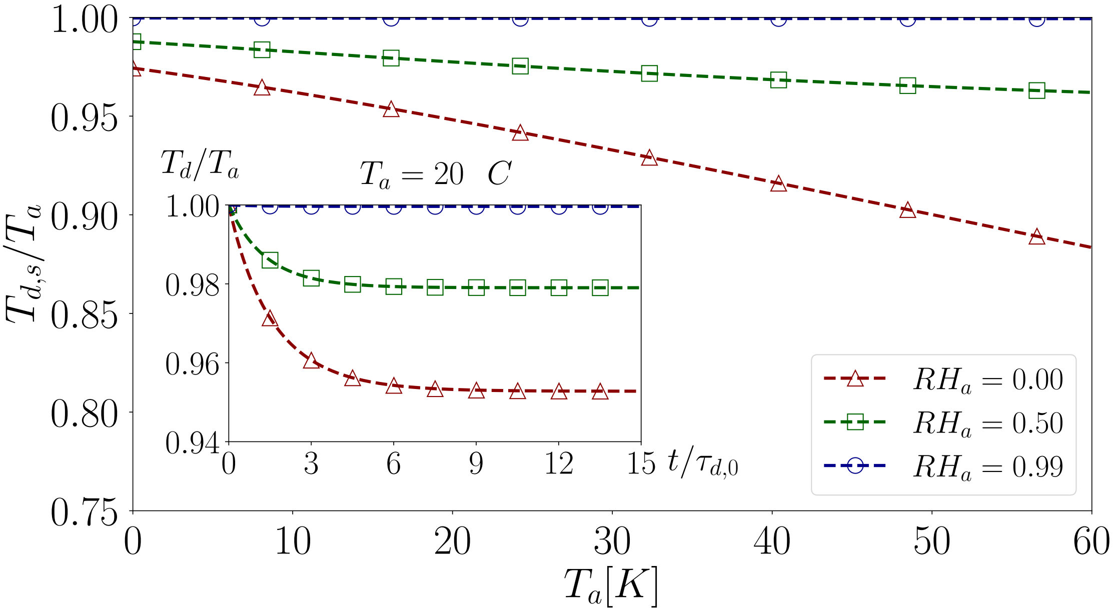

Figure 1: Main panel: the ratio between the asymptotic droplet temperature, $T_{d,s}$, computed according to equation (11) and ambient temperature, T_a, versus ambient temperature itself for an isolated water droplet. Inset: temporal evolution of the temperature of an evaporating water droplet; the time is normalized by $\tau_{d,0}$, the initial relaxation time. Data are obtained by the numerical solution of equation (2) and equation (3).

Let consider an evaporating droplet in an environment with uniform thermodynamic properties, T_a, p_a, ρ_a and RH_a being the uniform ambient temperature, pressure, density and relative humidity, respectively. Since H_m in equation (2) depends on the droplet temperature, ambient temperature and pressure, it can be assumed to be constant during evaporation. Under this assumption equation (2) can be integrated analytically:

$$D_d(t) = \sqrt{D_{d,0}^2 - kt}, \quad k = 4\frac{\rho_a}{\rho_d}\frac{Sh}{Sc_a}\nu_a H_m(T_d, T_a, p_a, RH_a), \tag{7}$$

with $D_{d,0}$ the droplet initial diameter and k a decay constant. When the effect of non-volatile matter is taken into account [2], one can estimate the droplet evaporation time as:

$$t_e = D_{d,0}^2(1-\psi^{2/3})/k. \tag{8}$$

with ψ being the volume fraction of non-volatile matter inside each droplet. In the present model, assuming for simplicity $\psi = 0$, equation (8) can be rewritten as:

$$t_e = D_{d,0}^2/k. \tag{9}$$

Equation (7) is historically referred to as $\mathcal{D}^2$-law since it predicts a linear temporal evolution of the square droplet diameter (surface), and it is used in the classical model of Wells, which implicitly assumed that the droplet temperature is fixed and equal to the initial one $T_{d,0}$ during the whole vaporization process. Under this assumption the constant k is:

$$k = 4\frac{\rho_a}{\rho_d}\frac{Sh}{Sc_a}\nu_a H_m(T_{d,0}, T_a, p_a, RH_a). \tag{10}$$

Nonetheless, this condition holds only for a short time of the order of few droplet relaxation times, $\tau_d = \rho_d D_{d,0}^2/(18\bar{\mu})$, as can be seen in the inset of figure 1. The initial droplet temperature is equal to the environmental one, T_a; nonetheless, after a time $t \simeq 6\tau_{d,0}$, the droplet temperature sets to an asymptotic value, $T_{d,s}$, which is lower than T_a depending on RH_a. Hence, the droplet temperature remains close to the ambient one only for $t \simeq \tau_{d,0}$, whereas, for the major part of the vaporization process, it keeps closer to an asymptotic temperature, $T_{d,s}$. By imposing $dT_d/dt = 0$ in equation (3), we obtain the following relation for the asymptotic temperature:

$$T_{d,s} + \frac{Pr_a}{Sc_a}\frac{Sh}{Nu}\frac{\Delta H_v}{c_{p,a}}H_m(T_a, p_a, RH_a, T_{d,s}) - T_a = 0, \tag{11}$$

$$H_m = ln\left(\frac{1 - Y_v(T_a, p_a, RH_a)}{1 - Y_{v,d}(T_{d,s}, p_a)}\right), \tag{12}$$

which can be easily solved for $T_{d,s}$. The latter can be employed to compute a more accurate value of the decay constant, k:

$$k = \frac{\rho_a}{\rho_d}\frac{Sh}{Sc_a}\nu_a H_m(T_{d,s}, T_a, p_a, RH_a). \tag{13}$$

By replacing the k constant in equation (7) with equation (13), Dalla Barba et al. [6] derived a revised D^2-law. It is worth noting that this revised model does not use any free fit parameter. The major difference between the classical and revised law relies on the assumptions made on droplet temperature. In the classical D^2-law this is assumed equal to the initial one. In the revised model, it results from the balance between the heat flux and latent enthalpy during the evaporation process. Considering an evaporating droplet with an initial temperature higher than, or equal to, the ambient temperature in quiescent air conditions, its temperature will tend to an asymptotic value, which is lower than the environmental temperature, after a short transition time. Hence, in the revised D^2-law, the droplet temperature is fixed and equal to this asymptotic value, instead of the initial one, that results in a constant evaporation rate lower than the one predicted by the classical model. The performance of this revised D^2-law has been tested against DNSs of turbulent water sprays with

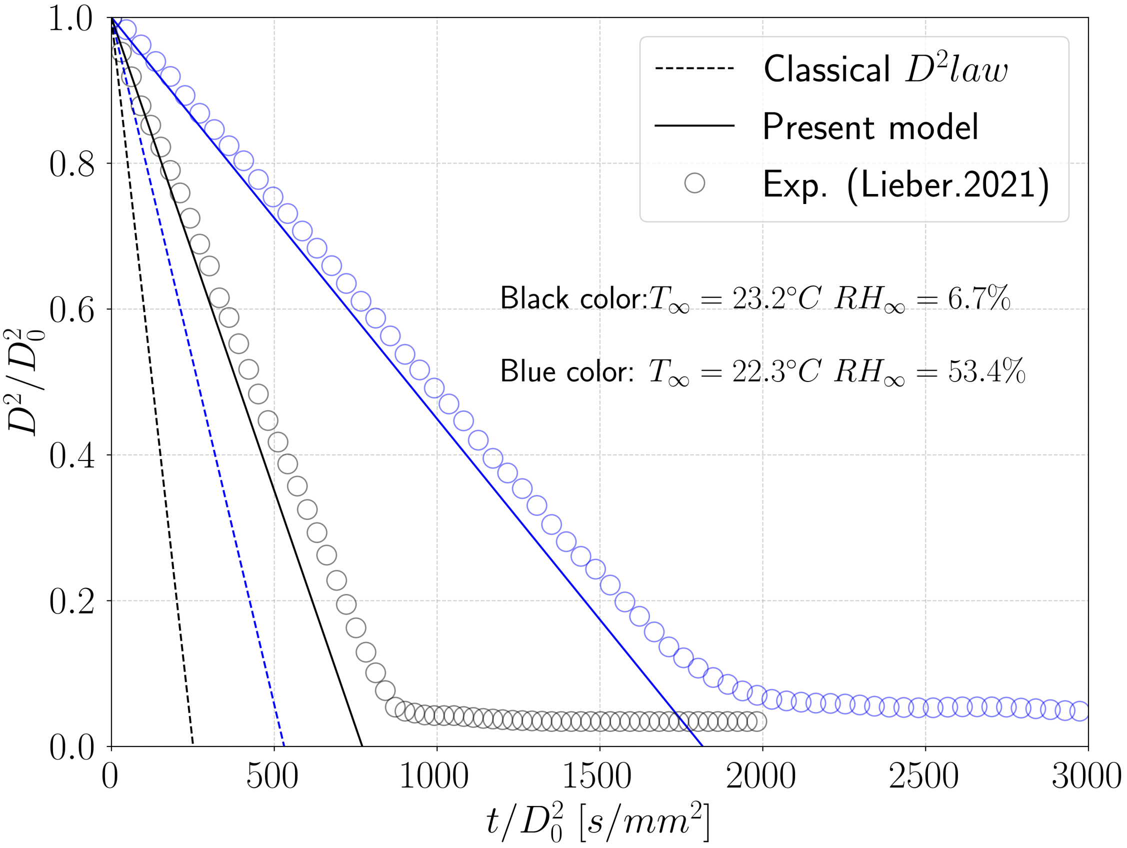

Figure 2: Comparison of the decay of the square droplet diameter of saliva droplets predicted by the classical D^2-law model (dashed lines), the present revised D^2-law model (solid lines) and experimental benchmark data (symbols) from Lieber et al. [10]. Different environmental conditions are considered: $T_\infty = 23.2°C$ $RH_\infty = 6.7\%$ and $T_\infty = 22.3°C$ $RH_\infty = 53.4\%$.

different dilute levels, as well as reference data of respiratory droplets from third parts, i.e. Ng et al. [12], exhibiting an excellent agreement. To further assess the reliability of the revised D^2-law in predicting the evaporation of a droplet we provide a comparison of our model against independent experimental data [10]. The experiments have been realized using an acoustic levitator under well-defined ambient and initial conditions, considering single water and saliva droplet [4, 10]. In figure 2 the decay of the square droplet diameter of saliva droplets predicted by the classical model, the present one and the experimental results from Lieber et al. [10] are shown. Two different environmental conditions are considered showing an approximatively linear decay. For both the cases, the revised D^2-law model shows superior performance than the classical one and very good agreement with the experimental data. As reported in Lieber et al. [10], a terminal size of around 25% of the droplet initial diameter, is reached at the end of the evaporation due to the non-volatile components inside the saliva droplet, like salts and protein. We attribute this reason to explain the slight deviation of the revised model from the experimental data at the late stage of evaporation. However, as mentioned in Dalla Barba et al. [6], some restrictions should be considered when using the revised D^2-law, i.e. single component droplets, micro/millimetre size, dilute regimes, and the different properties of turbulent jet/puff carrying the droplets and the ambient air. In fact, as shown in Figure 2B of the manuscript, the revised D^2-law fails to capture the mean behavior of droplet evaporation in low temperature and high relative humidity ambient conditions, which are strongly different from the initial jet ones. However, the obtained prediction is still much more accurate

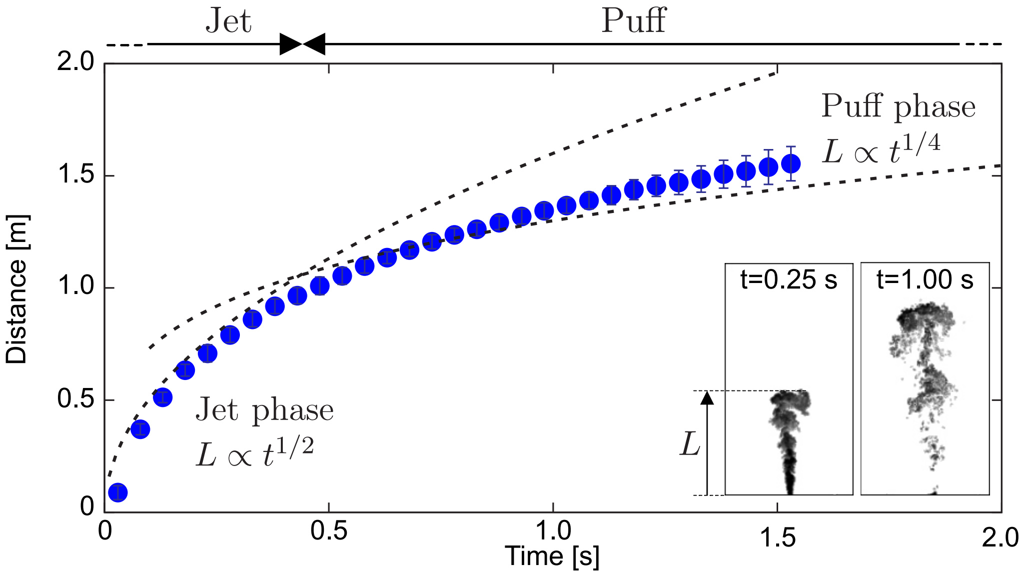

Figure 3: Distance travelled by the front of a turbulent jet/puff reproduced by experimental data from [14]. The two stages that characterize the flow, jet (early stage) and puff (late stage), are visible. The scaling laws for the jet, $L \propto t^{1/2}$, and puff phase, $L \propto t^{1/4}$, are reported as references with black dashed lines. Qualitative visualizations obtained from experiments showing the instantaneous tracers concentration (black-high; white-low) at different times ($t = 0.25$ s and $t = 1.00$ s, respectively) are reported as representative of the jet/puff evolution.

than the classical one, especially for long times.

Let consider equation (1) applied along the horizontal direction. If the droplet is sufficiently small, the term τ_d approaches zero and equation (1) becomes $u_d \simeq \bar{u}$. Hence, we assume that, along the horizontal direction, droplets move with the same velocity of the carrier flow. To estimate the axial speed of the carrier flow, we split the evolution of the exhaled flow into two different stages, as can be seen in the Fig 3. From $t = 0$ up to the time the flow is emitted from the oral cavity, $t = t_{inj}$ (injection time), we model the flow as an axial, steady round jet for which a well-established, self-similar velocity profile is known [13]. On the other hand, for $t > t_{inj}$, we model the flow as a free turbulent puff. For the latter, the distance travelled by a Lagrangian tracer is known to scale with a power law of $t^{1/4}$, $L/L_0 \sim (t/t_0)^{1/4}$ [9]. In this frame, for $t \leq t_{inj}$, by neglecting possible two-way coupling effects, an estimate of the length covered by droplets carried by the jet can be obtained by considering the self-similar behaviour of the mean jet centerline velocity, $U_c \simeq \bar{u}$, and supposing that the droplet mean axial velocity is approximated by $u_d \simeq U_c$:

$$\frac{U_c}{U_0} = \frac{2B}{\frac{x}{R_0} - \frac{x_0}{R_0}} \qquad \Longrightarrow \qquad \frac{R_0}{U_0}\frac{d}{dt}\left(\frac{x_d}{R_0}\right) = \frac{2B}{\frac{x_d}{R_0} - \frac{x_0}{R_0}}, \tag{14}$$

with $B \simeq 6$ a universal constant, x_0 the so-called jet virtual origin [7], x_d the droplet position along the jet axis, U_0 the bulk velocity at the exit of the oral cavity and R_0 the mouth radius (under the assumption of a nearly circular orifice). Then, integrating equation (14) and assuming a vanishing virtual origin, $x_0/R_0 \simeq 0$, it leads to:

$$L_d = x_d = \sqrt{4BU_0R_0}\, t^{\frac{1}{2}}. \tag{15}$$

For $t > t_{inj}$, we suppose that the exhaled moist air behaves like a puff. For the latter, the distance travelled by a Lagrangian tracer scales as $L/L_0 \sim (t/t_0)^{1/4}$ and its initial value has to match the one obtained by equation (15). Hence,

$$L_d = x_d = \sqrt{4BU_0R_0}\, t_{inj}^{\frac{1}{4}}\, t^{\frac{1}{4}}. \tag{16}$$

Finally, let consider equation (1) along the vertical direction. We suppose that large evaporating droplets, acting as ballistic particles, reach their terminal settling velocity with a negligible transient time. Hence, by setting $du_d/dt \simeq 0$ and $\bar{u} = 0$, considering the definition of the droplet relaxation time, $\tau_d = \rho_d D_d^2/(18\bar{\mu})$, as well as equation (7) and (13), we obtain:

$$u_d(t) = \frac{1}{18}\frac{f}{\bar{\mu}}(\rho_d - \bar{\rho})gD_d^2, \quad f = \frac{1}{1 + 0.15{Re_d}^{0.687}}. \tag{17}$$

By setting a null initial vertical velocity, the falling distance displaced by droplets, $H_d(t)$, can be obtained by integrating equation (17):

$$H_d(t) = \frac{f}{18}\frac{\rho_d - \bar{\rho}}{\bar{\mu}}g(D_{d,0}^2 t - \frac{k}{2}t^2) \tag{18}$$

Finally, the latter can be solved for the settling time, t_s, when the vertical distance is specified, e.g. $H_d = 2m$. The solution is provided in the following, skipping algebraic manipulation:

$$t_s = \frac{1}{k}\left(D_{d,0}^2 - \sqrt{D_{d,0}^4 - \frac{36\bar{\mu}kH_d}{(\rho_d - \bar{\rho})gf}}\right). \tag{19}$$

Model description

To further explain how the present model was developed step by step based on the classical framework, we show in figure 4 a comparison of the lifetime of free-falling, evaporating water droplets estimated with different models (lines), from A) to D), against the benchmarking data (symbols) collected from Xie's results [16]. The seminal theory introduced by Wells in the 1930s, based on the classical D^2-law and Stokes' law, highly overestimates droplet evaporation rate, leading to the prediction of very short evaporation times, as reported by recent studies [2, 3, 5, 14] and highlighted in Panel A of figure 4. Simply replacing the classical D^2-law with the revised one [6], a relevant improvement is observed, see Panel B. However, some discrepancies still subsist; these are attributed to the non-negligible transition time for droplets to reach the asymptotic temperature and the inaccuracy of Stokes' law in describing the settling velocity of evaporating droplets with inertia. These two deficiencies have been mitigated by considering a two-stage evaporation model and a fixed drag correction factor, as showed in Panel C and D of figure 4, sequentially.

Bibliography

[1] B. Abramzon and W. A. Sirignano. Droplet vaporization model for spray combustion calculations. *Int. J. Heat Mass Transf.*, 32(9):1605–1618, 1989.

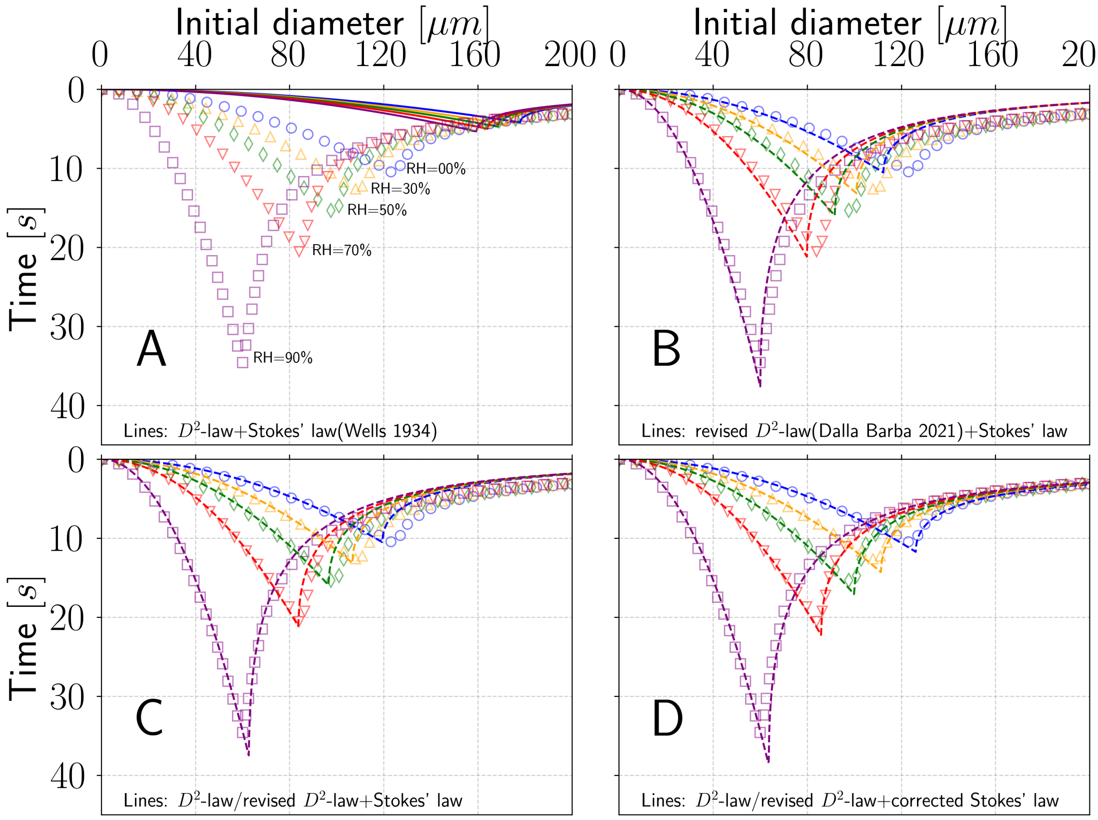

Figure 4: Comparisons of the lifetime of free-falling, evaporating water droplets with different initial sizes under different environmental conditions: A) Wells Theory; B) Revised D^2-law coupled with Stokes' law; C) Two-stages D^2-law coupled with Stokes' law; D) Two-stages D^2-law coupled with corrected Stokes' law. These predictions are shown in lines, whereas the symbols represent benchmarking data collected from Xie's results [16]. It is worth remarking that the prediction accuracy of the classical model can be improved by taking into account the revised D^2-law, the two-stages evaporation model and a fixed drag correction factor f.

[2] S. Balachandar, S. Zaleski, A. Soldati, G. Ahmadi, and L. Bourouiba. Host-to-host airborne transmission as a multiphase flow problem for science-based social distance guidelines. *Int. J. Multiph. Flow*, 132:103439, 2020.

[3] L. Bourouiba. Turbulent gas clouds and respiratory pathogen emissions: Potential implications for reducing transmission of covid-19. *JAMA*, 323(18):1837–1838, 2020.

[4] Swetaprovo Chaudhuri, Saptarshi Basu, Prasenjit Kabi, Vishnu R. Unni, and Abhishek Saha. Modeling the role of respiratory droplets in covid-19 type pandemics. *Phys. Fluids*, 32(6): 063309, 2020.

[5] Kai Leong Chong, Chong Shen Ng, Naoki Hori, Rui Yang, Roberto Verzicco, and Detlef Lohse. Extended lifetime of respiratory droplets in a turbulent vapor puff and its implications on airborne disease transmission. *Phys. Rev. Lett.*, 126(3):034502, 2021.

[6] F. Dalla Barba, J. Wang, and F. Picano. Revisiting d2-law for the evaporation of dilute droplets. *Phys. Fluids*, 33(5):051701, 2021.

[7] Federico Dalla Barba and Francesco Picano. Clustering and entrainment effects on the evaporation of dilute droplets in a turbulent jet. *Phys. Rev. Fluids*, 3(3):034304, 2018.

[8] Patrick Jenny, Dirk Roekaerts, and Nijso Beishuizen. Modeling of turbulent dilute spray combustion. *Prog. Energy Combust. Sci.*, 38(6):846–887, 2012.

[9] L. S. Kovasznay, H. Fujita, and R. L. Lee. Unsteady turbulent puffs. *Adv. Geophys.*, 18: 253–263, 1975.

[10] C. Lieber, S. Melekidis, R. Koch, and H.J. Bauer. Insights into the evaporation characteristics of saliva droplets and aerosols: Levitation experiments and numerical modeling. *J. Aerosol Sci.*, 154:105760, 2021.

[11] R. S. Miller, K. Harstad, and J. Bellan. Evaluation of equilibrium and non-equilibrium evaporation models for many-droplet gas-liquid flow simulations. *Int. J. Multiph. Flow*, 24(6): 1025–1055, 1998.

[12] Chong Shen Ng, Kai Leong Chong, Rui Yang, Mogeng Li, Roberto Verzicco, and Detlef Lohse. Growth of respiratory droplets in cold and humid air. *Phys. Rev. Fluids*, 6(5):054303, 2021.

[13] Stephen B. Pope. *Turbulent Flows*. Cambridge University Press, 2000.

[14] Jietuo Wang, Mobin Alipour, Giovanni Soligo, Alessio Roccon, Marco de Paoli, Francesco Picano, and Alfredo Soldati. Short-range exposure to airborne virus transmission and current guidelines. *Proc. Natl. Acad. Sci. U.S.A*, 118(37), 2021.

[15] Philipp Weiss, Valentin Giddey, Daniel W Meyer, and Patrick Jenny. Evaporating droplets in shear turbulence. *Physics of Fluids*, 32(7):073305, 2020.

[16] X. Xie, Y. Li, A. T. Chwang, P. L. Ho, and W. H. Seto. How far droplets can move in indoor environments – revisiting the wells evaporation–falling curve. *Indoor air*, 17(3):211–225, 2007. ISSN 0905-6947.